SCUOLA NORMALE SUPERIORE

PH. D. THESIS

IN MOLECULAR BIOPHYSICS

Aptamers against transferrin receptor: rational engineering of nanoscale platforms for targeted delivery of molecular payloads

CANDIDATE

David Porciani

ADVISORS

Fabio Beltram

Giovanni Signore

2015/16

Table of Contents

Introduction

Cancer remains one of the leading causes of death worldwide with high morbidity and mortality. Though significant advances have been made in the fundamental understanding of cancer biology, the treatment of some cancer forms remains elusive, and in general cancer treatments suffer from severe side effects. Cancer cells share many common features with the normal host cells from which they derive. As a consequence, traditional anticancer agents do not achieve the specific toxicity shown by bacterial and viral chemotherapeutics due to their lack of selectivity, and ultimately they lead to significant off-target effects.

Interestingly, cancer cells show different composition of cell membrane compared to healthy cells, with an enhanced expression of specific proteins (i.e. cell-surface markers) required to increase the provision of nutrients and to enhance cell-cell signaling and communication. Thus, a valid strategy to improve the selectivity of the treatments relies on the development of molecules able to discriminate between diseased and healthy cells by interacting with these cell-surface markers. Over the past decades an exciting trend in life sciences and biotechnology has been the rapid development of highly specific structures recognizing these cell-surface markers. Nanomedicine aims at exploiting these ligands to generate nanoscale platforms for targeted cancer therapy and diagnosis. In this way, non-selective therapeutics are localized and concentrated at the targeted site via ligands that recognize tumor-associated markers, thus leading to negligible off-target effect.

Aptamers are short single-chained DNA or RNA molecules able to recognize molecular targets with high affinity and specificity owing to their exclusive spatial conformation that are emerging as a class of biocompatible ligands with huge potential in diagnostics and therapeutics. Despite the rapid development of a wide variety of targeted delivery platforms exploiting aptamers as nanocarriers against cell-surface receptors, these strategies show some limitations that could hamper

the transition to clinical application, including elaborated design, difficult scale-up, and complex aptamer-payload conjugate preparation. Furthermore, aptamers as targeting moieties have been used mainly to deliver small drugs and small interfering RNAs. However, a modular aptamer-based platform to deliver large therapeutic payloads, such as therapeutic aptamers recognizing cancer-associated protein, was not developed yet, likely due to limitations in designing suitable assemblies in which the oligonucleotide modules retain their proper activity. Therefore, the work reported in this thesis addresses these restrictions in aptamer technology for targeted delivery applications.

In this thesis, I shall describe novel designs and molecular engineering strategies that lead to aptamer-based nanoassemblies with enhanced and innovative features as tools for targeted cancer therapy. These assemblies exploit known RNA and DNA aptamers recognizing a cell-surface protein, the transferrin receptor (TfR). Particularly, TfR was chosen as biomolecular target owing to (i) its upregulation in many solid tumors (e.g. breast, prostate, pancreatic, ovarian, lung) and (ii) its constitutive endocytic pathway. Thus, aptamers binding TfR may discriminate between tumor and healthy cells and aptamer-based platforms may selectively deliver into target cells therapeutic payloads upon binding to TfR via receptor-mediated endocytosis. To achieve these goals, this thesis work exploits the synergy among different studies of aptamer properties, in terms of folding stability, recognition of target cell population and efficiency of internalization into target cells.

The outline of the thesis is the following:

- ***Chapter 1*** provides a review of aptamers an emerging class of targeting ligands for cancer therapy. Emphasis on the advantages of aptamers compared to antibodies will be reported together with their drawbacks and the innovative solutions to overcome these limitations. The in vitro evolutionary selection process used for the aptamer generation will be described. Then, I shall introduce the main approaches and the most representative applications of cell-specific aptamers. Particularly, I shall focus on the conjugation designs used to deliver traditional anticancer drugs and functional therapeutic oligonucleotides.

- In ***Chapter 2*** I shall describe a molecular-engineering strategy to develop a drug-delivery system that is able to *(i)* target human tumor cells via an anti-transferrin receptor RNA aptamer and *(ii)* perform selective co-delivery of a chemotherapeutic drug (doxorubicin) and of an inhibitor of a cell-survival factor, the NF-κB decoy oligonucleotide. I shall demonstrate that this platform shows selective cytotoxicity activity towards tumor cells, owing to the targeting properties of the aptamer. Upon internalization, the NF-κB decoy does inhibit NF-κB activity, reducing tumor chemoresistance towards doxorubicin and enhancing its therapeutic efficacy specifically in target cells.

- In ***Chapter 3*** a biophysical study to unveil the conformation-dependent activity of an anti-mouse TfR DNA aptamer will be reported. I shall demonstrate the presence of competing folding pathways, which sensibly affected the aptamer activity. Indeed, two main aptamer conformers were identified and their activities investigated both in vitro and in living cells. Actually, only one conformer was able to bind mouse TfR. Starting from these observations I rationally designed variations of the parent sequence aimed at stabilizing the active conformation. This strategy led to an enhanced aptamer sequence with higher affinity and improved biological activity, which emerges as a valid targeting ligand both for *in vitro* and *in vivo* applications.

- In ***Chapter 4***, I shall report on the design and synthesis of a modular platform for aptamer-mediated cellular delivery of increasingly large RNA payloads (~50-60 kDa). In order to demonstrate the versatility of this platform, anti-TfR RNA and DNA aptamers, previously investigated in Chapter 2 and 3, will be exploited as targeting and delivery tools, and fluorescent RNA aptamers (known as RNAs mimic of GFP) as large functional RNA payloads. These aptamers were chosen as RNA sensors to monitor both their intracellular localization and to evaluate folding alterations within the oligonucleotide platform because their fluorescence depends on the retaining of the proper fold. Taking inspiration from the design of the delivery system described in Chapter 2, the assembly is generated through straightforward self-assembly by means of a short oligonucleotide bridge that contains regions complementary to both aptamers. In this chapter, I shall demonstrate the possibility to selectively deliver to living cells large functional

RNAs using different combinations of targeting and payload aptamers. This "proof of concept" is the first evidence of an aptamer-mediated aptamer delivery.

- In ***Chapter 5*** I shall summarize the main findings of this research activity and discuss some perspectives of the aptamer-based nanoscale platforms proposed in this thesis.

Chapter 1

Nucleic acid aptamers: new tools for targeted drug delivery applications

1.1 Brief overview on targeted therapy: passive and targeting drug delivery

One hundred years ago, Paul Ehrlich popularized the "magic bullet" concept as an ideal strategy for targeted therapy against virtually any disease. Theoretically, a magic bullet is a therapeutic agent able to overcome biological barriers, distinguish between diseased and healthy tissues and selectively kill only target cells, avoiding off-target effect[1]. Despite extensive research carried out in this field, safe and efficient drug delivery for the treatment of most disorders (e.g. cancer and infectious diseases) remains a major challenge both for clinical translation and the development of new therapies[2]. Conventional therapeutic agents are administered systemically and are unable to target the site of the disease, ultimately leading to unwanted side effects and to a reduction of the therapeutic index (i.e. the ratio between the dosage of a drug that causes a lethal effect and the dosage that causes a therapeutic effect). Nanomedicine aims at overcoming these drawbacks, allowing the construction of nanosized molecular devices (10-200 nm) for targeted delivery of therapeutic and/or diagnostic agents[3].

During the last decade, the rapid expansion of new nanotechnologies tailored to cancer treatment has been an exciting trend in nanomedicine. Compared with conventional therapy, nanomedicine offers significant advantages and new perspectives in which novel drug-delivery platforms exploit passive and active targeting to improve their therapeutic index[4]. Passive targeting takes advantage of the unique physiology and structure of the tumor microenvironment (e.g. highly permeable vasculature, and poorly-defined lymphatic system), which results in drug accumulation through the enhanced permeability retention (EPR) effect (Fig.1). This strategy can be achieved by modulating the size, shape, and surface properties of the drug delivery platform. To date, dozens of nanosized devices, named first-generation nanomedicines, were approved by the Food and Drug Administration (FDA) and proved to be well tolerated in patients[5,6]. However, several factors mainly dependent on patient and/or stage of disease (such as blood pressure, structure of neo-vasculature, and disease type and location) can adversely affect passive transport, often leading to inadequate drug concentration into target districts and lower therapeutic efficacy[3,7] (Fig.1).

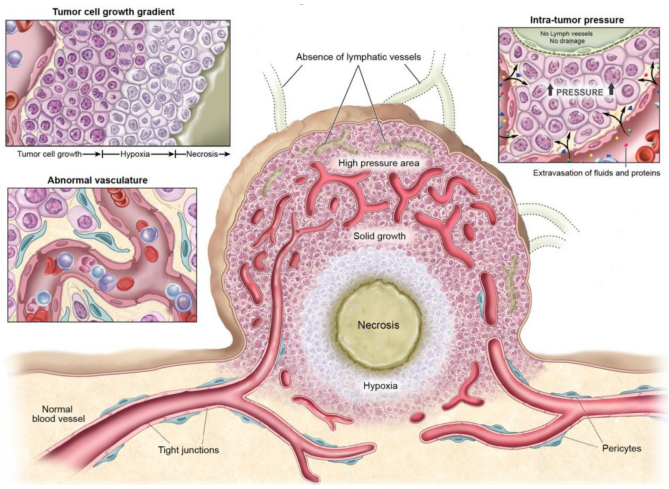

Fig 1 Physiological properties of tumor tissue and vasculatures that influence cancer drug delivery. Reprinted from Kobayashi et al.[8]; Copyright © Ivyspring International Publisher (2013).

Ultimately, passive targeting strategy does not discriminate satisfactorily between normal and cancerous cells; this in turn leads to modest improvements compared to conventional therapeutic strategies[9].

A common strategy to enhance selectivity relies on targeting specific biomolecules overexpressed on the surface of tumor cells. To this end, many ligands were developed and exploited to deliver potent nonspecific cytotoxic agents selectively to malignant cells. The general structure of these ligand-payload platforms involves a targeting moiety linked to a therapeutic payload via a spacer that often contains a cleavable bond[10]. Alternatively, specific targeting ligands can be conjugated and displayed on the surface of nanosized devices (or nanocarriers) designed for passive targeting drug delivery. When the suitable recognition motif is included in these nanocarriers, it endows the entire system with selectivity towards target cells, leading to more efficient "actively targeted" nanostructures, also called second-generation nanodevices[11] (Fig. 2).

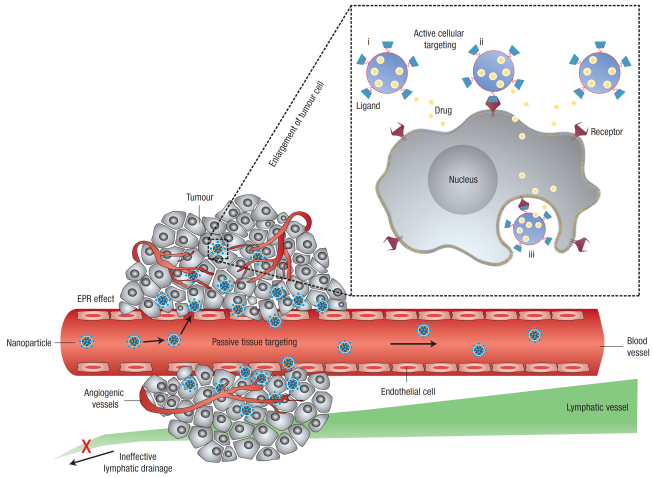

Fig. 2 Schematic representation of several mechanisms by which nanocarriers can deliver drugs to tumors. Nanocarriers are shown as blue circular structures. Passive tissue targeting is achieved by extravasation of nanoparticles through increased permeability of the tumor vasculature and ineffective lymphatic drainage (EPR effect). Active cellular targeting (inset) can be achieved by functionalizing the surface of nanoparticles with ligands that promote cell-specific recognition and binding. The

nanoparticles can (i) release their contents in close proximity to the target cells; (ii) adhere to cell membrane and act as an extracellular sustained-release drug depot; or (iii) internalize into the cell. Adapted from Peer et al.[12] Reprinted by permission from Macmillan Publishers Ltd: Nature Nanotechnology (Ref. 12), Copyright © 2007

1.2 Cell-surface markers: the gate at the entrance of diseased cells

Several genetic mutations lead to the deregulation of specific signaling pathways involved into cell proliferation, survival, or differentiation, causing uncontrolled cell growth and acquisition of neoplastic phenotype[13]. As a consequence of this mutated signal transduction, specific cell-surface and intracellular receptors show high expression levels in diseased tissue compared with other tissues (for example tumors versus healthy cells)[13,14]. An ideal target molecule is overexpressed on the surface of cancer cells rather than within its intracellular compartment (e.g cytoplasm or nucleus). Although several intracellular receptors (such as steroid receptors and retinoic acid receptors) are upregulated in cancer, a drug-delivery platform must be cell permeable to target and interact with them at an intracellular level. This would likely cause unwanted side effects due to nonspecific internalization[10]. In contrast, ligands that target cell-surface receptors can be engineered to be membrane-impermeable, reducing their nonspecific cell uptake[10]. Therefore cell-surface markers represent ideal targets for the specific delivery of therapeutics to malignant cells avoiding off-target effects. The two main features of the targeted cell-surface receptor that must be considered while designing a targeted drug delivery device are (i) the extent of its overexpression in cancer cells relative to normal cells and (ii) its ability to perform a receptor-mediated endocytosis of the drug delivery platform, allowing intracellular accumulation of therapeutic quantities. This latter property is tightly dependent on the type of targeted therapy. Internalization might be essential for optimal results in therapies such as antibody-drug conjugates or immunoliposomes[15,16]. In other cases, such as antibody-directed-enzyme-prodrug therapy (ADEPT)[17], no internalization is required for the targeted drug delivery tool used in this approach: i.e. an antibody-enzyme conjugate. Indeed, after

antibody recognition of a non-internalizing receptor, the antibody-enzyme conjugate must be located on the cell-surface to convert non-active prodrugs into active cell-permeable cytotoxic molecules through the enzyme portion[18]. In this strategy, however, the activated drugs that are released in the tumor interstitial space might diffuse and non-selectively internalize into the nearby normal cells that do not express the cell-surface marker, causing off-target effects[17]. Thus, internalization of the targeted receptor appears to be the preferential way to achieve a desired therapeutic effect with negligible side effects.

With regard to the high level of expression of the targeted receptor in tumor cells, a threefold upregulation is commonly considered sufficient to perform efficient targeted drug delivery, although higher expression enhancement is obviously preferred[10]. Note that many healthy tissues are quiescent (or non-mitotic): they do not show cell proliferation and are thus less sensitive to antimitotic chemotherapeutic drugs. In this context, even a threefold overexpression leads to a significant improvement of the selectivity compared with the corresponding non-targeted therapy. Notably, several targeted receptors currently under clinical investigation are expressed in two- to five-fold excess in malignant tissues[10].

Some tumor processes lead to cleavage of extracellular domains of cell-surface markers, shedding them into circulation[18]. These circulating domains may compete with the intact cell-surface markers for the binding of the ligand-payload platform, leading to accumulation in a body district away from the tumor tissue and reducing the therapeutic efficacy. The choice of candidate receptors should therefore avoid proteins undergoing this processing.

It is worth mentioning that in receptor-mediated drug delivery, the ligand-payload platform internalizes into target cells upon binding with its target molecule by a receptor-mediated endocytosis and then traffics through different intracellular vesicular compartments, depending on the receptor is exploited for the internalization. Some of the most common endocytic compartments encountered during intracellular trafficking include: endosomes (early, late and recycling) and lysosomes (Fig. 3).

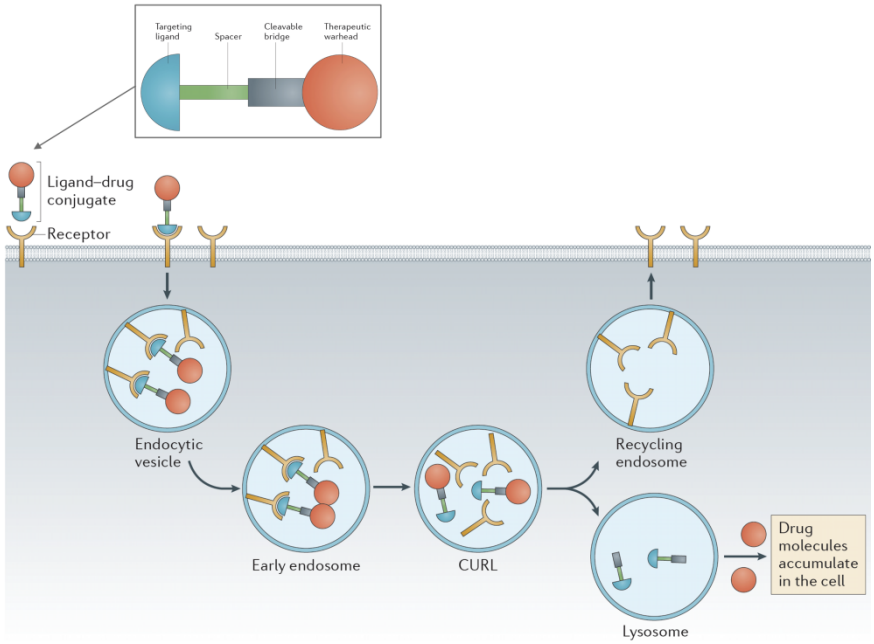

Fig. 3 Internalization pathway of a ligand-targeted therapeutic agent. The ligand-payload conjugate includes within its structure: a targeting ligand; a spacer; a cleavable bridge that is stable in circulation but that permits drug release following endocytosis into a target cell; and a therapeutic 'warhead'. Upon binding with the targeted receptor, the ligand–drug conjugate is internalized into the cells. During the intracellular trafficking of the ligand-payload conjugate several compartments are encountered including early endosome, compartments for uncoupling of receptor and ligand (CURLs), recycling endosome, and lysosomes. Adapted from Srinivasarao et al.[10] Reprinted by permission from Macmillan Publishers Ltd: Nature Reviews Drug Discovery (Ref. 10), Copyright © 2015.

Particularly, during the endocytosis pathway the intravesicular environment of the endosome undergoes alterations of pH, ion composition, and redox potential. According to these different features it is possible to distinguish early and late endosomes[19]. Overall, these environmental variations may lead to the dissociation of the ligand-payload platform from the receptor. Note that the compartment

where the dissociation occurs is termed compartment for uncoupling of receptor and ligand (CURL) and usually corresponds to the early endosome[20]. After that, the unbound receptor and the free ligand-payload can be sorted into separate vesicular compartments, allowing the receptor to be either degraded in the lysosomes or recycled on the plasma membrane for another round of endocytosis[21].

Importantly, the delivery platform can be engineered to release the therapeutic payload at the endolysosomal stage, where conventional chemotherapeutic drugs can freely diffuse to the cytoplasm and perform their anticancer activity[22,23].

A critical aspect in the receptor-mediated targeted delivery is the availability of receptors on the surface of cancer cells that can interact with the excess of ligand-payload platforms present on the extracellular side, in order to allow continuous drug uptake. In this context, an ideal targeted receptor will be one that either recycles frequently or is resynthesized rapidly following degradation[10]. Importantly, most cell-surface markers show enhanced receptor-recycling rate or resynthesis rate in malignant cells compared with healthy cells, thus allowing increased receptor-mediated delivery of therapeutics in cancer cells[10,24].

Here, I shall discuss the properties of three cell-surface receptors that were extensively investigated in the last decade. One of these proteins, the transferrin receptor, is also the target receptor exploited in this thesis for our drug delivery studies.

PSMA. Prostate-specific membrane antigen (PSMA) is a 100 kDa type II membrane glycoprotein expressed in all types of prostatic tissues, including normal epithelial cells[25], benign prostatic hyperplasia[26], prostatic intraepithelial neoplasia[27], and cancerous tissue[28]. Furthermore, very low levels of PSMA were detected in kidney, proximal small intestine, salivary gland, and brain[29]. In addition to full-length PSMA, several splice variants exist in prostatic tissue, namely PSM', PSM-C, PSM-D, and PSM-E. Notably, the N-terminally truncated PSMA variant, termed PSM', is the most frequently described alternatively spliced variant of PSMA and is the most prevalent form in healthy prostatic cells where it is located cytosolically[30]. During malignant progression, prostatic epithelial cells

express the transmembrane/extracellular form of the protein, PSMA. Therefore, the ratio of PSMA/PSM' mRNA was shown to correlate with cancer progression[31]. Note that, almost 95% of prostate cancers express PSMA, with the highest level of expression found in the most aggressive cancers[32].

Interestingly, besides being expressed in prostatic tissues, PSMA is also expressed in tumor-associated neovasculature of many solid cancers including prostate, lung, breast and colon[33]. Thus, targeting neoangiogenesis through PSMA may represent a valid diagnostic and therapeutic option in several solid tumors.

Although a PSMA-endogenous ligand was not discovered yet, PSMA can constitutively internalize into cells by receptor-mediated endocytosis via clathrin-coated pits[34]. In the last decade, several PSMA targeted ligands such as antibodies[35], aptamers[36] and peptides[37] were developed and exploited to perform targeted delivery of chemotherapeutics and imaging agents into PSMA-positive tumor cells both *in vitro* and *in vivo*[38]. Particularly, these ligands were internalized upon binding with PSMA on the cell membrane even without possessing agonist-like function.

HER2. The human epidermal growth factor receptor-2 (EGFR2 or HER2) is a member of the human epidermal growth factor receptor (EGFR) family, a class of Receptor Tyrosine Kinase (RTK). In fact, HER2 is a 185 kDa transmembrane receptor with an extracellular binding domain and an intracellular tyrosine kinase domain. Upon binding with specific extracellular ligands, receptor dimerization occurs with the formation of homodimers or heterodimers with HER3 or HER4 that triggers intracellular signaling cascades. The most activated downstream signaling pathways lead to increased proliferation and invasiveness. Notably, overexpression of HER2 is associated with subsets of multiple cancer types such as breast, ovarian, cervical, uterine, and gastric[39]. Particularly, overexpression in 25-30% of all breast cancers coincides with an aggressive phenotype and poor prognosis. This HER2-upregulation is due to a remarkable gene amplification (e.g. 25-50 copies of HER2 gene) that may lead up to a 40-to 100-fold enhanced protein expression[40,41].

Unlike other RTKs of this family whose extracellular domains shuttle between a closed inactive state and a ligand activated open state, HER2 exhibited a constitutively active open state. Additionally, HER2 has the strongest catalytic kinase activity and heterodimers containing HER2 exhibit the most effective downstream signaling activation. This feature suggests to target HER2 both for inhibiting this receptor and carrying therapeutic or diagnostic agents.

Interestingly, HER2 targeted agents were extensively used to treat HER2-positive breast cancer[41] Particularly, Trastuzumab (Herceptin®), a human monoclonal anti-HER2 antibody with inhibitory property, recently received FDA approval for the treatment of HER2 overexpressing breast cancer[42]. Trastuzumab can be used alone or in combination with chemotherapy drugs such as doxorubicin, cisplatin, cyclophosphamide, and either paclitaxel or docetaxel[43]. Although Trastuzumab is the first treatment for HER2 positive-breast cancer, several intracellular resistance mechanisms against this antibody were recently discovered that lead to a reduced therapeutic efficacy or insensitivity to Trastuzumab[44,45]. To date, novel targeted therapies and new systems to overcome Trastuzumab resistance are under investigation[46].

Finally, recent findings showed that HER2-targeted therapeutic agents also inhibited the growth of breast cancer stem cells found in HER2-negative patients suggesting the importance of HER2 as target for multiple types of breast cancer[47].

TfR. Transferrin receptor (also known as CD71) is a type II transmembrane homodimer glycoprotein (180 kDa) involved in the cellular uptake of iron and in the regulation of cell growth. The TfR monomer contains three domains: a large extracellular C-terminal domain, a single-pass transmembrane domain, and a short intracellular N-terminal domain. Iron uptake occurs via the internalization of iron-loaded transferrin (Tf) mediated by the interaction with the TfR (Fig. 4). Tf is a monomeric glycoprotein (called apo-Tf) that can transport one (monoferric Tf) or two (diferric Tf) iron atoms. Diferric Tf (also known as holo-Tf) has the highest affinity for the TfR; being 10- to 100-fold more affine to TfR compared with apo-Tf at physiological pH[48]. Upon binding TfR, the Tf/TfR complex is internalized in clathrin-coated pits through receptor-mediated endocytosis[48]. Particularly in the

endosomal compartment, the transferrin structure undergoes a conformational change due to pH decrease and iron is released from the protein. Tf still remains bound to its receptor at this pH and the apo-Tf/TfR complex is recycled back to the cell surface where apo-Tf is released ready to bind iron atoms in the extracellular milieu. Interestingly, TfR undergoes recycling constitutively, with or without binding to its ligand, transferrin[49].

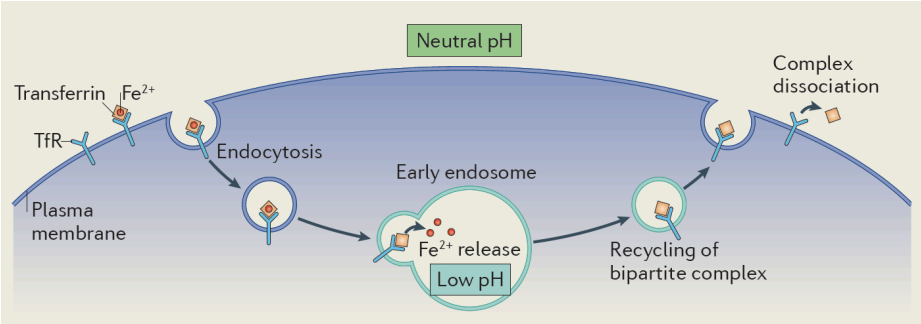

Fig. 4 Schematic representation of transferrin receptor-mediated endocytosis. The TfR is constiuitively internalized via receptor-mediated endocytosis. Upon binding of iron-loaded transferrin to TfR, internalization of the tripartite complex occurs. This complex is delivered into endosomes where the decrease in pH triggers the release of iron from the Tf/TfR complex. The bipartite complex is sorted to either its corresponding degradation or recycling pathways in the early endosome. The restoration of neutral pH following recycling to the cell surface induces the dissociation of the Tf/TfR complex Adapted from Hsu et al.[49] Reprinted by permission from Macmillan Publishers Ltd: Nature Reviews Molecular Cell Biology (Ref. 49), Copyright © 2012.

Iron is a co-factor involved in many enzymatic reactions including metabolism, respiration, and DNA synthesis[48]. The TfR is ubiquitously expressed on normal cells and its expression is sensitively increased on cells with a high proliferation rate that require large amounts of iron. Therefore, TfR is significantly upregulated in a variety of tumor cells (e.g. breast, prostate, pancreatic, ovarian, lung, chronic lymphocytic leukemia and non-Hodgkin's lymphoma) and in many cases increased expression correlates with tumor stage and is associated with poor

prognosis[48]. Note that, the expression of TfR in cancer cells can be up to 100-fold higher than the average expression of normal cells[50,51]. Moreover, high levels of TfR were found on the brain capillary endothelium of the blood-brain barrier (BBB) where it plays a crucial role in the receptor-mediated transcytosis of the iron-loaded Tf across the BBB[52]. As a consequence, TfR is one of the most widely investigated targeted receptor for drug delivery across the blood–brain barrier[53].

Owing to its enhanced expression in specific districts of the body (such as BBB) or in malignant tumor cells, its extracellular accessibility, and its ability to internalize, transferrin receptor represents an attractive target for targeted drug delivery applications and is an ideal marker in cancer diagnosis. Particularly, both monoclonal antibodies-[54] and transferrin- drug conjugates[55] have been extensively investigated as nanocarriers for the treatment of several solid tumors and for delivering therapeutic cargoes to the brain compartment[56]. However both these strategies display several limitations due to (i) the intrinsic drawbacks of monoclonal antibody technology and (ii) the competition between endogenous Tf and the exogenous Tf-drug conjugates. Specifically, transferrin receptors are nearly saturated by endogenous Tf under physiological conditions (concentration of circulating Tf is about 2.4 mg/ml i.e. ~25 mM)[57], and exceedingly high concentrations of exogenous Tf derivatives are necessary to ensure adequate delivery of payloads to target tissues[58].

1.3 Targeting ligands: the keys to open the gates of the diseased cells

An insightful comparison has been recently introduced between the cell and the castle structure[59]: if the plasma membrane represents the walls of the cellular fortress, and its overexpressed receptors are the fortress gates, the ligands recognizing these markers and internalizing into the cells will be the “keys of the castle”.

To date, there are several ways to unlock the fortress gates in the form of proteins (mainly antibodies and their fragments), oligonucleic acids (DNA and RNA aptamers), and other receptor ligands (peptides, vitamins, carbohydrates, and

protein-endogenous ligands such as transferrin, or epidermal growth factor)[4,12]. Here I shall describe the properties of the most investigated class of targeting ligands, the monoclonal antibodies (mAbs), shedding light on the antibody advantages and drawbacks. Then, I shall introduce a class of binders, the nucleic acid aptamers, which represents a promising alternative to the antibodies and that offers improved options for targeted delivery applications.

1.3.1 Antibodies

Over the past two decades the potential of mAbs as high-affinity binders for targeted therapy has been clinically demonstrated[60] with several therapeutic mAbs approved by FDA[61]. To date, more than 200 antibody-based targeted platforms were successfully translated into the clinical environment and are currently in preclinical and clinical trials[62]. However, this class of ligands shows several limitations. For example they are produced through a complex and expensive process that is difficult to scale-up to large-scale manufacturing without affecting product properties[18]. They have limited stability, are rapidly inactivated under acidic conditions, in the presence of proteases or at elevated temperatures[63]. Moreover, their large size (150-160 kDa and 12-15 nm) results in slow tissue penetration[64] and prevents access to many biological compartments, ultimately leading to an increase toxicity due to a long blood residence[65]. The most significant restriction, however, is related to their immunogenicity, which was observed mainly for first-generation of rodent antibodies. Indeed, injection of mouse mAbs into humans results in the production of human anti-mouse antibodies (HAMA), thus leading to serious immune reactions[66]. To overcome this limitation, recent developments in the field of antibody engineering have led to the production of antibodies that contain animal and human domains, called chimeric mAbs, then humanized mAbs, and fully human mAbs[60] (Fig. 5). Overall, these structures present a gradually reduced immunogenicity, with fully human and humanized antibodies carrying lower risk to induce immune response in humans than mouse or chimeric antibodies[67]. However, other problematic immune responses still exist, such as anti-idiotypic responses, with the production of anti-idiotypic antibodies, also called anti-drug antibodies, against humanized or fully

human antibodies that ultimately lead to the neutralization of their therapeutic effect[67].

Interestingly, the last frontier in the field of the antibody engineering led to the development of antibody fragments[18], which include monomer of antigen-binding fragments, dimers of antigen-binding fragments, and single chain variable (Fig. 5).

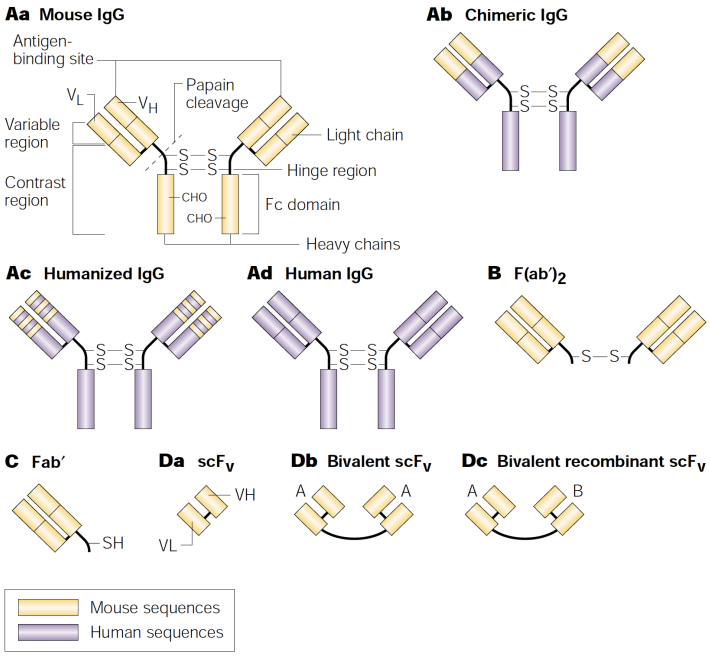

Fig. 5 Antibodies and antibody fragments. Targeting antibodies are normally monoclonal immunoglobulin G (IgG) (Aa) or IgG fragments (B–D). F(ab′)2 (B) or Fab′ (C) fragments can be made by enzymatic cleavage of the whole monoclonal antibody (mAb) (Aa) or by molecular biological techniques — for example, Fab′ (C), scFV (Da), bivalent (Db) or recombinant fragments (Dc). mAbs that are made from the traditional hybridoma technique are murine in origin. Recent developments have led to the production of chimeric, humanized or fully human antibodies or fragments (Ab–d). Fc, fragment crystallizable region; VH, variable heavy chain; VL, variable light chain. Adapted from T. M. Allen.[18] Reprinted by permission from Macmillan Publishers Ltd: Nature Reviews Cancer (Ref. 18), Copyright © 2002.

As shown in Fig. 5, only the antigen recognition domain is included in the antibody fragment structures, while the fragment crystallizable (Fc) region is removed in order to reducing their immunogenicity. Indeed the Fc domain is a double-edged sword: when mAb is bound to a tumor cell surface antigen, its Fc region can interact with Fc receptors expressed on the surface of effector cells of the immune system, such as natural killer cells,[68] evoking antibody-dependent cellular cytotoxicity and complement-dependent-cytotoxicity[18]. Note that, these effects play a significant role in enhancing the anticancer effect[69]. However, interaction between the Fc region and Fc receptors expressed on normal cells, as occurs with macrophages, can elicit immune response leading to increased immunogenicity[62,70].

Although antibody fragments are less immunogenic than whole mAbs, unfortunately they are less stable and tend to aggregate due to the absence of Fc region, which plays a role in the structural stability of mAbs[63,71]. Furthermore, as shown in Fig. 5 most antibody fragments have only one epitope-binding site included in their structure, which reduce their binding avidity[18,70].

Despite many advancements mAbs and antibody fragments still suffer limitations that hamper their applicability. Particularly, the use of mAbs and antibody fragments is often restricted to conditions resembling their physiological environment. In the presence of organic solvents or in other non-physiological conditions (e.g. elevated temperature, high pH and high salt concentration), they generally lose their function[63]. Moreover, mAbs are not easily conjugated to therapeutic molecules, reporter tags, or engineered scaffolds to create complex biomolecular architectures that may be used as targeting delivery platforms. Indeed, the synthetic approaches required for antibody conjugation to molecular partners are stochastic and lead to product mixtures and reduced antibody activity[72,73].

1.3.2 Aptamers

An alternative to antibodies should possess high stability, long-term storage, and ease of conjugation to molecular partners[7475]. In this context, it is worth noting that biological nucleic acids are not only able to store and code genetic

information assuming simple base pairing structures, but they can also fold into complex tertiary structures, and perform different functions including gene-regulation[76], catalytic activity[77], and ligand-binding[78]. Although this is true for biological nucleic acids, in 1990 a series of technological advances allowed the development of an *in vitro* evolutionary method for the selection and identification of synthetic oligonucleic acids, called aptamers, that bind specifically to molecular targets[79,80].

Nucleic acid aptamers are composed of short structured RNA or single-stranded DNA sequences, and are emerging as attractive targeting tools with huge potential in diagnostics and therapeutics. Aptamers are able to recognize and bind a definite target molecule with high affinity and selectivity, owing to their exclusive spatial conformation. In this regard, they are often termed "chemical antibodies"[9]. In general, aptamers may act similarly to antibodies and they can be used as activating ligands[81], therapeutic antagonists[82], or as vectors to deliver therapeutic and diagnostic payloads, especially in the field of targeted cancer therapy[9]. Compared with antibodies, aptamers are non-immunogenic, easy to synthesize, modify, and manipulate. Furthermore, their small size -usually 8-20 kDa and 3-5 nm- allows more efficient penetration into target tissues[72,83]. Importantly, aptamers do not include the Fc region of mAbs, thus avoiding undesired interactions with Fc receptors expressed on immune cells and other certain types of cells, which may result in immune stimulation or other unwanted side effects.

Aptamer technology was born twenty-five years ago; despite being a relatively new technology, one therapeutic aptamer is already available in the clinic and various other aptamer-based drugs and aptamer nanocarriers are currently in different stages of preclinical and clinical trial for diseases that span from cancer[84] and heart disease[85] to type II diabetes[86].

The first FDA-approved aptamer is called pegaptanib and it was approved in 2004 for the treatment of age-related macular degeneration (AMD) in the U.S. and the EU[82]. Pegaptanib (Macugen®; Pfizer and Eyetech) is an RNA aptamer that specifically recognizes human VEGF with high affinity (Kd~50 pM) and selectivity[87]. VEGF promotes angiogenesis and may be up regulated under certain conditions, (e.g. wound healing) or diseases (e.g. AMD and cancer)[88]. Pegaptanib

binds to the heparin-binding site of VEGF and blocks the interaction between VEGF and its receptors, which results in the prevention or reduction of the neovascularization. In 2004, pegaptanib became the first anti-angiogenesis drug for wet AMD therapy under intravitreal administration with a dosage of 0.3 mg per eye every 6 weeks[82,89].

The FDA approval of Pegaptanib represents a landmark in the development of aptamers as biological agents with applications in therapeutics, diagnostics and basic research.

In the next section, I shall mention the main groundbreaking studies that led to the aptamer discovery, and then I shall report an insightful analysis of the aptamer properties and the recent progresses in the development of targeted drug delivery platforms based on aptamer-drug conjugates or aptamer-nanomaterial assemblies[2].

1.4 Aptamers as novel "keys of the castle"

The first evolutionary experiments involving nucleic acids were reported in the 1960s by Spiegelman and his collaborators, which described the use of an RNA-dependent RNA replicase for the replication of a given RNA species[90]. Several years later, in 1986, the innovative discovery of the polymerase chain reaction (PCR) by Kary Mullis and co-workers has led to a technological revolution of the most biological fields (i.e. molecular biology, biochemistry) including evolutionary biology[91]. In 1990, three independent research groups described *in vitro* evolutionary methods for the selection of small nucleic acid ligands as binding partners for defined molecular targets. Particularly, Ellington and Szostak isolated short RNA molecules that bind to a small organic dye[79]. These small nucleic acid ligands were called aptamers (from the Latin *aptus* – to fit and the Greek *mero*s – part or region). Tuerk and Gold selected RNA molecules able to bind the bacteriophage T4 DNA polymerase and they named SELEX (systematic evolution of ligands by exponential enrichment) the iterative selection process they used[80]. Robertson and Joyce described the application of *in vitro* selection to convert a group I ribozyme having RNase activity into an enzyme able to preferentially cleave DNA than single stranded RNA[92]. These groundbreaking studies shed light on novel perspectives and opportunities for the *in vitro* selection

of functional nucleic acids with desired properties. Indeed, for the first time, it was demonstrated that artificial nucleic acids could be used as functional moieties besides as blueprints of the genetic code or as rigid scaffold for nanoarchitectures. Interestingly, Nature already makes use of several functional nucleic acids, such as noncoding RNA and riboswitches as regulatory elements to control gene expression in bacteria, eukaryotes, and higher organisms[91].

It is worth mentioning that few years later the aptamer discovery, the term "aptamers" was extended to include peptides with protein-binding properties[93,94]. However for the most part and for the purposes of this thesis the term is used to describe oligonucleotide molecules.

Since the invention of SELEX technology, a plethora of high-affinity RNA and DNA aptamers have been selected towards a wide range of different targets ranging from small molecules (i.e. metal ions, organic dyes, amino acids, and peptides)[95,96] to proteins[72] to complex targets (whole cells[2], viruses or bacteria[97]). Thus, during the last two decades aptamers found broad application across various biomedical fields: biomarker discovery, *in vitro* diagnosis, *in vivo* imaging, and targeted therapy[9].

Aptamers fold into distinct three-dimensional (3D) structures able to bind and recognize a particular molecular target with high affinity and specificity (Fig. 6a), with dissociation constants typically within the pico- to nanomolar range[3]. In fact, aptamers are not just linear nucleic acid molecules that simply carry genetic information, but rather they can assume a wide variety of secondary structures, such as hairpin loop, pseudoknot and G-quadruplex (Fig. 6b) generated by a combination of Watson–Crick and non-canonical intramolecular interactions that ultimately lead to complex spatial structures.

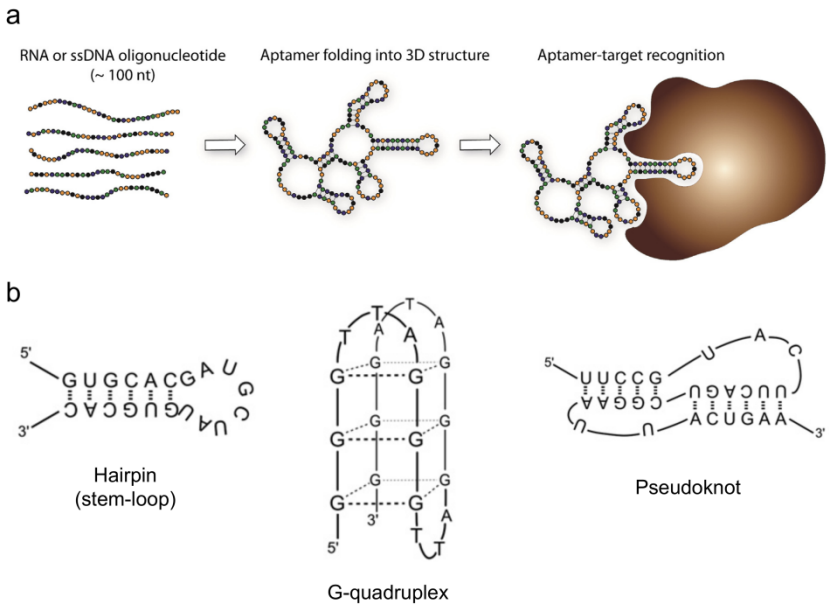

Fig. 6 Schematic representation of (a) aptamer–target interaction and (b) aptamer secondary structures. Figure (a) is reprinted from Biotechnology Advance 33 (2015) 1141–1161, Darmostuk et al.[98]; Copyright © (2015), with permission from Elsevier. Figure (b) is reprinted from Biotechnology Advances 31 (2013) 1260–1274, Radom et al.[99]; Copyright © (2015), with permission from Elsevier.

In contrast with other nucleic acid probes (such as antisense oligonucleotides and ribozymes), aptamers bind their targets through 3D structural recognition involving non-covalent interactions, similarly to the antigen-antibody reaction. Therefore, aptamers are also known as "chemical antibodies"[9]. However, aptamers possess significant advantages relative to their protein counterpart in terms of virtually no immunogenicity, thermal stability, low-cost chemical synthesis, and ease of conjugation or modification with different functional moieties[3] (Table 1). Compared with antibodies, aptamer production exploits a chemical technology with high batch fidelity, which is not prone to viral or bacterial contamination[100]. In addition, the process of chemical synthesis allows the site-specific introduction

of non-nucleotide linkers (e.g. hexaethylene glycol), or chemical functionalities useful for conjugation (such as primary amines, thiol precursors and aldehyde precursors), and the addition of fluorescent or other reporter moieties[72].

Moreover, thanks to their small size (aptamers: 25-70 nt equals 8-25 kDa; antibodies ~150–160 kDa), aptamers can penetrate into biological compartments more efficiently than antibodies, thus accessing target domains that might otherwise be inaccessible to bulky ligands.

Table 1. Comparison of aptamers and antibodies. Adapted from Sun et al.[3] Reprinted by permission from John Wiley and Sons Copyright © 2015; Small 11 (2015) 2352–2364 (Ref. 3)

Characteristics	Aptamers	Antibodies
specificity and affinity	high (pico- to nano-molar)	high (pico- to nano-molar)
molecular weight	8–25 kDa	~ 150 kDa
tissue barrier penetration	+++ (due to smaller size)	+
immunogenicity	–	+++ (even with humanized antibodies)
thermal stability	++	–
modification potential	easy, unlimited	difficult, limited
manufacture	chemical synthesis	mammalian cell systems
batch-to-batch variation	low	high
production time	hours	days to months
production cost	$	$$$
ranges of targets	proteins and non-protein molecules	limited to immunogenic proteins

Lastly, the nature of nucleic acids provides another important advantage compared with protein ligands. Since the function of the aptamer is tightly dependent from their 3D structures, it can be modulated for desired therapy and drug delivery application simply by using the complementary oligo sequence. The complementary base pairing can alter the aptamer spatial structure and ultimately disrupt the interaction with its target. This approach, known as aptamer antidote

strategy, allows a precise control of the aptamer activity by a rational design of the antidote sequence, and was firstly introduced by Sullenger and coworkers in 2002. Briefly, they developed an aptamer that targets the blood coagulation factor IXa[101], which induces anticoagulation in pigs and inhibits thrombosis in murine models[102]. However, a major risk associated with anticoagulant therapy is uncontrollable bleeding if reversal of the anticoagulation is not achieved[103]. Therefore, they also developed an antisense strand, complementary to 17 nucleotides of the aptamer, which was able to interfere with the aptamer structure (Fig. 7), inhibiting its activity both in animal models of cardiovascular disease and surgical trauma and humans[102,103].

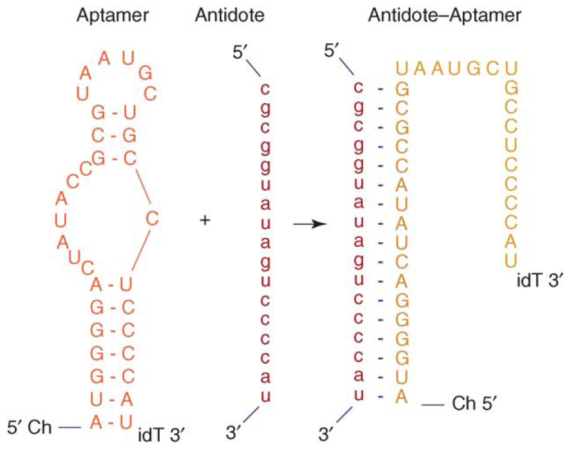

Fig. 7 Aptamer–antidote pair. The sequence and structure of the anti-factor IXa aptamer and its antidote are shown. Binding of the antidote to the aptamer inactivates the aptamer by disrupting its secondary and tertiary structure. Abbreviations: Ch, cholesterol; idT, inverse deoxythymidine. Reprinted from Current Opinion in Chemical Biology 10 (2006) 282–289, Lee et al.[104]; Copyright © (2006), with permission from Elsevier.

The therapeutic potential of aptamers is largely influenced by their pharmacokinetic property. As small nucleic acid molecules, natural RNA and DNA aptamers are highly susceptible to the nuclease-mediated degradation and

size-dependent clearance via renal filtration. However, both limitations can be addressed with appropriate chemical modifications.

Evidence shows that firstly the 2'-OH group of RNA and secondarily the phosphodiester bonds are the preferentially target sites of nucleases hydrolysis[9]. Note that, DNA molecules are naturally resistant to 2'-endonucleases owing to the lack of the 2'-OH group. Thus, the main approaches to overcome the nuclease sensitivity are aimed at increasing the in vivo stability of RNA aptamers. As seen for other therapeutic oligonucleotide agents[105], nuclease resistance can be achieved with substitutions of the 2'-OH RNA group, internucleotide linkage substitutions of the phosphodiester backbone with either boranophosphate or phosphorothioate, conformationally restricted ribose (locked nucleic acids), generation of mirror RNA sequences (Spiegelmers), introduction of functional groups at the nucleobase level, and the combination of these modifications[106] (Fig. 8). Since serum nucleases responsible for RNA turnover are largely directed towards pyrimidine nucleotides[107], the most prominent modification is the substitutions of 2'-OH group of pyrimidines by 2'-fluoro, 2'-amino, or 2'-O-methyl (Fig. 8b) that lead to nuclease-stabilized RNA molecules. Particularly, whereas natural RNA aptamers exhibit a very short serum half-life (estimated at 10 s), the widely used 2' fluoropyrimidine-containing RNAs have a sensibly longer serum half-lives (estimated at 80 h)[108]. This approach relies on the effective incorporation into RNA transcript of 2'-modified nucleotides using mutant forms of T7 RNA polymerase during the *in vitro* transcription[109,110].

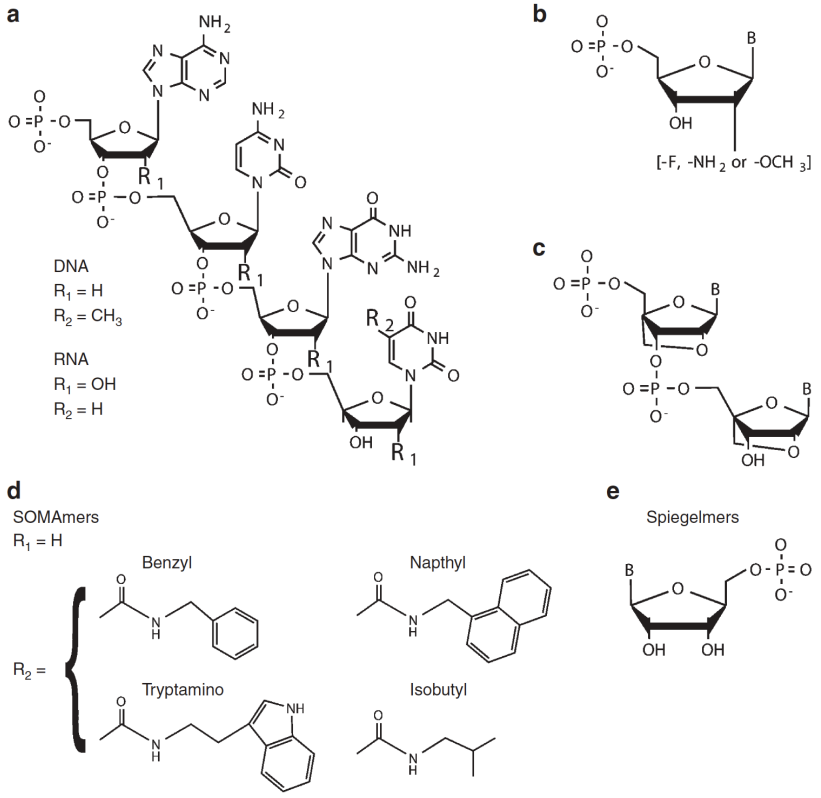

Fig. 8 Subset of modified nucleotides used for increase nuclease-resistance of aptamers. (a) In addition to the unmodified nucleotides of DNA and RNA, a wide variety of modified nucleotides have been used for improving stability, chemical diversity, and target binding potential of selected aptamers. (b) The most commonly used modified nucleotides contain modifications of the ribose sugar such as 2′-Fluoro, 2′-Amino, or 2′-OMethyl. (c) Locked nucleic acids (LNAs) contain modifications to the sugar phosphate backbone, and are more stable than DNA and RNA. (d) SOMAmers contain modifications (i.e., benzyl, napthyl, tryptamino, or isobutyl) on deoxyuridine nucleotide (dUTP), which improve the chemical diversity and thus the target interaction capacity of the aptamers. (e) Spiegelmers are derived from mirror-image (enantiomer) ribonucleotides. Spiegelmers are not recognized by natural nucleases that degrade wild type oligonucleotides. Adapted from Ozer et al. [111] Reprinted by permission from Nature Publishing Group: Mol. Ther. Nucleic Acids (Ref. 111), Copyright © 2014 The American Society of Gene & Cell Therapy.

Other approaches to the development of nuclease-resistant aptamers relies on modifications of the ribose motif using locked nucleic acid technology or generate "mirror" RNA sequence structures, termed Spiegelmers.

Locked nucleic acids (LNAs) bear a methylene ether bridge between the 2'-oxygen atom and 4'-carbon atom (Fig. 8c). Thus, in the LNA ribose the 3'carbon atom is locked in an endo (N-type) conformation with a consequent lower flexibility of the sugar motif and a high degree of nuclease resistance[112]. Spiegelmers are aptamers in which all the sugars are the enantiomers of wild-type nucleic acids (Fig. 8e). In the case of RNA Spiegelmers, the backbone is composed by L-riboses, instead of D-riboses present in native RNA, linked by phosphodiester bonds. As a consequence, nucleases are not able to recognize these molecules as substrates of their hydrolytic degradation. The first functional Spiegelmers were designed to bind to the small molecules arginine and adenosine[113,114], and they exhibited the expected biostability, as demonstrated for the D-adenosine specific L-RNA spiegelmer. Indeed, no evidence of degradation in human serum were detected over 60 hours of incubation at 37°C [114].

Modifications of nucleobases have also been reported, with derivatization at the C5-position of uridine and deoxyuridine being the most prevalent (see Fig. 8). Notably, the introduction of amino acid side chain-like groups (Fig. 8d) at this position conferred an increased chemical complexity together with a higher hydrophobic character of the aptamers, thus increasing both the range of available binding epitopes on the target proteins and the success rate of SELEX[115]. A class of DNA aptamers bearing these modifications is known as SOMAmer (Slow Off-rate Modified Aptamers) owing their high affinity towards their biomolecular targets[116].

When appropriate modifications to control nuclease-mediated degradation are included in the aptamer sequences, elimination via renal filtration becomes the main limitation to aptamer pharmacokinetics. The molecular mass cutoff for the renal glomerulus is 30-50 KDa, thus aptamers (8-25 kDa) can be conjugated to bulky groups in this size range to reduce the renal filtration rate. The most common strategy is the conjugation of either 5'-end or 3'-end of the aptamers to high molecular mass polyethylene glycol (PEG) (from 5 kDa up to 60 kDa)[108].

This method is better known as PEGylation and represents a typical modification when aptamers should be employed for in vivo applications. Importantly, nuclease-stabilized aptamer conjugated to 40 kDa-PEG can have circulating half-lives up to 1 day in mice[117] (Fig. 9).

Alternatively, other bulky groups that have been directly conjugated to the aptamers are cholesterol derivates, streptavidin (via biotinylated aptamer), and liposomes (through conjugation to lipid tags).

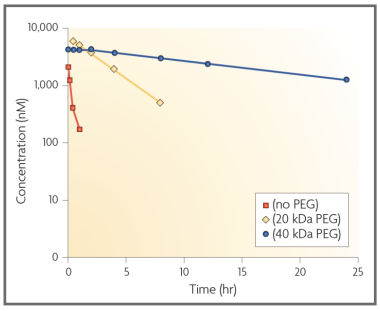

Fig. 9 The pharmacokinetics of aptamers conjugated to different molecular mass PEGs. Pharmacokinetic profiles of 39-mer 2′-deoxy purine, 2′-O-methyl pyrimidine composition aptamers. These aptamers were unconjugated or conjugated to either 20 kDa polyethylene glycol (PEG) or 40 kDa PEG and administered intravenously to CD-1 mice (n = 3 per time point) at 10 mg per kg. Adapted from Keefe et al.[72] Reprinted by permission from Macmillan Publishers Ltd: Nature Reviews Drug Discovery (Ref. 72), Copyright © 2010

1.5 In vitro selection of aptamers

SELEX technology is based on an iterative process of amplification and enrichment, in which a very large (~10^{14}) number of random oligonucleotide (either RNA or single-stranded DNA) is exposed to the target of interest for several repetitive rounds. During this process, the library is subjected to a selection pressure in parallel that allow an enrichment of the molecules with binding properties against the desired target. Typically, four main steps can be recognized into basic SELEX process (Fig. 10).

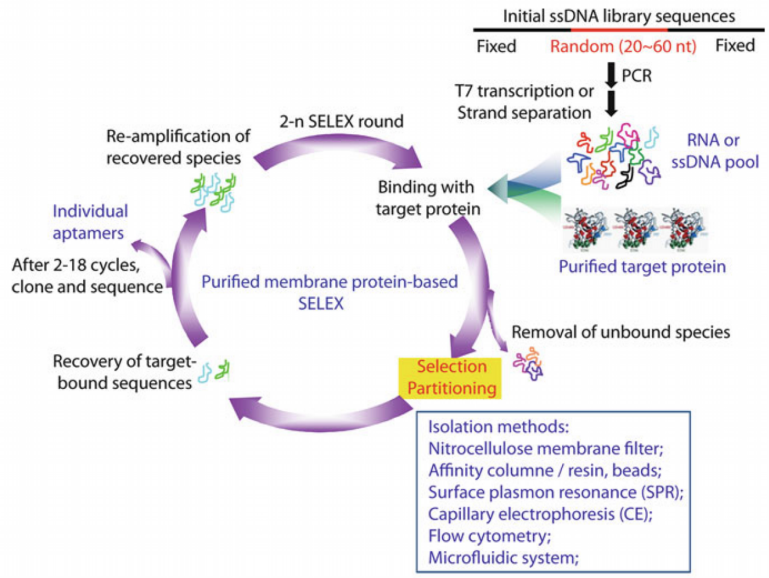

Fig. 10 Schematic illustration of aptamer selection procedures by SELEX. Generally, in a typical SELEX procedure, the initial single-stranded DNA/RNA pool contains a 20–60-nt random sequence to provide a sequence space that facilitates presence of structures with high binding affinity to the target protein. By repeating selection rounds, aptamers against any given targets can be routinely isolated from an initial combinatorial oligonucleotide library. A typical SELEX process consists of four main steps (1) binding to the target protein, (2) selective partitioning, (3) recovery of target-bound sequences, and (4) re-amplification of recovered species. Reprinted from RNA Interference from Biology to Therapeutics Cap. 10 "Aptamer-Mediated siRNA Targeting" 207–220, Zhou and Rossi[118] Copyright © (2013), with permission from Springer.

- The first step is the generation of the nucleic acid library. A single-stranded DNA library sequence that includes a random region composed by 20-50 residues in length, and flanking conserved sequences required for enzymatic manipulation is first designed and then synthesized[72]. PCR amplification of this single-stranded DNA library generates a double-stranded PCR product with high sequence variability. The initial oligonucleotide selection pool (for

either DNA or RNA aptamers) usually contains 10^{13}-10^{15} unique random molecules, although pools with a lower variability yielded functional aptamers[119,120]. In the case of DNA aptamer SELEX, the starting library of single-stranded DNA molecules is obtained after strand separation of double-stranded PCR product. In the case of RNA aptamer SELEX, the RNA library is prepared by *in vitro* transcription of double stranded DNA templates, using recombinant wild type or mutant T7 RNA polymerase, as previously described.

- The second step is the incubation of the oligonucleotide library with the target of interest for specific binding enrichment. Importantly, before this incubation the library is thermally denatured and cooled at room temperature to ensure proper oligonucleotide folding and consequently promote the formation of 3D structures.
- Next, the unbound fraction is discarded and separated from the target bound species.
- Finally, these binding oligonucleotide sequences are collected, purified and amplified by either PCR (for DNA aptamers) or by RT-PCR (for RNA aptamers) to generate a fresh oligonucleotide library ready for the next round of the *in vitro* selection.

SELEX process usually requires 4-20 rounds of amplification and enrichment[9] to obtain high affinity aptamers. The number of SELEX rounds is strongly affected by the nature of the aptamer target (such as a purified protein or a living cell line), by the type of library used, as well as by the evolution of the aptamer library during each selection cycle. After the last round of selection, a rational strategy deeply examines the oligonucleotide sequences to disclose the ligands with the best properties. First, the enriched library is cloned and, after sequencing, candidate aptamers are classified in several groups on the basis of their sequence homology. High-throughput sequencing methods (Next-Generation Sequencing – NGS) and bioinformatics analysis (such as FASTAptamer[121]) allow the identification of candidate aptamers. Once the candidates are identified, they are explored in terms of binding affinity, specificity, and desired properties such as target inhibition, cell internalization, and stability. These latter steps are so far the

most time-consuming part of the aptamer generation process. Lastly, the best selected aptamers and their relative secondary structures are rationally investigated (by computer simulation, and both chemical and enzymatic probing) in order to find out the minimal aptamer binding sequence required for the specific recognition of the target. Post-SELEX modifications can also be introduced to increase the aptamer properties in terms of nuclease resistance, *in vivo* biodistribution, and other parameters affecting the aptamer pharmacokinetic behavior (as described in the previous section).

Early SELEX protocols targeting proteins usually required several months to identify aptamers able to bind the desired target protein. Recently, the traditional SELEX method has been modified to improve the outcome of this technology. Particularly, some innovative SELEX strategies have been developed in order to (i) maximize affinity and selectivity (e.g. slow-off rate modified aptamers – SOMAmer)[116], (ii) to improve the evolution of the library and consequently the speed of selection and success rate (e.g. capillary gel electrophoresis-[122], microfluidic-[123], bead-based SELEX[124] and FACS-SELEX[125]), (iii) to provide additional properties to the selected ligands (e.g. cell-internalization SELEX[126]), (iv) to obtain aptamers against more complex targets (e.g Cell-SELEX[127], in vivo SELEX[128])[111]. A fruitful approach for increasing the activity of selected sequences is the "doped-SELEX", in which an original, successful aptamer sequence is partially randomized at some or all positions and reselected[129]. For example, each position in a doped library could contain 55% of the initial selected nucleotide, and 15% each of the other three nucleotides (45% doping)[130]. Moreover, the biomolecular target of this second selection could be the same of the original SELEX or closely related.

Table 2 shows a detailed scheme of the SELEX methods and offers a better comparison among these techniques. To date, thanks to these strategies, an *in vitro* selection takes only several days and aptamers are emerging as valid tools for basic research and biomedical applications.

The main drawback of the SELEX technology is the uncertain prediction of the success of the selection. It is not possible to judge the ability of a target molecule

to be suitable for the selection process and whether an aptamer can be successfully raised against the target (aptamerogenicity) a priori[91]

Table 2 Comparison of SELEX methods. Reprinted by permission from Nature Publishing Group: Mol. Ther. Nucleic Acids (Ref. 111), Copyright © 2014 The American Society of Gene & Cell Therapy.

SELEX methods	Pros[a]	Cons[a]
Nitrocellulose filter binding	Relative ease of selection	Restricted to proteins that can be captured by nitrocellulose filter
	No special equipment required	Large number of selection rounds necessary (8–20 rounds)
	Equilibrium, in solution aptamer-target binding	Relative abundance and quick enrichment of filter-binding aptamers (multi-G motif)
	Potential for parallel aptamer selections for multiple targets	
	Can also be used as medium-throughput binding assay	
Bead-based	Applicable to most targets (small-molecules, peptides, proteins, and cells)	Target or aptamer immobilization: restricted interaction surface
	Potential for serial and parallel aptamer selections for multiple targets	Nonequilibrium, flow binding (if used with fluidic devices)
	Rapid selection of aptamers (1–6 rounds of selection)	Fabrication of fluidic devices, and electronic instruments and flow pumps required for operation
	Equilibrium, in-solution binding	Density-dependent cooperativity for nonspecific interactions (as further described in Ozer *et al.* 2014)
	Ease in fine-tuning selection stringency	
Electrophoretic	Equilibrium, in-solution binding	Limited capacity for aptamer library (~10^{12} sequences)
	Rapid partitioning of target-bound and unbound aptamers	Restricted to targets that cause an electrophoretic shift on nucleic acid aptamers
		Capillary-electrophoresis instrument or fabrication of micro-electrophoresis devices are required
Microfluidic	Potential for serial and/or parallel aptamer selections for multiple targets	Target immobilization or encapsulation required
	Both equilibrium, in-solution and nonequilibrium, flow binding systems are available	Fabrication of fluidic devices, and electronic instruments and flow pumps required for operation
	Rapid selection of aptamers (1–6 rounds of selection)	
Microarray-based	Equilibrium binding with in-solution target and immobilized aptamer	Limited capacity for aptamer library (<10^5 sequences)
	Can be used as a large-scale binding assay	Currently limited to ssDNA aptamers
		Aptamer sequences need to be pre-determined (designed or derived from a pre-selected aptamer library)
		Relatively large number of selection rounds are necessary (~9 rounds)
		Costly and time consuming due to fabrication of a microarray with different sequences unique for each target
		Single target selections
		Prone to artifactual results due to design of sequences
		Requires microarray scanner to measure binding
Microscopic	Single-round selection reported	Limited capacity for aptamer library (<10^8 sequences)
		Requires expensive and specialized instrument (*i.e.*, Atomic Force Microscopy system)
		Immobilization of either target or aptamer is required
		Nonequilibrium binding
Cell-SELEX	Biomarker discovery	Restricted to molecules presented on cell surface
	Therapeutic potential of selected aptamers	Prone to artifacts due to dead cells in population
		Target(s) of the selected aptamers are unknown
		Selection of aptamers to an unintended target is very likely
In vivo SELEX	Selection of *in vivo* functional aptamers	Limited capacity for aptamer library (~10^4 sequences)
		Relatively large number of selection rounds are necessary (up to 14 rounds)
		Selection of aptamers to an unintended target is very likely
Small-molecule SELEX	Equilibrium, in solution binding	Complications of aptamer capture sequence within aptamer library random region
	No immobilization of small-molecule target	Relatively large number of selection rounds are necessary (~13 rounds)
		Depends on target binding-induced conformational change on aptamer for its release

1.6 Selection of aptamers recognizing cell-surface markers

As mentioned in the previous section, in the recent years innovative strategies have been introduced to enhance both performance and outcome of the conventional SELEX process. Here, I shall focus on the in vitro selection methods to generate aptamers targeting cell-surface markers or specific cell-types to exploit as targeted drug delivery agents. Two main approaches are typically employed: (i) traditional purified membrane protein-based SELEX and (ii) live cell-based SELEX.

In a typical protein-based SELEX the nucleic acid library is mixed with a target purified membrane protein, a cell surface antigen overexpressed and/or mutated in diseased cells. Traditional bead-, resin-, membrane-, or chip-based partition approaches are employed as affinity matrixes to separate target-bound sequences from unbound species. In this context, the immobilization of the recombinant purified protein on the affinity surface is the first step before the incubation of the target with the nucleic acid library. Protein-SELEX is a method in which low nonspecific binding and easy control of the conditions allow optimal enrichment of specific ligands. To date, most aptamers as targeting ligands have been successfully generated using purified membrane protein-based SELEX[2]. A strong limitation of this method is the conformational instability of target proteins, especially under the conditions of the selection process. Protein conformational changes can lead to a misleading selection with enrichment of oligonucleotide sequences that recognize a false 3D protein structure. Alternatively, a reduction of enrichment can also occur from one selection cycle to the other, in which the enriched pool suddenly is not more able to bind the target protein due to the conformational changes[91]. Additionally, purified recombinant proteins are generated by in vitro expression systems, which often not include the presence of post-translational modifications, such as glycosylation (N- and O-linked), phosphorilation of tyrosine, threonine or serine residues and addition of glycosylphosphatidylinositol (GPI), typically present in cell-surface receptors. Furthermore, in many cases cell-surface proteins are insoluble in their recombinant form, or they are functional only when tightly associated with other

cell components (e.g. G protein-coupled receptor) or when associated to form multimeric and/or multivalent structures[131]. Thus, RNA and DNA aptamers selected through a protein-SELEX approach might not be able to recognize the same target when embedded in a physiological milieu[132]. To overcome these limitations, an innovative SELEX method that uses whole living cells as target, termed live cell-based SELEX (or cell-SELEX) has been introduced[127]. This approach allows the identification of aptamers that bind cell-surface specific antigens in their native environment[133]. In contrast to protein-SELEX, cell-SELEX does not need information regarding native conformation, identity, and biological function of target proteins, and aptamers against unknown cell-surface antigens can be also generated. This method relies on the difference between the expression pattern of cell-surface receptors in target cell population (e.g cancer cells) and the receptor pattern in control cell line (e.g. healthy cells). Therefore, cell-SELEX involves two different selection steps (Fig. 11): (i) a negative selection (or counter selection) step to suppress nonspecific binding sequences, in which the oligonucleic acid library is incubated with non-target cells (or negative cells). Unbound sequences are recovered and (ii) a positive selection is performed with target cells (or positive cells) and target-bound ligands are recovered and amplified for the subsequent round of SELEX.

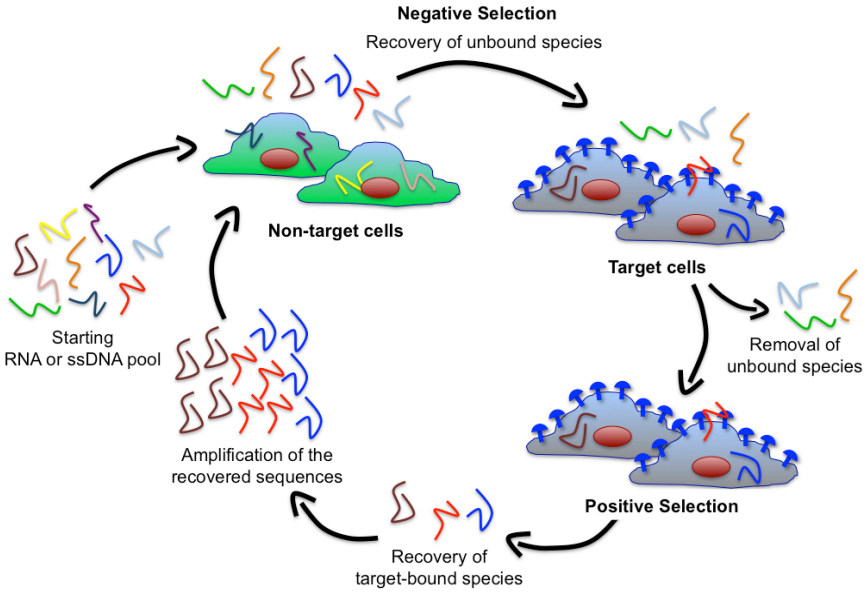

Fig. 11 Schematic illustration of cell-SELEX procedure. A live cell-based SELEX procedure consists of four main steps each round of selection: (1) counter-selection by incubating library with negative cells that do not express the target antigen, (2) positive selection by incubating recovered unbound sequences with positive cells expressing cell-surface receptors of interest, (3) recovery of target-bound sequences, and finally (4) re-amplification of recovered species.

Overall, cell-SELEX provides aptamer sequences able to bind a pool of different cell-surface antigens overexpressed or exclusively present in target cells. Using this approach several groups generated aptamers able to discriminate a particular cell population[2]. Tan group introduced for the first time this new strategy to select DNA aptamers able to discriminate T cells (CCRF-CEM cells, a human precursor T-cell acute lymphoblastic leukemia cell line) from a B cell line (Ramos cells, human Burkitt's lymphoma cells), in patient samples[127]. Despite the remarkable success of cell-based SELEX, one important drawback is related to the nonspecific binding to dead cells that can lead to low target-bound sequences

enrichment and sometimes even to the failure of aptamer selection[2]. Furthermore, the lack of knowledge about identity and expression level of the biomarker of interest might result in the enrichment of many unrelated/unwanted aptamers against off-target surface antigens coexpressed on the positive cells.

This strategy can provide sufficient selective pressure to favor the enrichment of target-specific aptamers even when nonspecific antigens are coexpressed on the surface of target cells; however, recent findings introduced an enhanced *in vitro* selection method called crossover SELEX. This method combines cell-SELEX and protein-SELEX protocols and simplifies and increases the success rate of the *in vitro* selection. Notably, crossover SELEX is readily applicable when the identity of the cell-surface target is known, and its iterative cycles exploit a first traditional selection against a recombinant protein, followed by a second selection using whole living cells as target[107]. It is worth noting that Hicke et al. firstly introduced this methodology to select RNA aptamers against tenascin C (TN-C), an extracellular matrix protein overexpressed in tumor growth and other different cellular processes[134]. In this study, however, several rounds of live cell-based SELEX were first performed as primary selection using U251 glioblastoma cells overexpressing human TN-C. Then, the enriched pools were incubated with purified TN-C performing two additional rounds of the second protein-based SELEX. Thanks to the final selection pressure two high affinity RNA aptamers were selected and, in a subsequent investigation, shown to be able to discriminate tumor tissue from healthy tissue into *in vivo* model on the basis of the different expression of TN-C[135].

Crossover SELEX is becoming very attractive to generate aptamer ligands as tools for targeted drug delivery applications[136], and has been recently exploited by Levy and coworkers to generate serum-stabilized RNA aptamers against human transferrin receptor (hTfR)[137].After 4 rounds of protein-SELEX using the traditional nitrocellulose membrane filter as partition method, the RNA enriched pool was incubated with live cancer cells for one additional round of selection. Importantly, during this cell-based enrichment round, Levy and coworkers employed a modified cell-SELEX approach, termed cell internalization SELEX[46]. This novel strategy leads to selection of aptamers able to bind to and enter target

cells, known as cell-penetrating or cell-internalizing aptamers[59,126]. Thanks to this strategy, the authors generated a minimized 2'-fluoro RNA aptamer, termed c2.min able to bind with high affinity hTfR and showing cell-penetrating properties towards several hTfR (+) cancer cells.

1.7 Cell-specific aptamer applications in targeted drug delivery

Thanks to the advancement of SELEX technologies, many aptamers targeting cell-surface biomarkers have been generated in the last decade and exploited as nanovectors for targeted drug delivery[2]. In this section, I shall introduce the main approaches and the most representative applications of cell-specific aptamers. Particularly, I shall focus on the conjugation designs used to deliver traditional anticancer drugs and functional therapeutic oligonucleotides. The two main strategies for targeted delivery using cell-surface aptamers are: (i) aptamer-drug conjugates, in which the aptamer motif is directly conjugated to the therapeutic payloads via either a physical non-covalent intercalation or a covalent linker and (ii) aptamer-nanomaterials system in which the surface of high-molecular-weight bioavailable nanomaterials is coated with several aptamer molecules.

1.7.1 Aptamer-chemotherapeutic conjugates

Non-covalent conjugation by intercalation of hydrophobic drugs, such as Doxorubicin (Dox), has been extensively used to create aptamer-drug complexes[138]. This approach is straightforward and does not require any chemical modification of drugs or aptamers (Fig. 12). Dox is an anthracycline anticancer drug that intercalates preferentially into G-C rich double stranded region of nucleic acids via its aromatic rings. Taking advantage of this propensity, Dox can be intercalated into helical strand of the aptamers to form physical conjugates. In 2006, Bagalkot and coworkers firstly used this strategy to generate a non-covalent complex between anti-PSMA RNA aptamer A10 and Dox[139]. Interestingly, compared with free Dox, the aptamer-Dox conjugate was selectively uptaken by PSMA (+) cells (LNCaP cells) and only negligible internalization was detected in a control cell line not expressing PSMA (PC3 cells). Most importantly, while free

Dox exhibited comparable anticancer effect towards both cell lines, aptamer-Dox was more cytotoxic towards LNCaP cells rather than to PC3 cells. After this pioneristic work, physical aptamer-Dox conjugates have been widely used in several other applications for targeted cancer therapy. For example, aptamers against HER2, Mucin1 (MUC1), and epithelial cell adhesion molecule (EpCAM) were exploited to target breast cancer, lung cancer, and cancer stem cells, respectively[2,138].

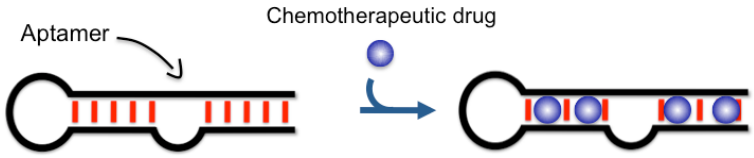

Fig. 12 Schematic diagram of non-covalent aptamer-chemotherapeutic drug conjugate. Chemotherapeutic drugs, such as Doxorubicin, can intercalate in double stranded region of either DNA or RNA. Thus, non-covalent approach exploits this feature to generate aptamer-drug conjugate.

Recently, more sophisticated designs relative to aptamer-drug conjugates have been also explored[138]. Particularly, Tan group used monovalent DNA aptamers able to recognize different cancer cell lines (T and B lymphoma cells) as "building blocks" to produce bispecific and trispecific aptamer nanostructures by DNA self-assembly (Fig. 13a)[140]. Thanks to this strategy a higher number of Dox molecules could be intercalated into the oligonucleotide structure, and the resulting complex showed enhanced specificity compared with parent monovalent aptamers. More recently, the same group elaborated a strategy to increase drug loading of the aptamer. A DNA trigger sequence was added as extended motif at 5'-end of a DNA aptamer (sgc8) against a cell-surface biomarker, protein tyrosine kinase 7 (PTK7) (Fig. 13b). When two hairpin oligonucleotides, called M1 and M2, containing Dox intercalation sites were self-assembled with the DNA aptamer, a train-like structure was generated. They called this model aptamer-tethered DNA

nanotrains (aptNTrs), in which the aptamer acted as a targeting locomotive and the two hairpins provided the boxcars delivering the drug[141]. Up to 50 molar equivalents of Dox was intercalated into the aptamer-nanotrain structure. Most importantly, sgc8-NTrs-Dox complex showed selective delivery and anticancer effect both *in vitro* and *in vivo*.

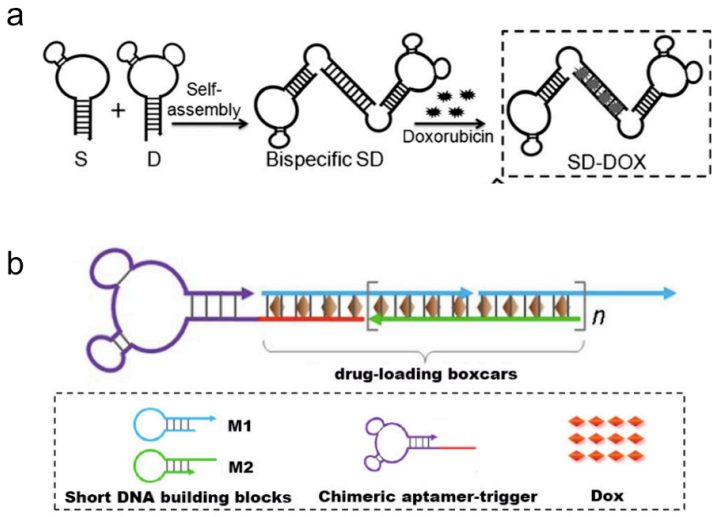

Fig. 13 Scheme for the self-assembly of two different aptamer-based drug carriers. (a) Bispecific SD-doxorubicin complex was self-assembled from molecularly engineered aptamers S and D, containing extended complementary sequences that lead to the formation of a double stranded DNA region upon hybridization. Then, Dox was intercalated in the DNA duplex motif. From "Self-Assembled Aptamer-Based Drug Carriers for Bispecific Cytotoxicity to Cancer Cells". (b) Schematics of the self-assembly of aptamer tethered DNA nanotrains (aptNTrs). Self-assembled from short DNA building blocks upon initiation from a chimeric aptamer-tethered trigger probe, significantly improve the drug payload capacity and the anti-tumor efficacy. Adapted from Zhu et al.[138]; Copyright © Ivyspring International Publisher (2014).

Non-covalent approaches have shown to be a promising strategy in targeted drug delivery applications; however, covalent conjugation of the drug is being investigated as a valid alternative method (Fig. 14). Indeed, the stability of

aptamer-chemotherapeutics complexes is affected by the intrinsically reversible nature of non-covalent interaction. Furthermore, intercalation of anticancer drugs in double stranded regions of the aptamer might alter the aptamer 3D structure, thus adversely affecting its biological activity.

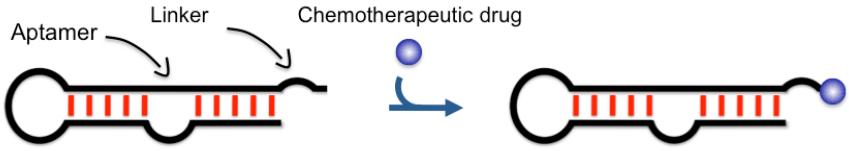

Fig. 14 Schematic diagram of covalent aptamer-drug conjugate. Aptamer bearing a functionalizing linker is covalently conjugated with a chemotherapeutic drug at 1:1 stoichiometry.

Various functional groups (e.g. amino, thiol, azide groups) can be readily included on the oligonucleotide sequence during the chemical synthesis of the aptamers. Thanks to the functionalization of these groups, a host of molecular payloads and nanomaterials has been covalently conjugated to nucleic acid aptamers[142]. For example, the sgc8 aptamer-Dox complex has been generated through an acid-labile acylhydrazone linker at 1:1 stoichiometry[143]. Upon binding with the aptamer target PTK7, the sgc8-Dox conjugate is internalized in target cells (CCRF-CEM T cells) through an endocytosis pathway, where the acid-labile linker is cleaved in the acidic endolysosomal compartment, releasing Dox and exhibiting antitumor activity. In another study, Boyaciogul and coworkers increased the aptamer payload capacity involving the assembly of polyvalent aptamers[144]. Dox was covalently conjugated through a different pH-sensitive linker (formaldehyde) to dimeric aptamer complexes (DACs) constituted by a DNA aptamer against PSMA. Formaldehyde-based linker leads to Dox release upon acid-mediated dissociation and promotes Dox binding to genomic DNA by formation of covalent adducts, increasing Dox-mediated apoptosis[145]. Compared

with the previously described sgc8 aptamer-Dox conjugate, each DAC could bind up to 4 molecules of Dox and the DAC-Dox assembly was stable under physiological conditions for ~8 hours. Lastly, DAC could perform selective delivery of Dox to PSMA (+) cells (C4-2 cells), where Dox localized in the nucleus after endolysosome release. As for other aptamer-Dox conjugates, DAC-Dox showed selective cytotoxicity towards target cells. Interestingly, a highly localized cytotoxicity was observed even when target tumor cells were cultured in close proximity to PSMA (-) cells (PC3 cells) within a co-culture model.

1.7.2 Aptamer-therapeutic oligonucleotide conjugates

In 1998 a groundbreaking study shed light on the role of RNA interference (RNAi) as potent genetic regulator[146]. Small interfering RNA (siRNA) and microRNA (miRNA) molecules are the main classes of small regulatory RNAs that inhibit gene expression by silencing target messenger RNA (mRNA) in a sequence-specific manner[147,148]. These powerful gene-silencing tools have been extensively studied along the last 15 years as a novel class of therapeutics[149]. However, these therapeutic oligonucleotides, as well as traditional drugs, lack of selectivity towards diseased cell/tissues. Therefore, cell-specific internalizing aptamers have been combined with RNAi technology to achieve selective gene targeting through covalent conjugation or physical assembly strategies.

In 2006, Sullenger and coworkers described the first-generation of aptamer-siRNA chimera[150]; the anti-PSMA RNA aptamer A10 (targeting motif) was conjugated to the sense strand of a siRNA and then annealed with unmodified antisense strand to generate the double stranded siRNA (payload motif) (Fig. 15). They demonstrated that conjugation did not affect the functional properties of either aptamer or siRNA. Indeed, the resulting RNA chimera is selectively internalized in PSMA (+) cells through the aptamer motif, and the siRNA portion knocks down the expression of tumor survival genes polo-like kinase 1 (Plk1) and Bcl-2 both *in vitro* and *in vivo*.

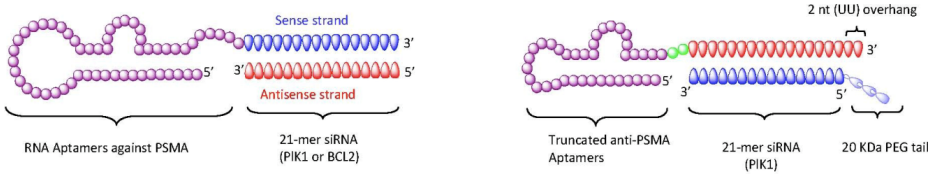

Fig. 15 First- and second- generation of covalent aptamer-therapeutic oligonucleotide conjugates. On the left, schematic of the first-generation anti-PSMA aptamer-siRNA chimeras. The 2'-Fluoro-modified aptamer and siRNA sense strand were co-transcribed, followed by annealing of the complementary siRNA antisense strand to complete the chimeric molecule. On the right, schematic of the optimized second-generation chimeras. Compared with the first generation chimeras, the aptamer portion of the chimera was truncated from 71 to 39 nucleotides, and the sense and antisense strands of the siRNA portion were swapped. A 2 nucleotide (UU)-overhang and a polyethylene glycol tail were added to the 3'-end of the guide strand and the 5'-end of passenger strand, respectively. Adapted from Zhou and Rossi[151]. Copyright © 2010 Zhou and Rossi; licensee BioMed Central Ltd.

Starting from this first design, Giangrande and colleagues rationally designed a second-generation aptamer-siRNA chimera[152] (Fig. 15). Three main differences were included in the A10-Plk1 chimera: (i) minimization of the aptamer portion (from 71 to 39 nucleotides) without affecting the high binding activity to generate aptamer sequences by large-scale chemical synthesis. (ii) 2-nucleotide (UU)-overhang were added at the 3' end of the antisense strand, and then sense and antisense strands of the siRNA portion were swapped to allow a more efficient incorporation of the siRNA by the cellular RNAi machinery. (iii) PEG tail were added to the 5'-end of passenger strand (sense strand) to extend the serum circulating half-life of the chimera. This optimized version of the aptamer-siRNA chimera was administered to a mouse model bearing human prostate cancer and resulted in a major growth suppression of PSMA-expressing tumor compared with the first-generation system. Most importantly, the therapeutic dose of the second-generation chimera was dramatically reduced from 1 nmol at every other day up to ten injections (first generation treatment) to 0.25 nmol at every other day for a total of ten days (second-generation treatment), minimizing both the cost of treatment and the risk of harmful side effects[152].

Non-covalent approaches are an alternative and elegant strategy to obtain aptamer-siRNA chimera. Different molecular connectors have been used to assemble aptamer and siRNA modules (Fig. 16). In 2006, Chu and coworkers focused on the highly specific non-covalent interaction between biotin and streptavidin to generate a multivalent construct composed by an anti-PSMA aptamer (A9) and 27-mer DsiRNAs against lamin A/C and GAPDH (Fig. 16a)[153].Thanks to the four biotin-binding sites present on this protein, two biotinylated aptamers were connected with two biotinylated siRNAs into a modular streptavidin connector. Moreover, a reducible disulfide linker was included between the sense strand of siRNA and the biotin group to enhance siRNA release in the cytoplasm. This multivalent aptamer-streptavidin-siRNA construct displayed PSMA receptor-mediated internalization via the aptamer module and specific silencing of the targeted mRNA transcripts in PSMA-expressing tumor cells via siRNA motif.

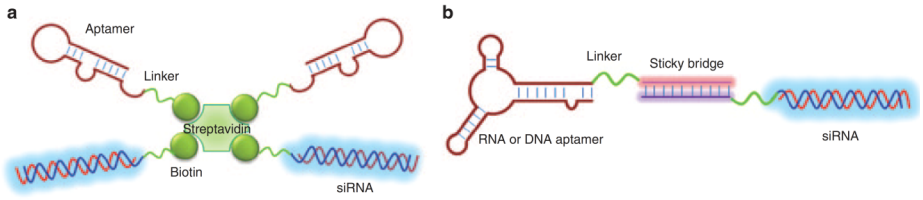

Fig. 16 Non-covalent aptamer-therapeutic oligonucleotide conjugates. (a) Schematic of the aptamer-streptavidin-siRNA conjugate. The two biotinylated siRNAs and two aptamers are non-covalently assembled via a streptavidin connector. (b) Schematic of the aptamer-sticky bridge-siRNA conjugate. The aptamer and siRNA that bearing extended complementary sequences are hybridized by simple Watson-Crick base pairing. Adapted from Zhou and Rossi[2]. Reprinted by permission from Nature Publishing Group: Mol. Ther. Nucleic Acids (Ref. 2), Copyright © 2014 The American Society of Gene & Cell Therapy.

Recently, Rossi group identified new anti-gp120 aptamers and introduced a 'sticky bridge' strategy to connect siRNA motif to the aptamer module[154] (Fig. 16b). In details, an extended short GC-rich sequence was added to the 3'-end of

the gp120 aptamer and its complementary sequence was included at the 3´-end of one of the siRNA strands. After annealing of these two strands by Watson-Crick base pairing, a double helix region was generated and exploited as bridge between the two modules. A flexible three-carbon atom linker (C3) was added as spacer between the extended GC-rich sequence and the 3'-end of the aptamer to allow spatial and structural flexibility both for the aptamer module and the sticky region. Most importantly, this strategy allows the interchange of various siRNAs with the same aptamer, without virtually altering the aptamer conformation. Indeed, in this proof-of concept study, three different siRNAs targeting HIV-1 dependency factors were combined with a single gp120 aptamer. The resulting aptamer-bridge-siRNA cocktail was selectively uptaken via gp120 into HIV-1 infected cells (CEM-T cells and human PBMCs), leading to suppression of HIV replication by targeted gene silencing.

1.7.3 Aptamer-conjugated nanomaterials

An effective strategy to generate aptamer-mediated drug delivery platforms with enhanced properties, lies on the aptamer conjugation on the surface of smart biocompatible nanomaterials. Besides sharing the common properties of nanomaterials, such as large surface area, uniform size and shape for an excellent biodistribution, the resulting aptamer-nanomaterials display several additional features: (i) improved nuclease resistance owing to the higher steric hindrance that hampers the nucleic acid sequence recognition by nucleases, (ii) reduced renal clearance rates with prolonged circulating half-life due to the molecular mass of this platform, (iii) enhanced aptamer affinity for their targets based on the presence of multiple aptamer copies on the nanomaterial surface, which leads to an increased aptamer local concentration, and (iv) higher drug payload capacity compared with aptamer-drug conjugates owing to the large surface area of the nanomaterials.

Importantly, several physicochemical properties of aptamer-nanomaterials, such as, ligand–receptor interaction valency, aspect ratios, orientation, and spacing of ligands need to be considered to obtain a proper recognition of the aptamer target receptors that ultimately triggers an intracellular uptake into target cells. For

example, rod-like particles with high aspect ratios are internalized more efficiently *in vitro* through receptor-mediated endocytosis compared with particles with low aspect ratios, such as spheres and cubes[155].

To date, various nanomaterials such as copolymers[156], liposomes[157], metal nanomaterials[158], and virus-like particles[159] have been combined with cell-specific aptamers for targeted delivery of diagnostics and therapeutics. Here, I shall briefly mention the more relevant studies, in which gold nanoparticles, superparamagnetic iron oxide nanoparticles, polymeric nanoparticles, and quantum dots were used as nanomaterials.

Gold nanoparticles. Thanks to their favorable characteristics, which include high stability, good biocompatibility, and straightforward conjugation, gold nanoparticles (AuNPs) have been widely explored in combination with targeting aptamers. For example, Ellington and colleagues combined an RNA aptamer against Epidermal Growth Factor Receptor (EGFR) with AuNPs using a non-covalent conjugation approach[160]. In details, short DNA capture sequences were first covalently conjugated to the surface of AuNPs, and then hybridized by Watson-Crick base pairing with complementary extended sequences tethered to the 5'-end of the anti-EGFR RNA aptamers (Fig. 17). This double stranded DNA spacer reduced the nonspecific interaction between the surface of the AuNPs and the aptamer molecules without affecting aptamer 3D conformation that could retain its biological activity. Indeed, AuNP-aptamer complexes were selectively internalized via receptor-mediated endocytosis in EGFR (+) cells. Most importantly, the nonspecific uptake exhibited by AuNPs was markedly reduced after conjugation with the RNA aptamer.

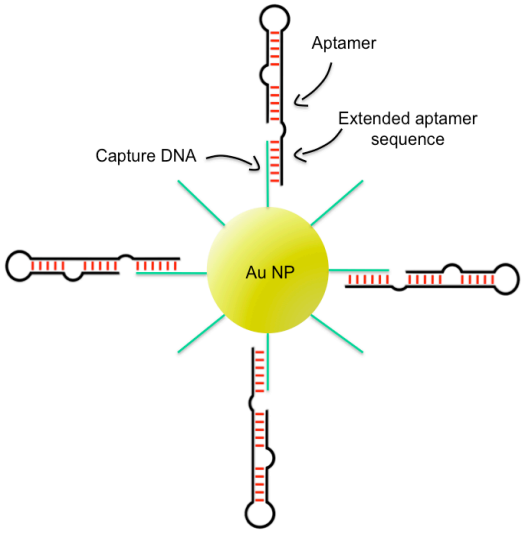

Fig. 17 Aptamer-functionalized gold nanoparticles. AuNPs are first coated with short capture DNA sequences (green) and then are hybridized with corresponding complementary sequences tethered to the 5′-end of the aptamer.

In a recent study, an RNA aptamer against CD30 -a diagnostic biomarker for Hodgkin's lymphoma and anaplastic large cell lymphoma- was chemically conjugated with negatively charged hollow gold nanospheres (HAuNS) via thiol-gold linkers[161]. The resulting aptamer-HAuNS conjugates were partially coated with PEG to enhance their biostability. Lastly, doxorubicin molecules were absorbed on the surface of these conjugates exploiting electrostatic interaction at physiological pH (7.4) between the positive amino group of Dox and the negative citrate present on the surface of HAuNS[22]. The aptamer-HAuNS-Dox complexes were sensitive to pH changes: they were quite stable at pH 7.4 but they released 80% of their drug payloads within 2 h at pH 5.0, a value similar to that found into lysosomal compartment. Most importantly, when incubated in mixed cell cultures (i.e. co-culture composed of both CD30-expressing lymphoma cells and CD30-

negative control cells), the aptamer-HAuNS-Dox was able to internalize and selectively kill lymphoma tumor cells without unwanted off-target toxicity.

Superparamagnetic iron oxide nanoparticles. Because of their superparamagnetic properties and their wide range of potential applications in catalysis, sensors, and MRI (magnetic resonance imaging), superparamagnetic iron oxide nanoparticles (SPIONs) have attracted a growing interest. SPIONs are iron oxide particles included α-Fe_2O_3 (hematite), γ- Fe_2O_3 (maghemite) and Fe_3O_4 (magnetite) of 1-100 nm or greater diameters[162]. The surface of the SPION can be coated with few layers of organic polymers to confer both anti-biofouling property that prevents the adsorption of plasma proteins or cells onto their surface and targeting capability with specific chemical groups. These functional groups can be covalently conjugated with targeting ligands to generate targeted nanoparticle platforms. In 2008, Farokhzad and coworkers designed and assembled a multifunctional theranostic system combining the anti-PSMA RNA aptamer targeting properties for targeted drug delivery and the SPION magnetic properties as diagnostic agent[163]. In details, the anti-PSMA RNA aptamers bearing an amino group at the 3'-end was conjugated via EDC/NHS coupling chemistry to the carboxyl groups of an antibiofouling polymer that coated the surface of the SPION. Doxorubicin was loaded into the aptamer-SPION conjugates both by intercalation into the duplex region of the aptamer module and by absorption onto the surface of the SPION through electrostatic interactions (Fig. 18). The potential of the aptamer-SPION conjugate as a targeted MR contrast agent was investigated by Nuclear Magnetic Resonance (NMR) studies. Particularly, by monitoring the longitudinal relaxation time (T1), and the transverse relaxation time (T2) of both the aptamer-SPION conjugate and non-targeted SPION in living cells, the aptamer targeted platform led to selective detection of PSMA-expressing tumor cells with high sensitivity. Furthermore, targeted drug delivery properties were assessed by in vitro cell viability measurements. Interestingly, Doxorubicin was selectively released from the aptamer-SPION platform in target prostate cancer cells leading to a specific anticancer effect.

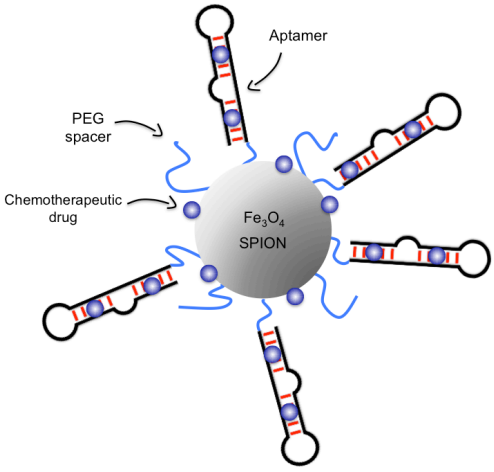

Fig. 18 Aptamer-functionalized SPIONs. The aptamer is covalently conjugated onto the surface of a SPION and then Dox is intercalated in the duplex region of the aptamer and also complexed with the SPION through charge interactions.

Polymeric nanoparticles. In the last decade, several groups have exploited aptamer-functionalized natural or organic polymeric materials for targeted drug delivery applications. Polymeric nanoparticles (polymeric NPs) exhibit excellent opportunities in terms of enhanced biodegradability and biocompatibility. Indeed, most of the first-generation nanomedicines approved for clinical applications are based on polymeric and liposomal formulations. In 2004, a pioneering work described the synthesis of an aptamer-polymeric NP platform as tool for targeted drug delivery[156]. Particularly, the anti-PSMA RNA aptamer was conjugated with biocompatible and biodegradable poly(lactic acid)-block-PEG copolymer tethering a terminal carboxylic acid functional group (PLA-PEG-COOH) Notably, using conventional EDC/NHS coupling chemistry, the amino group at the 5'-end of the aptamer was linked to the carboxyl acid on the polymer. The resulting aptamer-polymeric NP conjugate was internalized specifically in PSMA-expressing cells with an enhanced uptake up to 77-fold compared with control pegylated polymeric NPs. Exploiting this strategy, the same group generated a

nanoscale platform for targeted therapy having both targeting properties and controlled drug release properties[164]. In details, the anti-PSMA RNA aptamer A10 were used to functionalize the surface of biodegradable and biocompatible poly(lactic-*co*-gycolic acid)-block-PEG with a terminal carboxylic acid group (PLGA-PEG-COOH). Then, the complex was loaded in the inner part of the polymeric NP structure with Docetaxel, a hydrophobic chemotherapeutic drug (Fig. 19). Notably, in this platform PLA or PLGA helps to encapsulate and control drug release, while PEG enhances circulating half-life conferring anti-biofouling properties of the bioconjugate. Targeted drug delivery properties were observed both *in vitro* and *in vivo*. In cultured cells the aptamer-polymeric NP-Docetaxel conjugates showed enhanced selective cytotoxicity towards PSMA expressing prostate cancer cells. Most importantly, a single intratumoral injection of this platform in a xenograft tumor model resulted in significant tumor reduction with negligible off-target effect in the mice.

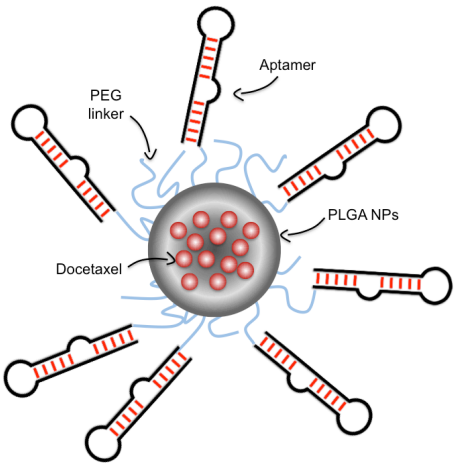

Fig. 19 Aptamer-functionalized polymeric nanoparticle. The aptamer is covalently functionalized onto the surface of the polymeric NPs. Antitumor drug, Docetaxel, is encapsulated into the hydrophobic core of the PLGA NPs.

An emerging trend in cancer therapy is the use of combinations of two different drugs to achieve a synergistic effect and improve the therapeutic index. This strategy is becoming really significant mostly for the treatment of chemotherapy-resistant tumors. However, the codelivery of two different drugs having different physicochemical properties is extremely difficult. An elegant approach based on aptamer-functionalized polymeric NPs was exploited to selectively deliver both hydrophilic doxorubicin and hydrophobic docetaxel in tumor cells overexpressing PSMA[165]. Particularly, docetaxel was first encapsulated in PLGA-PEG-COOH. Simultaneously, the 5'-NH_2-anti-PSMA RNA aptamer module was preloaded with doxorubicin by its intercalation into the double stranded region. Then, the final complex was formed through EDC/NHS chemistry coupling as previously described. The resulting drug-delivery platform was able to selectively deliver both doxorubicin and docetaxel into PSMA (+) prostate cancer cells. Most importantly, the codelivery strategy resulted in significantly higher cytotoxic effect compared with the treatment of the cultured cells after aptamer polymeric NP-mediated delivery of either doxorubicin or docetaxel.

Chapter 2

Aptamer-mediated codelivery of doxorubicin and NF-kB decoy enhances chemosensitivy of pancreatic tumor cells

This chapter was peer-reviewed and published previously with co-authors D Porciani, L Tedeschi, L Marchetti, L Citti, V Piazza, F Beltram & G Signore: "Aptamer-mediated codelivery of doxorubicin and NF-kB decoy enhances chemosensitivy of pancreatic tumor cells," Mol Ther Nucleic Acids. 2015 Apr 4:e235. doi:10.1038/mtna.2015.9. D Porciani, V Piazza, F Beltram and G Signore, contributed to design the study. D Porciani and G Signore analyzed both HPLC and fluorometer data. L Tedeschi and L Citti designed the NF-kB decoy sequence. D Porciani and L Tedeschi synthesized the oligonucleotide sequences. D Porciani and L Marchetti performed the western blot analyses. Unless otherwise specified, experiments and data shown in each figure were performed and analyzed by D Porciani.

As stated in the previous chapter, most therapeutic agents currently in clinical use are in general not engineered to selectively target the site of the disease. So far, targeting strategies using ligand-bound cell-surface markers to deliver small therapeutic agents have enhanced the selectivity of these drug delivery platforms. In this context, aptamers are emerging as a valid alternative to monoclonal

antibodies. As previously described, recent studies led to the development of a variety of targeted systems based on aptamer-chemotherapeutic drug conjugates, aptamer-therapeutic oligonucleotides conjugates or aptamer-nanomaterial assemblies. Although these platforms have been successfully used especially against many different types of cancer, intrinsic or acquired resistance to the cytotoxic effects of chemotherapy has emerged as a significant hurdle to effective cancer treatment. Indeed, tumors usually consist of mixed populations of malignant cells; a fraction of these cells is drug-sensitive while the other one is drug-resistant[166]. Therefore, chemotherapy kills only drug-sensitive cells, but is not able to overwhelm drug-resistant cells[166].

A key factor involved into chemoresistance is the nuclear factor κB (NF-κB), a ubiquitous transcription factor that inhibits apoptosis through induction of anti-apoptotic proteins and/or suppression of pro-apoptotic genes. In details, NF-κB is the generic name for a family of dimers formed by several proteins: NF-κB1 (also known as p50/p105), NF-κB2 (also known as p52/p100), REL, RELA (also known as p65/NF-κB3) and RELB. The different heterodimers can bind specific promoters to initiate transcription of a wide range of genes involved into inflammatory response as well as cell death and survival and tissue repair[167]. NF-κB is active in the nucleus and is inhibited through its sequestration in the cytoplasm by the inhibitor of κB (IκB), which binds NF-κB through a specific binding motif (Fig. 1). Several stimuli including growth factors, cytokines (such as interleukin-1 and tumor necrosis factor), hormones and other signals activate NF-κB by the phosphorylation of IκB. Indeed, the phosphorylated IκB is released from NF-κB, which can freely translocate to the nucleus where it promotes transcription of antiapoptotic genes such as X-linked inhibitor of apoptosis protein (XIAP) and Bcl-2 family genes, ultimately conferring resistance toward apoptotic stimuli.

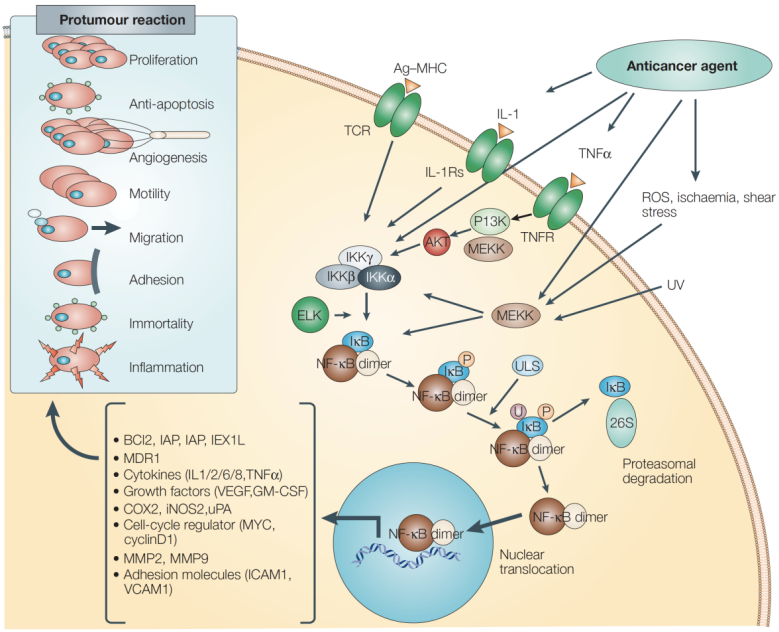

Fig 1 A scheme of the nuclear factor-κB (NF-κB) pathway activated by anticancer drugs. Anticancer drugs induce nuclear translocation of NF-κB, activation of NF-κB target genes, and the secondary production of NF-κB activators such as reactive oxygen species (ROS), interleukin-1 (IL-1) and tumor-necrosis factor-α (TNFα). All of these effects can lead to enhanced cell proliferation, angiogenesis, motility, migration, adhesion, immortality, inflammation and inhibition of apoptosis, through expression of genes coding for anti-apoptotic proteins, membrane transporters, cytokines, growth factors, cell-cycle regulators, cell-adhesion molecules and cell-surface proteases. Nitric oxide synthase 2 (iNOS2): 26S, 26S proteasome; BCL2, B-cell CLL/lymphoma 2; COX2, cyclooxygenase-2; GM-CSF, granulocyte–macrophage colony-stimulating factor; IAP, inhibitor of apoptosis protein; ICAM1, intracellular adhesion molecule 1; IEX1L, immediate early response gene X-1 longer transcript; IKK, IκB kinase; IL-1Rs, IL-1 receptors; IκB, inhibitor of κB; MDR1, multidrug resistance gene 1; MEKK, MAPK/ERK kinase kinase; MHC, major histocompatibility complex; MMP, matrix metalloproteinase; NF-κB, nuclear factor-κB.; PI3K, phosphatidylinositol 3-kinase; TNFR, tumor-necrosis factor receptor; ULS, ubiquitin ligase system; uPA, urokinase-type plasminogen activator; UV, ultraviolet; VCAM1, vascular cell-adhesion molecule 1; VEGF, vascular endothelial growth factor; XIAP, X-linked inhibitor of apoptosis protein. Reprinted by permission from Macmillan Publishers Ltd: Nature Reviews Cancer (Ref. 168), Copyright © 2005.

Constitutive NF-κB activation observed in many malignant tumors protects the cells from apoptotic stimuli, including anticancer treatments and might have a crucial role in the intrinsic chemoresistance. Genetic alterations affecting the genes encoding NF-κB or IκB are the main causes responsible for this constitutive activation. Intriguingly, several anticancer agents (such as doxorubicin) stimulate NF-κB activation, which can potentially lead to acquired chemoresistance[168]. Recent studies demonstrated that inhibition of NF-κB sensitizes tumor cells to doxorubicin-induced apoptosis in various cancer cells (breast cancer, pancreatic cancer, renal and hepatocellular carcinoma)[169,170].

In this scenario, a codelivery strategy, in which two or more therapeutics are simultaneously administered could represent an effective way to treat cancer and overcome both intrinsic and acquired chemoresistance. Drugs with distinct mechanisms of action can be combined in a precisely controlled manner leading to a synergistic therapeutic efficacy, to minimize side effects and inhibit specific effectors of chemoresistance[171].

In this chapter, I shall describe a molecular-engineering strategy to develop a drug-delivery system composed uniquely by oligonucleotide modules able to perform codelivery of therapeutic payloads towards human pancreatic tumor cells. This platform is composed by three main domains: (i) a targeting motif, i.e. an RNA aptamer against the human transferrin receptor (hTfR) (ii) a drug-loading region for a traditional chemotherapeutic drug, i.e. doxorubicin (Dox) and (iii) an oligonucleotide decoy having inhibitor properties towards NF-κB as secondary molecular payload. The whole system was designed with labile (pH and redox) linkers able to promote conditional release of the therapeutic payloads upon internalization in cells.

TfR was chosen as cell-surface marker owing to (i) its upregulation in many solid tumors and (ii) its constitutive endocytic pathway. Thus, aptamers targeting TfR can be easily internalized into the cells upon binding to TfR via a receptor-mediated endocytosis.

To reduce the chemoresistance of tumor cells and to increase the cytotoxic effect of Dox, as second molecular payload we decided to use NF-κB decoy oligonucleotide. Decoys are synthetic, double-stranded oligonucleotides (ODNs)

that selectively inhibit biological function of targeted transcription factors. In particular, NF-κB decoy ODNs are designed to mimic the κB consensus sequence recognized by NF-κB to the promoter regions of its target genes, thus ultimately preventing NF-κB binding to these sequences and hampering its transcriptional activity.

2.1 Rational design of aptamer–Dox conjugate

Our rational design of the therapeutic assembly started with the modification of a known cell penetrating RNA aptamer (c2.min) recognizing hTfR to generate an aptamer-Dox conjugate. In details, c2.min is the truncated version of a selected RNA aptamer against the hTfR[137]. Interestingly, despite the sequence homology between the human and mouse TfR is about 77%, c2.min is not able to bind the murine TfR and to internalize into mouse cells, being selective for the human receptor. Additionally, c2.min competes with the natural ligand, Tf, both for receptor binding and cell uptake. However, c2.min performs approximately twofold better than Tf in competition experiments, demonstrating that the aptamer binds to the receptor better than the natural ligand. As described in the first chapter two main strategies are reported in literature to generate aptamer-Dox conjugates: (i) non-covalent and (ii) covalent approach. In our design we decided to exploit the natural tendency of Dox to intercalate within DNA duplex through its aromatic rings (Fig. 2).

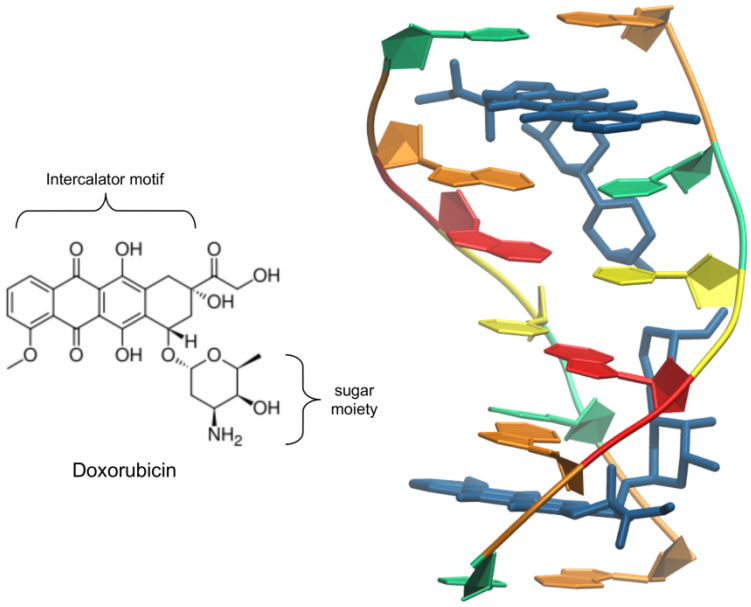

Fig 2 Doxorubicin intercalation in double-stranded DNA. The left panel reports the doxorubicin structure. On the right, the DNA-doxorubicin complex is shown with the two molecules of doxorubicin in blue, and the DNA bases that are depicted as follows: C in green, G in orange, A in red, T in yellow. The PDB code of the structure is 234D[172].

It is known that Dox preferentially binds to CG steps of double-stranded DNA regions with 5'-GC-3' or 5'-CG-3' sequences[173] (Fig. 2). Two trinucleotides are mainly involved in Doxorubicin intercalation within CG steps: CGA, which shows high flexibility, and the CGT, a rigid trinucleotide[174]. However, intercalation into the CGA trinucleotide shows tighter binding due to the formation of inter- and intra-molecular hydrogen bonds that are not observed with the CGT sequence[174].

It is worth noting that an analysis of c2.min secondary structure prediction evidenced only one Dox binding site with 5'-CG-3' sequence within the RNA aptamer (Fig. 3).

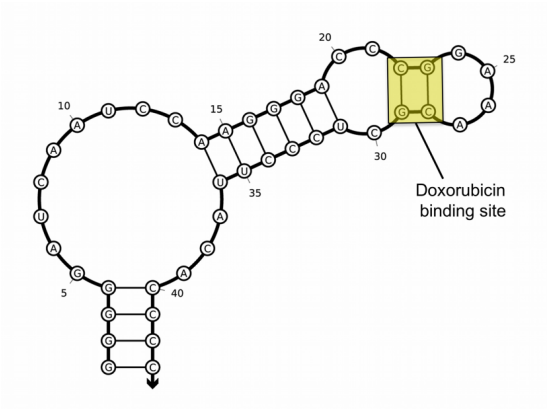

Fig 3 Secondary structure prediction of c2.min RNA aptamer recognizing human transferrin receptor obtained using NUPACK (Nucleic Acid PACKage)[175] tool. Yellow box on the secondary structure indicates possible Dox binding sites with 5'-GC-3' or 5' CG-3' sequences.

Thus, to improve the Dox-loading capacity of c2.min, we designed an elongated aptamer bearing a short DNA tail composed by CGA repeating units at 3'end to create a duplex GC-rich region upon hybridization with its complementary DNA sequence, hereafter called anti-tail. As shown in Fig. 4a, NUPACK secondary structure prediction of the hybridized complex composed by the extended c2.min (i.e. c2.min-tail) and anti-tail highlighted two distinct regions: (i) the RNA aptamer portion still in its proper fold and (ii) a drug-loading domain composed by a DNA double helix. The resulting oligonucleotide carrier structure (hereafter c2C) includes one Dox binding site on the RNA motif and six to seven possible binding sites on the duplex region, which raise the final loading to seven to eight Dox molecules/c2C. Additionally, NUPACK calculation was also able to provide a depiction of the helicity of the hybridized oligonucleotide c2C (green and red color, respectively for c2.min-tail and the anti-tail sequence in Fig. 4a). Most importantly, as shown in overall representation of the secondary structure, the DNA duplex domain does not interfere with the correct RNA aptamer folding (as

shown by a comparison between Fig 2 and 3a), in agreement with previous studies involving the same DNA extension[158].

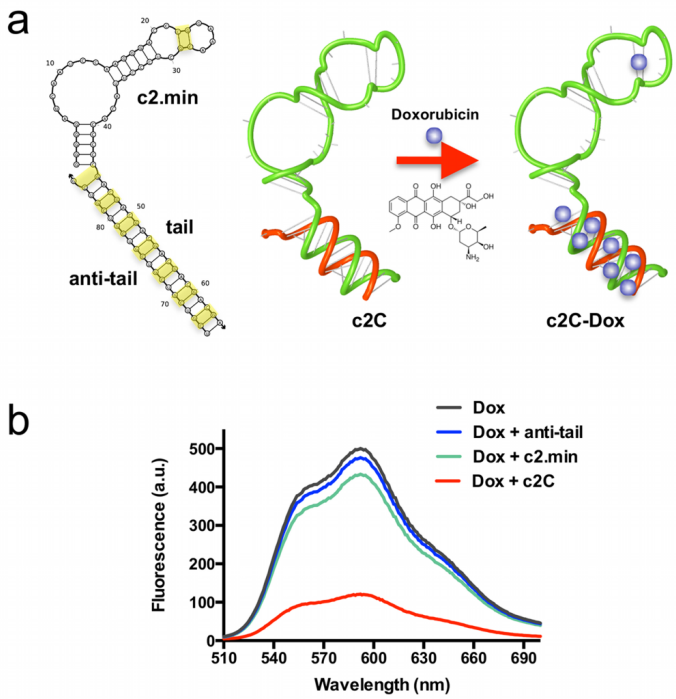

Fig 4 Rational design of c2C–Dox conjugate: (a) From left to right, secondary structure prediction of the hybridized assembly composed by the extended RNA aptamer (c2.min-tail) and anti-tail. Yellow boxes on the secondary structure indicate possible Dox binding sites within oligonucleotide structure. Note that each oligonucleotide is represented as an RNA sequence. (b) Fluorescence spectra of Dox solution (1.5 μM) incubated with: buffer, anti-tail, c2.min, and c2C (7.5 molar ratio Dox/c2C); Dox fluorescence in the conjugated molecule is quenched because of its intercalation in DNA duplex.

Note that the great advantage to use a non-covalent strategy lies in a straightforward and quick formation of the conjugate between c2C and Dox which can be easily monitored in real time. To this end, we evaluated Dox loading

efficiency by evaluating variation of its fluorescence emission, which is known to decrease upon intercalation into DNA duplex due to a Förster resonance energy transfer between the anthracycline ring and DNA double stranded[139].

As shown in Fig. 4b, Dox fluorescence sensibly decreased upon incubation with the hybridized oligonucleotide c2C (7.5 molar ratio Dox/c2C) in agreement with the predicted presence of seven to eight Dox binding sites. Most importantly, only minor fluorescence quenching was detected in presence of c2.min and no quenching effect was observed in absence of the hybridization between the tail and anti-tail portions (Fig. 4b). This result confirms the formation of the correct, predicted c2C fold, in which the essential role of Dox loading is tightly related to the DNA duplex region. An electrophoretic mobility shift assay (EMSA) using a native polyacrylamide gel was also performed to confirm the effective formation of the hybridized complex c2C. As shown in Fig. 5, the band of the oligonucleotide assembly, c2C, migrated more slowly than the band of the free c2.min-tail owing to the larger size of the complex that reduces its migration rate during the electrophoresis analysis[176]. Importantly, no band of c2.min-tail was detected in the mixture of the two oligos (lane 3), suggesting the complete hybridization between c2.min-tail and anti-tail.

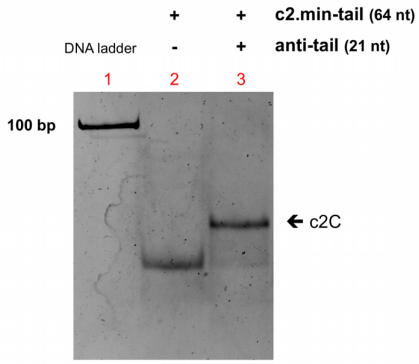

Fig 5 Electrophoretic mobility shift assay EMSA) to assess the formation of the oligonucleotide complex among the extended aptamer (c2.min-tail) and the anti-tail. Lane 1: 100 bp range DNA ladder. Lane 2: c2.min-tail. Lane 3: c2.min-tail+anti-tail. Native PAGE 8%; Band detection was performed by ethidium bromide staining.

Next, we evaluated the stability of the c2C-Dox conjugate in a serum-containing medium to quantify Dox release from the complex. This experiment aimed at evidencing the correct formation of the oligonucleotide carrier structure and to evaluate the stability of this complex and its potential use in an *in vitro* tumor model. After the physical assembly of the conjugate, the c2C-Dox was added with either 1% or 5% serum-containing medium and incubated at 37°C for 0, 0.5, 1, 2, and 24 hours. Fluorescence emission of Dox was measured at each specific time to evaluate the extent of Dox release from the double helix (Table 1). Interestingly, c2C-Dox complex did not release Dox after 1h incubation in serum-containing medium (1% and 5%) at 37°C, and only minor leakage was observed (<10%) after 2h incubation. Most importantly, even at longer incubation (24h) the assembly is quite stable, and the leakage from the double helix was about 25% in both serum conditions. Notably, no serum-concentration dependence was observed; this might suggest that leakage is likely due to a slow Dox thermally-driven desorption from double helix that does not involve interaction with serum proteins.

Table 1: Doxorubicin release from aptamer in serum-containing media

Time	*Dox released (%) (1% serum)*	*Dox released (%) (5% serum)*
0 min	0.0	0.0
30 min	0.5	5.7
60 min	1.4	3.3
120 min	8.5	11.4
24 h	27.0	26.5

Then, we investigated whether c2.min still conserved its activity to bind hTfR and internalize into hTfR-expressing cells even when bearing the sterically demanding drug-loading region, i.e. GC-rich DNA duplex. To this end, we performed an internalization assay in living cells using a dual-labeled c2C assembly. Both c2.min-tail and anti-tail bear an amino group at the 5'-end. Each group was conjugated with a small organic dye, namely ATTO 633 to c2.min-tail and Alexa Fluor 488 to the anti-tail module. The dual labeling of the c2C complex

allows a simultaneous visualization of the two components, which is essential to evaluate the structural integrity of c2C complex inside the cells.

We assessed uptake of this dual-labeled c2C in human pancreatic tumor cells (MIA PaCa-2), which are known to overexpress hTfR[177]. The endocytosis process of dual-labeled c2C was monitored by confocal microscopy (Fig. 6). Complete colocalization of the two dyes in subcellular vesicles was observed 20 minutes after the addition of the dual-labeled c2C, consistently with the uptake and retention of the entire complex[144]. Interestingly, considerable perinuclear localization was observed at longer times (120 minutes) for both dyes, suggesting that at least a fraction of c2C is not recycled during the endocytosis process. Overall, the endocytosis of the whole complex demonstrates the capability of c2.min to retain its activity even when embedded in a more complex ODN structure.

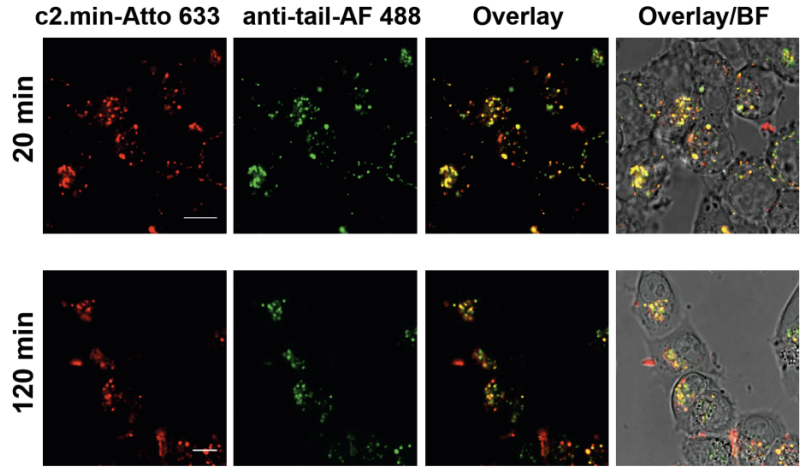

Fig. 6 Cellular uptake of dual-labeled c2C (Alexa Fluor 488, green and ATTO 633, red) in pancreatic tumor cells (MIA PaCa-2). Extensive colocalization was observed both at early (20 minutes) and at longer (120 minutes) times. Scale bars: 10 µm

Taken together, these results highlight that our aptamer-Dox conjugate is easily generated by (i) a straightforward Watson-Crick base pairing and (ii) by a subsequent intercalation with Dox. Additionally, both targeting motif and drug loading region retain their proper structural folds that are tightly connected with their activities. Most importantly, Dox leakage from the construct in serum-containing media is negligible at short times and limited ad longer times. This fact evidences the good stability of the assembly in conditions usually employed in cell treatment, and promotes its suitability for live cell applications.

2.2 Aptamer-mediated tumor targeting and Dox release mechanism

The first step in the preparation of a drug delivery platform for codelivery is represented by the evaluation of its ability to effectively deliver each single drug. Thus, we started to evaluate whether our non-covalent aptamer-Dox conjugate (c2C-Dox) could be selectively uptaken in tumor cells (MIA PaCA-2). Nontumoral mouse fibroblasts (NIH-3T3) were used as negative control to monitor the extent of the off target effect[178]. To this end, we monitored Dox fluorescence by confocal imaging microscopy after cell treatment with either the whole complex or free Dox, keeping constant both Dox concentration (1.5 μM) and Dox/c2C ratio (7.5:1). This approach allows a better comparison of the internalization pathway and efficiency, especially between free Dox and c2C-Dox.

As expected, free Dox readily diffuses through the plasma membrane and accumulates into the nuclei of both hTfR(+) and hTfR(-) cells with nearly identical efficiency (Fig. 7). In contrast, when c2C-Dox conjugate is added to the cells, the aptamer-mediated uptake of Dox is markedly different in tumor and control cells. Indeed, c2C-Dox is readily internalized in MIA PaCa-2 cells, as shown by Dox fluorescence detected both in endocytic vesicles and into the nucleus, whereas only a weak cytoplasmic signal was detected in control cells (NIH-3T3), likely due to either negligible nonspecific internalization of the complex or minimal Dox release from the double helix during the 2h incubation.

Most importantly, free Dox and c2C-Dox display different uptake mechanisms by MIA PaCa-2 cells. Free Dox mainly accumulates in the nuclear region, while c2C-Dox shows both nuclear fluorescence and vesicular signal, in keeping with a subcellular compartmentalization of Dox within endosomes and lysosomes (endolysosomes). This behavior is in agreement with previous studies that showed cytoplasmic localization of Dox released from transferrin-Dox conjugates[179]. Overall these results and observations suggest that c2C-Dox is effectively internalized in human tumor cells via a receptor-mediated endocytosis.

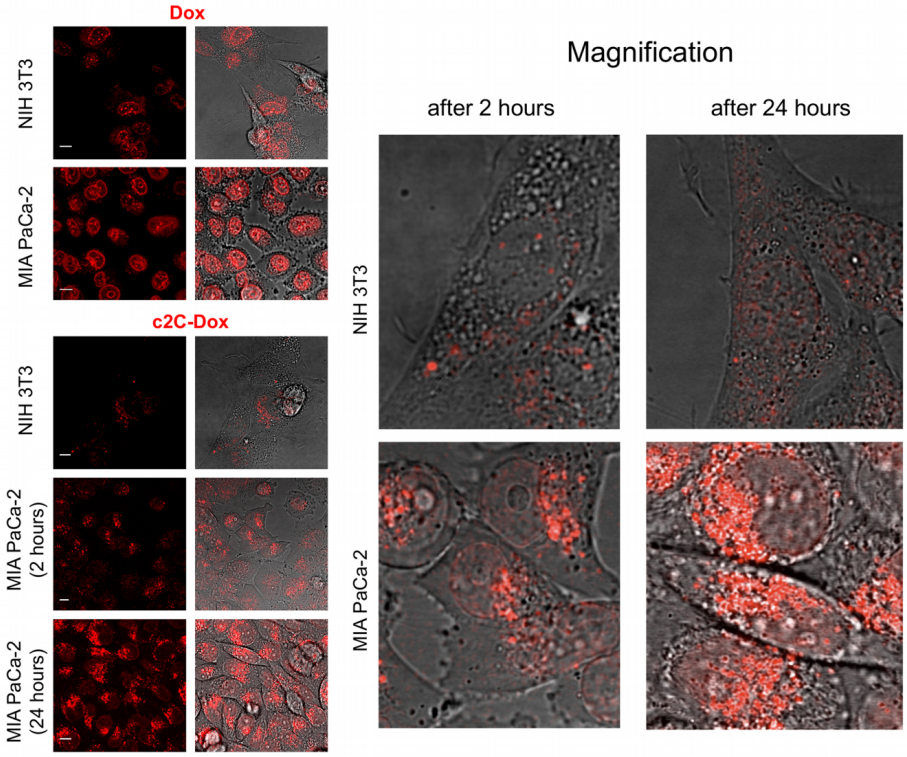

Fig. 7 Selective internalization of the c2C–Dox conjugate in targeted tumor cells. Confocal imaging microscopy shows the intracellular distribution of free Dox and Dox released from c2C–Dox complex (red fluorescence) in tumor cells (MIA PaCa-2) and control cells (NIH-3T3). Scale bars: 10 µm.

Next, we evaluated the intracellular release of Dox from the oligonucleotide complex in both cells at longer times (24 hours after treatment). As shown in the magnification of Fig. 7, a higher fluorescence signal was observed both in the cytoplasm and in the nucleus of MIA PaCa-2 cells. Conversely, only a slight increase of fluorescence was detected in NIH 3T3 cells, in agreement with a markedly lower uptake of c2C-Dox.

The fluorescence enhancement observed in tumor cells suggests releasing of Dox from DNA duplex during late stages of the endocytosis pathway. Indeed, upon release of Dox from the double helix, the quenching effect due to the Dox intercalation may disappear and its fluorescence is restored.

To investigate the nature of this fluorescence enhancement, we reproduced in vitro conditions matching those found in physiological conditions during late stages of TfR-mediated endocytosis pathway, and we monitored the fluorescence of c2C-Dox sample within this environment. As described in the first chapter, the intravescicular pH sensitively drops along the endocytic pathway from pH 6.0–6.5 in early endosomes to pH 4.5–5.5 in late endosomes and lysosomes[180]. Therefore, c2C-Dox (1.5 μM Dox concentration) was incubated in solutions at different pH (7.4, 6.5, 5.8, 5.5, 5.0) and its fluorescence was monitored spectrophotometrically in real time. A free Dox sample at the same concentration was used as control to compare the variation of Dox fluorescence at each pH value.

As shown in Fig. 8, Dox release was negligible (<10%)in a simulated early endosomal environment (pH 6.0-6.5). However, considerable Dox fluorescence enhancement related with a Dox release of ~40% at pH 5.5 and ~55% at pH 5.0 occurred at lower pH values, which mimic those found in the late endosomes and lysosomes (5.0-5.5). Interestingly, this result is in excellent agreement with previous observations regarding Dox release in acidic solution[181]. It is well known that lysosomes contain several types of digestive enzymes including nucleases[182]. Thus, to better simulate the physiological condition of a lysosomal compartment, we added DNA nucleases (i.e DNase II) to the c2C-Dox sample at pH 5.0. As expected, Dox release increased from ~55% to ~98% within 2 hours at room temperature due to the degradation of the DNA duplex region on c2C structure.

These findings highlight the essential role of these hydrolytic enzymes in the mechanism of Dox release.

We hypothesized that the observed pH dependency might be tightly related to the protonation of $-NH_2$ groups on Dox that occurs at low pH (<6)[22]. This event might reduce the hydrophobic π stacking interaction between the aromatic ring of Dox and the nitrogenous bases of DNA duplex.

It is worth noting that this pH- and nuclease-dependent Dox release from c2C-Dox conjugate is consistent with the Dox fluorescence enhancement detected in MIA PaCa-2 cell cytoplasm at longer times (24 hours after treatment). Overall, these results support the hypothesis of pH- and enzymatic Dox release at endolysosomal level during receptor-mediated endocytosis pathway.

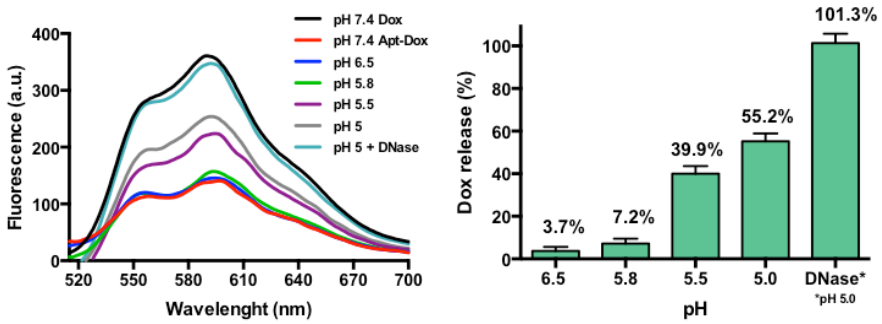

Fig. 8 pH- and nuclease-triggered Dox release. On the top are shown the fluorescence spectra of Dox solution (1.5 μM) incubated with: buffer (pH 7.4), and c2C (7.5 molar ratio Dox/c2C) at different pH: 7.4, 6.5, 5.8, 5.5 and 5. The fluorescence of Dox at pH 5 was measured either before or after DNase treatment.

2.3 Antitumor efficacy of c2C-Dox

Next, we assessed the therapeutic potential of this promising c2C-Dox conjugate. Thus, to evaluate whether the observed selective internalization could be translated to a specific anticancer effect we measured c2C-Dox cytotoxicity towards both tumor and control cells. To this end, we performed a standard water-

soluble tetrazolium salt (2-(2-methoxy-4-nitrophenyl)-3-(4-nitrophenyl)-5-(2,4-disulfophenyl)-2H-tetrazolium, monosodium salt, WST-8) assay to monitor the cell viability[183] after treatment with either free Dox or c2C- Dox. Additionally, a c2 scrambled sequence (i.e. c36), which is known to be unable to recognize hTfR[137] was used as control. This ODN sequence bears the same extended tail at the 3'-end, and a c36C-Dox was easily prepared by using the same straightforward procedure, previously described to generate c2C-Dox. Furthermore, a cervical cancer cell line (HeLa) was also employed to assess the cytotoxicity effect in a different tumor model, which may show a different sensitivity towards Dox.

Dose dependence was demonstrated for all cell lines using the WST-8 assay (Fig. 9).

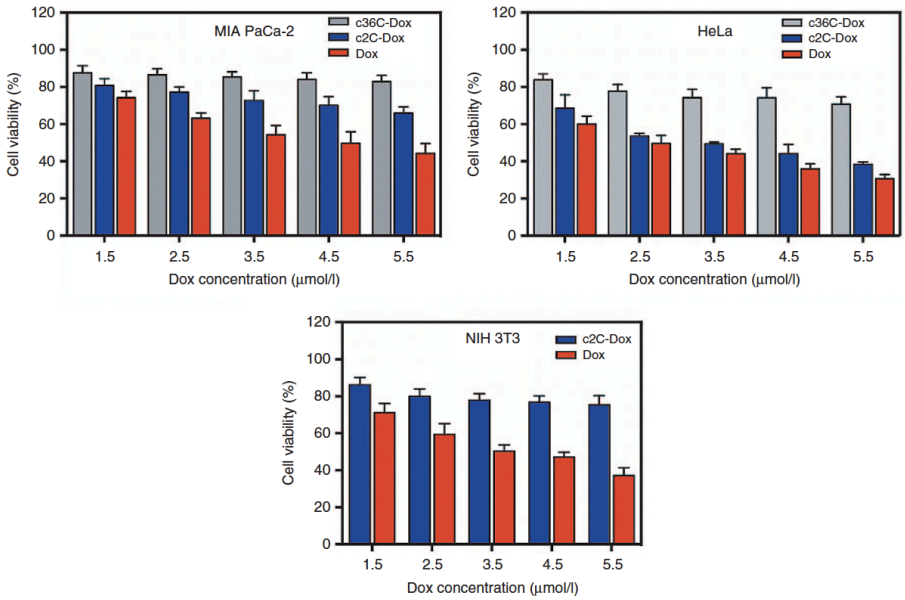

Fig. 9 Cell viability assay of MIA PaCa-2, HeLa, and NIH-3T3 cells after treatment with free Dox (red), c2C–Dox (blue), and c36C–Dox (gray). Cells were incubated with the drugs for 2 hours and cell viability was assessed after 24 hours. Cell viability on incubation with c2C alone (see experimental part for further details) was 93.4 ± 2.0, 90.7 ± 2.6, and 88.7 ± 3.2 for MIA PaCa-2, HeLa, and NIH 3T3, respectively. Error bars represent the SD from three or more independent experiments

As depicted in Fig. 9, free Dox shows an expected dose-dependent cytotoxicity in all cell lines. Conversely, c2C-Dox shows selective dose-dependent cytotoxic effect only towards MIA-PaCa-2 and HeLa cells and a remarkable lower cytoxicity in control cells. In contrast, c36C-Dox did not show appreciable cytotoxicity in any cell line. Interestingly, the very low cytotoxicity exhibited by this scrambled sequence was comparable with the effect displayed by c2C-Dox towards control cells. This might suggest that this minor contribution is due to either partial Dox leakage from the complex during incubation, or nonspecific uptake. This result demonstrates that the observed cytotoxicity shown by c2C-Dox towards tumor cells is actually related to an active targeting process.

To further confirm that the observed cytotoxicity was actually an apoptotic effect related to the intracellular Dox release, we performed a fluorescence-based assay for apoptosis detection (Alexa Fluor 488-Annexin V/Propidium Iodide)[184,185]. This well-assessed assay allows discriminating among early apoptotic, late apoptotic, necrotic, and viable cells (green, green/red, red, and no fluorescence, respectively) on the basis of signals arising from annexin V and propidium iodide. In details, MIA Paca-2 cells were treated with either c2C-Dox or free c2C, and fluorescence emission was monitored by confocal microscopy. As shown in Fig. 10, treatment of cells with c2C-Dox evidenced the presence of both green fluorescence, mainly on the plasma membrane, and red fluorescence arising from nuclei, a pattern typical of the late apoptotic cells. Conversely, treatment with free c2C did not induce appreciable fluorescence, indicating non-apoptotic cellular condition.

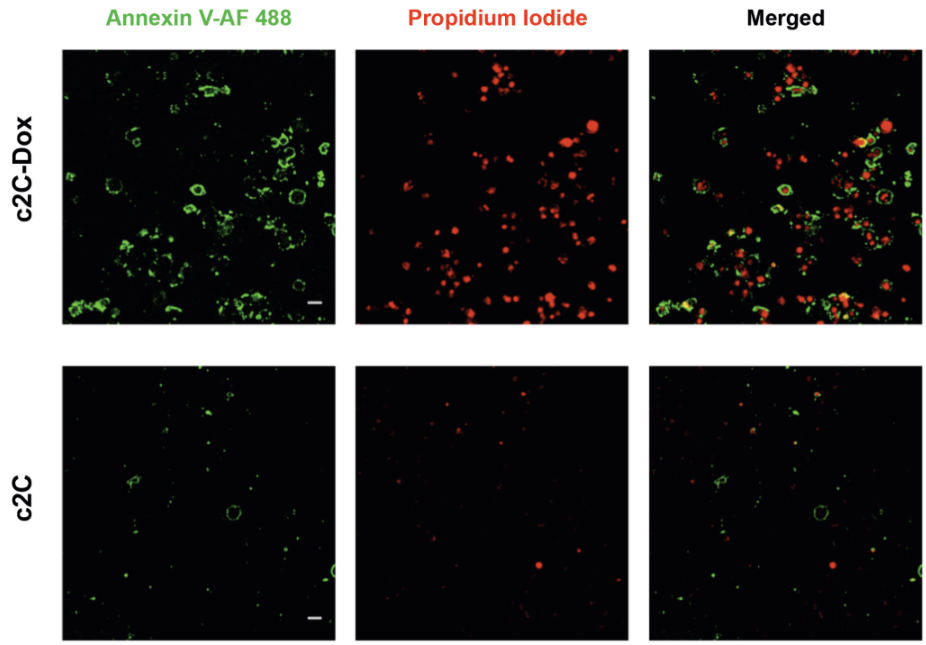

Fig. 10 Cell apoptosis assay. MIA PaCA-2 cells were incubated with Apt-Dox conjugate (1.5 µM Dox concentration) or aptamer alone (0.2 µM aptamer concentration) for 24 hours. Scale bars: 10 µm

It is worth noting that the cervical cancer cells displayed a higher Dox sensitivity when compared with the pancreatic tumor model (see Fig. 9). As a consequence of this effect, both free Dox and c2C-Dox showed a higher -and similar- cytotoxicity towards HeLa compared with MIA PaCa-2. This effect strongly suggests the presence of a different chemoresistance efficacy by these two cell lines against Dox. Despite its lower effect against pancreatic tumor cells, Dox is sensitively more effective than c2C-Dox in this cell line. This behavior might be ascribed to the presence of a subset of pancreatic cancer stem cells expressing lower TfR levels and hence recognized with minor efficacy by the aptamer-Dox conjugate[186,187]. Notably, some cancer stem cells are maintained in a quiescent state, which preserves their self-renewal capacity[188] while TfR is

expressed mainly in proliferative cells[187]. Conversely, the passive translocation process of free Dox does not discriminate among different subsets of cells, thus targeting the whole cell population.

Another hypothetical explanation could be related with different internalization mechanism of the two systems. Notably, free Dox diffuses freely through the plasma membrane and accumulates in the nuclear domain. In contrast Dox released from c2C-Dox can accumulate into cytoplasm and consequently into the nucleus only after a receptor-mediated endocytosis, release from DNA duplex and a subsequent diffusion across the vescicular membranes of the endolysosomal compartment. Moreover, since the internalization route of c2C-Dox is different than free Dox, the chemoresistance mechanism into the cells can play different role in response to the Dox chemotherapeutic effect, and this effect is cell line-dependent as observed by the different Dox sensitivity exhibited by HeLa and MIA PaCa-2 cells.

2.4 Design, synthesis and Dox-loading of a novel aptacoy chimera

Although c2C-Dox conjugate retains a potential interest as drug delivery platform, its therapeutic effect towards resistant pancreatic tumor cells was barely convincing to be taken in consideration for further clinical investigations. Indeed, as shown in Fig. 9 the cytotoxicity of the aptamer-Dox conjugate was less than 50% even at the highest Dox concentration (5.5 μM). Thereby, the anticancer effect of the released Dox should be enhanced, still retaining the targeting properties of c2C-Dox. To this end, an intriguing option lies on the inhibition of pro-survival pathways tightly involved in chemoresistance.

As described in the first section of this chapter, NF-κB is one of the most important molecular effector involved in both intrinsic and acquired chemoresistance. It was also extensively demonstrated that NF-κB activation suppresses the apoptotic potential of Dox, ultimately leading to increased chemoresistance. Moreover, recent studies demonstrated that inhibition of NF-κB sensitizes tumor cells to Dox-induced apoptosis in various cancer cells (breast

cancer, pancreatic cancer, renal and hepatocellular carcinoma)[168,189]. Therefore, we investigated a novel codelivery strategy to selectively release two synergistic drugs, i.e. Dox and an inhibitor of NF-κB in tumor cells. To date, several approaches were proposed to inhibit NF-κB activation[168,190,191]. One elegant strategy is to block NF-κB activity by interfering with its nuclear translocation. Indeed, during translocation NF-κB is potentially susceptible to hijacking by decoy molecules bearing the consensus binding sequence recognized by NF-κB[192]. Upon binding, nuclear translocation of NF-κB – and hence downstream activation of antiapoptotic genes- is inhibited (Fig. 11). Synthetic double-stranded DNA oligonucleotides with high affinity for NF-κB, known as NF-κB decoys, have been extensively used to block NF-κB-mediated induction of gene expression both in vitro and in vivo[193,194].

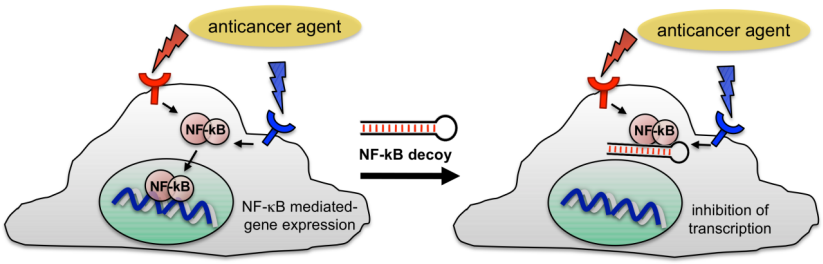

Fig. 11 Schematics of the NF-κB decoy mechanism. Anticancer drugs, such as doxourbicin induce nuclear translocation of NF-κB, which leads to the NF-κB-mediated activation of target genes. Upon binding between the transcription factor and NF-κB decoy, the nuclear translocation is inhibited as well as the NF-κB transcriptional activity.

As stated in the first chapter, several designs of aptamer-therapeutic ODN conjugates are reported in literature. Inspired from the most relevant studies, we designed a novel chimeric oligonucleotide, named aptacoy, composed by c2C portion directly conjugated to a NF-κB decoy by a disulfide linker. This latter is a critical part of our design: the linker is stable in the extracellular medium but is

easily cleaved in reducing intracellular environment, such as cytoplasm and lysosomes[195]. Furthermore, there are many evidences in which TfR-based vector have shown enhanced delivery efficacy of molecular payloads when a disulfide bond is included within the vector design[196].

We designed NF-κB decoy with a self-complementary sequence to obtain the suitable double-stranded DNA recognized by NF-κB simply via intramolecular folding[197]. As shown in Fig. 12, the secondary structure prediction of this ODN results very stable and does not affect the overall folding of c2C owing to the presence of thirteen intramolecular Watson-Crick base pairings. Additionally, we decided to use a whole phosphorothioate ODN to increase the nuclease resistant of this sequence. Several groups have successfully used this type of modification within the decoy backbone for inhibiting NF-κB[198,199]. Most importantly, the nature of the phosphorothioate bond increases the hydrophobic properties of NF-κB decoy compared with the traditional phosphodiester ODNs[200] and may allow overcoming many physiological barriers, such as plasma membrane and membrane vesicles of the endocytic pathway[201]. This feature might provide a significant aid to the endosomal escape of this molecular payload.

The oligo conjugation between NF-κB decoy and anti-tail was performed through two sequential steps (Fig. 12).

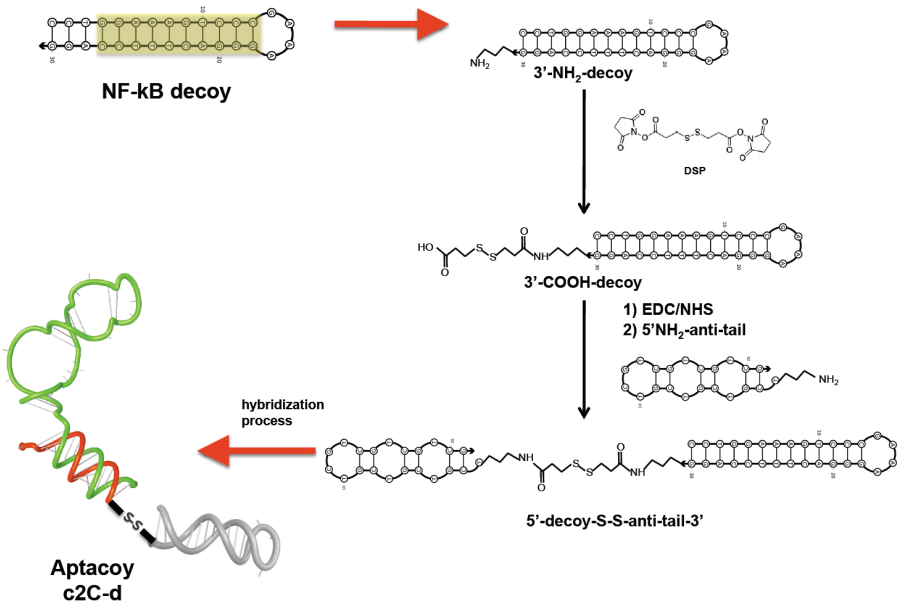

Fig. 12 Synthesis of NF-κB decoy-anti-tail conjugate. On the top is depicted the secondary structure prediction of NF-κB. The yellow box highlights the consensus region recognized and bound by NF-κB. The first reaction is the conjugation of the DSP linker to the amino residues at 5'-end of the NF-κB decoy. Next, a two-step process affords the chemical conjugate between carboxyl residue of the linker on derivatized decoy and the amino group at 5'-end of the anti-tail. Purified conjugate was hybridized with the extended sequence of RNA aptamer to generate the Aptacoy complex (bottom) represented on the basis of its helicity

First, the amino residue at 3'-end of NF-κB decoy was derivatized with dithio-bis(succinimidyl propionate) (DSP), an amine-reactive homobifunctional crosslinker with a cleavable disulfide bond in its spacer arm. Then, the conjugate was further reacted with 5'-amino anti-tail using standard EDC/NHS conjugation protocols. The desired product was purified by anion exchange HPLC (Fig. 13a). After this process, the resulting conjugated ODN was hybridized with the tail portion of c2, to obtain the aptacoy structure, hereafter c2C-d.

To verify the correct folding of c2C-d, we incubated c2C-d and free decoy with a suitable amount of Dox (Dox/c2C-d ratio 7.5:1) and we compared their quenching effect. Indeed, the presence of a double-stranded helix in the decoy domain of the construct might introduce additional sites for Dox intercalation and at same time could affect the folding of the entire structure. The physical conjugate between c2C-d and Dox, hereafter c2C-d-Dox (i.e. aptacoy-Dox) showed a quenching effect comparable with c2C-Dox (Fig. 13b). In contrast, this effect was quite smaller than that shown by hybridized complex (Fig. 13c) albeit we detected a noticeable Dox fluorescence quenching when free decoy was incubated with Dox. Overall, these results confirmed that maximum quenching effect was due to the formation of the aptacoy-Dox complex.

Despite the presence of additional binding sites, Dox/c2C-d molar ratio was kept constant at 7.5 in subsequent experiments to obtain a fair and unbiased comparison of the therapeutic efficiency of both complexes (c2C-Dox vs c2C-d-Dox). However, it is worth noting that greater Dox/c2C-d ratios could be easily achievable by exploiting the additional binding sites present on the double-stranded decoy.

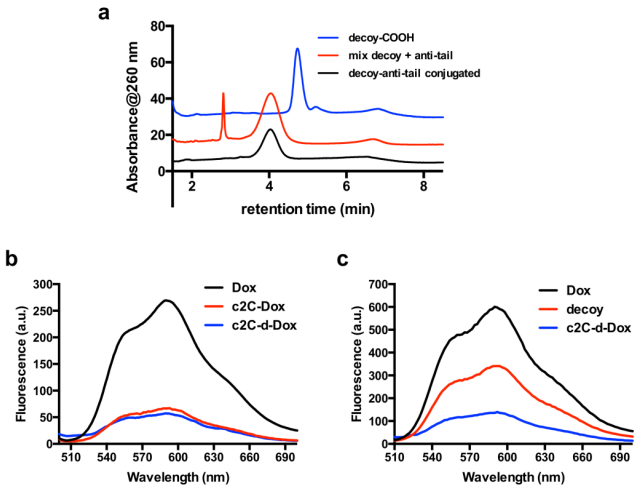

Fig. 13 (a) HPLC traces of conjugation crude reaction mixture and (b) Dox quenching after intercalation with c2C, c2C-d and (c) decoy alone.

2.5 Codelivery of Dox and NF-κB decoy via anti-TfR aptamer in living cells

Next, we investigated whether the NF-κB decoy could be effectively released in cytoplasm from the chimera, and whether it could bind to NF-κB, inhibiting its nuclear translocation. To this end, MIA PaCa-2 cells were treated with the aptacoy or with control assemblies, and the intracellular localization of NF-κB after each treatment was detected by a fluorescence immunostaining and compared with an assessed nuclear marker, DAPI, via a colocalization experiment.

NF-κB was found mainly in the cell cytoplasm of resting MIA PaCa-2 cells (treated only with c2C, Fig. 14a), as confirmed by the lack of colocalization between NF-κB and DAPI. However, stimulation with the most important NF-κB inducer, Tumor Necrosis Factor-α (TNF-α)[202] (20 ng/mL) led to estensive accumulation of NF-κB in cell nuclei, as shown by the complete colocalization between NF-κB and DAPI (Fig. 14b). Interestingly, when MIA PaCa-2 cells were pretreated with c2C-d and then stimulated with TNF-α, nuclear translocation of NF-κB was significantly reduced and NF-κB was found both in the cytoplasm and nucleus (Fig. 14c). The inhibition of TNF-α-induced NF-κB activation indicates that NF-κB decoy was actually released in the cytoplasm where it could bind NF-κB, ultimately hampering its nuclear translocation[202].

Additionally, cell treatment with free doxorubicin triggered a prominent nuclear translocation of NF-κB (Fig. 14d), in agreement with previous studies on different cell lines[169,170]. However, when MIA PaCA-2 cells were co-treated with free Dox and c2C-d, we observed a remarkable decrease of doxorubicin-induced NF-κB nuclear translocation (Fig. 14e), thus confirming the inhibitory activity exhibited by the decoy towards NF-κB.

It is worth mentioning that the actual mechanism of endosomal escape remains unknown for most therapeutic oligonucleotides (siRNAs, miRNAs, antagomirs, antisense oligos and hammerhead ribozymes)[203–205]. In the case of our NF-κB decoy, we could hypothesize that its enhanced hydrophobic character owing to the phosphorothioate linkages can increase the likelihood of NF-κB decoy to freely

diffuse through the membrane of the endocytic vesicles and enter into the cytoplasm.

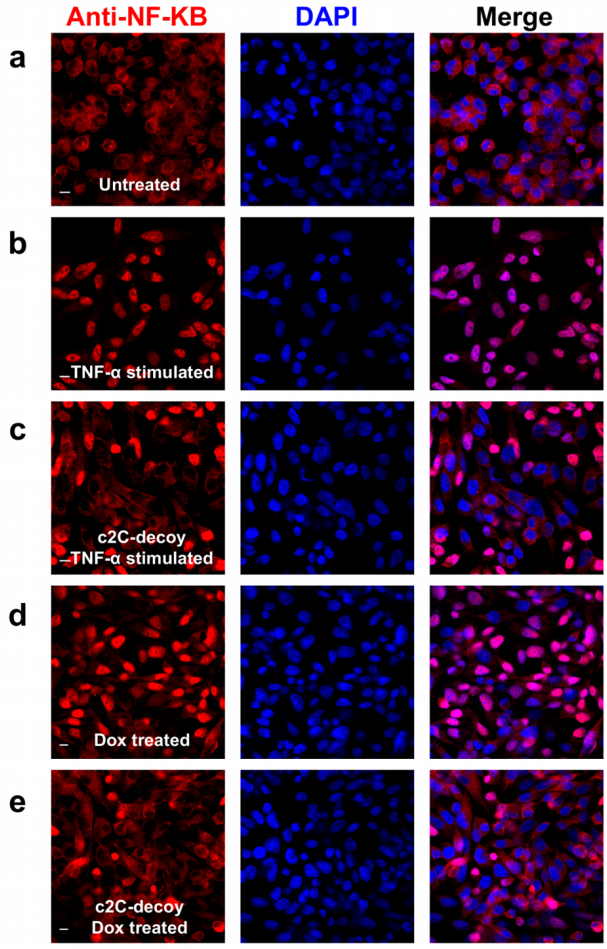

Fig. 14 c2C-d conjugate inhibits NF-κB activity and sensitizes MIA PaCa-2 cells to Dox-induced apoptosis. Immunofluorescent staining of NF-κB assesses its cellular localization. MIA PaCA-2 cells were incubated with c2C-d or c2C alone for 24 hours and stimulated either with TNF-α (20 ng/ml) for 1 hour or with Dox for 24 hours before immunofluorescent staining of NF-κB (red). The nuclei were stained blue with DAPI. Scale bars: 10 μm

Once demonstrated that the NF-κB decoy is effectively released from the aptacoy chimera, we performed a codelivery application of Dox and NF-κB decoy via our platform, i.e. c2C-d-Dox. Our aim was to evaluate whether c2C-d-Dox could improve sensitization of tumor cells to the apoptotic effect of released Dox. To this end, we performed cell-viability assays on pancreatic tumor and control cells, comparing the cytotoxicity of c2-Dox and c2C-d-Dox. To assess the nonspecific cytotoxicity of a phoshorothioate ODN, we also examined the effect induced by a scrambled decoy sequence, which does not bear the consensus sequence recognized by NF-κB. The scrambled decoy (sd) was chemically conjugated to c2C module, via the two-step procedure previously described, to generate a c2C-sd chimera, and the final c2C-sd-Dox was obtained after Dox intercalation within DNA duplex.

Pancreatic tumor cells were treated with either c2C-d-Dox or c2C-sd-Dox and dose dependence was observed for each treatment (Fig. 15a). Notably, cytotoxicity of c2C-d-Dox significantly exceeded in a dose-dependent manner that found for c2C-Dox and was quite comparable with free Dox. Most importantly, c2C-sd-Dox did not show an increased cytotoxicity, yielding analogous effects to the administration of c2C-Dox. This behavior evidences a negligible impact of the phosphorothioate on the cell viability, and highlights the essential role of NF-κB decoy in the enhanced cytotoxicity of aptacoy-Dox towards MIA PaCa-2 cells.

Besides showing increased cytotoxicity, the aptacoy-Dox platform should also display targeting properties to specifically deliver Dox in tumor cells. Therefore, we treated tumor and control cells with the c2C-d-Dox and we evaluated its cytotoxic effect after continuous treatment (24 h). Cell viability assay highlights that our platform still retains unaltered its capability to target pancreatic tumor cells, showing negligible cytotoxicity towards NIH-3T3 cells (Fig 15b). Tumor and control cells were also treated either with free Dox or c2C-Dox using the same conditions. Interestingly, c2C-d-Dox shows higher cytotoxic effect than c2C-Dox even at a single killing dose and after continuous treatment, demonstrating to be able to increase the sensitivity of MIA PaCa-2 cells towards the chemotherapeutic effect of Dox.

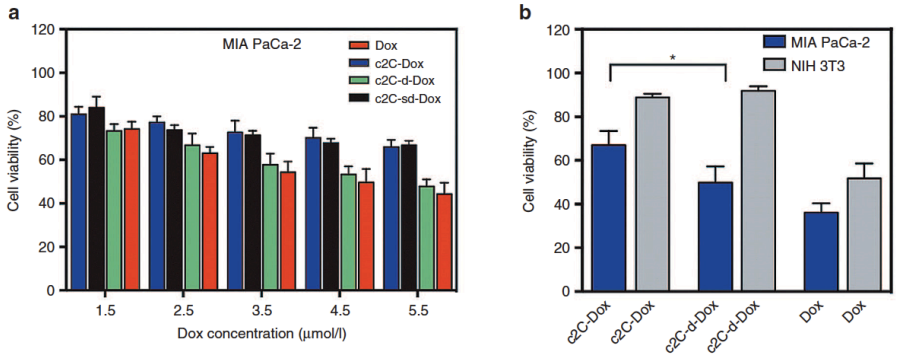

Fig. 15 (a) Cell viability assay of MIA PaCa-2 cells after treatment with free Dox (red), c2C-Dox (blue), c2C-d-Dox (green) and c2C-sd-Dox (black). Cells were incubated with the drugs for 2 hours and cell viability was assessed after 24 hours. (b) Cell viability assay of MIA PaCa-2 (blue) and NIH-3T3 (grey) cells after treatment with free Dox, c2C-Dox, c2C-d-Dox or c2C for 24 hours. Error bars represent the SD from three or more independent experiments ($P < 0.05$).

To better understand the nature of this enhanced cytotoxicity, we evaluated by Western blot analysis the expression of two parameters in MIA PaCA-2 cells: (i) the extent of poly-(ADP-ribose) polymerase (PARP) cleavage, an assessed apoptotic marker[206] and (ii) the expression of X-linked inhibitor of apoptosis protein (XIAP) whose expression is tightly regulated by NF-κB[190] (Fig. 16a). Particularly, PARP cleavage was monitored to demonstrate that the enhanced cytotoxic effect was actually related to an increased apoptotic process. On the other hand, through the expression of XIAP we could measure the extent of NF-κB inhibition to demonstrate that the improved sensitivity of pancreatic tumor cells towards Dox was tightly associated to the NF-κB decoy inhibition mechanism.

As shown in Fig. 16b remarkable PARP cleavage was observed upon treatment with either free Dox or c2C-d-Dox. Conversely, resting cells and c2C-treated cells did not present significant accumulation of cleaved PARP. Most importantly, by measuring the band intensity of the cleaved and full-length bands, we found that PARP cleavage (calculated using the following formula: cleaved band / (cleaved +

full-length bands)*100) was ~40% and ~30% in cells treated with c2C-d-Dox and unconjugated Dox, respectively. This outcome highlights that the apoptotic processes are enhanced after treatment with c2C-d-Dox compared to unconjugated Dox.

It is worth noting that, although aptacoy-Dox shows higher apoptotic effect than free anthracycline, their cytotoxicity (measured by WST-8 assay) is quite similar. Taken together, these results might confirm our hypothesis about the presence of a subset of pancreatic cancer stem cells, recognized with minor efficacy by the aptacoy, which ultimately leads to an underestimated cytotoxic potential of c2C-d-Dox.

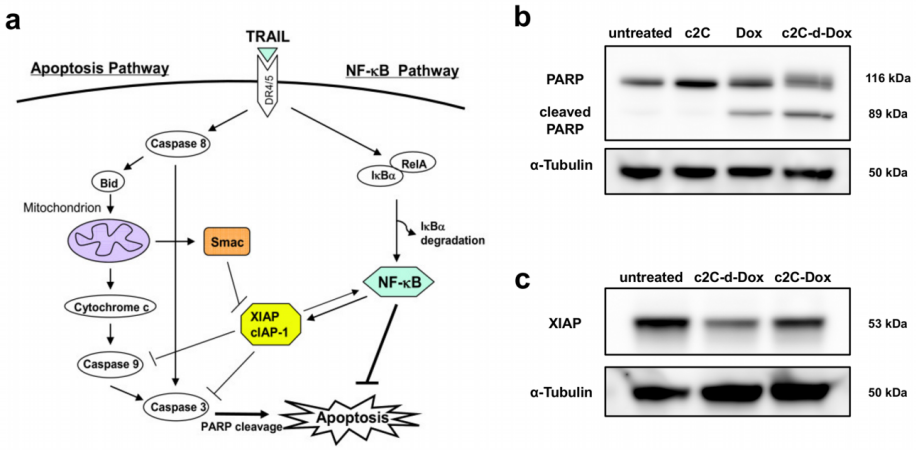

Fig. 16 (a) Schematics of NF-κB pathway involved in apoptosis process. TRAIL (TNF-related apoptosis-inducing ligand) triggers apoptosis via both the death-receptor (DR4/DR5) and mitochondrial pathways, by activating initiator caspase-8 and -9, and effector caspase-3. Furthermore, both Bid and PARP are cleaved by caspases, which are typical apoptosis markers. NF- κB activates gene expression of XIAP and cIAP-1, which are involved in the inhibition of the caspase cascade, ultimately leading to a pro-survival effect. Adapted from Dai et al.[207] Copyright © Dai et al. 2009; licensee BioMed Central Ltd. **On the left is shown the western blot analysis performed on MIA PaCa-2 cells using antibodies specific for (b) PARP and (c) XIAP. Note that, α-Tubulin was used as loading control in both evaluations.**

It is commonly accepted that chemoresistant pancreatic cancer cells display both enhanced NF-κB activity and consequent upregulation of XIAP[190,208]. Therefore, we investigated the extent of decoy-mediated NF-κB inhibition monitoring the expression of this downstream product. XIAP is a protein belonging to the family of inhibitor of apoptosis proteins (IAPs) and is directly involved in caspases inhibition to protect cell against death (Fig. 16a). Interestingly, western blot analysis displayed a substantial decrease of XIAP expression in cells treated with c2C-d-Dox compared to resting and c2C-Dox treated cells (Fig. 16c). In details, from a comparison of the band intensity, XIAP expression was ~75% and ~50% compared to the one related to resting cells upon treatment with c2C-Dox and c2C-d-Dox, respectively. This trend perfectly matches with the reported repression of XIAP gene expression induced by doxorubicin[209], which is significantly improved by the effective inhibition of NF-κB activity after aptacoy-Dox treatment. This result further confirms that the increased cytotoxicity of aptacoy-Dox complex was due to the effective inhibition of NF-κB, which ultimately leads to sensitization of pancreatic tumor cells towards Dox-mediated apoptosis.

2.6 Concluding remarks

In this chapter, I presented a molecular-engineering strategy to design a drug-delivery platform composed uniquely by oligonucleotides. This assembly exploits receptor-mediated internalization to perform selective delivery of doxorubicin in tumor pancreatic cells, and sensitizes them to Dox-induced apoptosis. We combined the targeting ability of an RNA aptamer that recognizes tumor cells expressing human TfR, and the inhibitory effect of a DNA decoy towards NF-κB. The complex was generated by DNA self-assembly between two complementary single-stranded DNA sequences: one located within targeting RNA aptamer and one covalently linked to NF-κB decoy with a disulfide bridge. Both payloads were released under conditions found in the receptor-mediated endocytic pathway, such as low pH and reductive environment.

This platform is able to perform a targeted codelivery of Dox and decoy towards resistant pancreatic tumor cells; in this strategy, NF-κB decoy inhibitsconstitutive NF-κB activity in target cells, ultimately leading to enhancement of doxorubicin-mediated apoptotic effect.

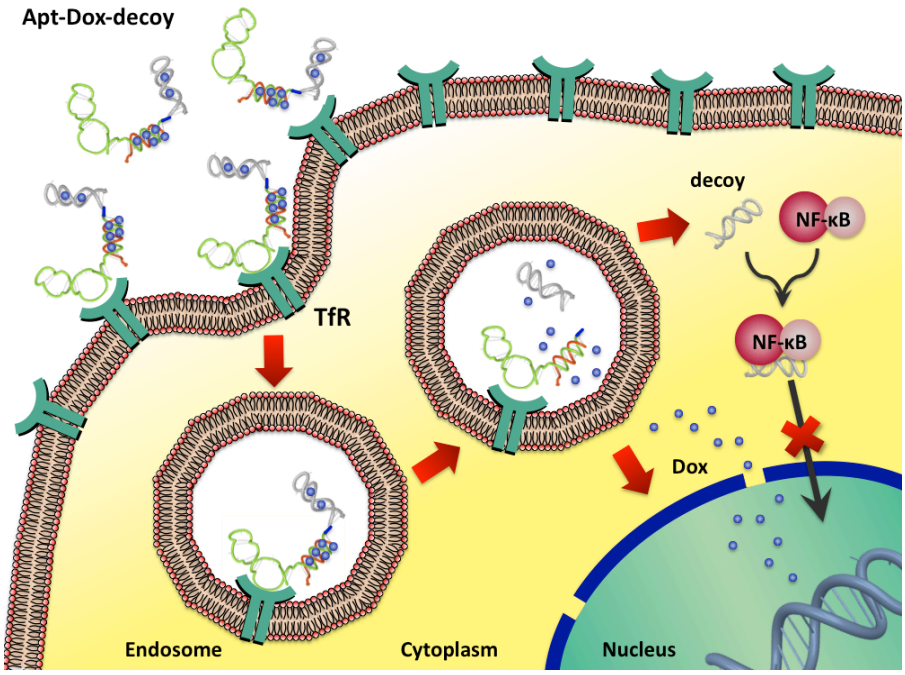

Fig. 17 Schematic representation of codelivery of Dox and NF-κB decoy via an RNA aptamer recognizing hTfR

2.7 MATERIALS AND METHODS

2.7.1 Materials

All chemicals were purchased from Sigma Aldrich unless otherwise specified, and were used as received. RNA and DNA oligonucleotides were purchased from Integrated DNA Technologies (IDT, Coralville, IA, USA). They were stored in lyophilized form and suspended before use in the appropriate volume of nuclease-free water to reach a concentration of 100 μM.

2.7.2 Oligonucleotide sequences

The sequence of the anti-TfR RNA aptamer (c2.min) with a short DNA tail $(CGA)_7$ at the 3'end was the following (tail sequence is underlined):

5'-GGGGGAUCAAUCCAAGGGACCCGGAAACGCUCCCUUACACCCCCGACGACGACGACGACGACGA-3'

The sequence of the scrambled aptamer (c36) with a short DNA tail $(CGA)_7$ at the 3'end was the following (extended sequence of aptamer is underlined):

5'-GGCGUAGUGAUUAUGAAUCGUGUGCUAAUACACGCCCGACGACGACGACGACGACGA-3'

All pyrimidines of the RNA aptamer motif were substituted by 2'-fluoro-pyrimidines. All synthesized oligonucleotides contained a 5'amino group attached by a C-6 alkyl chain.

The anti-tail sequence was the following:

5'-TCGTCGTCGTCGTCGTCGTCG-3'

The sequence of the phosphorothioate NF-κB decoy was the following (consensus sequences are underlined):

5'-CCTGGAAAGTCCCGAAAGGGACTTTCCAGG-3'

The sequence of scrambled phosphorothioate NF-κB decoy was the following (complementary sequences are underlined)

5'-GCCGTACCTGACTTAGCCGAAAGGCTAAGTCAGGTACGGC-3'

All synthesized phosphorothioate oligonucleotides contained a 3'amino group attached by a C-6 alkyl chain.

2.7.3 Absorption and fluorescence measurements

Absorption data were recorded at 25°C in a JASCO V550 spectrophotometer (JASCO Europe, Cremello, Italy) using 1 nm band-pass, 0.5 nm step-size and 0.25s integration time. Appropriate quartz cuvettes (Hellma, Milan, Italy) displaying an absorption/excitation optical path of 1 cm were used in all experiments. Fluorescence intensity was carried out with a Cary Eclipse fluorometer (Varian, Palo Alto, CA), using 1 nm step-size and 1.0 s integration time. Slits for both excitation and emission were set at 10 nm. A 100 µl quartz cuvette (Hellma, Milan, Italy) with an optical path of 1 cm was used in all experiments.

2.7.4 Cell culture

Mouse embryonic fibroblast cells (NIH-3T3) and human pancreatic carcinoma cells (MIA PaCA-2) were purchased from the American Type Culture Collection (ATCC). NIH-3T3 cells were grown in Dulbecco's modified Eagle Medium (DMEM) purchased from Invitrogen (Carlsbad,CA) with 10% calf serum (CS) and MIA PaCa-2 were grown in DMEM with 10% fetal bovine serum (FBS). Culture media were supplemented with 4mM L-Glutamine, 100 U/ml penicillin and 100 mg/ml streptomycin (Invitrogen). Cells were maintained at 37°C in a humidified 5% CO_2 atmosphere. For live cell microscopy cells were plated onto glass-bottom petri dishes (WillCo®-dish GWSt-3522) and imaged at 37°C, 5% CO_2.

2.7.5 HPLC analyses

All HPLC analyses were performed on a Dionex Ultimate 3000 HPLC, equipped with automated analytical Autosampler with Fraction Collector WPS-3000FC, UltiMate 3000 Diode Array and Multiple-Wavelength Detectors, UltiMate 3000 Thermostated Column Compartment Series and controlled by Chromeleon Management Software.

2.7.6 Confocal imaging of cells

Cells were imaged using a Leica TCS SP5 SMD inverted confocal microscope (Leica Microsystems AG) interfaced with a diode laser (Picoquant) for excitation at 405 nm, with Ar lasers for excitation at 488 and 561 nm and with a HeNe laser for excitation at 633 nm. Glass bottom Petri dishes containing cells were mounted in a thermostated chamber at 37°C (Leica Microsystems) and viewed with a 63x 1.2 NA water immersion objective or 40x 1.5 NA oil immersion objective (Leica Microsystems). The pinhole aperture was set to 1.0 Airy. All data collected were analyzed by ImageJ software version 1.44o.

2.7.7 Secondary structure and hybridization predictions

Oligonucleotide secondary structure predictions were obtained using the Internet tool NUPACK nucleic acid package (http://www.nupack.org/)[175] with the default settings. Hybridization prediction between the tail sequence on the RNA aptamer structure and its short DNA complementary sequence (anti-tail) were obtained with NUPACK analysis algorithms software, representing each oligonucleotide as an RNA sequence. The NUPACK generated secondary structures were used to obtain three-dimensional structures exploiting the utilities of the NUPACK software.

2.7.8 Oligonucleotide labeling

The amino residues at 5'-end of the extended RNA aptamer (c2.min-tail) and anti-tail were conjugated respectively to the ATTO 633 NHS fluorophore (ATTO-TEC GmbH, Germany) and Alexa Fluor 488 NHS fluorophore (Invitrogen, Carlsbad, CA) by means of standard NHS coupling procedures between the primary amine of the oligonucleotides and NHS-derivative of the fluorophores. The labeling reaction was performed as follows: 10 nmoles of aptamer sample were dissolved in sodium bicarbonate buffer 150 mM at pH 8.5 and mixed with 20-fold molar excess (100 nmol, 75 μl in DMSO) of dye NHS ester derivative, in a final volume of 200 μl. The reaction mixture was stirred overnight at 4°C. Analytical evaluation of labeling reaction and purity of the labeled aptamer

samples was performed at 25°C using a RP-HPLC on a Clarity® 5 µm Oligo-RP, LC Column 250 x 4.6 mm (Phenomenex) using Triethylammonium bicarbonate (TEAB) 50 mM pH 9 (Eluent A) and acetonitrile (Eluent B) at 1.0 ml/min. Purified labeled aptamer was freeze-dried, resuspended in DNase-free water and quantified by UV-VIS. Dye-to-oligo ratio was evaluated from absorbance measured at 260 and 488 (or 633) nm and was 1 within experimental error.

2.7.9 Oligonucleotide annealing protocol

To assemble the extended sequence of the RNA aptamer with its complementary DNA sequence, these two oligonucleotides were mixed with equal molar concentration in a buffer solution, (PBS 1X containing 1 mM $MgCl_2$). The mixture was placed in a thermoblock and heated to 90°C for 1 minute to denature the nucleic acid structures. Then the entire apparatus was placed on the workbench for 30 minutes and denatured oligo sample was slowly cooled to allow correct hybridization between the two complementary strands. The hybridized product was always freshly prepared before each evaluation.

2.7.10 Doxorubicin intercalation in double helix region of the hybridized aptamer

A physical conjugate between hybridized aptamer carrier sample (c2C, c36C, c2C-d and c2C-sd) and doxorubicin was made by addition of 1:7.5 molar ratio of aptamer to Dox in binding buffer (PBS 1X containing 1 mM $MgCl_2$). Dox fluorescence was measured (excitation: 480 nm, emission: 500-700 nm). Slits for both excitation and emission were set at 10 nm. The resulting complex (c2C-Dox, c36C-Dox, c2C-d-Dox and c2C-sd-Dox) was freshly prepared before each experiment.

2.7.11 Doxorubicin release from aptamer in serum-containing media

After physical conjugate preparation between c2C and Dox, the c2C-Dox complex was added to either 1% or 5% serum-containing medium, and incubated at 37°C for 0, 30, 60, 120 minutes, and 24h. Dox fluorescence was measured (excitation: 480 nm, emission: 540-700 nm. Slits for excitation and emission were

set at 20 and 10 nm, respectively). The amount of Dox released was determined by comparison with that of a Dox sample incubated in the same conditions, assuming the fluorescence intensity of the starting complex and of free Dox sample as 0 and 100%, respectively.

2.7.12 Assessment of cellular uptake by confocal microscopy

Internalization assay in MIA PaCa-2 cells was performed using a dual-labeled conjugate, in which the extended c2.min was labeled with ATTO 633 and the anti-tail was labeled with Alexa Fluor 488. MIA PaCa-2 cells were seeded 24 h before the experiment in WillCo dishes to reach 80-90% confluence. Standard conditions for incubation consisted in 15 min incubation at 37°C, 5% CO_2 in DMEM containing 1% BSA, 0.2 mg/ml calf thymus DNA and 0.2 μM of dual-labeled probe in a total volume of 500 μl. After incubation, cells were washed three times with PBS, fresh serum-containing medium was added and the sample was imaged by confocal microscopy about 20 minutes after the administration of the aptamer sample.

Cellular uptake of free Dox and c2C-Dox conjugate was assessed through confocal imaging evaluation both on MIA PaCa-2 cells and NIH-3T3 cells. Briefly, the cells were seeded 24 h before experiment in WillCo dishes to reach 80-90% confluence. Then, the cells were incubated with a 1% serum-containing medium with either free Dox, or c2C-Dox (1.5 μM Dox concentration) for 2 hours at 37°C. After incubation, cells were washed three times with PBS then fresh 1% serum-containing medium was added and the sample was imaged by confocal microscopy either immediately (i.e. after 2 hours of incubation) or after additional 22 hours of incubation with drug-free culture medium (i.e. after 24 hours). Dox fluorescence in living cells was detected by confocal microscopy using 488 nm as excitation wavelength. All experiments were performed in triplicate.

2.7.13 WST-8 Cell viability assay

Cytotoxicity of free Dox and Apt-Dox complexes was evaluated by using a tetrazolium salt, 2-(2-methoxy-4-nitrophenyl)-3-(4-nitrophenyl)-5-(2,4-disulfophenyl)-2*H*tetrazolium, monosodium salt (WST-8) assay. MIA PaCA-2

cells, HeLa cells and NIH-3T3 cells ($1x10^4$ cells per well) were seeded in 96-well plates. After culture for 24 hours, the cells were incubated with a 1% serum-containing medium with either free Dox, or oligo-Dox conjugates for 2 hours. After 2h incubation, cells were washed twice with PBS then fresh 1% serum-containing medium was added. After 24 hours from the treatment the medium was removed and cells were incubated with WST-8 reagent (10 μL) and 1% serum-containing medium (90 μL) for 3 hours. Dose dependence for MIA PaCa-2, HeLa and NIH 3T3 was determined using increasing drug concentrations (1.5, 2.5, 3.5, 4.5 and 5.5 μM as Dox concentration and 0.20, 0.33, 0.46, 0.6, 0.73 μM as oligo concentration) according with a 7.5:1 as Dox/c2C molar ratio. The unconjugated aptamer cytotoxicity (c2C) was evaluated treating the cells with the higher aptamer concentration (0.73 μM) employed in dose-response experiments. Absorbance (450 nm) was measured using a microplate reader (Infinite F50, Tecan). The percentage of cell viability was determined by comparing drug-treated cells with the untreated cells (100% viability). Data represent the average of three or more independent experiments. Error bars represent the SD from three or more independent experiments.

2.7.14 Statistical analysis

Data obtained from cell viability assay were statistically analyzed using one-way ANOVA followed by Tukey's HSD test for multiple comparison analysis. Data are expressed as mean with 95% confidence intervals for all groups. P values < 0.05 were considered statistically significant. Statistical analyzes and graphs were assembled using GraphPad PRISM (version 6, GraphPad software for Science, San Diego, CA).

2.7.15 Apoptosis assay

Apoptosis evaluation was performed as described below, using Alexa Fluor 488 annexin V/Dead Cell Apoptosis Kit (Life Technologies, Carlsbad, CA). Cells were seeded ($2x10^5$ cells per well) in Willco dishes. After culture for 24 hours, the cells were incubated with 1% serum-containing medium supplemented with either

c2C-Dox conjugate (1.5 μM Dox concentration) or free c2C (0.2 μM aptamer concentration) as negative control for 24 hours. The subsequent procedures were performed in accordance with the manufacturer's protocol. Confocal microscopy was used to monitor qualitatively the cellular staining using a dual filter set for Alexa Fluor 488 and Propidium Iodide (PI) and a 40x 1.5 NA oil immersion objective. Qualitative apoptosis evaluation was determined by comparing drug-treated cells with the untreated cells. The experiment was performed in duplicate with the acquisition of an elevated number of random regions of interest (ROI) for each experiment.

2.7.16 pH- and nuclease-dependent drug controlled release

Dox release in cuvette was studied as follows: the c2C-Dox conjugate (1.5 μM Dox concentration) was incubated into binding buffer solution (PBS containing 1 mM $MgCl_2$) with different pH values: 7.4, 6.5, 5.8, 5.5 or 5.0. pH values were adjusted by the addiction of different aliquots of HCl 1 M to each sample. The samples were placed in a quartz cuvette and Dox fluorescence was monitored in real time spectrophotometrically. The acquisition for each sample was completed when fluorescence intensity became stable. In order to mimic lysosomal environment, 2 μL of DNase II (2000 units/mL; New England Biolabs) were added to the c2C-Dox sample at pH 5.0, and the sample was incubated at room temperature. During this incubation, Dox fluorescence was recorded at regular time intervals (10-15 measurements per hour). Fluorescence of free Dox samples was measured for each pH value, and measured fluorescence changes were used to normalize signals detected for the c2C-Dox samples. Percentage of Dox released was calculated by comparing fluorescent signals of free Dox at pH 7.4 (100%) with the signals of the c2C-Dox samples. Data represent the average of two or more independent experiments. Error bars represent the SD from two or more independent experiments.

2.7.17 Synthesis of the NF-κB decoy-anti-tail conjugate

The amino residues at 3'-end of the NF-κB decoy were conjugated to the dithio-bis(succinimidyl propionate) (DSP) using the following protocol: 10 nmoles of

decoy were dissolved in sodium bicarbonate buffer 0.15 M at pH 8.5 and mixed with 40-fold molar excess (400 nmol, in 20 mL of DMSO) of DSP, in a final volume of 200 μL. The reaction mixture was stirred overnight at 4°C. Analytical evaluation of the chemical conjugation reaction was performed at 25°C using RP-HPLC analysis. The derivatized decoy was purified from unreacted DSP by dialysis using dialysis membrane (MWCO 1000) (Spectrum Laboratories), concentrated using centrifugal filter units (3 K MWCO) and quantified by UV-VIS analysis. Next, a two-step reaction was performed to conjugate the carboxyl residue of the linker on derivatized decoy with the amino group at 5'-end of the anti-tail. Carboxyl group was activated with EDC (1000-fold molar excess) and Sulfo-NHS (10-fold molar excess) in PBS buffer for 20 minutes. Then, 5'-amino-anti-tail (3-fold molar excess) was added, and the reaction mixture was stirred 6 hours at room temperature in PBS buffer containing triethylamine (TEA) 1mM at pH 7.8. Purification of the decoy-anti-tail conjugate was performed with an IE-HPLC on a DNA Pac PA200 4x250 mm (Dionex) at 1.0 ml/min, using Tris HCl 20 mM pH 9.5, ACN 10% (Eluent A), and $NaClO_4$ 400 mM, Tris HCl 20 mM pH 9.5, ACN 10% (Eluent B) as mobile phase at 25°C. Absorbance was measured between 200 and 650 nm. The desired product was separated by means of IE-HPLC from the excess of the anti-tail and collected. The collected fraction was then dialyzed using dialysis membrane (MWCO 1000), concentrated using centrifugal filter units (3 K MWCO) and quantified by UV-VIS analysis. Finally, an aliquot was analyzed in IE-HPLC to check the purity of desired product.

2.7.18 Detection of NF-κB by immunofluorescence staining of p65

Immunofluorescence staining on MIA PaCA-2 cells using an antibody against p65 subunit of NF-κB was performed as follows: rabbit polyclonal anti-NF-κB p65 (phospho S536, Abcam, Cambridge, UK) was used as primary antibody and the Alexa Fluor 647-donkey anti-rabbit IgG (H+L) antibody (Life Technologies, Carlsbad, CA) as secondary antibody.

Cells were seeded ($2x10^5$ cells per well) in Willco dishes. After culture for 24 hours, cells were incubated with 1% serum-containing medium supplemented with c2C-d conjugate or with c2C alone (0.2 μM oligonucleotide concentration) as

negative control for 24 hours. After this incubation, cells were treated with TNF-α (20 ng/ml) for 1 hour. In order to assess doxorubicin effect on NF-κB nuclear translocation in presence and in absence of the decoy, the cells were coincubated with Dox (1.5 μM) either c2C-d or c2C alone as negative control for 24 hours.

Then, the cells were first fixed with 4% paraformaldehyde and 4% sucrose in PBS (15 min, room temperature) and subsequently permeabilized with 0.25% triton X-100 (6-8 minutes, room temperature). After fixation and permeabilization treatment, the cells were incubated with a PBS solution containing 1% bovine serum albumin (BSA) as blocking agent (30 minutes, room temperature) before incubation with the primary antibody diluted 1:100 in 0.5% BSA/PBS (1 hour, room temperature). Next, the cells were washed three times with PBS and incubated with the secondary antibody diluted 1:150 in 0.5% BSA/PBS (45 minutes, dark, room temperature). Finally, the cells were mounted using Vectashield Mounting Medium with DAPI (Vector Labs). Confocal microscopy was used to evaluate the cellular localization of NF-κB. The experiment was performed in duplicate with the acquisition of an elevated number of randomly regions of interest (ROI) for each experiment.

2.7.19 Western Blot analysis

MIA PaCa-2 cells were seeded ($7x10^5$ cells per well) in a six-well plate. After 24 hours, cells were incubated with 1% serum-containing medium supplemented with either free Dox or c2C-d-Dox or with c2C alone (1.5 μM and 0.2 μM as Dox and oligonucleotide concentration, respectively) for PARP detection for 2 hours. Alternatively cells were treated with either c2C-d-Dox or c2C-Dox at the same conditions described above for XIAP detection. After 2h incubation, cells were washed twice with PBS then fresh 1% serum-containing medium was added. After 24 hours from the treatment the medium was removed and cells were washed in ice-cold PBS and lysed in RIPA buffer (Sigma) supplemented with proteases and phosphatases inhibitors (Roche). After clarification, each post-nuclear supernatant was quantified for protein content by Bradford assay (Pierce), and 30 μg of each protein extract were resolved on 4-12% Criterion™ XT Bis-Tris gradient gel (Bio Rad). Proteins were electrotransferred to polyvinylidene difluoride membranes

(Bio Rad). These were washed and blocked in TBST + 5% w/v either non-fat dry milk (recommended for PARP) or BSA (recommended for XIAP). The membranes were then incubated with either rabbit monoclonal antibody to PARP (1:1000 diluted, 9542, Cell Signaling Technology) or rabbit monoclonal antibody to XIAP (1:1000 diluted, 9770, Cell Signaling Technology) in blocking solution for 2 hours at room temperature. Immunodetection was performed using anti-rabbit horseradish peroxidase-linked secondary antibody (1:2000 diluted, Cell Signaling Technology). Filters were developed using Clarity^{TM} Western ECL substrate (Biorad) and chemoluminescence signals detected by Image Quant LAS4000 (GE healthcare). The same membranes were also stripped and blotted against a rabbit monoclonal antibody to α-Tubulin (1:2000, clone B-512, Sigma) as loading control. Obtained images were subjected to linear contrast enhancement after image analysis.

Chapter 3

An enhanced aptamer sequence as tool for targeted drug delivery: rational engineering of a DNA aptamer against transferrin receptor

This chapter was peer-reviewed and published previously with co-authors D Porciani, G Signore, L Marchetti, P Mereghetti, R Nifosì & F Beltram: "Two interconvertible folds modulate the activity of a DNA aptamer against transferrin receptor," Mol Ther Nucleic Acids. 2014 Jan 28;3:e144. doi:10.1038/mtna.2013.71. D Porciani, G Signore and F Beltram contributed to design the study. D Porciani and G Signore analyzed both HPLC and microscopy data. D Porciani and R Nifosì analyzed the anisotropy measurements. D Porciani, R Nifosì,and L Marchetti engineered novel aptamer sequences. P Mereghetti performed molecular dynamic simulations. Unless otherwise specified, experiments and data shown in each figure were performed and analyzed by D Porciani.

Aptamers against transferrin receptor have great potential as targeting tools in drug delivery applications. As described in the previous chapter an RNA aptamer (c2.min) against human transferrin receptor was able to selectively codeliver two synergistic drugs into human pancreatic tumor cells, ultimately showing enhanced and selective cytotoxic effect. It is worth noting that this RNA motif competes

with the natural ligand, transferrin, for receptor binding and cell uptake, actually performing slightly better than Tf in competition experiments[137]. However, the high concentration of circulating transferrin (ranging from 1 to 2.4 mg/ml)[57] might sensitively reduce the binding of c2.min to TfR when administered to animal models, ultimately limiting the aptamer potential as targeting ligand for *in vivo* applications.

Therefore, aptamers that bind transferrin receptor in different sites compared to Tf might represent a valid alternative, thus avoiding the competition with the natural ligand.

In addition, c2.min is not able to recognize and bind the murine transferrin receptor. This lack of cross-reactivity may strongly restrict the anti-TfR aptamer applications especially when mouse tumor models are used for *in vivo* studies. Indeed, although human xenograft growing in immunodeficient mice is a well-established and useful model for studying human tumor biology, mouse allograft tumor systems, also known as syngeneic models, closely mimic the physiology of a tumor microenvironment and represent a more significant model to evaluate the off-target effect of targeting ligands[210]. Furthermore, when the aptamer activity is investigated using human xenograft tumor models, *in vivo* results may be further complicated by the fact that mouse transferrin binds the human transferrin receptor with weaker affinity[137]. Thus, a real competition between c2.min and the natural ligand will not be properly replicated in this in vivo model.

On the basis of these observations, we turned our attention to aptamers that bind TfR in alternative binding sites. Recently, Chen et al. selected cell-penetrating DNA (GS24) and RNA (FB4) aptamers that bind selectively the extracellular domain of mouse TfR (mTfR), apparently with no competition with transferrin, and explored the suitability of GS24 aptamer as vector to deliver a lysosomal enzyme for enzyme-replacement therapy[211].

Although these cell-penetrating aptamers are selective for mTfR rather than hTfR, they expand our set of TfR ligands thanks to absence of competition with transferrin. Indeed, one of the main goals of this thesis is to design and *in vitro* validate targeting and delivery properties of novel drug delivery platforms, exploiting aptamers as targeting ligands. To this end, a modular plug and play

engineering in which different combinations of targeting aptamers and molecular payloads are used, might offer a valid approach to assess the efficacy of these platforms.

Thereby, we decided to investigate the targeting property of these anti-mTfR aptamers, focusing on the more stable GS24 DNA aptamer. Indeed, although GS24 and FB4 share the same binding property towards mTfR, GS24 was preferentially used as nanocarrier owing to its greater nuclease resistance than FB4[211].

Chen and coworkers selected this anti-mTfR DNA aptamer using a combination of partition methods. In details, the oligonucleotide DNA library was incubated with the purified recombinant extracellular domain (ECD) of mTfR at room temperature using Nickel-agarose affinity column as partition method. Because no significant enrichment was observed after five rounds of selection, the authors decided to switch to a gel-shift assay for the subsequent round. Target-bound sequences were collected, cloned and sequenced. Then, each clone was assessed for its ability to bind TfR-ECD by gel-shift assay. At the end of this screening step, 10 out of 40 analyzed sequences showed significant binding, including a full length GS24 aptamer. Afterward, this latter was rationally truncated to a minimal GS24 sequence, sharing the common structural motifs of the full-length molecule (Fig. 1).

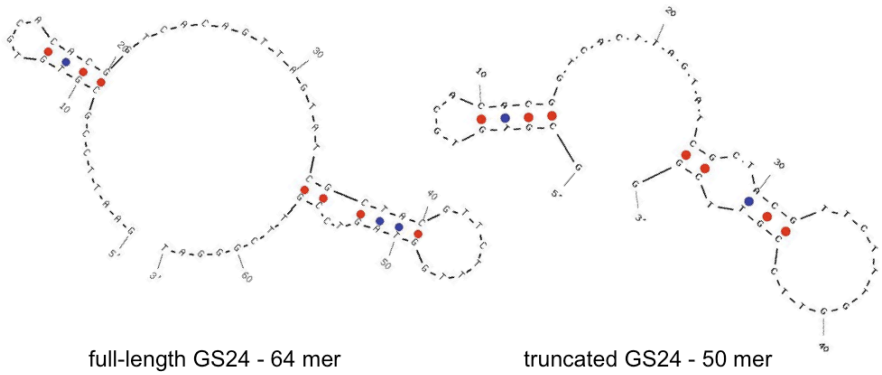

Fig. 1 Mfold secondary structure predictions[212] of full-length (on the left) and minimal GS24 (on the right).

It is worth mentioning that in a SELEX experiment, the selection pressure after each round gradually increases due to increasingly stringent conditions (different incubation temperature, buffer conditions and so on) to allow proper enrichment of target-bound sequences possessing the most suitable 3D shapes[130]. However, DNA or RNA molecules have the ability to assume multiple folds via reversible pathways[213,214]. Thus, when the selection pressure is not optimal to isolate the best ligand sequences, misfolded structures can be to some extent enriched together with target-bound sequences. The presence of a misfolded fraction unable to bind the target can significantly reduce the aptamer biological activity[215].

Therefore, investigation on the presence and activity of such different folds can help unveiling the actual action mechanism and provide cues for the design of aptamers with optimized activity. In this chapter, I shall describe a biophysical study aimed to elucidate the relationship between GS24 aptamer folding and its interaction with transferrin receptor both *in vitro* and in living cells. This study allows the identification and purification of two aptamer conformers by means of chromatographic techniques. Fluorescence-anisotropy measurements and internalization assay in living cells highlight that only one fold is able to bind mouse transferrin receptor. Additionally, I shall describe a rational engineering strategy where GS24 mutant sequences were specifically designed to enhance the structural stability of the active fold, thus improving the aptamer activity. After a description of the properties of the mutated sequences and of the protocol used in this engineering approach, I shall introduce a novel enhanced anti-mTfR DNA aptamer sequence that result as a valid tool for targeted drug delivery applications. This aptamer can be orthogonally used in combination with anti-hTfR aptamer as targeting ligand of drug delivery platform in a modular “plug and play” fashion.

3.1 Folding conformation analysis

The aptamer activity relies on their defined 3D structures, which allow binding and recognition of biomolecular targets via non-covalent interactions with high affinity and specificity. Thus, precise knowledge and control of aptamer conformation is needed to optimize aptamer activity and selectivity. In this

section, I shall describe a chromatographic study to explore the presence of different aptamer conformers.

We first performed an HPLC weak anion-exchange analysis in native conditions at 25°C. This weak anion exchange (WAX) analysis is based on the interaction of the negatively charged ODN with tertiary amine present on the stationary phase[216], opposed to the more commonly used strong anion exchange (SAX) chromatography, where the stationary phase is functionalized with quaternary ammonium ions[217]. A mobile phase with increasing percentage of ionic concentration is used to compete with the negatively charged ODN on the interaction with the positively charged stationary phase. Thus, shorter sequences with less negative charge elute at ionic strength of the eluting mixture.

It is well known that ODNs with weak secondary structures are easily analyzed and purified by this method and show a single chromatographic peak related to one distinct conformation[218]. In contrast, DNA sequences with higher percentage of guanosine or RNA and modified RNA may possess strong secondary structures and when analyzed by anion exchange HPLC, at neutral pH and room temperature may result in multiple peaks[218,219].

Interestingly, our analysis on GS24 sequence showed the presence of two main peaks (black line in Fig. 2a) at 20:80 molar ratio, as estimated from their chromatographic area. To assess whether these two peaks were related with two distinct interconvertible/non-convertible folding conformations, three different chromatographic analyses were performed (Fig. 2):

- The chromatographic pattern of GS24 was evaluated after thermal denaturation (unfolding) followed by a slow cooling to room temperature (refolding) (Fig. 2a). Indeed, if the two peaks correspond to native structures and these are different conformers in thermodynamic equilibrium, the same initial pattern must be observed after a denaturation/refolding process[213,220].
- Temperature dependence of the molar ratio between these two peaks was studied by monitoring changes in their chromatographic area at 25, 37, 40, 42 and 50°C, respectively (Fig. 2b).

- Interconversion kinetics of each peak was analyzed after HPLC purification (Fig. 2c). Particularly, each sample was kept at 25°C and was analyzed at different times by HPLC to monitor if the initial pattern could be restored.

The first analysis of GS24 showed a total disappearance of native elution profile under denaturing conditions with a single peak detected at longer retention time (red line in Fig 2a) in agreement with the increased number of charges exposed by unfolded ODNs[221]. This single peak is perfectly in keeping with the presence of only one secondary structure (unfolded state). Most importantly, denatured aptamer shows a complete recovery of the native pattern after refolding at room temperature (blue line in Fig 2a). Therefore, this result revealed the presence of two distinct conformers, which we termed A-1F (first peak) and A-2F (second peak) with a relative free energy difference $\Delta G_{2.1}$ of approximately 0.88 kcal/mol, as estimated from their 20:80 molar ratio.

Next, five GS24 aptamer samples were heated and eluted using WAX-HPLC at 25, 37, 40, 42 and 50°C, to monitor the temperature dependence of the molar ratio between A-1F and A-2F. Interestingly, molar ratio between the conformers was strongly dependent on temperature (Fig. 2b). In particular, area of A-2F gradually decreases by increasing the temperature: at 37, 40 and 42°C the A-1F:A-2F molar ratios were 31:69, 52:48 and 68:32, respectively (Fig. 2b - inset). The initial pattern almost disappears at 50°C and chromatographic profile shows only a single peak (blue line in Fig 2b), suggesting an early stage of oligonucleotide denaturation and unfolding. It is worth noting that in the temperature range of 40-42°C the two folds become equally populated (grey and red lines). Such temperature dependence is particularly relevant for biological purposes, since *in vivo* and living-cell studies are performed near 37°C.

Finally, we examined whether the two folds were interconvertible. The two conformers were purified by WAX-HPLC, dissolved in a suitable buffer, and maintained at 25°C under stirring. We monitored equilibration of the two species by analysis of samples collected at different times. As shown in Fig. 2c the two species shows recover of initial conditions (i.e. 20:80 molar ratio) with different conversion rates, highlighting that A-1F and A-2F are indeed interconvertible folds. Then, we calculated both the interconversion kinetics and relative stability

of the two conformers. The kinetics of recovery of the 20:80 molar ratio was described by a single exponential (Fig. 2c, left panel). Interestingly, conversion of A-2F into A-1F occurred with $\tau_{(2\rightarrow1)}$= 5.33 h, a sufficiently extended period to perform various biological studies without any appreciable conformational change. In contrast, A-1F showed a significantly higher conversion rate ($\tau_{(1\rightarrow2)}$ = 1.33 h) resulting markedly less stable than A-2F. The two different interconversion rates are consistent with the calculated value for $\Delta G_{2.1}$, i.e. $\tau_{(2\rightarrow1)}$ /$\tau_{(1\rightarrow2)}$=exp(-$\Delta G_{2.1}$/RT) (Fig 2c, right panel).

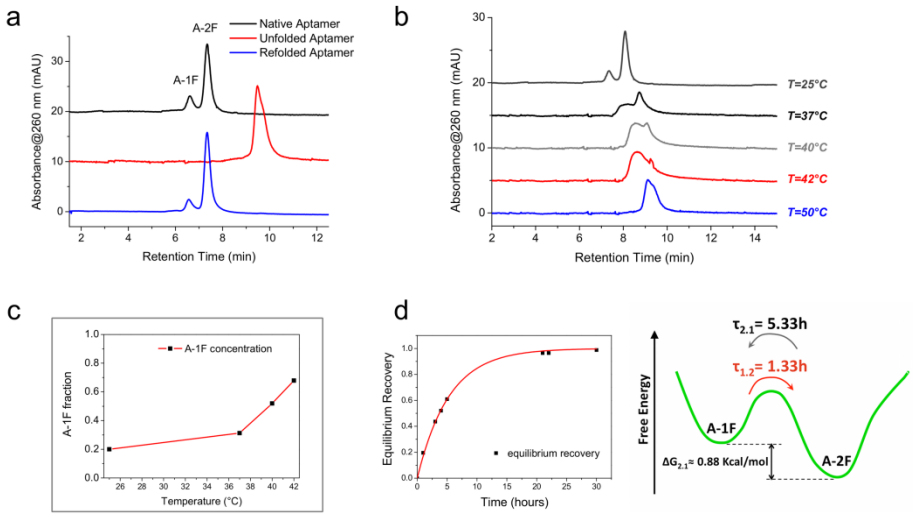

Fig. 2 Folding conformation analysis. (a) HPLC analysis of GS24 performed in native conditions (black line) revealed the presence of two main structures in 20:80 molar ratio. Chromatographic run performed in denaturing conditions at 80°C (red line) showed a single component (unfolded structure). Analysis in native conditions performed after a slow refolding process (blue line) showed a complete recovery of the initial pattern with a 20:80 molar ratio (named A-1F and A-2F on the basis of the different retention time). (b) Temperature dependence of the fold molar ratio. The aptamer sample was heated and eluted at 25, 37, 40, 42 and 50°C. (c) Temperature dependence of A-1F fraction in the mixture. Notably, A-1F fraction changed from the initial value of 0.20 at 25°C to 0.31, 0.52, and 0.68 at 37, 40, 42°C respectively (d) Kinetics of the equilibrium recovery of the purified A-2F (left panel) showed a

complete return to the initial molar ratio after 30 h from folds purification. The energy landscape of two confomers (right panel) shows a free energy difference $\Delta G_{2.1}$ of approximately 0.88 kcal/mol.

Interconversion between two folds with different structure can lead to significant changes in aptamer biological activity, thus we first evaluated the secondary structure predictions and then we performed a molecular dynamic simulation to assess the structural properties of these two conformers (such as the conserved motifs and the effective total charge).

Secondary structure prediction obtained using Mfold software[212] highlights the presence of two conformers with an estimated free energy difference ($\Delta G_{\alpha\beta}$ = -1.53 kcal/mol at 25°C) that was similar to our experimental value ($\Delta G_{2.1}$ = 0.88 kcal/mol) (Fig. 3). Thus, we related the more stable fold α to the more populated A-2F on the basis of the predicted free energies. Afterwards, the secondary structures were converted into two 3D conformations. Molecular dynamics (MD) simulations were then employed to assess the structural properties of the two folds. For each fold, we analyzed a combined trajectory formed by ten 10-ns explicit-solvent molecular dynamics simulations performed using different initial velocities. A representative structure was obtained from each combined trajectory using cluster analysis (Fig. 3).

Furthermore, we related HPLC retention times to the electrostatic properties of these 3D conformations to unequivocally identify more stable fold α as A-2F and fold β as A-1F. Indeed, HPLC retention time for ion exchange chromatography is based on the interaction between the ODN negative charges and the positive charges of the stationary phase. Thus, shorter sequences or sequence with less exposed surface charge elute at shorter retention times. Then, we computed an "effective total charge" for each conformation and we related it to HPLC retention times. Effective net charge was obtained by computing the electrostatic potential of 100 conformations within each cluster of the molecular dynamic simulation (see Methods for further details). The calculated "effective total charge" for conformer α is -13.9 ± 0.4 *e* and is greater than that calculated for conformer β (-11.7 ± 1.3 *e*). This result confirmed our stated structural assignment: fold α (most

stable conformation with highest exposed surface charge) actually corresponds to A2F (most stable fold with longer retention time) and consequently fold β matches with A-1F.

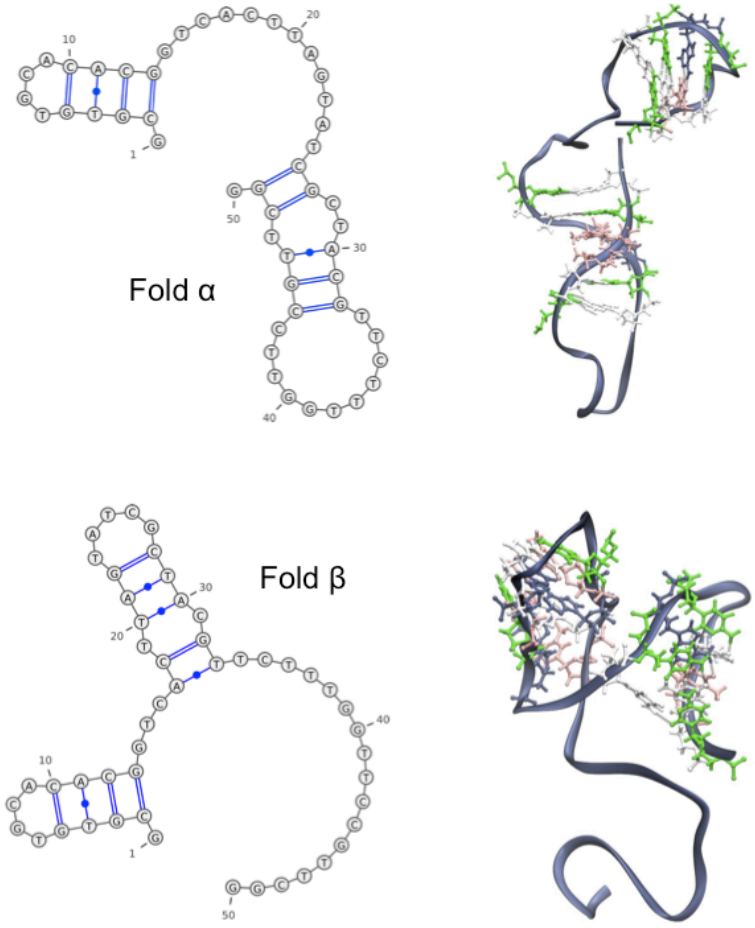

Fig. 3 Mfold secondary structure predictions of the two lowest-energy folds of GS24 sequence and corresponding structures from MD simulations: structure of representative conformation (centroid) of the most populated cluster. (Figure based on data generated by P. Mereghetti).

3.2 Fluorescence anisotropy assay

The previous analysis on the aptamer folding shed light on the presence of two interconvertible folds at or near physiological temperature. Thereby, it is extremely important investigate the binding property of these conformers to clarify their relationship with the aptamer activity. Indeed, the presence of two different 3D structures might have either a cooperative binding effect or they might negatively affect TfR recognition. The former effect was demonstrated by L. Niu group, which described a single RNA aptamer adopting two different, not interconvertible structures. Interestingly both conformers are essential to exploit aptamer biological activity, i.e. selective inhibition of one of the subunits of the glutamate ion channel family[213]. In contrast, a negative effect on the recognition of target receptor should represent a strong limitation to use this anti-mTfR aptamer as targeting ligand especially for *in vivo* application.

Importantly, an analysis of the receptor-binding affinity of the original DNA (GS24) and RNA (FB4) aptamer against mTfR was not previously described. Thus, an investigation of the aptamer binding properties can clarify behavior of the aptamer as ligand, a feature that is quantified by the Kd value.

To this end, we decided to use fluorescently labeled aptamer conformers to assess first the receptor-binding affinity of each fold, and then their internalization property in living cells. It is worth mentioning that in previous studies both 5'- and 3'- ends of GS24 could be modified with different molecules without loss of binding affinity for the receptor[211,222]. Thus, we employed a 5'-aminohexyl modified analog of GS24 and we labeled it with a fluorescent tag (ATTO 633). This modification allowed us to perform reliable *in vitro* binding experiments and to accurately track the aptamer during endocytosis in living cells. Compared with other labeling strategies that exploit bulky fluorescent tags (such as the previously-used biotin-streptavidin labeling approach)[211] the use of organic dyes has the advantage of a reduced interference on the 3D structure, and hence on the biological activity of the aptamer. This strategy was chosen to allow an unbiased evaluation of the activity of GS24 conformers.

As *in vitro* binding assay we decided to perform fluorescence anisotropy (FA) experiments[223,224] in which we could compare the receptor-binding affinity of GS24, A-1F and A-2F. We performed all measurements at 25°C consistently with the *in vitro* binding assay initially performed during the SELEX process leading to GS24 identification[211], to ease comparison of the experimental results.

We first incubated GS24 (as mixture of the two folds with 20/80 molar ratio) with increasing concentration of recombinant murine TfR (mTfR) ranging from 0 to 2500 nM. As shown in Fig. 4a,[211] FA increased in the presence of mTfR owing to protein-aptamer complex formation. Note that the trend of the binding curve is compatible with a monophasic ligand-receptor binding (Fig 4a, red line/black sample)[225].

Afterwards, we measured the FA of the purified folds separately, at mTfR concentration of 600 nM (Fig. 4b). Although the measured interconversion rate is sufficiently slow to allow fluorescence anisotropy measurements, a partial re-equilibration of the two fold populations took place during the course of FA assays. We quantitated this effect by performing HPLC analysis of purified A-1F and A-2F samples immediately after anisotropy measurements (Fig. 4c). We found that A-1F and A-2F samples contained 55:45 and 3:97 molar fractions, respectively in agreement with their different interconversion rates. Most importantly (Fig 4b), we found that the measured anisotropy for A-2F sample (3:97 molar ratio) exceeded that found for GS24 (20:80 molar ratio), which in turn was higher than that relative to the A-1F sample (55:45 molar ratio). A scrambled sequence (GS24mt) which is unable to recognize mouse transferrin receptor[222] was also incubated with 600 nM of mTfR, and revealed a remarkably lower anisotropy change when compared with GS24 (Fig. 5a).

The measured anisotropy values for A-2F, GS24 and A-1F correspond to a fraction of bound aptamer (f_B) of 0.85, 0.69, and 0.46, respectively. These f_B values are proportional to the measured population of A-2F in the three samples (i.e. 97%, 80% and 45%). Therefore, these results did unveil an essential functional property of GS24, i.e. that A-2F is the only fold able to bind mTfR. This conclusion is also in agreement with the monophasic ligand-receptor binding

curve measured for GS24. Indeed, binding of A-1F with a different Kd would have resulted in a biphasic curve of the anisotropy[225].

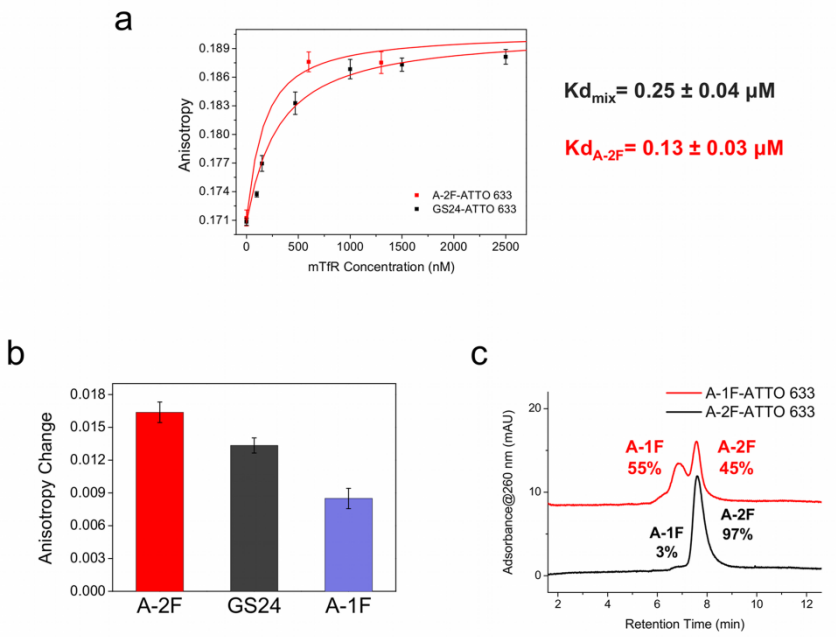

Fig. 4 Fluorescence anisotropy assay. (a) Titration of GS24-ATTO 633 (50 nM) with mTfR (0-2500 nM) at 25°C. A-2F binding was examined at 600 and 1300 nM, the latter considered as concentration close to the saturation. The curve of the mixture (black squares) was obtained by fitting the anisotropy values as a function of mTfR concentration. The fit afforded both K_d and A_B (anisotropy in saturating condition). The curve of A-2F (red squares) was obtained as above, using the value of A_B obtained from the fitting of GS24 anisotropy curve. (b) Binding efficiency of the two folds and GS24 was measured at [mTfR]=600 nM. In this case the anisotropy change is defined as the difference between aptamer anisotropy in the presence and in absence of protein. (c) HPLC analysis after FA measurements. Immediately after FA assay, the samples were analysed by IE-HPLC. A-1F and A-2F samples contained 55:45 and 3:97 molar fractions, respectively. This clearly indicates that an interconversion between two folds occurred during anisotropy measurement.

Then we measured anisotropy of A-2F sample in saturating conditions ([mTfR]=1300nM) and we found a value comparable with the measured anisotropy of GS24. This behavior is extremely important and implies that the unbound fraction eventually equilibrates between the two folds during the course of FA measurements. Within this assumption, the Kd of the mixture and that of the purified A-2F should be related by $Kd_{mix}=(1+L)Kd_{A\text{-}2F}$, L being the molar ratio between A-1F and A-2F (L=0.25 from the HPLC assay).

Fitting the FA data yields a dissociation constant for the mixture $Kd_{mix} = 0.25 \pm 0.04$ μM, and a theoretical estimate for $Kd_{A\text{-}2F} \approx 0.2$ μM. The FA results obtained from the A-2F sample yield an estimate of a lower $Kd_{A\text{-}2F} = 0.13 \pm 0.03$ μM. This discrepancy probably stems from an incompletely equilibrated molar fraction during the titration of the GS24 mixture. Thus, A-2F displays higher affinity for mouse TfR than GS24 since the latter is actually a mixture of the two folds.

After our investigation on GS24 affinity we turned our attention to the selectivity property of GS24. We incubated GS24 aptamer with saturating amounts of bovine serum albumin (BSA) and transferrin (Tf) and then the measured FA values were compared with the anisotropy change recorded in presence of 600 nM of mTfR (Fig. 5a). Interestingly, only negligible anisotropy change was observed after incubation with either BSA or Tf. A similar result was found even when the unconjugated fluorophore was incubated with 600 nM of mTfR. Overall, these results suggest that the significant anisotropy enhancement observed during FA is mainly dependent on aptamer structure, and is due to the interaction between mTfR and the A-2F conformation, rather than to nonspecific adsorption.

Interestingly, we also detected a substantial anisotropy change when GS24 was incubated with the human recombinant TfR (600 nM) (Fig 5a), suggesting that GS24 might effectively recognize the human receptor, possibly via its active form A-2F. Therefore, we compared the FA of GS24, A-2F and A-1F when incubated with hTfR at concentration of 600 nM. As shown in Fig. 5b these three species exhibit a similar anisotropy trend even towards hTfR (A-2F > GS24 > A-1F). Furthermore, addition of hTfR to the scrambled sequence GS24mt under identical conditions caused only a minor anisotropy change (Fig. 5a). Overall, these results

indicate that GS24 via A-2F is actually able to bind hTfR albeit with lower efficiency compared with that detected for mTfR (fluorescence anisotropy is 7.6 ± 0.5 and 13.3 ± 0.7 for hTfR and mTfR, respectively).

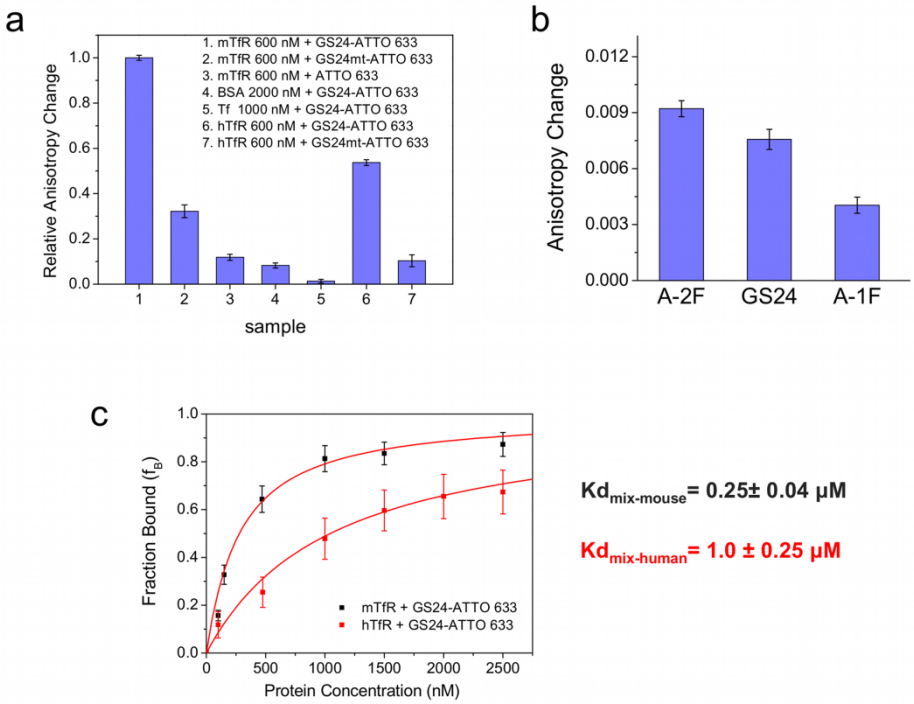

Fig. 5 Fluorescence anisotropy assay. (a) Aptamer selectivity control experiments. Anisotropy change was measured for GS24 mutant (GS24mt) and unconjugated ATTO 633 (50 nM) in presence of 600 nM mTfR respectively. Next, GS24 aptamer selectivity was tested incubating the sample (50 nM labeled GS24) with saturating amounts of BSA, Tf and hTfR. The anisotropy change of each sample was compared with the anisotropy measured in the presence of 600 nM mTfR. GS24mt was also tested in presence of 600 nM of hTfR (b) Binding efficiency of the two folds, and GS24 was measured at [hTfR]=600 nM. In this case the anisotropy change is defined as the difference between aptamer anisotropy in presence and in absence of the human receptor. (c) Fraction bound of aptamer (f_B) for mouse (black squares) and human (red squares) TfR was calculated from the corresponding anisotropy titration curves. The mixture of two folds (GS24) showed a different affinity for each protein.

Therefore, we investigated the affinity of GS24 towards the human receptor. To this end, we performed a second titration experiment using increasing concentrations of hTfR against GS24-ATTO 633 conjugate. By applying the same model described above the calculated Kd for human receptor was 1.0 ± 0.25 μM (Fig. 5c).

It is worth noting that Kd_{GS24} towards hTfR is about four-fold higher than the measured Kd_{GS24} for mTfR. Although the sequence homology between hTfR and mTfR is about 77%, the capability of GS24 to bind both receptor species might indicate that the aptamer binding site is located nearby a conserved –yet not identical- portion of the receptor.

These results unveiled the receptor-binding property of each conformer, identifying the only active fold (A-2F) of the aptamer. Interestingly, we also revealed intriguing aptamer cross-reactivity towards both the murine receptor (the biomolecular target used during the selection process) and its human counterpart.

3.3 Internalization assay in living cells

Receptor-binding property is not the only feature required for targeting ligands. Indeed, a targeting aptamer should be able to interact with a cell-surface marker and internalize into target cells upon binding with it. Thereby, we evaluated whether the different binding activities of the two folds observed *in vitro* lead to different cell-internalization properties. To this end, we first performed internalization assays on mouse fibroblasts (NIH 3T3) using the purified folds and the scrambled aptamer sequence. Each sample (A-1F, A-2F and GS24mt) was incubated in cultured cells for 25 minutes at a concentration of 1 μM. Short incubation times (e.g. 10-30 minutes) and relatively low oligonucleotide concentrations (< 5 μM) are critical to minimize nonspecific aptamer uptake that could occur through fluid-phase endocytosis, such as pinocytosis[226]. Indeed, the receptor-mediated endocytosis, in particular TfR-mediated internalization, is kinetically more efficient than pinocytosis[226]. Furthermore, BSA and calf thymus DNA were added as competitors for nonspecific binding sites[227,228]. Minimization

of nonspecific endocytosis is an essential step to avoid misleading results due to internalization of oligonucleotide sequences through a TfR-independent uptake.

After the incubation, we monitored by confocal microscopy the fluorescently labeled aptamer during its endocytosis process. Fig 6 qualitatively shows the three endocytic patterns for GS24mt (panel a), A-1F (panel b), and A-2F (panel c).

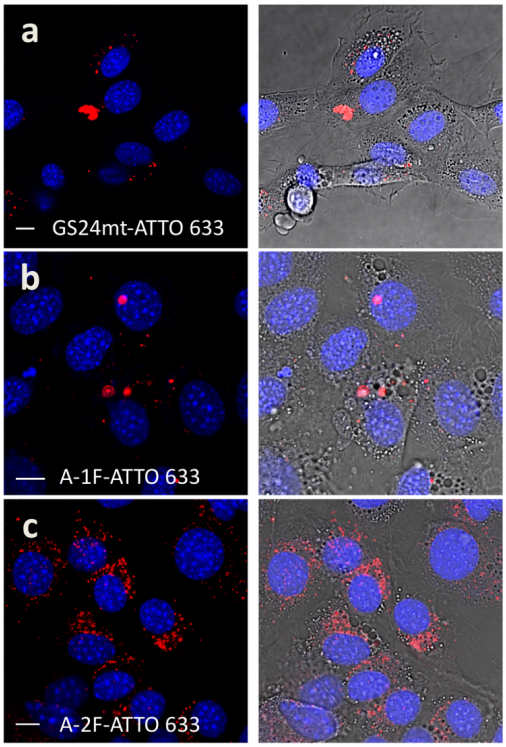

Fig. 6 Internalization assay of the labelled aptamer folds in mouse fibroblasts (NIH 3T3). Each sample was incubated in cultured cells at a concentration of 1 µM and endocytosis was monitored by confocal fluorescence microscopy. (a) GS24mt-ATTO 633 probe was not able to recognize and bind mTfR, consequently only weak vesicular signal was detected into the cells. (b) Vesicular signal of A-1F-ATTO 633 was weakly detected into the cell cytoplasm, indicating a negligible activity, likely due to partial conversion in the active fold A-2F during incubation. (c) A-2F-ATTO 633 showed strong perinuclear vesicular signals. Scale bars: 10 µm.

Notably, only A-2F sample displays cell-internalization properties with an intense vesicular fluorescence signal located in the perinuclear region. It is worth noting that this endocytic pattern is in keeping with the punctate pattern typical of a receptor-mediated endocytosis process. On the other hand, A-1F shows negligible uptake, which is not significantly different from that of the scrambled sequence GS24mt. It is tempting to hypothesize that the weak vesicular signal displayed upon treatment with A-1F stems from the small fraction of A-1F converting to A-2F during the short 25-minutes incubation. Thereby, besides showing different *in vitro* binding affinities towards transferrin receptor, A-1F and A-2F also display remarkably different cell-internalization efficiency in living mouse fibroblast cells.

Next, we investigated in more details the mechanism of the A-2F internalization in living cells. First, in order to verify that the observed internalization is an active, receptor-mediated process, we performed time-lapse imaging at low temperature (4°C)[229] after treatment with this aptamer conformer. Indeed, the low temperature should inhibit significantly any active energy-dependent transport process across the membrane, including TfR-mediated endocytosis[230,231]

Interestingly, when cells were kept at 4°C only a cell membrane staining was detected and consequently no internalization occurred. In contrast, A-2F-ATTO 633 was rapidly internalized upon warming to 37°C as expected from an active energy-dependent process[230] (Fig. 7). This result together with the negligible internalization signal detected upon treatment with the scrambled sequence, confirm that the cell uptake of the active conformer, i.e. A-2F, is effectively due to TfR-mediated endocytosis.

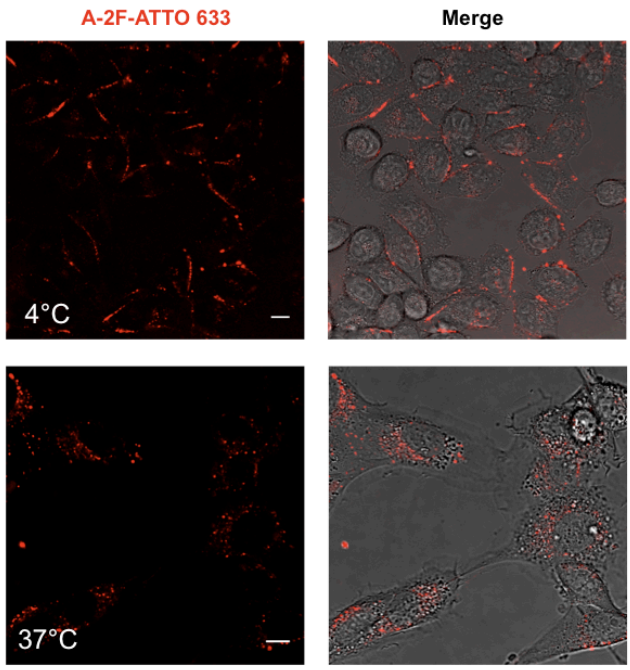

Fig. 7 A-2F-ATTO 633 internalization pattern after incubation at 4°C and after warming to 37°C. Scale bars: 10 µm.

After that, we performed a colocalization assay between A-2F-ATTO 633 and lysosomal marker, lysosensor green, to monitor the intracellular fate of A-2F at longer time. As shown in Fig. 8a, we found partial colocalization of A-2F with lysosomes after 120 minutes. This result is in agreement with previous GS24 findings by Chen et al. on the internalization process of GS24[211]. It is worth mentioning that internalized, not-recycled molecules are actually located mainly in the lysosomal compartment during the final stages of receptor-mediated endocytosis[232].

Interestingly, the fluorescence signal arising from A-2F-ATTO 633 is still detectable in the cells with a vescicular pattern even at longer times (180 minutes) (Fig. 8b). Most importantly (Fig. 8c), A-2F was also internalized in living cells

after a short 25-minutes incubation at lower concentration (200 nM), demonstrating high affinity towards mTfR even in a cellular physiological context.

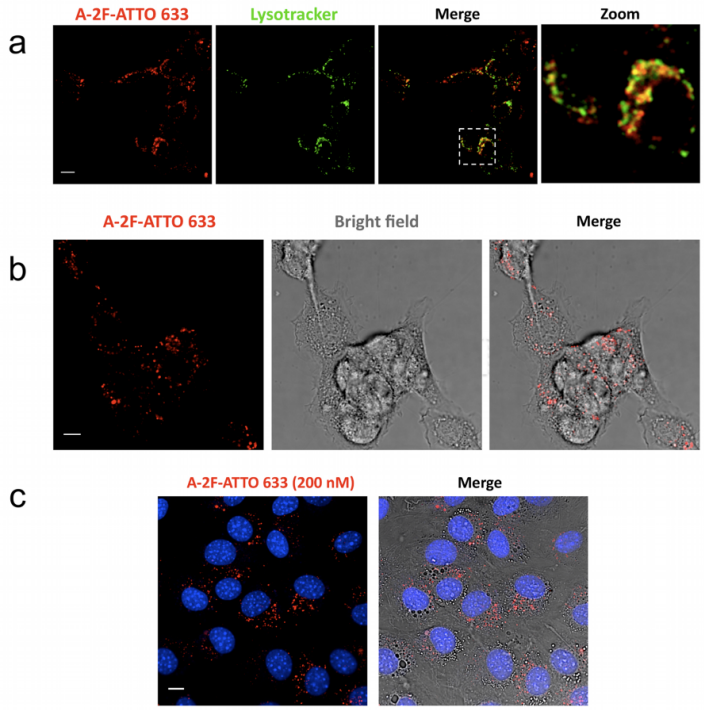

Fig. 8 (a) Aptamer intracellular fate in mouse fibroblasts (NIH 3T3). Partial colocalization between A-2F-ATTO 633 (red) and lysosomes (Lysotracker green) was observed 120 minutes after administration. Colocalized vesicles were mainly found close to the perinuclear region. (b) Aptamer signal 3 hours after administration to mouse fibroblasts (NIH 3T3). A-2F-ATTO 633 showed remarkable fluorescence in cell cytoplasm even 180 minutes after administration. (c) A-2F tested in mouse fibroblasts (NIH 3T3). A-2F-ATTO 633 is internalized via a receptor-mediated endocytosis, even at lower concentration (200 nM) with respect to usual amount used in all other evaluations. Scale bars: 10 µm.

Overall, these results confirm what observed during the *in vitro* fluorescence anisotropy measurements: A-2F is the only effective conformer of GS24 able to bind mTfR with high affinity and to internalize in mouse fibroblasts via a receptor-mediated endocytosis.

In addition, the *in vitro* binding assay clearly demonstrates that GS24 is able to bind the recombinant form of the human transferrin receptor –albeit with lower affinity- inducing a significant anisotropy change. Therefore, we performed an internalization assay to assess whether the aptamer maintains this capability even in a cellular physiological context. It is worth noting that in previous works administration of GS24 (as mixture of conformers) to human cell lines did not result in a significant cellular uptake. On the basis of these results and given the lower in vitro aptamer affinity towards hTfR, we decided to (i) use the purified active fold, i.e. A-2F, (ii) increase the aptamer concentration (3 μM vs 1 μM, i.e the standard concentration used on mouse cell investigations) though still using short incubation time, and (iii) test it into a cell line overexpressing hTfR, e.g. the human pancreatic tumor cells (MIA PaCa-2) we used in the previous chapter for testing the aptacoy-Dox activity.

As shown in Fig. 9a, A-2F was able to bind the cell-surface receptor on the plasma membrane upon short incubation, showing a cell membrane staining. Notably, at longer times (60 minutes), we could detect vesicular fluorescence signal arising from the cell cytoplasm, but yet a certain amount of aptamer was present on the cell surface (Fig. 9b). Interestingly, at a later stage (140 minutes) no fluorescence signal was detected from the plasma membrane, while the endocytic pattern displayed vesicular signals in the perinuclear region (Fig. 9c).

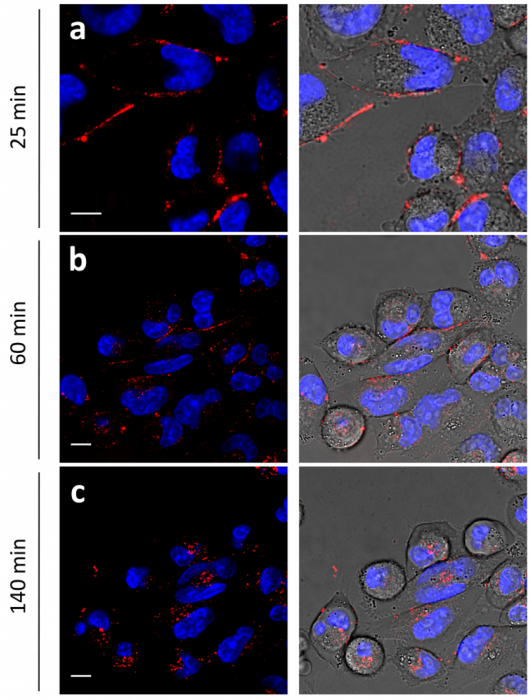

Fig. 9 Endocytosis of the A-2F in human pancreatic tumor cells (MIA PaCa-2). 3 µM A-2F-ATTO 633 was incubated in cultured cells. (a) After incubation, fluorescence signal was mainly present on plasma membrane. (b) Significant vesicular signals could be observed into cell cytoplasm after 60 minutes since incubation, but A-2F fluorescence was still present on the cell surface. (c) At longer times (140 minutes) all A-2F was internalized into the cells and perinuclear signals were observed. Scale bars: 10 µm.

In contrast, when the scrambled aptamer sequence (GS24mt) was tested, only a negligible intracellular fluorescence was observed (Fig. 10a), in keeping with the endocytic pattern observed in mouse cells. Although we employed a higher aptamer concentration during the incubation, we observed almost null absence of fluorescence signals after treatment with the scrambled sequence. This result strongly suggests that internalization of A-2F is not due to nonspecific fluid phase

uptake. This result strongly suggests that actually A-2F conformer may bind hTfR on the cell-surface, being taken up in human cells by constitutively present internalization mechanisms.

To assess whether the cell-internalization property exhibited by A-2F was due to a TfR-mediated endocytosis, we performed a colocalization experiment between A-2F and the monoclonal antibody anti-hTfR (mAb anti-CD71). In details, cells were incubated with both A-2F and mAb anti-CD71; after 60 minutes, we observed extensive, although not complete, colocalization between the aptamer and the antibody in many vesicular compartments, as assessed by a Pearson's correlation coefficient of 0.63 (Fig. 10b).

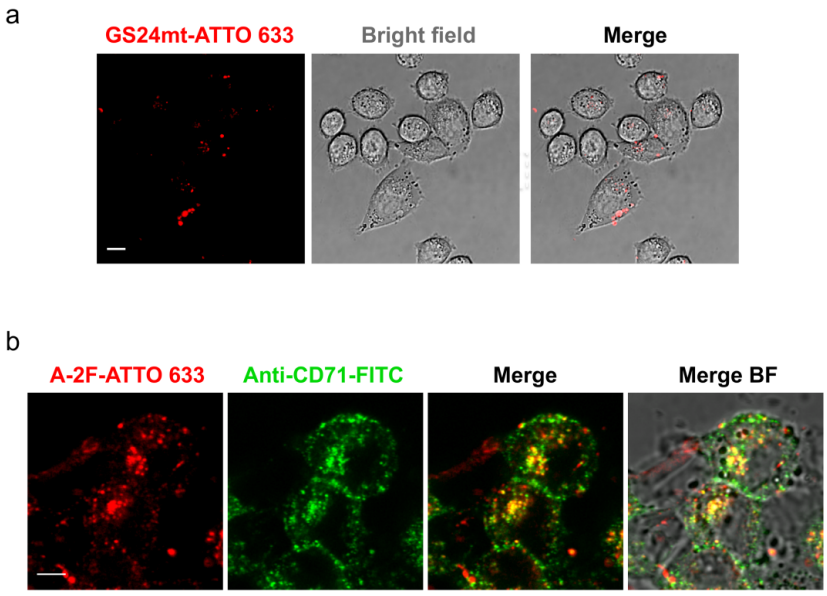

Fig. 10 (a) Endocytosis of GS24mt into human cells (MIA PaCa-2). Only weak vesicular signal was detected into the human pancreatic cancer cells when the GS24mt-ATTO 633 (3 µM) was used. (b) Colocalization assay between A-2F-ATTO 633 and mAb anti-CD71-FITC probes in human cells. Confocal images of MIA PaCa-2 cells treated with A-2F-ATTO 633 (3 µM) and monoclonal antibody anti-CD71-FITC (1:250 dilution, Invitrogen) show extensive vesicular colocalization into the cell cytoplasm. Scale bar: 10 µm.

Overall, these results suggest that the active conformer of GS24 aptamer can recognize and bind even human transferrin receptor both *in vitro* and in living human cells, allowing cell-internalization via a receptor-mediated endocytosis. The slower kinetics of internalization observed in this case suggests that the Kd in a live cell context might be higher than the affinity measured in vitro by FA assay. Indeed, the high A-2F concentration incubated in the MIA PaCa-2 cells is not sufficient to balance the lower affinity towards hTfR, allowing a fast internalization also in human cells.

3.4 Rational engineering of GS24 aptamer

Next, we turned our attention to the identification of conserved motifs within GS24 structure responsible for its receptor-binding property with the aim to generate an enhanced aptamer sequence endowed with higher binding affinity. Consequently we started our investigation with a closer inspection of the two GS24 conformers, A-1F and A-2F. As shown in Fig. 3, secondary-structures predictions and our molecular dynamics simulations revealed a significant difference in the region including nucleotides 16-50. Particularly, A-2F displays a folded domain comprising residues 26 to 50, which is completely absent in the A-1F conformation.

It is worth mentioning that the anti-mTfR DNA aptamer (GS24) and RNA aptamer (FB4) generated by Chen et al. were selected using the same recombinant extracellular domain of mouse transferrin receptor (mTfR-ECD) and displayed similar functional properties, in terms of binding selectivity and no competition with Tf[211]. Indeed, the authors used these sequences as interchangeable ligands in their biological applications. This suggests that GS24 and FB4 sequences might share conserved structural domains needed for mTfR recognition. Therefore, we examined and compared the secondary structures prediction of both full-length and truncated DNA and RNA aptamers. Importantly, as shown in Fig. 11, all sequences share a highly-conserved stem-loop domain, approximately located in a central region, which contains a conserved nonamer (CGTTSTYTG; where S = G or C, Y = T or C. Note that in the RNA structure U replaces T). This conserved

sequence is also included in the folded region within the 26-50 sequence of A-2F conformation.

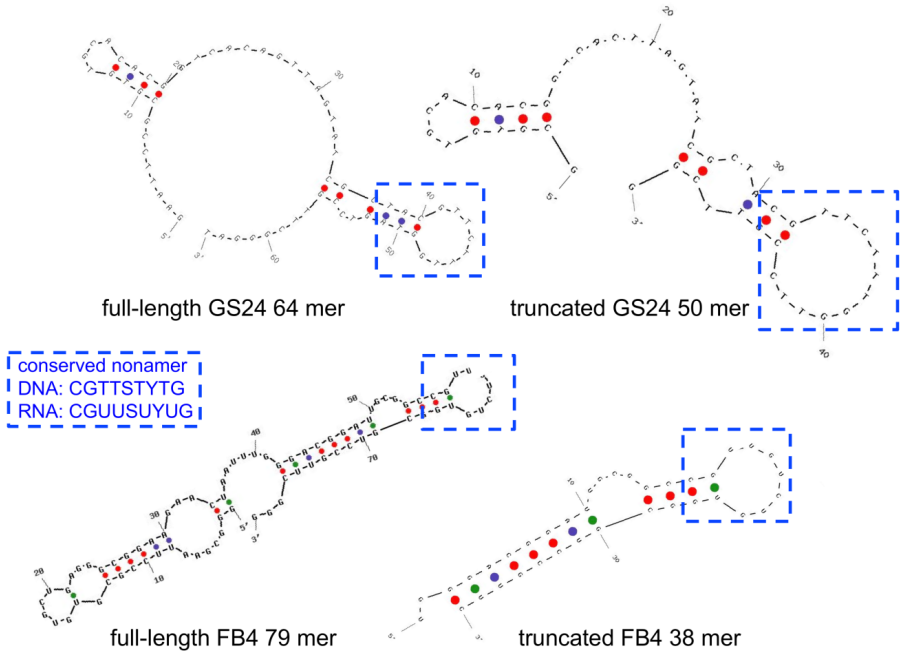

Fig. 11 Secondary structure prediction of DNA aptamer GS24 and RNA aptamer FB4 (full-length and truncated versions) originally selected by Chen *et al.*, highlights that all sequences share a highly conserved stem loop domain (dashed boxes), approximately located in a central region. This domain is constituted by a conserved nonamer (CGTTSTYTG; where S = G or C, Y = T or C. Note that in the RNA structure U replaces T).

On the basis of these observations, we decided to further minimize the GS24 sequence. In details, we designed a truncated sequence that still retains the folded region of GS24 (A-2F conformation) but lacks the 5'-end domain, i.e. the less conserved motif of GS24 and FB4 secondary structures. Moreover, the 5'-end domain of GS24 is the only common region included in the A-1F and A-2F conformers, suggesting that this domain might play a minor role during the

binding of TfR. Thus, we designed a truncated version of GS24 comprised of 35 nucleotides, hereafter referred to as minimal GS24 (GS24min). As shown in Fig. 12 secondary structure predictions of GS24 (A-2F) and GS24min showed a remarkable structural homology and GS24min secondary structure still displayed the conserved stem-loop regions.

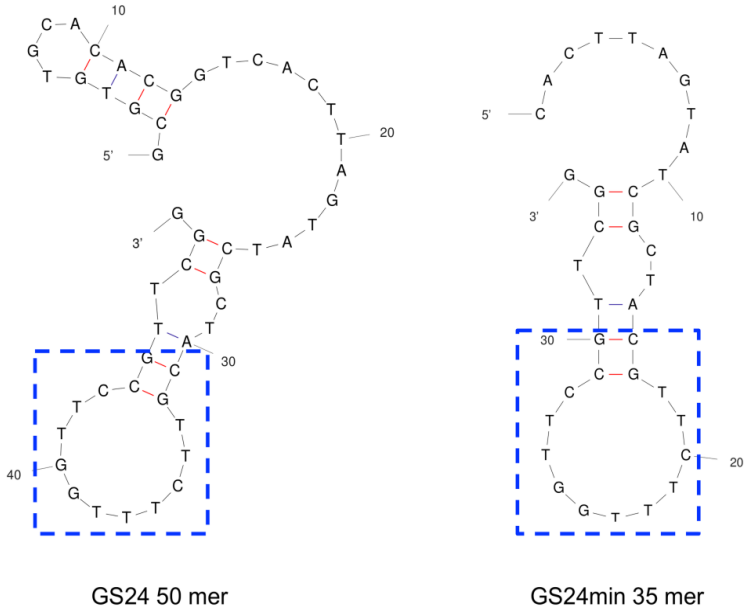

Fig. 12 Mfold secondary structure predictions of DNA aptamer GS24 (A-2F) and GS24min. Notably, GS24min still shows the conserved stem-loop domain (dashed boxes).

The minimization process aimed at unveiling the minimal, essential aptamer motif required to bind the target receptor. To this end, we investigated two important features of GS24min, such as (i) the presence of different conformers by native HPLC analysis, and (ii) the *in vitro* binding affinity towards mTfR by FA measurements.

In details, HPLC investigation displayed one major peak for our truncated sequence with only two minor shoulders present on the descending phase of the peak (Fig. 13a). This result suggests that our truncation led to a significant reduction of competing folding pathways. Although GS24min showed a reduced amount of misfolded material, the FA assay performed to calculate the Kd towards the recombinant mouse receptor displays a reduced affinity. Indeed, as shown in Fig. 13b the measured Kd was nearly five times higher than the dissociation constant of GS24 (1.2 ± 0.39 μM vs 0.25 ± 0.04 μM for GS24min and GS24 respectively).

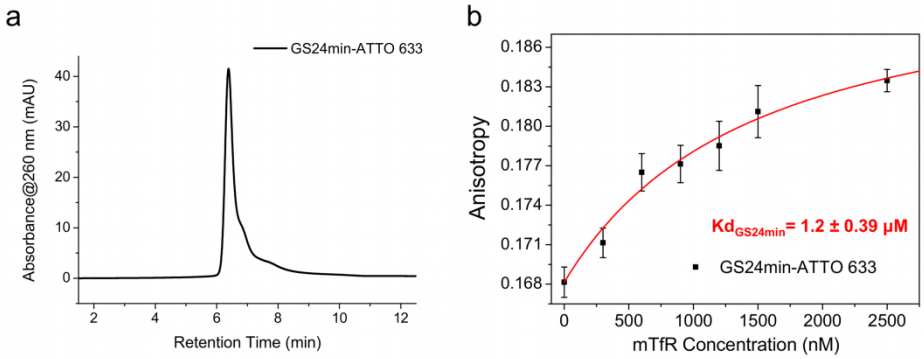

Fig. 13 (a) HPLC analysis of GS24min performed in native conditions revealed the presence of two main structures in 80:20 molar ratio (top panel). (b) Fluorescence anisotropy assay (bottom panel). FA of GS24min-ATTO 633 (50 nM) was measured with increased amount of mTfR (0-2500 nM) at 25°C. The aptamer titration curve was obtained by fitting the anisotropy values as a function of mTfR concentration. The fit afforded both K_d and A_B (anisotropy in saturating condition).

It is worth mentioning that reduction of aptamer affinity towards its biomolecular target is a quite common issue occurring during aptamer minimization. For example, the anti-hTfR c2.min, deeply investigated in the previous chapter, exhibits a dissociation constant that is five times higher than the full-length c2 sequence (102 nM vs 17 nM, respectively)[137], the same reduction that we found for GS24min compared with GS24.

Next we assessed whether GS24min is as effective as the parent sequence in binding to mTfR even in a physiological cell context. A critical feature in monitoring the endocytosis of relatively small aptamers (e.g. 25-35 mer in length) binding cell-surface markers is represented by the possibility to be internalized through nonspecific receptors. Indeed, over the last two decades, it has been reported that at very low concentration (< 0.5 μM) small oligonucleotides (< 30 mer in length) may internalize in cells in a saturable, size-dependent manner compatible with receptor-mediated endocytosis[233]. Particularly, smaller oligonucleotides (e.g. 5-15 mer in length) displayed higher efficiency of internalization than longer sequences[205]. In contrast, at high concentration (micromolar), the receptor-mediated endocytosis is rapidly saturated and small oligonucleotides are generally internalized via a slower nonspecific pinocytotic process. The identity of the receptor involved in the uptake of free oligonucleotides is still unknown. However, several attempts were performed to identify it, but much of this literature is controversial[234]. The main evidence seems that there is no a universal cell-surface receptor but rather a cell-dependent mechanism, which exploits various unidentified proteins depending on the cell type[235].

Thus we evaluated the cell-internalization property of GS24min in living cells, performing endocytosis assays both on mouse fibroblasts (NIH 3T3) and on human pancreatic tumor cells (MIA PaCa-2). As stated above, short incubation time (25 minutes) was employed to minimize the uptake due to pinocytosis. In addition BSA and calf thymus DNA were added as competitors for nonspecific binding sites. Interestingly, while the labeled GS24min was internalized in mouse cells, very weak vesicular signal was detected in human cells even at high concentration (i.e. 3 μM) (Fig 14a). As shown in Fig. 14, the endocytic pattern of GS24min is similar to that of A-2F. Spotty vesicular signals were found in the perinuclear region of NIH 3T3 cells that partially colocalize, as in the case of parent sequence A-2F, with the lysosomal compartment (Fig. 14b). Overall, these results together with the FA measurement (Fig. 13b) indicate that GS24min is still able to bind the mTfR in its native physiological form and to internalize upon binding with it via TfR-mediated endocytosis. It is worth noting that the existence

of a single fold within GS24min suggests that our rational minimization stabilized the most stable and active structure removing the trend of GS24 (A-2F) to equilibrate with other inactive conformations.

However, the negligible uptake in the human cells strongly suggests that truncated sequence GS24min either does not recognize the human receptor, or that its affinity towards hTfR is remarkable decreased.

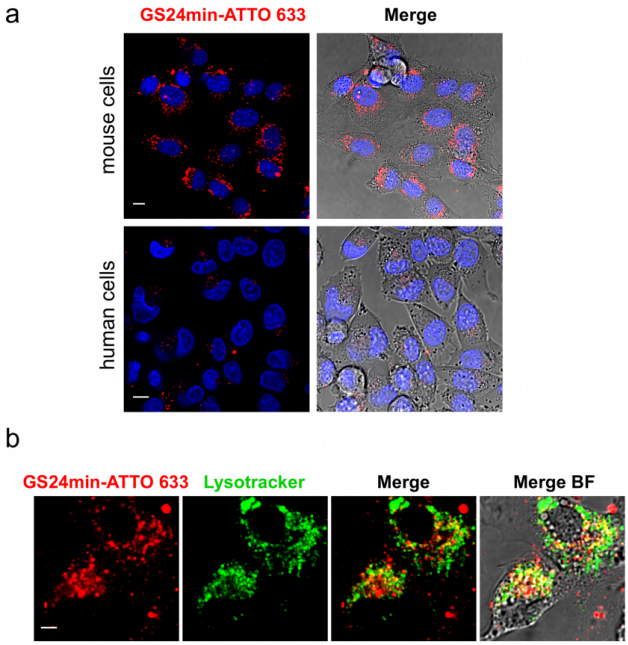

Fig. 14 Endocytosis of GS24min in mouse fibroblasts (NIH 3T3, upper panels) and in human pancreatic tumor cells (MIA PaCa-2, lower panels). Aptamer concentration during incubation with NIH 3T3 and MIA PaCa-2 cells was 1 and 3 µM respectively. (a) Significant vesicular signals could be observed into cell cytoplasm after incubation in mouse cells with labeled GS24min. In contrast weak spotty cytoplasmic signals were detected into human cells after incubation of GS24min. Scale bars: 10 µm. (b) Intracellular fate of the truncated aptamer sequence (GS24min) in mouse fibroblasts (NIH 3T3). Partial colocalization between GS24min-ATTO 633 (red) and lysosomes (Lysotracker green) was observed 120 minutes after administration. Colocalized vesicles were mainly found close to the perinuclear region. Scale bar: 5 µm.

Thereby, to increase A-2F stability and minimize the presence of misfolded structures, we moved to a more conservative approach based on point mutations performed on the basis of secondary structure predictions and molecular modeling approaches (Fig. 15). In details, we turned our attention to the folded domain comprising bases 26-50 in order to enhance its stability and shift the thermodynamic equilibrium towards the most stable and active fold (A-2F). Molecular dynamic simulation depicted in Fig. 15a led to the identification of two critical base pairs: T29-T47 (which, in our simulations, showed a non-canonical base-pairing), and A30-T46. These two base pairs (highlighted in Fig. 15) were selected as sites critically involved in the stabilization of the folded domain comprising bases 26-50, destabilizing at the same time the inactive conformer (Fig. 14b).

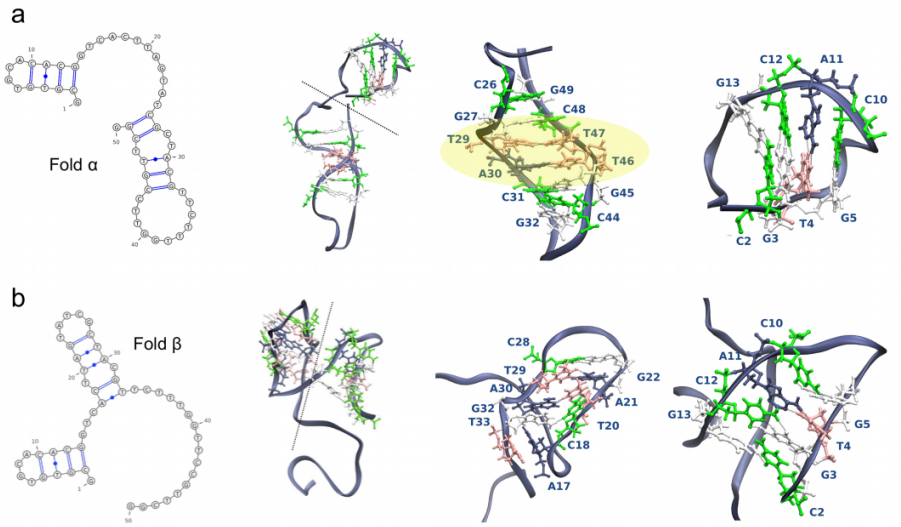

Fig, 15 Mfold predictions of the two A-1F (fold β) and A-2F (fold α) conformers and corresponding structures from MD simulations. From left to right, secondary-structure diagrams, structure of representative conformation (centroid of the most populated cluster), magnification of the domains. A dashed line in the complete 3D structure separates the two domains. (Figure based on data generated by P. Mereghetti).

Most importantly, mutations at these sites did not change the conserved nonamer sequence in the stem-loop region. Thus, we designed four mutants: T29A; T29G T47C; A30G T46C; T29G A30G T46C T47C; hereafter called DW1, DW2, DW3 and DW4, respectively. These mutants were chosen as candidates capable of stabilizing the active fold by either transforming a non-canonical pairing into a more stable Watson-Crick coupling, or strengthening an A-T base pair by mutation into a stronger G-C.

To identify the best mutant sequence several parameters were took in consideration:

- Calculation of the predicted ΔΔG between the two lowest-energy structures.
- HPLC analysis in native conditions to quantify the percentage of the inactive fold.
- *In vitr*o binding affinity towards the mouse recombinant TfR.
- Cell-internalization properties in living mouse cells.

Table 1 summarizes all parameters for each mutant sequence. Notably, all mutants displayed an increased difference in the ΔΔG of the two conformers as calculated by MFold. The percentage of the inactive fold for each structure was investigated by HPLC analysis both at 25ºC and at physiological temperature, 37ºC. Interestingly, percentage of the active fold is higher in all mutants, compared with the parent structure GS24. In two cases (DW2 and 4), the percentage of the inactive fold was nearly identical to that attained for A-2F after the HPLC purification of GS24 (3%). It is worth noting that both DW2 and DW4 showed limited amount of the secondary conformer even at 37°C (≤ 10%).

As expected, percentage of inactive fold was unaffected by insertion of a fluorophore (ATTO 633) at 5' end of the sequences, confirming that this small fluorescent tag did not alter the aptamer conformation and the ratio between the two folds.

TABLE 1: Fold molar ratio and anisotropy change comparison of GS24 mutants

Structure	*Predicted* $\Delta\Delta G^a$ *(25°C)*	*% inactive 25°C*	*% inactive 37°C*	*Anisotropy change* $(x10^{-3})^b$
GS24	-1.53	19.8%	31.3%	13.3
DW1 (T29A)	-2.01	9.9%	14.6%	13.9
DW2 (T29G T47C)	-3.21	4.6%	10.2%	14.5
DW3 (A30G T46C)	-3.64	9.9%	17.6%	14.3
DW4 (T29G A30G T46C T47C)	-3.64	5.3%	8.5%	15.9
GS24min	-	-	-	8.4
A-1F[c]	-	55%	-	8.5
A-2F[c]	-	3%	-	16.4

[a] ΔΔG were calculated from the folding ΔG of α and β conformers as ΔΔG=ΔGα-ΔGβ: [b]All values were obtained as the average of two or more independent measurements, with errors (SD) in the range 0.5-0.9; [c]Freshly purified; partial equilibration occurred within 1-2 hours

Then, we assessed the *in vitro* binding affinity of all mutants towards mTfR by FA measurements. As rapid screening of the aptamer binding property, we evaluated the anisotropy change at a single protein concentration (600nM) by using the same protocol adopted in the case of the purified folds. As shown in table 1, all mutations showed increased binding efficiency compared with GS24. This result is consistent with the increased percentage of the active fold exhibited by each mutant. Moreover, all fluorescently labeled aptamer mutants were also able to internalize in living mouse fibroblasts (NIH 3T3), demonstrating that our mutations did not affect the capability to bind mouse receptor in its native form. Interestingly, for each mutant we observed a slightly enhanced intracellular fluorescence signal when compared with the parent aptamer sequence (GS24) but no significant difference in internalization kinetics or efficiency, compared with the active fold (A-2F).

At the end of this screening, DW4 was identified as the most promising sequence in terms of thermodynamic stability and *in vitro* binding capability. Thus, a further investigation of its properties was performed, firstly building an

anisotropy titration curve to calculate the in vitro dissociation constant towards mTfR (Fig. 16a). In details, our results yielded Kd = 0.19 ± 0.01 μM, 25% lower than the value found with GS24 (0.25 ± 0.4 μM), in keeping with the lower amount of inactive fold in DW4 sample. Notably, although this value is somewhat higher than the calculated value for pure A-2F (0.13 ± 0.03 μM), one must consider that the present mutant outperforms the purified fold in terms of thermal stability, ease of manipulation, and overall potential for *in vitro* and *in vivo* use.

Finally, we investigated whether DW4 retains cell-internalization property also in human pancreatic tumor cells. Importantly, not only this mutant sequence was internalized also in MIA PaCa-2 cells in the same experimental conditions used for A-2F, but it showed a faster uptake rate compared with A-2F. Indeed, intense vesicular signal was already present immediately after 25-minutes incubation while only weak plasma membrane staining was detected (Fig. 16b). Note that, Fig. 16b highlights similar endocytic pattern for DW4 in both mouse and human cell lines.

To investigate the nature of this enhanced uptake in human cells, we evaluated the in vitro binding property of DW4 towards hTfR at a single protein concentration (600nM). A comparison of the measured fluorescence anisotropy enhancements detected for GS24, A-1F, A-2F and DW4 is shown in Fig. 16c. Interestingly, we found that DW4 has a higher anisotropy change compared with A-2F (11.8 ± 0.6 and 9.2 ± 0.4 respectively). This result is consistent with the faster endocytosis kinetics exhibited by DW4 towards human cells.

It is worth noting that a differential rate of TfR internalization in living cells has been recently observed upon treatment with anti-TfR antibodies having different affinity. In particular, high-affinity anti-TfR (Kd= 20 nM) induced a higher uptake, over the first 20 min after antibody addition, compared with low-affinity antibodies (Kd= 600 nM)[236]. This interesting analogy between the differential antibody endocytosis and our findings on DW4 and A-2F, lays the foundations for further experiments needed to clarify the different aptamer behavior in human cells.

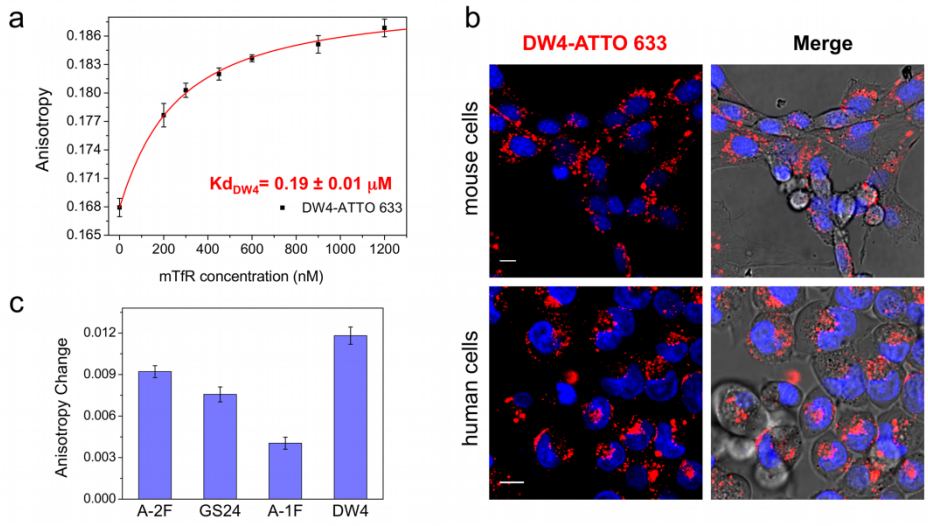

Fig. 16 (a) Fluorescence anisotropy assay. FA of DW4-ATTO 633 (50 nM) was measured with increased amount of mTfR (0-1200 nM) at 25°C. The aptamer titration curve was obtained by fitting the anisotropy values as a function of mTfR concentration. The fit afforded both K_d and A_B (anisotropy in saturating condition). (b) Endocytosis of GS24min and DW4 in mouse fibroblasts (NIH 3T3, upper panels) and in human pancreatic tumor cells (MIA PaCa-2, lower panels). DW4 shows efficient internalization both in mouse and human cells. Scale bars: 10 µm. (c) Binding efficiency of the two folds, GS24 and the mutant DW4 was measured at [hTfR]=600 nM. In this case the anisotropy change is defined as the difference between aptamer anisotropy in presence and in absence of the human receptor.

It is worth noting that the rational mutations present on DW4 increase significantly the capability of this sequence to bind the hTfR. Indeed DW4 shows improved binding properties compared with A-2F towards the human receptor. On the other hand, DW4 and A-2F can bind mTfR with similar binding affinities. This outcome is really interesting and might be exploited to set up a second SELEX experiment exploiting a doped-library to obtain a novel sequence able to bind both mouse and human receptor with similar high affinity. Indeed, starting from DW4 sequence, the positions involved in the folding stability might be

randomized and a doped-SELEX[130] experiment could be performed for few rounds using the human recombinant TfR as biomolecular target. This approach might lead to novel aptamer sequences able to bind efficiently both mouse and human TfR.

3.5 Concluding remarks

In this chapter, I described a rational engineering strategy to generate a novel aptamer sequence with enhanced binding property towards mouse transferrin receptor. In details, starting from the observation that an anti-mTfR aptamer (GS24) is actually a mixture of two interconvertible folds (A-1F and A-2F), we investigated how their presence affects the biological activity of GS24. The presence of two folds might be rationalized by considering the SELEX strategy that led to GS24 selection, which did include only *in vitro* binding assays at 25°C to evaluate aptamer affinity for the receptor. This strategy does not provide significant selection pressure to identify the best ligands, but only provides information regarding the average activity of a given mixture of conformers, but is intrinsically unable to report on the presence -and hence the activity- of different conformers sharing the same primary structure.

Thanks to fluorescence anisotropy measurements and cell internalization assays, we found that only one of these folds (A-2F) recognizes its target and internalizes in living cells. This observation suggests that the main conformational difference between the two folds occurs in a region critically involved in binding to mTfR. The results obtained with the engineering of GS24, and in particular those related to the minimization process and the point mutations strategy, confirm this hypothesis.

Our engineering of GS24 led to a novel sequence (DW4), which shows enhanced activity compared to the parent molecule. Thermal dependence of molar ratio showed that with this sequence the inactive fold is less than 10% both at 25°C and 37°C. Furthermore, this sequence is also able to bind the hTfR, although with a lower affinity when compared with the natural target, i.e. mTfR.

This novel sequence, DW4 can be used in combination with anti-hTfR aptamer, c2.min to target both mouse and human TfR in targeted drug delivery applications

using different models (such as allograft and xenograft tumor models). Indeed, it is extremely important possess targeting aptamers with cross-reactivity to test them in different physiopathological contexts in order to evaluate the effective potential of a drug delivery platform for targeted therapy.

Based on this observation, in the next chapter, I shall describe an application of this modular plug-and-play engineering using both DW4 and c2.min as targeting ligands embedded in a more complex oligonucleotide nanostructure.

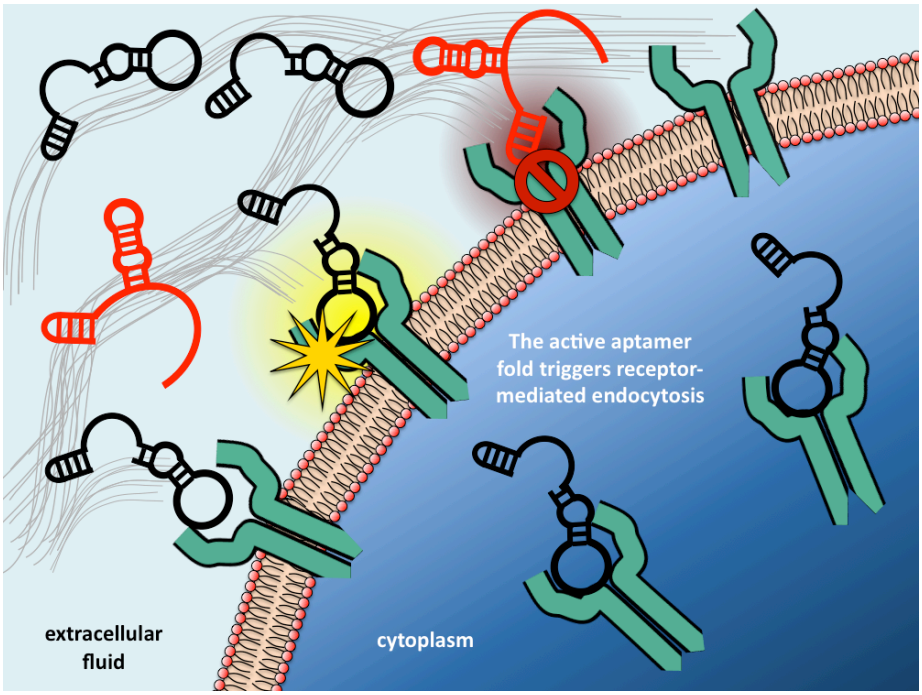

Fig. 17. DNA aptamer GS24 activity modulated by two conformers with different binding properties.

3.6 MATERIALS AND METHODS

3.6.1 Materials

All chemicals were purchased from Sigma Aldrich unless otherwise specified, and were used as received. Human pancreatic carcinoma cells (MIA PaCA-2), human cervical cancer cells (HeLa) and mouse embryonic fibroblast cells (NIH-3T3) were purchased from the American Type Culture Collection (ATCC). All cell lines were growth using the same protocol reported in the experimental section of Chapter 2. Recombinant mouse and human transferrin receptor (TFRC/CD71) were purchased from Sino Biological Inc. (Beijing, China). Proteins were dissolved in 20 mM HEPES with 1mM EDTA (pH 7.4). Transferrin-Alexa Fluor 488 conjugate, monoclonal antibody anti-human CD71-FITC conjugate (clone T56/14), Lysotracker green and Hoechst dye were purchased from Invitrogen. All oligonucleotides were purchased from Integrated DNA Technologies (IDT, Coralville, IA, USA) and HPLC purified. Synthetic aptamer samples were dissolved in DNase free water and stored at -20°C. The concentration of oligonucleotides was measured by UV spectrophotometry at 25°C using a JASCO V550 spectrophotometer (JASCO Europe, Cremello, Italy). All sequences contained a 5'amino group attached by a C-6 alkyl chain.

The sequence of full-length DNA aptamer (GS24) was the following:

5'-GCGTGTGCACACGGTCACTTAGTATCGCTACGTTCTTTGGTTCCGTTCGG-3'

The minimal sequence of GS24 aptamer (GS24min) was the following:

5'-CACTTAGTATCGCTACGTTCTTTGGTTCCGTTCGG-3'

The mutant sequences of GS24 were the following.

DW1 (T29A):

5'-GCGTGTGCACACGGTCACTTAGTATCGCAACGTTCTTTGGTTCCGTTCGG-3'

DW2 (T29G T47C):

5'-GCGTGTGCACACGGTCACTTAGTATCGCGACGTTCTTTGGTTCCGTCC GG-3'
DW3 (A30G T46C):
5'-GCGTGTGCACACGGTCACTTAGTATCGCTGCGTTCTTTGGTTCCGCTC GG-3'
DW4 (T29G A30G T46C T47C):
5'-GCGTGTGCACACGGTCACTTAGTATCGCGGCGTTCTTTGGTTCCGCCC GG-3'
The scrambled sequence of DNA aptamer (GS24mt) was the following:
5'-GCCATTGCCATTGCCATTGCCATTGCCATTGCCATTGCCATTGCCATT GCCATTG-3'

3.6.2 Chromatographic analyses, and purification of labeled folds

All HPLC analyses were performed using the HPLC equipment described in the experimental section of Chapter 2. Analytical analysis of oligonucleotide samples and purification of labeled GS24 aptamer folds (labeled A-1F and A-2F) GS24min and DW1, DW2, DW3, DW4 aptamer mutants were performed with an IE-HPLC on a Clarity® 10 µm Oligo-WAX, LC Column 100 x 4.6 mm (Phenomenex) at 2.2 ml/min, using Tris HCl 20mM pH 8.0, ACN 10% (Eluent A), and NaCl 1.2 M, Tris HCl 20 mM pH 8.0, ACN 10% (Eluent B) as mobile phase. Chloride gradient was 0.36-1.2 M NaCl during 15 minutes. Native conditions analysis was performed at 25°C. Analyses in denaturing condition were performed at 80°C. In this experiment aptamer samples were heated in a thermoblock at 95°C for 5 minutes, and then analyzed by IE-HPLC. Absorbance was measured between 200 and 650 nm.

The amino residue at 5'-end of oligonucleotide sequences (GS24, GS24mt, truncated and mutants GS24) was conjugated to the ATTO 633 NHS fluorophore by means of standard NHS coupling procedures between the primary amine of aptamer and NHS-derivative of the fluorophore as described in Chapter 2.

Purification of the labeled folds was performed as follows: the folds were separated by means of IE-HPLC, and collected. Each fold was then rapidly desalted on illustra™ NAP-25 Columns containing Sephadex G-25 DNA grade

(GE/Healthcare) equilibrated with DNase free water. The collected fractions were freeze-dried, resuspended in appropriate volume of DNase free water and stored at -20°C. The whole process, from separation to freeze-drying, usually lasted less than 30 minutes. Finally, an aliquot of each sample was quantified by UV-VIS analysis and analyzed in IE-HPLC to check the purity of each fold.

Dye-to-aptamer fold ratio was evaluated from absorbance measured at 260 and 633 nm and was 1 within experimental error.

3.6.3 Fluorescence anisotropy assay

Fluorescence intensity and anisotropy measurements were carried out with a Cary Eclipse fluorometer (Varian, Palo Alto, CA). Excitation was set at 630 nm and emission at 650 nm. Slits for both excitation and emission were set at 10 nm. A 100 µl quartz cuvette (Hellma, Milan, Italy) was used in all experiments. The G factor, i.e. the ratio of I_{HV} to I_{HH}, where I_{HV} and I_{HH} are the observed intensities at horizontal or vertical orientations of the polarizers, was determined before the first experiment and this value was used throughout the experiments in which instrumental factors (emission wavelength and spectral bandpass) were kept constant.

During fluorescence-anisotropy measurements, a highly concentrated (~15 µM) solution of mouse and human TfR was used for each titration to minimize dilution effects (final volume after titration was 1.15 times the initial volume). Equilibrium binding isotherms were constructed by titrating 50 nM of aptamer-ATTO 633 probe (labeled GS24, GS24min and DW4) with increasing concentration of TfR in PBSM buffer (PBS containing 1 mM $MgCl_2$) at 25°C. The anisotropy value was automatically calculated by the instrument. The integration time was set to 1.0 s for each anisotropy measurement, while the acquisition time for each protein concentration was 30 minutes for mouse TfR and 60 minutes for human protein. The average anisotropy-value used for data processing was calculated on at least 40 data points for each protein concentration. Equilibrium binding isotherms were evaluated also for the labeled GS24, A-1F, DW1, DW2, DW3, DW4 at [mTfR]=600 nM and for A-2F at 600 nM and 1300 nM.

Data represent the average of two or more independent experiments. Error bars represent the SD from two or more independent experiments.

3.6.4 Fluorescence Anisotropy Data Analysis

The aptamer fraction bound (f_B) is related to the measured anisotropy by:

$$f_B = \frac{A - A_F}{A - A_F + q(A_B - A_F)}, \quad (1)$$

where A, A_F, and A_B are the anisotropies of the sample, free aptamer, and aptamer saturated with protein, respectively. The factor q takes into account fluorescence quantum yield changes upon binding[237] and is given by:

$$q = \frac{(I_{VV} + 2I_{HV})_{bound}}{(I_{VV} + 2I_{HV})_{free}}, \quad (2)$$

where I_{VV} and I_{HV} are the observed intensities at different orientations of the polarizers as described earlier. The value of q was 0.89 for GS24 and 0.82 both for minimal GS24 and DW4. Binding was assumed to be described by a 1:1 binding model: L + P → LP where L, P, and LP are free aptamer, TfR, and aptamer/TfR complex, respectively. The aptamer fraction bound (f_B) is given by:

$$f_B = \frac{(L_T + P_T + K_d) - \sqrt{(L_T + P_T + K_d)^2 - 4L_T P_T}}{2L_T} \quad (3)$$

where L_T and P_T are the total aptamer and TfR concentrations, respectively.

Frequently, the aptamer anisotropy in saturating condition (A_B) cannot be measured directly. In order to avoid the self-consistent evaluation of A_B we preferred to fit directly the anisotropy A as a function of TfR concentration. This fit directly gave both K_d and A_B, and was performed using the following expression:

$$A = A_F + qA_F(A_B - A_F)\frac{1}{f_B^{-1} - (1-q)}, \quad (4)$$

where f_B is taken from Eq. 3. This procedure yielded both a better estimate of A_B and its error. Using the experimentally determined values of A, A_F, and q, the anisotropy data were fitted by nonlinear least squares regression to Eq. 4 with both K_d and A_B as parameters using Origin Pro 8S0 (One Roundhouse Plaza Northampton MA 01060 USA).

3.6.5 Secondary and tertiary structure generation

Secondary structure prediction was obtained using the webserver Mfold[212] with the default settings. Using these parameters the two lowest free-energy structures were retained. The Mfold generated secondary structures were used to obtain two coarse three-dimensional structures using the software RNA2D3D[238].

3.6.6 Simulated annealing

We performed a simulated annealing scheme imposing Watson and Crick hydrogen bond constraints to refine the two folds obtained with RNA2D3D.

Simulated annealing were performed using AMBER software version 12[239]. The AMBER forcefield ff12SB was used. Each fold was solvated in a dodecahedral box of minimum 0.8 nm distance from the aptamer using TIP3P water model. Sodium and Chloride ions were added to reach an ionic strength of 150 mM reproducing the experimental environment. The solvent was minimized using 1000 steepest-descent steps keeping the nucleic acid structure restrained. Then, the full system was minimized by 500 conjugate-gradient steps. The minimized structure was subjected to a simulated annealing procedure in the NVT ensemble. The temperature was first raised to 600 K and slowly decreased to 300 K in 50 ns. Temperature was kept constant using Langevin dynamics with the collision frequency parameter set to 2 ps^{-1}, The SHAKE algorithm was used to constraint bonds length, allowing to use a 2 fs integration time step. Van der Waals and Coulomb interactions were truncated at 0.8 nm. Long range electrostatic interactions where calculated using the Particle-mesh Ewald (PME) summations

scheme. Distance restraints were applied on the Watson and Crick hydrogen bonds (using AMBER parameters nmropt = 1 and ipnlty = 1).

3.6.7 Molecular dynamics simulations

We assessed the stability of two folds given as output from simulated annealing procedure by performing NPT molecular dynamics (MD) simulations without hydrogen bond distance restraints. The same parameters described for the simulated annealing were used here with the addition of the pressure coupling. Pressure was kept constant at 1.013 bar using a relaxation time of 1.0 ps. To improve conformational sampling, ten 10 ns simulations were carried out starting from different initial velocities. The ten trajectories were then combined into a single trajectory, which was used for all subsequent analysis.

Hierarchical cluster analysis was performed using the average linkage criteria[240]. The root mean squared deviation between the backbone atoms was used as distance metric.

3.6.8 Electrostatic properties

Effective net charge was obtained by computing the electrostatic potential of 100 conformations within each cluster solving the non-linear Poisson-Boltzmann equation using the UHBD software[241]. Each electrostatic potential was radially averaged and then averaged over the ensemble of 100 conformations. The Debye-Hückel potential was fitted on the average monodimensional electrostatic potential leaving the total charge (z) as free parameter.

According to the Debye-Hückel theory of dilute electrolyte solutions, all ions in the solvent are treated as point charges while each macromolecule is treated as a sphere with diameter a (the radius of gyration was used) and net charge z. The electrostatic potential is given by:

$$V(r) = \frac{z^2 e^2 \exp^{-\kappa(r-a)}}{4\pi\varepsilon_0\varepsilon_r(1+\kappa a)}, \qquad (5)$$

where *e* is the elementary charge, *r* is the distance form the center, ε_0 is the vacuum permittivity, ε_r is the relative permittivity of the solvent and κ is the inverse of the Debye length and is proportional to the ionic strength.

3.6.9 Endocytosis assays in living cells

In a typical endocytosis assay in mouse fibroblasts, NIH-3T3 cells were seeded 24 h before the experiment in WillCo dishes to reach 80-90% confluence. Standard conditions for incubation consisted in 25-min incubation at 37°C, 5% CO_2 in DMEM containing 1% BSA, 0.2 mg/ml calf thymus DNA, 5 µg/ml of Hoechst dye and 1 µM of aptamer-ATTO 633 probe (labeled A-1F, A-2F, GS24 mt, GS24min, DW1, DW2, DW3 and DW4) in a total volume of 500 µl. After incubation, cells were washed three times with PBS, fresh serum-containing medium was added and the sample was imaged by confocal microscopy. All experiments were performed in triplicate. Cells were imaged using the same microscopy setup described in Chapter 2.

Colocalization experiments in mouse fibroblasts were performed as follows: NIH-3T3 cells were coincubated for 25 min at 37°C with aptamer-ATTO 633 probe (either A-2F or GS24min) and Lysotracker green to a final concentration of 1 µM and 70 nM, respectively. After incubation, the sample was washed three times with PBS, fresh serum-containing medium was added and the sample was imaged by confocal microscopy.

To verify that aptamer endocytosis was an active, receptor-mediated process, NIH-3T3 cells were left 12 h before the experiment in DMEM with 2% serum. Cells were then kept on ice for 15 min, and incubated for 25 min on ice with 1 µM of A-2F-ATTO 633. After incubation, cells were washed with cold PBS and fresh serum-containing medium (10% serum) pre-heated at 37°C was added. Real-time monitoring of endocytosis was performed by confocal microscopy.

In internalization assays in human pancreatic carcinoma cells, MIA-PaCa-2 cells were seeded 24 h before experiment in WillCo dishes to reach 80-90% confluence. Six hours before each experiment the complete growth medium was replaced with a 2% serum-containing medium. At time of assay, cells were incubated for 25 min with a medium composed of DMEM containing 1% BSA,

0.2 mg/ml calf thymus DNA, 5 μg/ml of Hoechst dye and 3 μM of aptamer-ATTO 633 probe (A-2F, GS24mt, GS24min and DW4) in a total volume of 500 μl. After incubation, cells were washed three times with PBS then fresh 10% serum-containing medium was added and the sample was imaged by confocal microscopy.

Colocalization experiments in human tumor cells were performed as follows:

MIA PaCa-2 cells, growth in WillCo dishes, were coincubated for 30 min at 37°C with A-2F-ATTO 633 (3 μM) and monoclonal antibody anti-CD71-FITC conjugate following manufacturer's protocol with minor modification (1:250 diluition, Invitrogen). At the end of incubation, the cells were washed with PBS and fresh 10% serum-containing medium was added. Cells were incubated at 37°C for further 30 min and then fixed with 4% paraformaldehyde and 4% sucrose in PBS for 20 min. Fixed cells were washed with PBS and the sample was imaged by confocal microscopy. All experiments were performed in triplicate. Pearson’s coefficient was calculated by using the JaCoP ImageJ plugin.

Chapter 4

Aptamer-mediated delivery of large functional RNA

The work in this chapter was carried out in collaboration with Dr. Donald H. Burke and Khalid K. Alam at the University of Missouri - Columbia. It is anticipated that it will be submitted for peer-reviewed publication in modified form. DH Burke designed the study. D. Porciani and DH Burke designed the aptamer-aptamer complex and analyzed the data. D. Porciani and K. K. Alam performed the electrophoretic mobility shift assay and synthesized all RNA sequences. Unless otherwise specified, experiments and data shown in each figure were performed and analyzed by D Porciani.

As stated in the first chapter, cell-type-specific aptamers have been used to deliver a variety of molecular payloads, such as small drugs and small interfering RNAs. Therapeutic aptamers, larger RNAs, such as long non-coding RNA (lncRNA), messenger RNA (mRNA) and engineered RNA nanostructures, offer tremendous potential as therapeutic and regulatory agents. Unfortunately, their aptamer-mediated delivery into cells has not yet been demonstrated. A critical point of this strategy is to design assemblies in which the structured oligonucleotide modules retain their proper folding with no unwanted inter- and intra-molecular interactions. First, the aptamer motif should retain its folded structure to interact with its biomolecular target and perform an aptamer-mediated

targeted delivery. Additionally, the released payload should assume its correct 3D structure to exhibit the therapeutic effect (e.g. binding and inhibition of cancer-associated protein). Thus, testing the potential of several designs and monitoring both folding properties and the effective cargo delivery into targeted cells might be a very time-consuming process.

To address these limitations, we took inspiration from the design used to generate aptamer-siRNA conjugates as starting point for further rational engineering. In addition, the use of fluorescent RNA aptamers as payloads may greatly accelerate the testing of various designs. The benefit is twofold: their successful delivery into targeted cells is readily detected by fluorescence microscopy, and this fluorescence readout is sensitive to structural variations, highlighting potential perturbations of the aptamer folding.

Fluorescent RNA aptamers are RNA mimics of the green fluorescent protein, in that they are able to bind small molecules structurally similar to the GFP chromophore[242]. These molecules are poorly fluorescent in solution but become highly fluorescent within the folded protein or upon formation of a complex with the aptamer. This property is also perfectly suited to the SELEX approach, which indeed has been used to identify nucleic acid sequences able to activate their fluorescence. Among the selected aptamers, one can cite the brightest sequence, termed “Spinach”, which binds an analogous of GFP chromophore, (Z)-4-(3,5-difluoro-4-hydroxybenzylidene)-1,2-dimethyl-1H-imidazol- 5(4H)-one (DFHBI), affording a green-emitting complex[242,243]. Free DFHBI exhibits low background fluorescence in cells, thus fluorescence signals are readily attributable to Spinach−DFHBI complexes (Fig. 1). Although Spinach aptamer has been used as a fluorescent reporter of native RNA trafficking (Fig. 1)[242,244], it can be used also as payload to track its fluorescence signal during endocytosis, and to evaluate folding alterations within the oligonucleotide platform.

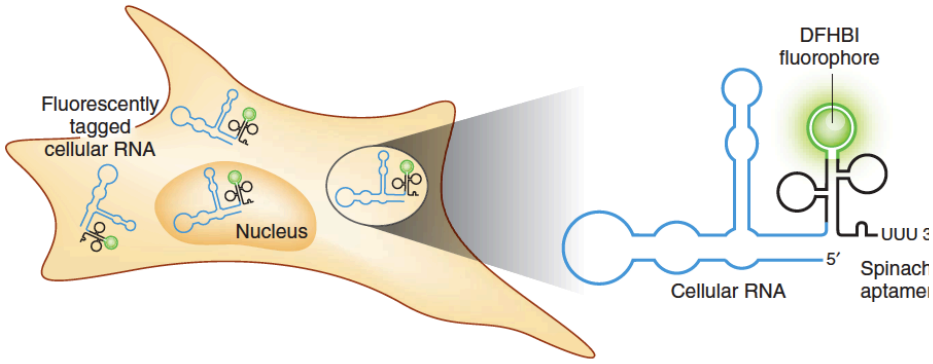

Fig. 1 Detection of RNA localization and dynamics by fluorescent RNA aptamers. The sequence encoding the cellular RNA of interest is fused to the Spinach aptamer and transcribed by its natural promoter or an artificial promoter. The aptamer binds the cell-permeable fluorophore DFHBI. Binding leads to green fluorescence, allowing the RNA of interest to be visualized and its movement tracked in live cells. Adapted from Mattick and Clark.[245] Reprinted by permission from Macmillan Publishers Ltd: Nature Biotechnology (Ref. 240), Copyright © 2011

Starting from the Spinach-DFHBI system, novel enhanced RNA mimics GFP such as Spinach2 and Broccoli, together with and an improved GFP-like fluorophore (DFHBI-1T) were recently generated[246–248]. These new generations of fluorescent RNA aptamers were selected to overcome some intrinsic limitations linked to the poor intracellular folding shown by Spinach. Jaffrey and coworkers used a systematic mutagenesis to generate an enhanced RNA aptamer, named Spinach2, which shows higher thermal stability and greater fraction of properly folded aptamer than the parent sequence[246]. In addition, Spinach2 was fused to the tRNA sequence, which acts as folding scaffold[249], further increasing the percentage of properly structured Spinach2[246].

In 2014, two parallel studies revealed that the crucial part of Spinach involved into binding of DFHBI folds in a G-quadruplex structure[243,250]. In particular, the Spinach G-quadruplex motif and its adjacent nucleotides stabilize the planar conformation of the DFHBI fluorophore and restrict its rotational motion,

inhibiting non-radiative decay and enhancing fluorescence quantum yield. The interactions between DFHBI and the nucleotide residues of the G-quadruplex are mainly based on π-π aromatic stacking and hydrogen bonds. Starting from these findings, the authors generated a minimal aptamer sequence, termed Baby Spinach, which retains the same properties of its parent sequence[243].

The structures of the two GFP-like fluorophores recognized by the Spinach aptamer's family are shown In Fig. 2a, and the secondary structures of Spinach and its sequence variants based on crystallographic and NMR analyses are shown in Fig. 2b.

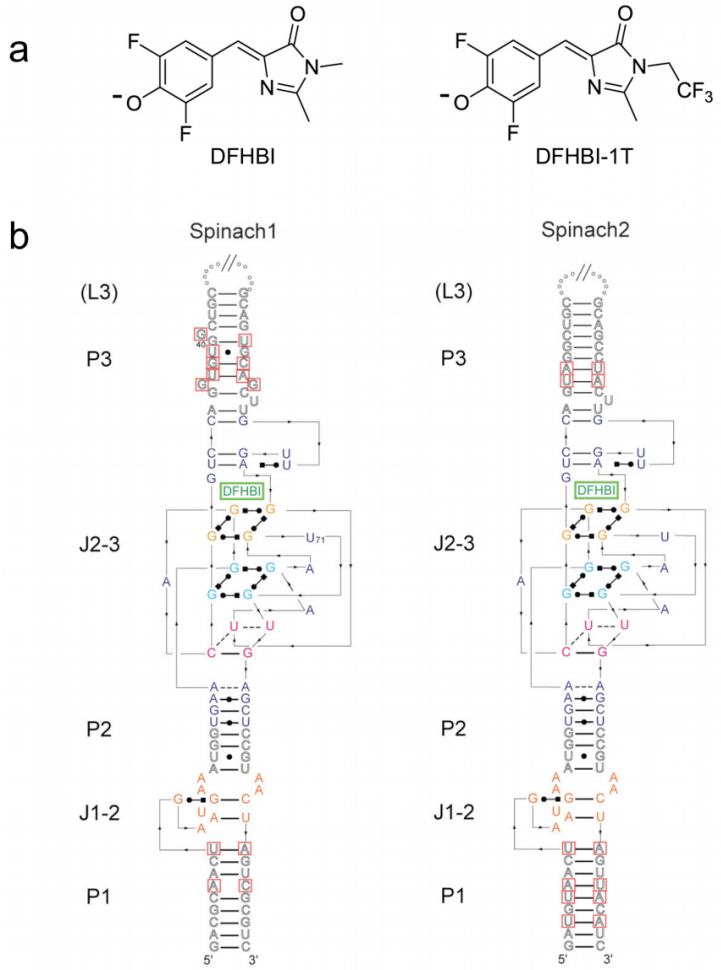

Fig. 2 (a) GFP-like fluorophore structures (DFHBI and DFHBI-1T) designed on the basis of the GFP chromophore (HBI). (b) Secondary structure of Spinach and its sequence variant, Spinach2, based on the crystal structure of the Spinach-DFHBI complex. Abbreviations: DFHBI, (Z)-4-(3,5-difluoro-4-hydroxybenzylidene)-1,2-dimethyl-1H-imidazol-5(4H)-one. DFHBI-1T is the 1,1,1-trifluoroethyl derivative of DFHBI. DFHBI-1T [(Z)-4-(3,5-difluoro-4-hydroxybenzylidene)-2-methyl-1-(2,2,2-trifluoroethyl)-1H-imidazol-5(4H)-one)]. Reprinted by permission from Macmillan Publishers Ltd: Nat. Struct. Mol. Biol (Ref. 238), Copyright © 2014

Notably, a further improved RNA aptamer, named Broccoli, was generated at the end of 2014 by using a SELEX–FACS approach[248]. Broccoli aptamer has the same high folding efficiency *in vitro* as Spinach2, but exhibits markedly lower dependence on magnesium for folding and increased thermal stability, leading to enhanced brightness in living cells.

In this chapter, I shall report on the design and synthesis of a modular plug-and-play platform for the aptamer-mediated cellular delivery of increasingly large RNA payloads (~50-60 kDa). In details, anti-transferrin receptor aptamers described in the first chapters (c2 and DW4) were used as cell-penetrating aptamers ("delivery modules") and were annealed via a short oligonucleotide bridge to fluorescent RNA aptamers ("payload modules"). In addition to c2 and DW4, we also used a novel cell penetrating RNA aptamer, termed Waz, which binds the human transferrin receptor in a different binding site than the natural ligand. This sequence was kindly provided by Levy group and it is currently under a restrictive patent (N° WO 2013163303 A2).

The modular design of this assembly should allow swapping in virtually any targeting aptamer and any regulatory cargo, making this experimental platform quite powerful and flexible for a broad range of applications.

4.1 Design and synthesis of a plug-and-play platform for targeted delivery

To generate a self-assembling aptamer-aptamer complex, we took inspiration from the aptacoy design already described in chapter 2. In this design, the delivery aptamer bears an extended sequence (tail) at the 3'-end that forms a duplex region upon hybridization with its complementary sequence (anti-tail). In turn, this anti-tail part is directly conjugated with the molecular payload, i.e. decoy ODN. Starting from this design, we decided to exploit the same tail $(CGA)_7$ at the 3'-end of the delivery aptamers and to design a novel extended sequence $(GAT)_7$ for the payload module. As shown schematically in Fig. 3, the final platform is generated through self-assembly by means of a synthetic oligodeoxynucleotide bridge (ODN bridge) that contains regions complementary to both tails. Delivery aptamer

carries a tail GC-rich, and payload aptamer bears a tail AT-rich. These oligonucleotide tails do not interact with each other, thereby limiting undesired intermolecular interactions and impaired self-assembly.

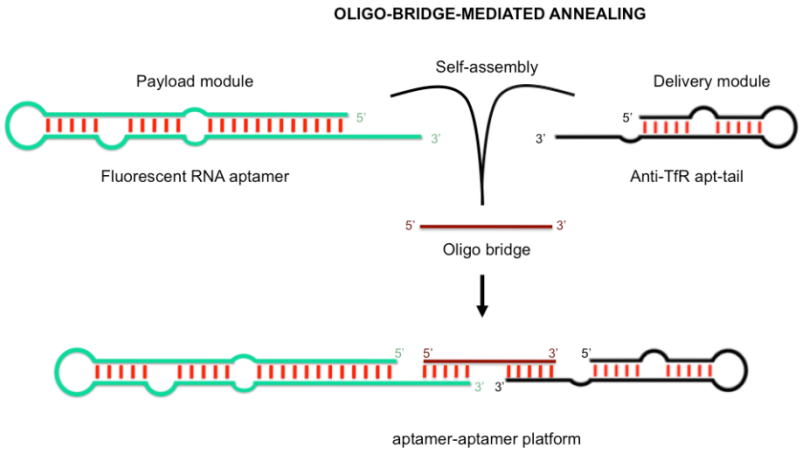

Fig. 3 Self-assembly of the aptamer-aptamer platform. Proposed design for our plug-and-play platform, which exploits the nucleic acid annealing between the bridge and the two aptamer modules.

Secondary structure predictions were performed using NUPACK tool[175] to assess the potential for correct hybridization of each module, to identify some potential misfolding structures and consequently to monitor whether each aptamer still retain its proper folding within the platform. As shown in Fig. 4, computational results suggest that after hybridization with Spinach2 both DW4 and c2 do not affect Spinach folding, but retain their predicted minimum free energy secondary structure. Note that in all our evaluation Spinach2 was fused to the tRNA sequence to increase its folding property[246]. Hereafter, I refer to the Spinach2-tRNA as Spinach2, unless the tRNA form is specifically indicated.

It is worth mentioning that, the Spinach2 region is not accurately reproduced in the secondary structure prediction of the whole complex (Fig. 4), as expected owing to the presence of G-quadruplex motif and several non-canonical base

parings, which make the structure very difficult to predict by basic computational approaches such as NUPACK. Indeed, as mentioned before, the correct structure of Spinach2 was resolved only after crystallographic and NMR studies, and is reported in Fig. 2. However, the secondary structure of the tRNA domain is correctly predicted (Fig. 4) pointing to a reliable conformation also for the annealing region.

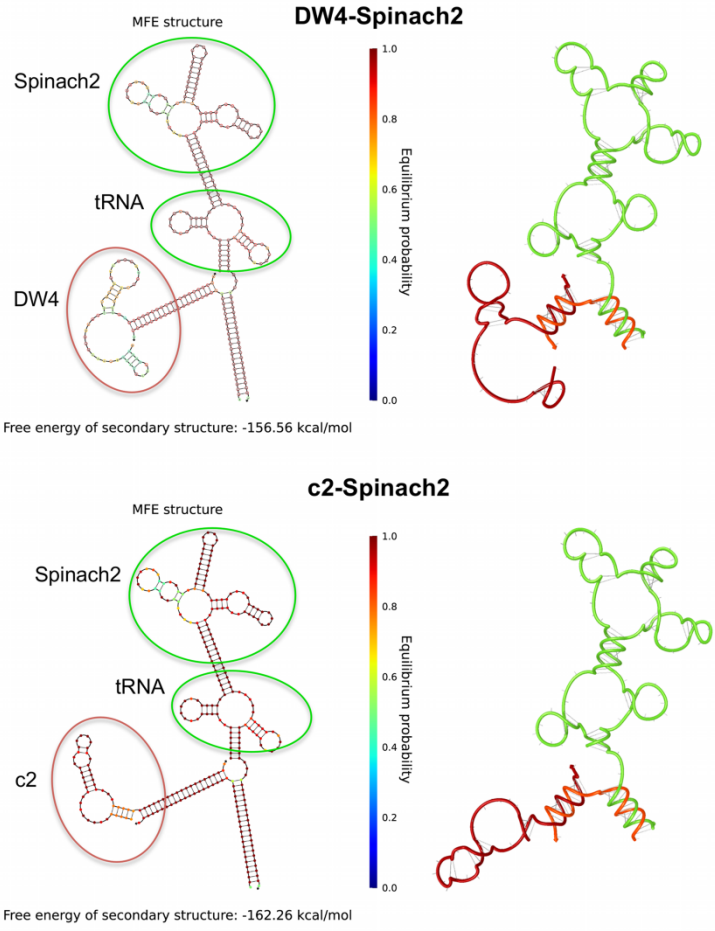

Fig. 4 Secondary structure predictions of DW4-Spinach2 and c2-Spinach2 complexes. On the left secondary structures predictions after hybridization simulation of

DW4/c2, Spinach2 and oligo bridge by NUPACK calculation. On the right depiction of the helicity of the hybridized oligo complexes. Color legend. Green: Spinach2. Dark red: delivery aptamers (DW4 and c2). Light red: bridge

It is worth noting that secondary structure predictions offer a good starting point to elucidate some potential misfolding limitations. However, only experimental analyses may provide a deep understanding of the folding properties related to structured nucleic acids as well as any other folded biomolecule.

4.1.1 Assembly of aptamer-aptamer complexes: annealing reaction with equimolar concentration of aptamer modules and excess of bridge

Formation of self-assembled ternary oligonucleotide complexes (i.e. payload aptamer-bridge-delivery aptamer) was assessed by electrophoretic mobility shift assay (EMSA). Maximum efficacy in terms of hybridization yields critically depends on several important parameters during the hybridization phase.

Particularly, the molar ratio of the oligonucleotides in the mixture plays an important role to avoid the presence of residual unreacted oligonucleotides. Indeed, the presence of free payload aptamer could affect the fluorescence microscopy analysis in living cells. Thereby, we aimed at reducing the fraction of free Spinach2 resulting by the hybridization reaction. First, we evaluated the performance of the annealing process using a slight molar excess of the bridge i.e. 1.2 fold excess with respect to “delivery” and “payload” aptamer. Thus, in this mixture the aptamer modules represent the “limiting reagent” and ideally should completely interact with the bridge sequence.

Additionally, a gradual cooling/annealing step is essential when dealing with sequences with such significant secondary structure. Therefore, the oligo mixture was first heated at high temperature and then slowly cooled to room temperature over 45–60 minutes to allow correct hybridization among the complementary strands.

Next, we assessed the formation of the assembly by monitoring the band shift into a native polyacrylamide gel electrophoresis (native PAGE). To better

understand the efficiency of the annealing process, we estimated the band intensity of three species for each sample: unconjugated Spinach2, Spinach2-bridge complex, and ternary oligonucleotide complex (Spinach2-c2 and Spinach2-DW4). Starting from the band intensity values, we calculated an approximate value of hybridization yields for all samples. It is worth noting that Spinach2 does not show complete hybridization with the ODN bridge sequence. An estimation of the band intensity of both free Spinach2 and Spinach2-bridge complex in the lane 2 indicates that only ~50% of total amount of Spinach2 is actually annealed with the ODN bridge (Fig. 5). Furthermore, we found that the annealing process is tightly dependent by the delivery aptamer employed in the annealing step. Indeed, different hybridization yields were observed with c2 and DW4. Particularly, a very low amount (~20%) of the whole conjugate was generated with c2 aptamer (lane 3). In contrast, the annealing process with DW4 led to the formation of a higher amount of the final conjugate (~50%). Consequently, a negligible band was detected for the Spinach2-bridge (~10%) in this sample (lane 4). Note that an almost constant amount of free Spinach2 was present in all annealing samples, in percentage ranging from 40 to 50% (Fig. 5). The existence of a fraction of unconjugated Spinach2 might be linked to the presence of misfolded structures. Indeed, as mentioned above, it has been recently demonstrated that the fraction of properly folded Spinach2-tRNA is ~80% at 25 °C and ~60% at 37°C[246]. Our findings are consistent with the latter value since we estimated that the free/misfolded fraction is about 40% of Spinach2. Thereby, taking into account only the hypothetical aptamer folded fraction represented here by the amount of Spinach2 effectively annealed with the bridge (~60% in lane 3 and 4), the calculated hybridization yields exceed the previously found values. Indeed, we estimated that ~30% of the Spinach2-bridge (calculated from band intensities according to the following formula: ternary complex/(ternary complex + Spinach2-bridge)*100) is actually able to generate the ternary oligonucleotide complex through self-assembly with c2 (lane 3). On the other hand, the annealing efficiency rises to ~85% when the Spinach2-bridge is annealed with DW4 (lane 4).

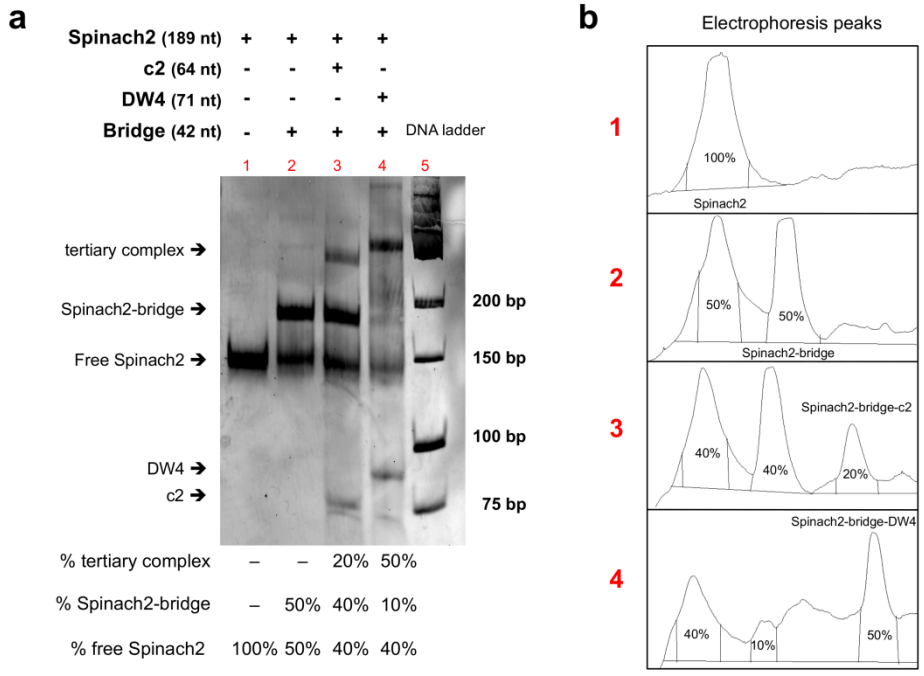

Fig. 5 Electrophoretic Mobility Shift Assay (EMSA) to assess the formation of the ternary complex among the payload aptamer (Spinach2), oligo bridge and the delivery aptamer (c2 or DW4). The molar equivalents were 1:1:1.2 for Spinach2, c2/DW4, and bridge, respectively. Lane 1: free Spinach2. Lane 2: Spinach2+bridge. Lane 3: Spinach2+bridge+c2. Lane 4: Spinach2+bridge+DW4. Lane 5: low range DNA ladder.

4.1.2 Assembly of aptamer-aptamer complexes: annealing reaction with an excess of delivery aptamers and bridge

In view of these considerations on the Spinach2 folding, we explored different conditions to improve the hybridization yields and reduce the fraction of unconjugated Spinach2. To this end, a different molar ratio and a different annealing protocol were employed. In details, we used a slight molar excess of both ODN bridge and delivery aptamer (1.4 and 1.6) compared to the molar

concentration of Spinach2 (molar ratio for Spinach2, ODN bridge and delivery aptamer: 1:1.4:1.6). Moreover, we prepared different annealing mixtures containing the ODN bridge with either the payload or delivery aptamer to increase the folding performance of both aptamer modules during the cooling step. The mixture was denatured at high temperature and slowly cooled at room temperature. Meanwhile, the payload or delivery aptamer was denatured and added to the corresponding sample during the cooling phase when the temperature was at ~45°C. For this evaluation, beyond c2 and DW4 we employed a third anti-TfR aptamer, a 2'-fluoro-modified RNA, termed Waz.

As shown in Fig. 6 the assembly of the final ternary complex was still dependent on the delivery aptamer present in the annealing mixture and on the nature of the aptamer added later during the cooling step. Particularly, we observed preferential annealing and improved yields when the RNA aptamers, c2 and Waz, were added at 45°C (lane 3 and 7). In contrast, addition of Spinach2 during the cooling step led to the formation of a remarkably lower amount of the same ternary complex (lane 4 and 8). It is worth noting that when the delivery RNA aptamers were added at a later stage in the process, we barely observed the presence of unreacted Spinach2-bridge (~5%). Thus, taking into account only the Spinach2 fraction effectively hybridized with the ODN bridge, the yield for the ternary complex formation is about 90% for both c2 and Waz.

On the other hand, when the DNA aptamer DW4 was used as delivery module (lane 5 and 6), we estimated similar annealing efficiency both when DW4 was added at 45°C during the cooling phase and when it was directly incubated with the ODN bridge. Interestingly, both approaches afforded lower hybridization yields compared with our first annealing protocol (see Fig. 5, lane 4).

Note that, even in this second EMSA evaluation, each sample containing all the oligo sequences showed a quite constant amount (~50-55%) of free Spinach2, which might be actually related to misfolded aptamer structures.

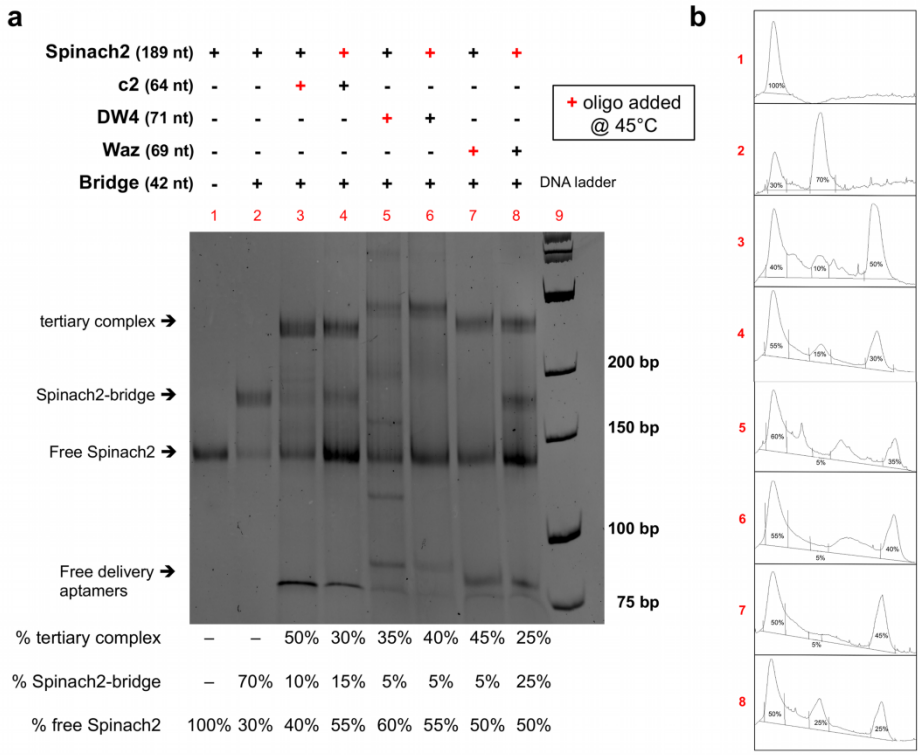

Fig. 6 Electrophoretic Mobility Shift Assay (EMSA) to assess the formation of the ternary complex among the payload aptamer (Spinach2), oligo bridge and the delivery aptamer (c2, DW4, or Waz). The molar ratio were 1:1.4:1.6 for Spinach2, bridge and c2/DW4/Waz, respectively Lane 1: Spinach2. Lane 2: Spinach2+bridge. Lane 3: Spinach2+bridge+c2 (secondary addition of c2). Lane 4: Spinach2+bridge+c2 (secondary addition of Spinach2). Lane 5: Spinach2+bridge+DW4 (secondary addition of DW4). Lane 6: Spinach2+bridge+DW4 (secondary addition of Spinach2). Lane 4: Spinach2+bridge+DW4. Lane 7: Spinach2+bridge+Waz (secondary addition of Waz). Lane 8: Spinach2+bridge+Waz (secondary addition of Spinach2). Lane 9: Low range DNA ladder.

Overall, these results highlight some limitations in the assembly of the ternary oligonucleotide complex. Particularly, the folding property of Spinach2 and its

relatively limited thermal stability (melting temperature for Spinach2 in absence of tRNA is T_m~ 38°C) affect its capability to fully interact with the complementary strand. This behavior led to lower than expected hybridization yields, with a fraction of unconjugated Spinach2 still present in the annealing mixture. Furthermore, it is worth noting that delivery aptamers interfere at different degrees with Spinach2, leading to different hybridization yields in dependence on their structural nature (DNA or RNA).

In the next section, I shall describe results of the investigation on functional properties of both payload and delivery aptamers within the ternary complex. To this end, the aptamer-aptamer conjugations were performed using tailored protocol for each delivery module employed based on the results described above. Particularly, to maximize the hybridization yield, c2 and Waz were added during the annealing/cooling step using 1.6 molar ratio delivery aptamer (c2 or Waz)/Spinach2. In contrast DW4 was directly incubated and denatured in presence of Spinach2 and bridge using equimolar concentration of the two aptamers.

4.2 Aptamer functional assays

4.2.1 Spinach2 fluorescence assay

The assembled complex was subjected to functional assays to clarify whether both aptamers (delivery and payload) still retain their functions even when embedded in the aptamer-aptamer platform. To this end, we firstly monitored emission of Spinach2 module within the oligonucleotide complexes in cuvette. The fluorescence emission of Spinach2-DFHBI complex is directly dependent on aptamer folding, thus fluorescence variations are tightly related with its structural changes. We measured fluorescence emission of each assembly (Spinach2-bridge, Spinach2-DW4, Spinach2-c2 and Spinach2-Waz) and we compared them with what found for Spinach2 alone; this step was necessary to understand to what extent conjugation with the different modules affects the ability of Spinach2 to bind DFHBI. In all our annealing experiments, we employed a binding/annealing

buffer containing cytosolic ion concentrations and increased magnesium concentration (5 mM)[246].

As shown in Fig. 7, fluorescence emission spectra from all samples retain the same shape. Therefore, we directly compared the fluorescence emission of each assembly with the value recorded for Spinach2 alone. Note that conjugation of Spinach2 with the delivery RNA aptamers (c2 and Waz) causes a modest reduction of Spinach2-DFHBI fluorescence. Indeed, brightness of Spinach2-c2 and Spinach2-Waz samples was ~85% of what shown by unconjugated Spinach2. On the other hand, annealing with the bridge (i.e. Spinach2-brigde) and DW4 (i.e. Spinach2-DW4) does not affect significantly fluorescence emission (Fig. 7b). As expected, when the same concentration of DFHBI (10 μM) was incubated in presence of binding buffer, we detected minimal fluorescence emission[247,248].

It is worth noting that hybridization with the bridge sequence might stabilize Spinach2 folding, as shown by the slightly increased fluorescence intensity compared with Spinach2 alone. This behavior is likely due to the presence of a flexible free tail at the 3'-end of Spinach2 that may, to some extent, affect RNA folding. Upon hybridization of the tail with its complementary sequence on the bridge, a stable double helix is generated at the 3'-end of Spinach2, leading to enhanced stability.

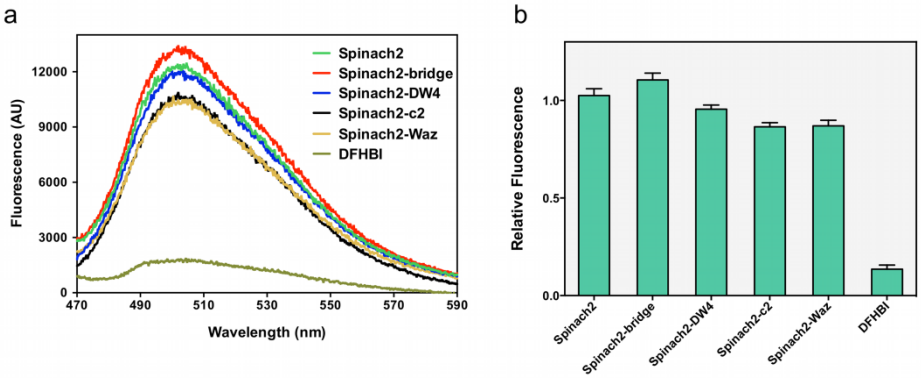

Fig. 7 Fluorescence emission of free Spinach2, Spinach2-bridge, Spinach2-DW4, Spinach2-c2, and Spinach2-Waz. (a) Fluorescence emission spectra from 0.1 μM of indicated RNAs and 10 μM DFHBI, measured at 25°C. Fluorescence was excited with

450 nm light and emission was recorded from 470 nm to 600 nm. All curves are represented as average of three independent experiments. (b) Fluorescence intensity measured for all samples as fluorescence spectrum area measured from 480 and 560 nm, and then normalized for the intensity recorded for Spinach2.

After this evaluation, we could affirm that the Spinach2 module still retains its ability to activate the fluorescence of DFHBI when inserted into the aptamer-aptamer complex.

Next, we turned our attention to the development of a nuclease resistant Spinach2 variant. Indeed, the presence of serum nucleases can hamper both *in vitro* but especially *in vivo* applications of this fluorescent RNA aptamer. To this end, we replaced the natural pyrimidine nucleotides (uridine and cytidine) with different combinations of 2'-modified pyrimidines (2'-fluoro, 2'-deoxy, and 2'-O-methyl pyrimidines). We generated through *in vitro* transcription several RNA Spinach2 transcripts and then we tested their ability to bind DFHBI on the basis of fluorescence readout. Interestingly, only cytidine derivatives, 2'-fluoro cytidine (Fig. 8) and 2'-deoxy cytidine (data not shown), retained the fluorescence properties of the RNA Spinach2 transcripts although with a reduced brightness (~50%) with respect to wild type Spinach2 (Fig. 8). In contrast, all our attempts to replace the uridine nucleotide led to significant reduction of the Spinach2 fluorescence property with almost complete loss of activity. Indeed, RNA transcripts with either 2'-fluoro or 2'-deoxy uridine were ~15-20% as bright as Spinach2, and the brightest molecule (~30%) was obtained after insertion of 2'-O-methyl-uridine.

It is worth mentioning that while our measurements were ongoing, Jaffrey and coworkers determined the 3D structure of Spinach2 and Spinach2-DHBI complex, unveiling the essential role of two uridine residues (U32 and U61) for binding of DFHBI[243]. Particularly, the 2'-hydroxyl group of U61 is implicated in a hydrogen bond to stabilize the interaction with the dye. Thereby, our findings related to the loss fluorescence emission of 2'-modified uridine RNAs are fully consistent with the proposed 3D conformation of Spinach2-DFHBI complex. Indeed, all our

modified Spinach2 transcripts did not include in their structure the 2'-hydroxyl group of the U61.

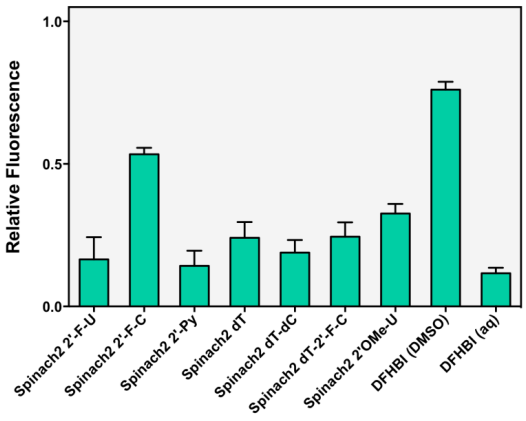

Fig. 8 Fluorescence properties of 2'-modified Spinach2 transcripts. Fluorescence signal from 0.4 μM of indicated RNAs and 2 μM DFHBI, measured at 25°C and normalized to the fluorescence intensity recorded for wild type Spinach2. Abbreviations: Spinach2 2'F-U (included 2'-flurouridine); Spinach2 2'F-C (included 2'-flurocytidine); Spinach2 2'F-Py (included both 2'-flurouridine and 2'-flurocytidine); Spinach2 dt (included 2'-deoxythymidine); Spinach2 dT-dC (included both 2'-deoxythymidine and 2'-deoxycytidine); Spinach2 dt-2'F-C (included both 2'-deoxythymidine and 2'-flurocytidine); Spinach2 2'-OMe-U (included 2'-O-methyluridine); DFHBI (DMSO), fluorescence measured in DMSO; DFHBI (aq), fluorescence measured in aqueous solution. Each measure represents average values for three independent experiments.

Finally, we also recorded the fluorescence emission spectrum of free DFHBI in organic solvent (DMSO), and we compared it with that found in aqueous solution. The shape of the spectrum did not change; however, DFHBI itself (2 μM) in an organic environment was ~75% as bright as Spinach2-DFHBI complex in aqueous solution. Conversely, as previously observed, the unbound dye did not show appreciable fluorescence in an aqueous milieu (~10%). This phenomenon, which is frequently observed with many other solvatochromic dyes[251], is likely due to the

lack of deactivation pathways induced by polar protic solvents such as water, and might lead to unwanted background fluorescence due to interaction of the dye with hydrophobic intracellular compartments, such as viscous membrane bilayers.

4.2.2 Endocytosis assay

Once verified that the Spinach2 module is still functional within the aptamer-aptamer assembly, we turned our attention to cell internalization of the delivery aptamers. Particularly, we assessed whether their ability to internalize into specific cell lines was retained even in presence of a large RNA molecule (Spinach2) as payload. Therefore, we performed an internalization assay using two different cell lines: mouse fibroblast cells (NIH 3T3) and human cervical cancer cells (HeLa) as target cells for DW4 and c2, respectively. The aptamer-aptamer complexes (Spinach2-DW4 and Spinach2-c2) were generated in presence of 20-fold molar excess of DFHBI (10 μM). In addition, the previously described scrambled aptamer sequences for DW4 and c2 (GS24mt, hereafter renamed scrDW4, and c36) were used as negative control.

It is worth mentioning that the Spinach-DFHBI complex displays relatively fast fluorescence decrease under continuous light irradiation due to *cis-trans* photoisomerization of the fluorophore[252]. However, in contrast with the irreversible photobleaching mechanism of GFP, the fluorescence of Spinach-DFHBI can be easily restored. Indeed, *cis-trans* photoisomerization induces fast unbinding of DFHBI from Spinach; consequently, a new ground-state (i.e. *cis*) DFHBI molecule can interact with Spinach, thus apparently restoring fluorescence of the complex in a [DFHBI]-dependent manner.

Therefore, before treatment with the oligonucleotide complexes, cultured cells were pre-treated with free DFHBI to ensure the presence of a large molar excess of dye in the intracellular compartments, and to interact with the internalized Spinach2, ultimately increasing the fluorescence recovery rate of the Spinach2-DFHBI complex. Moreover, since proper fold of Spinach2 only occurs in the presence of high levels of magnesium, we supplied exogenous magnesium to the culture media to increase its intracellular concentration.

The internalization of the oligonucleotide complexes was monitored by confocal microscopy. As stated in the previous chapter, we shortly incubated (30 minutes) the samples at very low oligonucleotide concentration (~0.5 μM) to minimize the nonspecific internalization of the aptamer-aptamer via pinocytosis. Additionally, BSA and tRNA were added as competitors for nonspecific binding sites. However, as shown in Fig. 9, for both cell lines (NIH 3T3 and HeLa), we detected similar fluorescence signal in the aptamer-aptamer complex-treated cells and after treatment with either DFHBI alone or the scrambled aptamer-Spinach2 complexes. The very low signal-to-noise ratio did not allow a clear distinction of the internalization property of each assembly. Interestingly, Jaffrey group has already described the presence of a low-level background fluorescence in DFHBI-treated cells, in absence of Spinach, with punctate fluorescence signals that reflect interactions of DFHBI with intracellular debris-like structures[247]. This is not uncommon between lipophilic dyes, which accumulate nonspecifically in many subcellular organelles[251] and the very dim fluorescence emission lead to low signal-to-noise ratio, which hampered a clear understanding of the internalization property of each assembly.

The significant background fluorescence exhibited by free DFHBI is consistent with our measurements related to the activation of DFHBI fluorescence in presence of an aprotic relatively non-polar solvent, such as DMSO. Indeed, this nonspecific signal is likely due to the interaction of this dye with hydrophobic intracellular compartments.

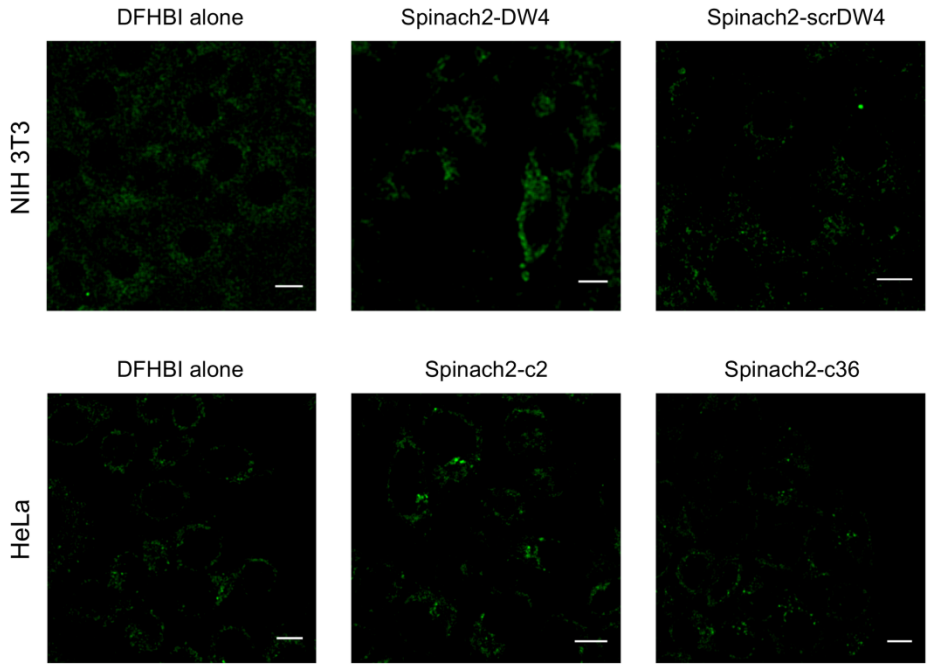

Fig. 9 Internalization assay of the aptamer-aptamer complexes in mouse fibroblasts (NIH 3T3) and human cervical cancer cells (HeLa). Confocal imaging microscopy shows the intracellular fluorescence of DFHBI alone, Spinach2-DW4 and Spinach2-scrDW4 in mouse fibroblasts and DFHBI alone, Spinach-c2 and Spinach2-c36 in human cervical cancer cells. Scale bars: 10 μm

Note that, besides showing considerable background fluorescence, DFHBI suffers also from another limitation for live cell imaging: Spinach-DFHBI complex exhibits spectral properties (e.g. fluorescence excitation maximum at 447 nm) that do not fully match with the filters commonly used for GFP in fluorescence microscopes. Then, we decided to replace DFHBI in our analysis with its improved version, DFHBI-1T, which exhibits reduced background fluorescence, higher extinction coefficient (22000 $M^{-1}cm^{-1}$ and 31000 $M^{-1}cm^{-1}$ respectively for Spinach2-DFHBI and Spinach2-DFHBI-1T) and better quantum yield (0.72 and 0.94 respectively for Spinach2-DFHBI and Spinach2-DFHBI-1T).

In addition, the resulting Spinach2-DFHBI-1T complex has spectral properties that are more compatible with the existing microscopy filter sets (e.g. fluorescence excitation maximum at 482 nm)[247] The enhanced optical properties of DFHBI-1T are particularly relevant when dealing with processes occurring during endocytosis. In fact, the intravesicular pH drops along the endocytic pathway from the neutrality into the clathrin pits to pH 6.0–6.5 in early endosomes and finally to pH 4.5–5.5 in late endosomes and lysosomes. These pH changes shift the equilibrium from the deprotonated form (which is the most represented at physiological pH) to the protonated, nonfluorescent, one. In the pioneristic work that led to the first fluorogenic RNAs, Spinach-DFHBI complex exhibited a reduction up to 50% of its brightness at pH 6[242]. This translated in an overall loss of sensitivity during the endocytosis process, which can be circumvented to a certain extent by using a dye with higher brightness, such as DFHBI-1T.

Analogously to what already done for DFHBI, we generated aptamer-aptamer-DFHBI-1T conjugates, and measured fluorescence of the Spinach2-DFHBI-1T complex within each assembly. As expected, Spinach2 was able to bind also DFHBI-1T after annealing with the delivery aptamers, exhibiting similar relative fluorescence properties, and confirming the results shown in Fig. 7.

We next evaluated the DW4-mediated uptake of Spinach2 in mouse fibroblasts. Cells were treated with either the whole complex or Spinach2-scrDW4 assembly, and fluorescence arising from the two cell samples was compared with that of DFHBI-1T-treated cells (Fig. 10). Upon incubation, vesicular signals were detected inside the cells after treatment with Spinach2-DW4. Conversely, in the case of Spinach2-scrDW4 only a weak signal was detected into the cells appearing as cytosolic dots, possibly due to negligible nonspecific internalization of this complex. Most importantly, DFHBI-1T-treated cells showed almost null fluorescence, highlighting the reduced background fluorescence arising from this dye compared with its parent version, DFHBI. Notably, only some punctate signals could be detected in this sample, likely due to the interaction of DFHBI-1T with intracellular debris-like structures[247]. Thanks to the enhanced properties of DFHBI-1T, we could observe different internalization properties exhibited by

each complex, demonstrating that the large RNA Spinach2 was effectively internalized into the mouse cells via the DW4 aptamer (Fig. 10).

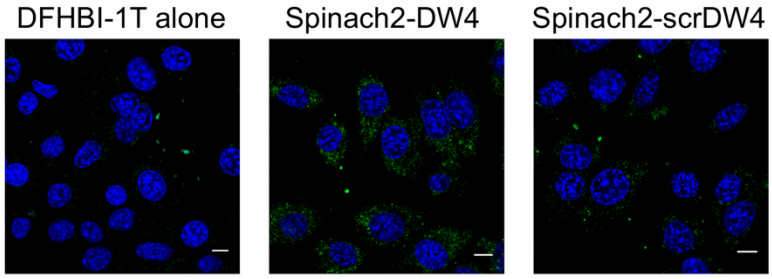

Fig. 10 Internalization assay of the aptamer-aptamer complexes in mouse fibroblasts (NIH 3T3). Confocal imaging microscopy shows the intracellular fluorescence (green) of DFHBI-1T alone, Spinach2-DW4, Spinach2-scrDW4, and Hoechst nuclear marker (blue) in mouse fibroblasts. Scale bars: 10 μm

Importantly, analogous results were obtained when Spinach2-c2 and Spinach2-Waz complexes were incubated in the presence of human cervical cancer cells (HeLa) (Fig. 11). It is worth noting that endocytic signals showed by this scrambled sequence (i.e. c36) exceeded that found for the DW4 scrambled aptamer (scrDW4) used as negative control towards mouse cells. This result might be linked to the use of serum-free medium during our incubation, an experimental condition that could lead to increased nonspecific binding with cell membrane, ultimately resulting in nonselective uptake. Unfortunately, as scrambled sequence, c36 has been identified by Levy group and its activity and nonspecific internalization have been always tested in presence of serum-containing medium[137]. In contrast scrDW4 has been identified as non-internalizing sequence in absence of serum[222]. The poor nuclease resistance of the RNA Spinach2 module, however, did hamper the use of serum during our endocytosis assay, and each sample was incubated in a serum-free medium (see methods for further details).

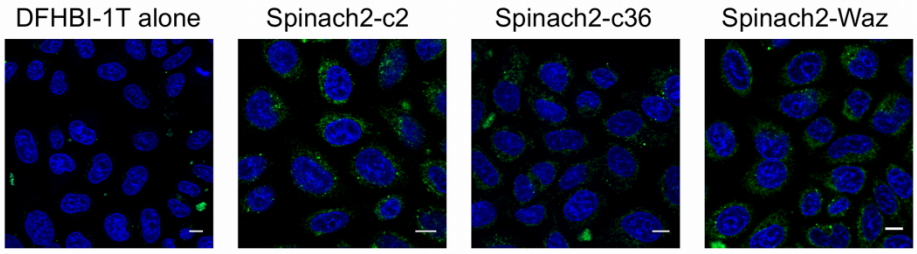

Fig. 11 Internalization assay of the aptamer-aptamer complexes in human cervical cancer cells (HeLa). Confocal imaging microscopy shows the intracellular fluorescence (green) of DFHBI-1T alone, Spinach-c2, Spianch2-Waz, Spinach2-c36, and Hoechst nuclear marker (blue) in human cervical cancer cells. Scale bars: 10 μm

To test whether the aptamer-aptamer complexes still retain their cell specificity, we incubated Spinach2-c2 and Spinach2-DW4 with their non-target cells, mouse and human cells, respectively (Fig. 12). As expected, the two assemblies showed weak intracellular signals, suggesting that DW4 and c2 were not able to deliver Spinach2 in cells lacking target receptor. Very low fluorescence was detected in mouse fibroblasts after treatment with Spinach2-c2 owing to the specificity exhibited by c2 towards the human transferrin receptor. On the other hand, Spinach2-DW4 showed a slightly higher fluorescent signal in HeLa cells, which is likely due to the ability of DW4 to recognize even hTfR although with lower affinity (see Chapter 3). Indeed, the aptamer-aptamer complexes were incubated at very low concentration (~0.5 μM), possibly below the effective Kd range of DW4 towards hTfR.

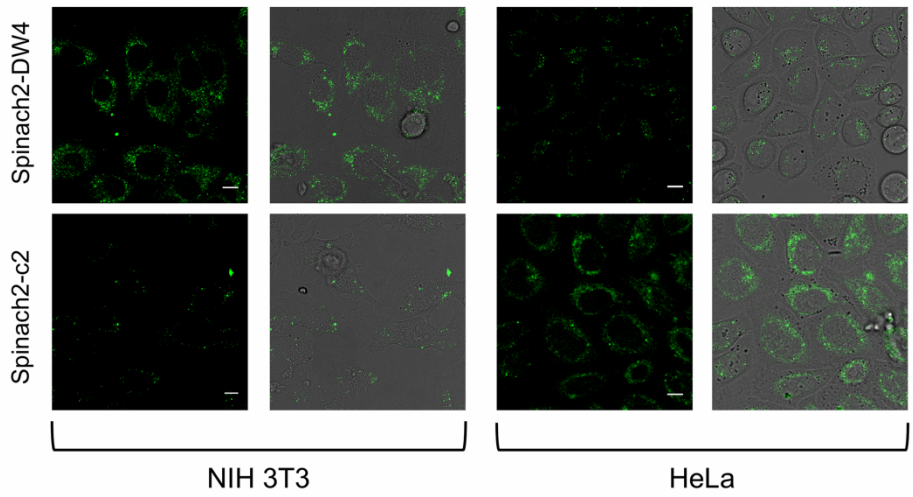

Fig. 12 Endocytosis of Spinach2-DW4 and Spinach2-c2 in mouse fibroblasts (NIH 3T3) and human cervical cancer cells (HeLa). Confocal imaging microscopy shows the intracellular fluorescence of, Spinach2-DW4 and Spinach2-c2 in NIH 3T3 and HeLa cells. Scale bars: 10 µm

Overall, these results are the first evidence of an aptamer-mediated aptamer delivery. Most importantly, each delivery aptamer is able to promote cell-specific aptamer-mediated endocytosis of Spinach2. These findings demonstrate the modularity of our platform design with the possibility to swap the delivery module without losing its selective uptake property.

4.3 An improved fluorescent aptamer sequence: rational multimerization of Baby Spinach

Besides exploiting different cell-penetrating aptamers as delivery module, we aimed to assess the possibility to swap even the payload portion of our platform in a “plug-and-play” fashion. Thus, we performed a rational multimerization of the

Spinach system to replace the Spinach2 aptamer with a novel fluorescent aptamer having enhanced brightness and folding stability.

As previously mentioned in this chapter, Jaffrey and coworkers recently generated a truncated version of the Spinach aptamer, termed Baby Spinach, with fluorescence comparable to that of the parental RNA[243]. The reduced size of this aptamer sequence (51 nt of Baby Spinach versus 97 nt of Spinach2 without the tRNA scaffold) provides a flexible tool to study multimerization engineering. Taking into account the Baby Spinach folding, we designed a linear multimeric sequence containing up to 5 copies of Baby Spinach. As shown in Fig. 13 the stem region, or paired region (P2), at the 5'- and 3'- ends of Baby Spinach was extended to improve the folding stability of each aptamer module within the multimeric structure by increasing the number of base pairings. Thus, we decided to call this extended Baby Spinach sequence "s-Baby Spinach", where "s" stands for both stemmed and stabilized. Note that the choice of these "extended stem sequences" was quite critical. We performed secondary structure predictions to verify and test each designed sequence, excluding those that induced alteration of the aptamer folding, especially in the stem region (P2). In addition, the flanking sequences between each s-Baby Spinach module were designed with a unique nucleotide composition, thus we could generate the single monomer, dimer, trimer, tetramer and pentamer using the appropriate couple of PCR primers. Then, the proper PCR amplicon was transcribed *in vitro* to generate the corresponding RNA transcript.

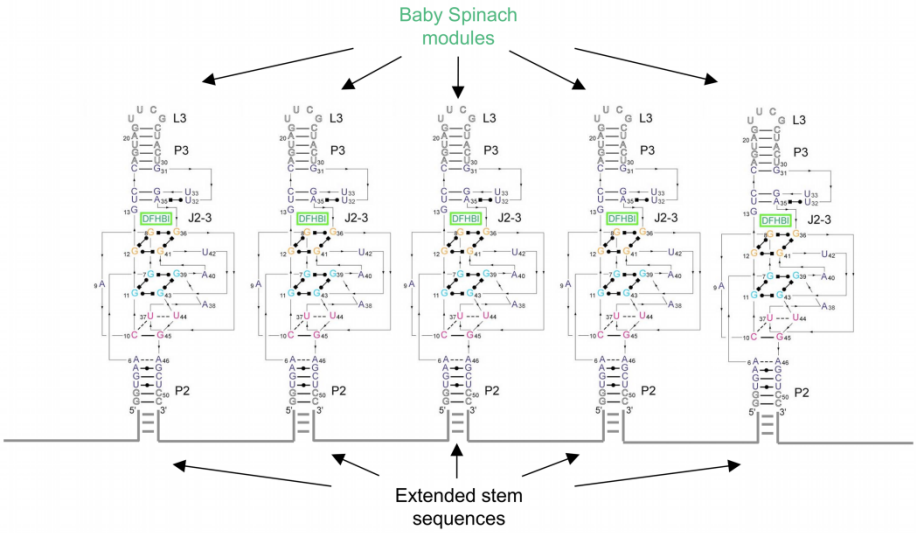

Fig. 13 Multimerization of Baby Spinach. Secondary structure predictions of Baby Spinach are based on previously findings on the crystal structure of both unbound Spinach and Spinach-DFHBI complex. The extended stem sequences and the flanking sequences between each module are depicted in grey. Each module of the linear multimeric sequence is composed by s-Baby Spinach unit (s=stemmed).

To determine whether the multimerization of Baby Spinach affects the ability of each aptamer module to activate DFHBI fluorescence, we performed fluorescence measurements using identical RNA concentration (0.1 μM) and an excess of DFHBI (10 μM), normalizing each value to the monomer fluorescence at 25°C. Importantly, both dimeric and trimeric s-Baby Spinach showed increased fluorescence emission, respectively, of 1.7 and 1.8 times compared with the monomer (Table 1). However, fluorescence enhancement induced by the presence of multiple copies of s-Baby Spinach did not show a linear trend. In particular, the efficiency detected for each aptamer unit, or module, within the multimeric structures significantly decreases with increasing of the number of copies. This trend might suggest the presence of undesired intramolecular interactions that affect folding of each aptamer, ultimately lowering their ability to bind DFHBI

and activate its fluorescence. In particular, the unit of Baby Spinach could potentially hybridize each other. Indeed, the strands from one aptamer might interact with the complementary strand in another aptamer, leading to an interaptamer hybridization that could prevent the binding with DFHBI. Another possible explanation is related to the presence of several fluorophores confined within the same biomolecular architecture, which might contribute to the loss of fluorescence signal due to self-quenching. Note that a reduction of fluorescence has been reported for multiple-fluorophore labeled antibodies and proteins (e.g. four to six dyes per molecule)[253]. Indeed, the increase in the number of fluorophores conjugated to the same antibody/protein leads to a self-quenching effect, thereby reducing the overall fluorescence.

TABLE 1: Fluorescence properties of the multimeric Baby Spinach at 25°C

Sample	*Fluorescence enhancement*[1]	*ODN length (nt)*[2]	*Unit efficiency*
s-Baby Spinach monomer	1.0	90	1
s-Baby Spinach dimer	1.7	159	0.8
s-Baby Spinach trimer	1.8	228	0.6
s-Baby Spinach tetramer	1.0	297	0.2
s-Baby Spinach pentamer	1.7	366	0.3
Spinach2-tRNA	1.2	189	1

[1] All values were obtained as the average of two or more independent measurements, with errors (SD) in the range 0.05-0.1; [2]The oligonucleotide length includes both the extended stem sequence and the annealing sequence to hybridize with the ODN bridge

Despite the known stability of Spinach2-tRNA, which compares favorably both with its parent Spinach sequence and with Baby Spinach, our measurements display that Spinach2-tRNA is only 1.2 times brighter than our monomer (s-Baby Spinach) at 25°C. This is likely due to the presence of the extended stem sequence in our s-Baby Spinach design that leads to enhanced folding stability. The generation of a shorter RNA aptamer sequence with fluorescence properties comparable with Spinach2-tRNA offers significant advantages. In particular, it is known that tRNAs precursors are recognized by specific RNases, resulting in the

cleavage near the base of the tRNA[254]. Additionally, it has been recently demonstrated that tRNA scaffold is rapidly targeted by endonucleases, leading to RNA cleavage, degradation and instability both in bacterial and mammalian cells[255]. Thus, the presence of these highly susceptible tRNA motifs might represent a strong limitation when used as scaffold for live cell applications. In this context, our tRNA-free multimeric versions of Baby Spinach offer valid alternatives to the Spinach2-tRNA. On the basis of the improved brightness (~1.7 and ~1.5 times higher than s-Baby Spinach and Spinach2, respectively) and unit efficiency (~80% of each module is still functional), dimeric s-Baby Spinach was the most promising sequence (Table 1). Therefore, we termed this molecule as Twins and we sought to investigate its fluorescence property both *in vitro* and in living cells, aiming to perform a live cells imaging of our aptamer-aptamer platform.

In conclusion, the proposed multimerization strategy results a valid method to generate enhanced multimeric sequences containing up to two to three copies of fluorescent RNA aptamer per molecule. However, it suffers for some limitations related to the synthesis of RNA sequences with a high number of fluorescent units. It is worth mentioning that insertion of point mutations might potentially reduce the probability of interaptamer hybridization. Furthermore, insertion of additional stabilizing elements, such as longer stem sequences or three-way junction (3WJ) motifs originated from the bacteriophage phi29[176], might lead to enhanced folding stability even for the multimeric sequences with a high number of copies.

Before testing the enhanced fluorescence property of Twins in living cells, we performed an EMSA to assess the annealing property of this new sequence with delivery aptamers (Fig.14).

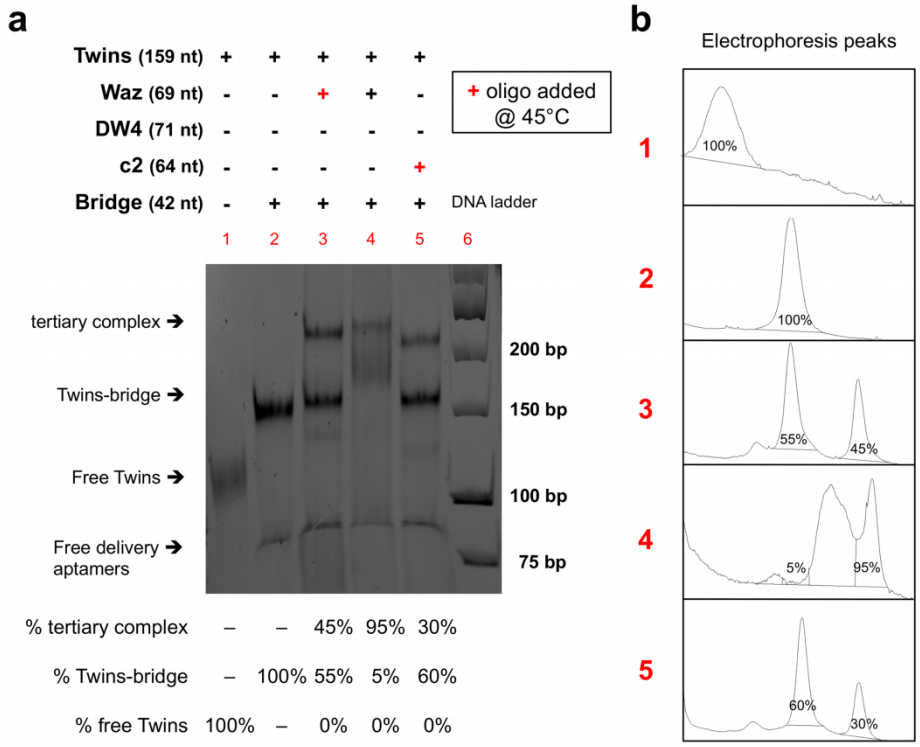

Fig. 14 Electrophoretic Mobility Shift Assay (EMSA) to assess the formation of the ternary complex among the payload aptamer (Twins), oligo bridge and the delivery aptamer (DW4, Waz and c2). The molar equivalents were 1:1.4:1.6 for Spinach2, bridge and c2/DW4/Waz, respectively Lane 1: free Twins. Lane 2: Twins+bridge. Lane 3: Twins+bridge+Waz (secondary addition of Waz) Lane 4: Twins+bridge+DW4 Lane 5: Twins+bridge+c2 (secondary addition of c2) Lane 6: Low range DNA ladder.

We observed, for the first time, complete hybridization of the payload aptamer with the bridge sequence, as shown by complete disappearance of the band related to free Twins (Fig. 14, lane 2). This behavior was observed even when Twins and bridge were incubated with delivery aptamers to generate the aptamer-aptamer complex (Fig. 14, lane 3-5). This suggests that Twins exhibits a higher aptamer

folded fraction than Spinach2, thus allowing complete annealing with the bridge. These findings are consistent with the similar fluorescence properties exhibited by Spinach2 and s-Baby Spinach in our previous measurements (table 1). Indeed, although is known that Baby Spinach shows a significantly reduced fluorescence than Spinach2, the insertion of an extended stem sequence leads to enhanced folding stability, and consequently s-Baby Spinach displays improved fluorescence properties and its dimeric version (Twins) exhibits full hybridization with the bridge.

Despite the excellent annealing efficiency between Twins and bridge, overall hybridization yields are still strictly dependent on the nature of the delivery aptamer included in the annealing mixture, confirming our previous findings (see Fig. 5 and 6). Particularly, DW4 shows best annealing properties compared with Waz and c2 (lane 3-5). The poor hybridization yield (~30%) obtained with c2 led us to exclude this delivery aptamer for the assessment of the aptamer-mediated Twins delivery in living cells. Therefore, only Twins-DW4 and Twins-Waz, showing respectively ~95% and ~50% yields, were incubated with their target cells. The scrambled aptamer c36 (i.e Twins-c36), which showed a hybridization yield comparable with that found for Waz, was used as negative control.

Before performing the endocytosis assay, we measured the fluorescence of Twins-DFHBI-1T complex within each assembly. As shown in Fig. 15, annealing with delivery aptamers did not affect the ability of Twins to bind and activate the fluorescence of DFHBI-1T.

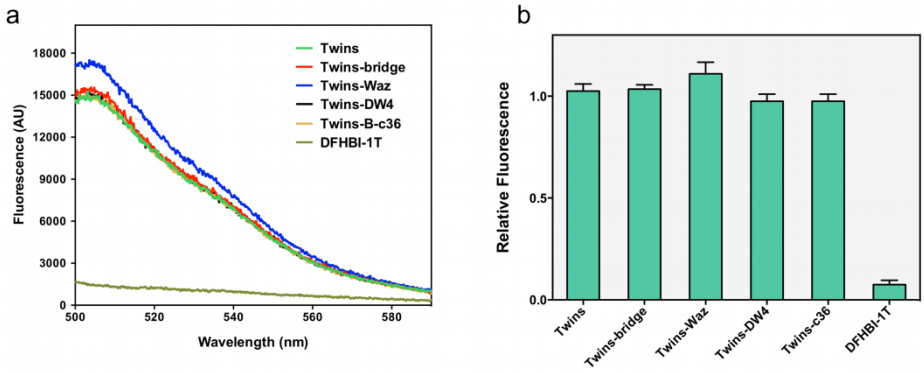

Fig. 15 Fluorescence properties of free Twins, Twins-bridge, Twins-DW4, Twins-c2, and Twins-Waz. (a) Fluorescence emission spectra from 0.1 µM of indicated RNAs and 10 µM DFHBI-1T, measured at 25°C. Fluorescence was excited with 480 nm light and emission was recorded from 500 nm to 600 nm. All curves are represented as average of three independent experiments. (b) Fluorescence intensity measured for all samples as fluorescence spectrum area measured from 500 and 560 nm, and then normalized for the intensity recorded for Twins.

This result confirms that besides Spinach2, even another payload aptamer still retain its original folding and functionality when embedded in a more complex structure.

Finally, we evaluated the aptamer-mediated uptake of Twins both in mouse fibroblasts and human cervical cancer cells. Upon incubation, punctate cytoplasmic signals were detected after treatment with both Twins-DW4 and Twins-Waz in NIH 3T3 and HeLa cells, respectively (Fig. 16). In contrast, DFHBI-1T-treated cells showed almost null intracellular signal. Notably, the intracellular fluorescence related to the Twins-Waz complex exceeded that found for Twins-c36, confirming our previous observations.

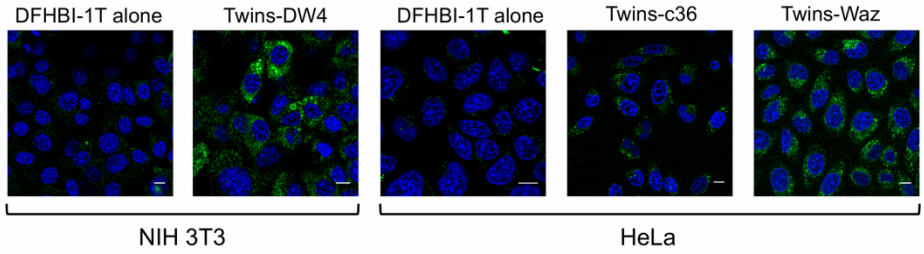

Fig. 16 Internalization assay of the aptamer-aptamer complexes in mouse fibroblasts (NIH 3T3) and human cervical cancer cells (HeLa). Confocal imaging microscopy shows the intracellular fluorescence (green) of DFHBI-1T alone, Twins-DW4 in mouse fibroblast and DFHBI-1T alone, Twins-Waz and Twins-c36 in human cervical cancer cells, and Hoechst nuclear marker (blue) in both cell lines. The image processing was performed using ImageJ and the HiLo LUT plugin for the subtraction of the measured background fluorescence. Scale bars: 10 μm

As shown in Fig. 17, all the complexes containing Twins as payload aptamer show somewhat increased cellular fluorescence signal compared with the Spinach2-aptamer assemblies.

It is worth noting that, besides showing an enhanced fluorescence than Spinach2 (1.5 times higher), Twins does not exploit tRNA as aptamer scaffold, which is targeted in the intracellular environment by endonucleases, leading to RNA cleavage and hence to a reduction of the cellular fluorescent signal. This important feature yields Twins a novel fluorogenic RNA tool with enhanced potential than Spinach2.

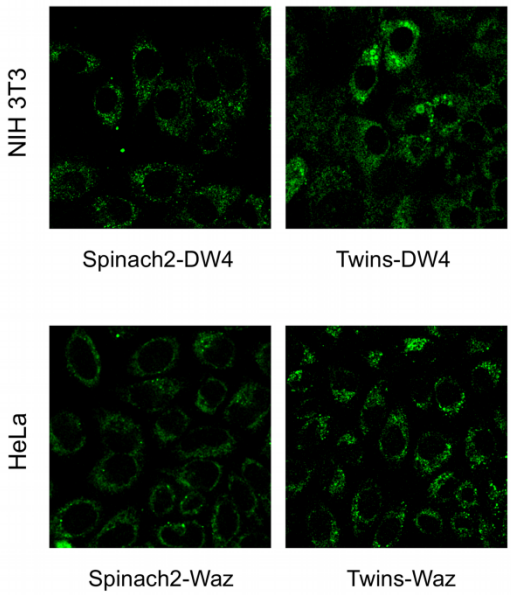

Fig. 17 Comparison of the intracellular fluorescence signal related to the Spinach2-aptamer (Spinach2-DW4 and Spinach2-Waz) and Twins-aptamer (Twins-DW4 and Twins-Waz) complexes in mouse fibroblasts (NIH 3T3) and human cervical cancer cells (HeLa). The image processing was performed using ImageJ and the HiLo LUT plugin for the subtraction of the measured background fluorescence.

Overall, these results demonstrate that our Twins aptamer could represent an improved tool for RNA imaging in living cells. However, although Twins shows improved fluorescence properties, the reported fluorescence enhancement is still limited, and is only ~1.5 higher than Spinach2 and ~1.7 than the parental RNA (i.e. s-Baby Spinach). Thus, Twins may represent a useful starting point for further optimization of the Spinach system, and our strategy may pave the way to further multimerization strategies aiming to increase the sensitivity of RNA imaging. In addition, the limitations of our approach related to the development of multimeric sequences with a high number of fluorescent aptamer units, might offer useful hints on which aptamer domains and sequences should be engineered to reduce the

intraptamer interactions, increasing folding stability and ultimately the fluorescence properties.

4.4 Concluding remarks

In this chapter, an approach to design and generate a modular plug-and-play drug-delivery platform to perform an aptamer-mediated aptamer delivery was presented. This platform exploits (i) targeting and delivery abilities exhibited by anti-transferrin receptor aptamers and (ii) fluorescence properties of RNA mimics of GFP. We demonstrated that both the delivery and payload modules of our platform could be swapped using different combinations of aptamers, highlighting the modularity of our design. Most importantly, both anti-mouse TfR aptamer (DW4) and anti-human TfR aptamer (c2) were able to deliver Spinach2 into their specific target cells with limited nonspecific cell uptake. In addition, the ability to track the internalized fluorescent RNA aptamers (Spinach2 and Twins) during the endocytic pathway, suggested that these RNAs still retain their folding and functionality during early stages of the endocytosis process. This proof-of-principle is the first demonstration of aptamer-mediated delivery of large functional RNA and may represent a useful starting point for further targeted delivery applications in living cells, simply swapping the fluorescent RNA aptamers with therapeutic and regulatory RNAs, such as, therapeutic aptamers, long non-coding RNA (lncRNA), messanger RNA (mRNA), and engineered structure containing multiple copies of miRNAs or siRNAs.

However, although our oligonucleotide platform exhibits remarkable features as delivery system, further molecular engineering strategies may increase and overcome some intrinsic limitations related to the hybridization step, reducing unwanted intra- and inter- molecular interactions and increasing the folding stability. To this end, middle-term goals include insertion of aptamer scaffolds, or stabilizing sequences (such as 3WJ motifs) within the platform, to increase the conformational stability of each module, ultimately increasing the annealing properties. In addition, novel designs of the oligo bridge sequence will be evaluated, including the presence of cleavable linkers, such as disulfide bond, to facilitate intracellular release of the payload RNAs at the early- or late- endosomal

stage of the endocytosis process. Although endosomal escape is an essential step in many therapeutically relevant applications, such as RNAi-mediated gene silencing, other strategies aim at targeting only endosomes. Indeed, the endosomal system is not a simple transient environment for the degradation or recycling of cell-surface receptors and uptake of nutrients, it is also an essential site of signal transduction mediated by different classes of receptors, such as receptor tyrosine kinases (RTKs), G protein-coupled receptors (GPCRs) and Toll-like receptors (TLRs)[256]. Particularly, in several form of cancers, mutations affecting either some of these receptors (e.g. mutations in RTKs that maintain them in hyperactivated states of dimerization and/or phosphorylation) or adaptor proteins involved in the signal transduction lead to tumorigenesis[257]. In the endosomes these mutated receptors trigger different signals from those at the plasma membrane both mechanistically and temporally, resulting in distinct physiological responses, such as uncontrolled cell proliferation, and enhanced cell survival[256,257].

Our flexible aptamer platform could be exploited, for instance, to perform endosomal delivery of therapeutic aptamers able to inhibit either specific domains that are inaccessible at the plasma membrane level or signaling components exclusively localized to endosomes, thus affecting only the endosomal signaling.

In the context of targeted therapy a strategy that targets endosomal signaling relevant to disease offers a more selective tool with potentially minor side effects than targeting primary steps of receptor signal transduction.

4.5 MATERIALS AND METHODS

4.5.1 Reagents, oligonucleotides, and transcription templates

All chemicals were purchased from Sigma-Aldrich unless otherwise noted, all restriction enzymes were obtained from New England BioLabs (NEB) and all cell culture products were purchased from Gibco BRL/Life Technologies. DFHBI ((Z)-4-(3,5-difluoro-4-hydroxybenzylidene)-1,2-dimethyl-1H-imidazol-5(4H)-one) and DFHBI-1T ((Z)-4-(3,5-difluoro-4-hydroxybenzylidene)-2-methyl-1-(2,2,2-trifluoroethyl)-1H-imidazol-5(4H)-one) were purchased from Lucerna Technologies.

DNA aptamer DW4, scrambled DW4 (scrDW4), DNA oligo-bridge, DNA templates and primers for PCR were purchased from Integrated DNA Technologies (IDT, Coralville, IA, USA). They were stored in lyophilized form and suspended before use in the appropriate volume of TE buffer (10 mM Tris-HCl at pH 7.5, 0.1 mM EDTA at pH 8.0) to reach a concentration of 100 μM. The concentration of all DNA and RNA suspensions was measured by UV spectrophotometry using a Nanodrop 1000 spectrophotometer (Thermo Scientific). All enzymatic amplification reactions were performed using high-fidelity PhusionDNApolymerase (NewEngland Biolabs) or TaqDNA polymerase (NEB) according to the manufacturer's protocols. The pET28-Spinach2 plasmid was a kind gift of Samie Jaffrey (Cornell University) and contains the Spinach2 aptamer inside a tRNA scaffold.

4.5.2 Aptamer sequences

The sequence of the anti-human TfR RNA aptamer (c2.min) with a short tail $(CGA)_7$ was the following (tail sequence is underlined):

5'-
GGGGGAUCAAUCCAAGGGACCCGGAAACGCUCCCUUACACCCCCGACG
ACGACGACGACGACGACGA-3'

The sequence of the anti-human TfR RNA aptamer (Waz) with a short tail $(CGA)_7$ was the following (tail sequence is underlined):

5'-GGGUUCUACGAUAAACGGUUAAUGAUCAGCUUAUGGCUGGCAG UUCCCCGACGACGACGACGACGACGA-3'

The sequence of the scrambled aptamer (c36) with a short tail $(CGA)_7$ was the following (extended sequence of aptamer is underlined):

5'-GGCGUAGUGAUUAUGAAUCGUGUGCUAAUACACGCCCGACGAC GACGACGACGACGA-3'

All pyrimidines of the RNA aptamer motif were 2'-fluoro-modified.

The sequence of the anti-mouse TfR DNA aptamer DW4 with a short tail $(CGA)_7$ was the following (tail sequence is underlined):

5'-GCGTGTGCACACGGTCACTTAGTATCGCGGCGTTCTTTGGTTCCGC CCGGCGACGACGACGACGACGACGA-3'

The scrambled sequence of DNA aptamer scrDW4 with a short tail $(CGA)_7$ was the following (tail sequence is underlined):

5'-GCCATTGCCATTGCCATTGCCATTGCCATTGCCATTGCCATTGCCA TTGCCATTGCGACGACGACGACGACGACGA-3'.

The sequence of DNA oligo-bridge was the following:

5'- ATCATCATCATCATCATCATCTCGTCGTCGTCGTCGTCGTCG -3'

The sequence of RNA aptamer Spinach2-tRNA with a short tail $(GAU)_7$ was the following (tail sequence is underlined while tRNA-derived sequences are highlighted in bold):

5'-**GCCCGGAUAGCUCAGUCGGUAGAGCAGCGGCCG**GAUGUAACU GAAUGAAAUGGUGAAGGACGGGUCCAGUAGGCUGCUUCGGCAGCC UACUUGUUGAGUAGAGUGUGAGCUCCGUAACUAGUUACAUC**CGGC CGCGGGUCCAGGGUUCAAGUCCCUGUUCGGGCGCCA**GAUGAUGA UGAUGAUGAUGAU-3'

The sequence of the RNA aptamer s-Baby Spinach monomer was the following (extended stem sequences are underlined):

5'-AAAAAGCAGGGUGAAGGACGGGUCCAGUAGUUCGCUACUGUUG AGUAGAGUGUGAGCUCCCUGCAAAAC-3'

The sequence of the RNA aptamer s-Baby Spinach dimer was the following (extended stem sequences are underlined):

5'-AAAAAGCAGGGUGAAGGACGGGUCCAGUAGUUCGCUACUGUUG
AGUAGAGUGUGAGCUCCCUGCAAAACAAGAAGGUCGGUGAAGGAC
GGGUCCAGUAGUUCGCUACUGUUGAGUAGAGUGUGAGCUCCGACC
ACACA-3'

The sequence of the RNA aptamer s-Baby Spinach trimer was the following (extended stem sequences are underlined):

5'-AAAAAGCAGGGUGAAGGACGGGUCCAGUAGUUCGCUACUGUUG
AGUAGAGUGUGAGCUCCCUGCAAAACAAGAAGGUCGGUGAAGGAC
GGGUCCAGUAGUUCGCUACUGUUGAGUAGAGUGUGAGCUCCGACC
ACACAAUAAAGCCUGGUGAAGGACGGGUCCAGUAGUUCGCUACUG
UUGAGUAGAGUGUGAGCUCCAGGCUAGAG-3'

The sequence of the RNA aptamer s-Baby Spinach tetramer was the following (extended stem sequences are underlined):

5'-AAAAAGCAGGGUGAAGGACGGGUCCAGUAGUUCGCUACUGUUG
AGUAGAGUGUGAGCUCCCUGCAAAACAAGAAGGUCGGUGAAGGAC
GGGUCCAGUAGUUCGCUACUGUUGAGUAGAGUGUGAGCUCCGACC
ACACAAUAAAGCCUGGUGAAGGACGGGUCCAGUAGUUCGCUACUG
UUGAGUAGAGUGUGAGCUCCAGGCUAGAGAAAAAGUAGGGUGAAG
GACGGGUCCAGUAGUUCGCUACUGUUGAGUAGAGUGUGAGCUCCC
UACGAUAA-3'

The sequence of the RNA aptamer s-Baby Spinach pentamer was the following (extended stem sequences are underlined):

5'-AAAAAGCAGGGUGAAGGACGGGUCCAGUAGUUCGCUACUGUUG
AGUAGAGUGUGAGCUCCCUGCAAAACAAGAAGGUCGGUGAAGGAC
GGGUCCAGUAGUUCGCUACUGUUGAGUAGAGUGUGAGCUCCGACC
ACACAAUAAAGCCUGGUGAAGGACGGGUCCAGUAGUUCGCUACUG
UUGAGUAGAGUGUGAGCUCCAGGCUAGAGAAAAAGUAGGGUGAAG
GACGGGUCCAGUAGUUCGCUACUGUUGAGUAGAGUGUGAGCUCCC
UACGAUAAAAAAAGCUGGGUGAAGGACGGGUCCAGUAGUUCGCUA
CUGUUGAGUAGAGUGUGAGCUCCCAGCACCUC-3'

The sequence of the RNA aptamer s-Baby Spinach dimer (Twins) with a short tail $(GAU)_7$ was the following (tail sequence is underlined):

5'-AAAAAGCAGGGUGAAGGACGGGUCCAGUAGUUCGCUACUGUUG
AGUAGAGUGUGAGCUCCCUGCAAAACAAGAAGGUCGGUGAAGGAC
GGGUCCAGUAGUUCGCUACUGUUGAGUAGAGUGUGAGCUCCGACC
ACACAGAUGAUGAUGAUGAUGAUGAU-3'

4.5.3 Secondary structure and hybridization predictions

All DNA and RNA secondary structure predictions and intra- and intermolecular interactions were analyzed using the NUPACK server (http://www.nupack.org/)[175] as described in Chapter2.

4.5.4 In vitro RNA transcription

All RNA aptamers (both delivery and fluorogenic RNAs) were PCR amplified with primers that appended a T7 promoter and PCR amplified DNA duplexes were resolved by agarose gel electrophoresis and visualized by ethidium bromide staining to check the yield of PCR reactions and confirm the proper size of the PCR amplicons. Spinach2 transcription templates were amplified using primers specific to the flanking plasmid sequence (pET28-Spinach2 plasmid).

For *in vitro* run off transcription reactions was performed by incubating the PCR product in buffer containing 120 mmol/l HEPES–KOH, pH 7.5, 30 mmol/l $MgCl_2$, 40 mmol/l DTT, 4% wt/vol PEG 8000, 4 mmol/l NTPs and mutant Y639F T7 RNA polymerase for 3 hours at 37°C. 2'-fluoro modified CTP and UTP (TriLink Biotechnologies) or 2'-O-Methyl CTP and UTP were used to generate 2'-modified RNAs. Mutant Y639F/H784A T7 RNA polymerase was used to yield 2'-O-Methyl-modifed RNAs. At the completion of the reaction 1–2 µL aliquots were analyzed by denaturing PAGE.

4.5.5 Denaturing PAGE and RNA purification

The 6-8% polyacrylamide gels containing 7M urea were prepared using 40% acrylamide and bis-acrylamide solution, 19:1 (Bio-Rad) in 1X TBE buffer (89 mM Tris Base, 89 mM Boric acid, 2 mM EDTA at pH 8.0) containing 0.04%

ammonium persulphate and 0.1% TEMED. An equal volume of 2X denaturing dye (7 M urea, 1X TBE, 50% glycerol, 50 mm EDTA, 0.1% bromophenol blue and 0.1% Xylene Cyanol) was added to the RNA samples, incubated at 65°C for 3 min, and then stored on ice until loading. GeneRuler Low Range DNA Ladder (Thermo Scientific) was used as size marker. The run was performed at 400 V at room temperature for about 1 hour, thus glass plates could reach ~50°C. The gel was wrapped in a transparent film and placed on a silica gel plate containing Fluorosyl, and the bands were visualized by UV shadowing at 354 nm, which shows a detection limit around 300 pmoles of nucleic acid. Alternatively, gels were stained for 10 min with ethidium bromide (Life Technologies) prior to visualization on the Typhoon LFA 7000 (GE Healthcare). For RNA purification, desired bands were excised from the gel and the RNA was eluted using the "crush and soak" method using ammonium acetate 0.3 M, pH 5.5 as elution buffer. The suspension was shaked overnight or at least 16 hours at 4°C. The supernatant containing the RNAs was recovered and oligonucleotides were ethanol precipitated, then RNA pellets were washed once in 70% ethanol, and finally resuspended in the desired volume of nuclease-free water or TE buffer.

4.5.6 Preparation of self-assembled aptamer-aptamer complexes

Two distinct protocols were used to generate ternary oligonucleotide complexes with DNA aptamer (DW4) and RNA aptamers (c2 and Waz) as cell penetrating aptamers. To generate the ternary complex with DW4, this delivery aptamer, fluorogenic RNA aptamer (either Spinach2 or Twins) and bridge were mixed with 1:1:1.2 molar ratio (final strand concentration, 1 μM of fluorescent RNA aptamer) in a binding buffer solution, (40 mM HEPES pH 7.4, 125 mM KCl, 5 mM $MgSO_4$). The mixture was placed in a thermoblock and heated to 90°C for 1 minute to denature the nucleic acid structures. Then the entire apparatus was placed on the workbench for 30 minutes and denatured oligo sample was slowly cooled to allow correct hybridization of complementary strands.

To generate the ternary complex with c2 and Waz, fluorogenic RNA aptamer (either Spinach2 or Twins) and bridge were firstly mixed with 1:1.4 molar ratio (final strand concentration, 1 μM of fluorescent RNA aptamer) in a binding buffer

solution, (20 mM HEPES pH 7.4, 125 mM KCl, 5 mM $MgSO_4$). After denaturation at high temperature, 1.6 fold-molar excess of delivery RNA aptamer (either c2 or Waz) was added at 45°C during the slow cooling step. Electrophoretic mobility shift assay was performed to monitor the efficiency of annealing.

4.5.7 Electrophoretic Mobility Shift Assay

Native 6% polyacrylamide gels were prepared to check the "band-shift" relative to the formation of ternary complexes. Gels were prepared using 40% acrylamide and bis-acrylamide solution, 19:1 (Bio-Rad) in 1X TBE buffer (89 mM Tris Base, 89 mM Boric acid, 2 mM EDTA at pH 8.0) containing 0.04% ammonium persulphate and 0.1% TEMED. An equal volume of 2X native loading dye (1X TBE, 50% glycerol, 50 mm EDTA, 0.1% bromophenol blue and 0.1% Xylene Cyanol) was added to the oligo samples. GeneRuler Low Range DNA Ladder (Thermo Scientific) was used as size marker. The run was performed at 230 V at 4°C for about 1 hour to avoid increase of temperature of gel plates and consequently separation of annealed strands. Gels were stained for 10 min with ethidium bromide (Life Technologies) prior to visualization on the Typhoon LFA 7000 (GE Healthcare). In case the efficiency of annealing was rather high, no purification of the bands was performed.

For ODN complex purification, desired bands were excised from the gel and the ODN was eluted using the "crush and soak" method using water as elution buffer. The suspension was shaked overnight or at least 16 hours at 4°C. The temperature of this step is essential to avoid melting of duplex region within the nucleic acid structure. The supernatant containing the ODNs was recovered and nucleic acid samples were concentrated using centrifugal filter units (3 K MWCO) and quantified by UV-VIS analysis. Hybridized complexes were incubated with 100-fold molar excess of DFHBI (or DFHBI-1T) for 30 minutes at room temperature, and then fluorescence and internalization properties were evaluated.

4.5.8 Measurement of Spinach Fluorescence

Free Spinach2, s-Baby Spinach (monomer, dimer, trimer, tetramer and pentamer), Spinach2-aptamer complexes, and Twins-aptamer complexes were incubated with 100-fold molar excess of DFHBI (or DFHBI-1T) for 30 minutes in 20 mM HEPES pH 7.4, 100 mM KCl, 5 mM NaCl, 100 μM $MgCl_2$, at 25°C. Fluorescence was measured in cuvette for each RNA and ODN assembly under the following conditions: 0.1 μM RNA (or ODN complex) and 10 μM of DFHBI (or DFHBI-1T). Fluorescence was normalized to that of 0.1 μM Spinach in 20 mM HEPES pH 7.4, 100 mM KCl, 5 mM NaCl, 100 μM $MgCl_2$, and 10 μM DFHBI (or DFHBI-1T). Final concentrations for Spinach2 and Spinach2 mutants (2'-modified RNAs) were 0.4 μM RNA and 2 μM DFHBI. In this case fluorescence was normalized to that of 0.4 μM Spinach incubated with 2 μM DFHBI. Fluorescence measurements were performed, at least in triplicate, using a 96-well EnSpire Multilabel plate reader (PerkinElmer Life Sciences) using the following instrument parameters: DFHBI excitation: 450 nm, emission 480-600 nm; DFHBI-1T excitation 480 nm, emission 500-600 nm.

4.5.9 Endocytosis in living cells and cell imaging

In a typical endocytosis assay, 2×10^5 HeLa cells and NIH-3T3 cells were seeded 24 h before the experiment in 8-well chamber slide (Nunc™ Lab-Tek™ chamber slide, Thermo Scientific) to reach 80-90% confluence. Thirty minutes prior to experiment, DMEM supplemented with 10% fetal bovine serum (FBS) was replaced with pre-treatment medium: DMEM (or PBS) supplemented with 5% FBS, 1% BSA, 20 μM tRNA, 5 μg/ml of Hoechst 33342, and 20 μM of DFHBI-1T (or DFHBI). BSA and tRNA were used as competitors for nonspecific binding sites. This step allows internalization and intracellular accumulation of the cell-permeable DFHBI-1T. After that, cells were washed twice with PBS and incubated in a free-serum medium (to avoid nuclease-mediated degradation of the RNA aptamer, i.e. either Spinach2 or Twins): DMEM containing 0.5 μM ODN assembly, 5 mM $MgSO_4$, 125 mM KCl, and 20 μM DFHBI-1T. After 30-minute incubation at 37°C, cells were washed twice with PBS and fresh DMEM

supplemented with FBS (10%), 20 μM DFHBI-1T, 5 mM $MgSO_4$, 125 mM KCl was added. About 35 minutes after the administration of the aptamer complex, the sample was imaged by confocal microscopy. Cells were imaged using a Leica TCS SP8 SMD inverted confocal microscope (Leica Microsystems AG) interfaced with a diode laser (Picoquant) for excitation at 405 nm, and with an Ar laser for excitation at 488 and. Glass bottom chamber slides containing cells were mounted in a thermostated chamber at 37°C (Leica Microsystems) and viewed with a 63x 1.2 NA water immersion objective (Leica Microsystems). The pinhole aperture was set to 1.0 Airy. All data collected were analyzed by ImageJ software version 1.44o. HiLo LUT plugin was used during image processing for the subtraction of the measured background fluorescence.

Chapter 5

Concluding remarks and research perspectives

The main purpose of this work was the development of novel aptamer-based nanoscale platforms for targeted cancer therapy having versatile designs, ease of scale-up and straightforward aptamer-payload preparation.

To discriminate between tumor and healthy cells, the delivery system should possess a targeting moiety able to recognize proteins that are expressed differentially -or exclusively- on the surface of cancer cells. Thus, I identified in the research of the proper cell-surface marker to perform targeted cancer therapy the starting point for my investigation. Transferrin receptor (TfR) is one of the most investigated tumor-associated receptors owing to its upregulation on a variety of cancer cell types over the last decade (Chapter 1) and its endogenous ligand, transferrin (Tf), has been widely investigated as targeting nanocarrier. However, exogenous Tf derivatives compete with saturating concentration of endogenous Tf, thus limiting adequate delivery of payloads to target tissues. Aptamers recognizing TfR have been recently introduced using the SELEX technology and they offer a valid alternative to Tf since they can bind different sites on TfR, avoiding the competition with the endogenous Tf or even show higher affinity towards TfR compared to the natural ligand. Importantly, besides

having potential targeting properties, these aptamers are able to internalize upon binding to TfR via receptor-mediated endocytosis.

In Chapter 2, I presented a molecular-engineering strategy to generate a drug-delivery platform able to co-deliver a chemotherapeutic agent (doxorubicin) and an inhibitor of a cell-survival factor, the NF-κB decoy oligonucleotide to human pancreatic cancer cells via an anti-human TfR RNA aptamer (c2). First, I rationally designed an extended c2 sequence bearing a double stranded DNA region to exploit the natural tendency of doxorubicin to intercalate into DNA duplex and generate an aptamer-doxorubicin conjugate. Secondary structure prediction analysis and internalization assay using dual-labeled assembly confirmed that the cell-penetrating aptamer still retain its activity after the rational modification. I assessed the stability of this complex and its potential use in an *in vitro* tumor model. Aptamer-doxorubicin complex did not release the anticancer drug after 1h incubation in serum-containing medium at 37°C, and only minor leakage was observed (<10%) after 2h incubation. The assembly resulted quite stable even at longer incubation (24h) when the leakage from the double helix was about 25%. Next, I demonstrated that aptamer-doxorubicin assembly was selective internalized into pancreatic tumor cells; intracellular release of doxorubicin was triggered by pH changes that occur at the endolysosomal compartment; negligible cytotoxic effect was detected after treatment of non-tumoral cells; doxorubicin-mediated apoptosis were specifically observed towards two different cancer cell lines (pancreatic and cervical cancer cells) though with different cytotoxicity. Particularly, cervical cancer cells displayed higher sensitivity to doxorubicin compared with the pancreatic tumor model. To sensitize resistant pancreatic cancer cells to Dox-induced apoptosis, I performed a codelivery strategy aimed at inhibiting a cell-survival factor, NF-κB, which is activated to suppress the apoptotic potential of doxorubicin, leading to chemoresistance. I designed and generated a self-assembling structure to conjugate the targeting RNA aptamer with a well-known NF-κB inhibitor, the NF-κB decoy oligonucleotide. The self-assembly process is straightforward and exploits two complementary single-stranded DNA sequences: one located within c2, which is also essential for doxorubicin intercalation, and one covalently linked to NF-κB decoy with a

disulfide bridge. I called aptacoy, the chimera generated by one aptamer and one decoy. Upon doxorubicin loading, I demonstrated that the resulting aptacoy-doxorubicin assembly was able to perform a targeted codelivery of doxorubicin and NF-κB decoy towards resistant pancreatic tumor cells, sensitizing them to doxorubicin-mediated apoptosis owing to selective inhibition of constitutive NF-κB activity.

To expand our set of TfR ligands and demonstrate the flexibility of the platform design presented in the Chapter 2, I turned my attention on a DNA aptamer (GS24) recognizing mouse TfR with no competition with the natural ligand. Particularly, this aptamer can be orthogonally used in combination with anti-human TfR aptamer as targeting ligand of drug delivery platform in a modular "plug-and-play" fashion. Chemical and biophysical studies revealed the presence of competing folding pathways, which sensibly decreased the activity of GS24 (Chapter 3). In details, chromatographic analysis shed light on the identification of two interconvertible aptamer conformers (A-1F and A-2F). Fluorescence-anisotropy measurements and internalization assay in living cells highlighted that only one fold (A-2F) was effectively able to bind mouse transferrin receptor and internalize into mouse cells. The purified active fold could also bind human TfR, albeit with a lower affinity, and it was internalized in a human pancreatic cancer cell line, which is known to overexpress human TfR. Most importantly, the two folds become nearly equimolar in the 40–42 °C interval. These data imply that the actual active form present when GS24 is administered in living cells or *in vivo* is markedly lower than expected from the nominal aptamer concentration. Thus, before to investigate the flexibility of our delivery system using GS24 as targeting tool, I fine-tuned a molecular engineering strategy aimed to stabilize the active aptamer conformation and generate a sequence with enhanced biological activity. Particularly, I exploited the synergy between molecular dynamic simulations and point mutations of GS24 to unveil the essential part involved in the folding stability of A-2F. Based on this approach, I generated four aptamer mutants and I evaluated for each sequence the percentage of the inactive fold by chromatographic analysis, the *in vitro* binding affinity towards mouse TfR, and cell-internalization properties in living mouse cells. The screening of these

aptamer features allowed us to identify an enhanced sequence, termed DW4, which exhibits increased binding efficiency and improved folding stability than the parental sequence (the inactive fold is less than 10% at 37 °C). Furthermore, this sequence was also able to bind the hTfR, more effectively than the purified active fold (A-2F) but still with a lower affinity when compared with its natural target, i.e. mTfR. Besides introducing an enhanced ligand for targeted delivery applications, this biophysical study might pave the way to a second SELEX experiment, using a doped-library. Indeed, starting from DW4 sequence, the positions involved in the folding stability might be randomized and a novel brief-selection could be performed using the human recombinant TfR as biomolecular target. This approach might lead to novel aptamer sequences able to bind efficiently both mouse and human TfR.

In Chapter 4, I reported the design and the synthesis of a modular system tailored for delivery large functional RNAs (~50-60 kDa). Starting from the platform design described in Chapter 2, I studied a strategy to generate a self-assembling oligonucleotide structure composed of two distinct modules: *(i)* a cell penetrating aptamer that promotes selective internalization in tumor cells and *(ii)* a large fluorescent RNA aptamer used as payload to track its fluorescence during endocytosis, and to evaluate folding alterations within the oligonucleotide platform. The anti-transferrin receptor aptamers (c2 and DW4) described in Chapter 2 and 3 were used as cell-penetrating aptamers ("delivery modules") and were annealed via a short oligonucleotide bridge to Spinach2, a fluorescent RNA aptamer, ("payload module"). I investigated different conditions of annealing monitoring the efficiency of hybridization among the two aptamers and the bridge. Then, aptamer-aptamer assemblies were subjected to functional assays to clarify whether both aptamers (delivery and payload) still retained their functions even when embedded in the complex. On one side, I demonstrated that Spinach2 was still able to induce the fluorescence of GFP-like chromophores after hybridization with the delivery aptamers without significant changes in its fluorescence emission. On the other, internalization assay in living cells highlighted that both anti-mouse TfR aptamer (DW4) and anti-human TfR aptamer (c2) were able to deliver Spinach2 into their specific target cells with limited off target effect. To

demonstrate the flexibility of our platform, another anti-human TfR aptamer (Waz) and an engineered dimeric version of Baby Spinach (Twins) I generated were successfully employed respectively, as delivery aptamer and fluorescent RNA payload. This work is the first demonstration of an aptamer-mediated aptamer delivery. Based on these findings, one might swap the fluorescent RNA aptamer on the platform with other therapeutic and regulatory large RNAs, such as, therapeutic aptamers, long non-coding RNA (lncRNA), and engineered structure containing multiple copies of miRNAs or siRNAs for different targeted delivery applications in living cells.

In this thesis the potential of anti-transferrin receptor RNA and DNA aptamers as targeting and delivery tools was explored. Aptamer-based nanoscale platforms were designed and generated through straightforward self-assembly, exploiting the ability of nucleic acids to yield stable complexes after annealing. Different molecular payloads ranging from an anticancer drug and a small therapeutic oligonucleotide to large fluorescent RNAs were selectively delivered in target cells via cell penetrating aptamers where they could exhibit respectively, their therapeutic activity or fluorescence. I believe that thanks to these findings further aptamer-based targeted nanocarriers will be generated taking inspirations from the designs and the strategies described in this thesis. Thanks to their flexibility, our platforms represent useful starting points for further engineering with the intriguing possibility to use appropriate combinations of aptamer ligands, therapeutic oligonucleotides and anticancer drugs that could pave the way to the development of highly functional targeted therapy representing a “magic bullet” for clinical treatments.

Bibliography

1. Sun, T. *et al.* Engineered nanoparticles for drug delivery in cancer therapy. *Angew. Chem. Int. Ed. Engl.* **53,** 12320–64 (2014).
2. Zhou, J. & Rossi, J. J. Cell-type-specific, Aptamer-functionalized Agents for Targeted Disease Therapy. *Mol. Ther. Nucleic Acids* **3,** e169 (2014).
3. Sun, H. & Zu, Y. Aptamers and Their Applications in Nanomedicine. *Small* 1–13 (2015). doi:10.1002/smll.201403073
4. Yu, M. K., Park, J. & Jon, S. Targeting strategies for multifunctional nanoparticles in cancer imaging and therapy. *Theranostics* **2,** 3–44 (2012).
5. Murdock, N. Nanopharmaceuticals (part 1): products on the market. 4357–4373 (2014).
6. Guzman-villanueva, D. Nanopharmaceuticals (part 2): products in the pipeline. 1245–1257 (2015).
7. Steichen, S. D., Caldorera-Moore, M. & Peppas, N. a. A review of current nanoparticle and targeting moieties for the delivery of cancer therapeutics. *Eur. J. Pharm. Sci.* **48,** 416–427 (2012).
8. Kobayashi, H., Watanabe, R. & Choyke, P. L. Improving conventional enhanced permeability and retention (EPR) effects; what is the appropriate target? *Theranostics* **4,** 81–9 (2013).
9. Sun, H. *et al.* Oligonucleotide aptamers: new tools for targeted cancer therapy. *Mol. Ther. Nucleic Acids* **3,** e182 (2014).
10. Srinivasarao, M., Galliford, C. V. & Low, P. S. Principles in the design of ligand-targeted cancer therapeutics and imaging agents. *Nat. Rev. Drug Discov.* (2015). doi:10.1038/nrd4519
11. Sanna, V., Pala, N. & Sechi, M. Targeted therapy using nanotechnology: focus on cancer. *Int. J. Nanomedicine* 467–483 (2014). at <http://www.ncbi.nlm.nih.gov/pmc/articles/PMC3896284/>
12. Peer, D. *et al.* Nanocarriers as an emerging platform for cancer therapy. *Nat. Nanotechnol.* **2,** 751–60 (2007).
13. Kolch, W., Halasz, M., Granovskaya, M. & Kholodenko, B. N. The dynamic control of signal transduction networks in cancer cells. *Nat. Rev. Cancer* (2015). doi:10.1038/nrc3983
14. Martin, G. Cell signaling and cancer. *Cancer Cell* **4,** 167–174 (2003).
15. Park, J. W. *et al.* Anti-HER2 Immunoliposomes : Enhanced Efficacy Attributable to Targeted Delivery 1. **8,** 1172–1181 (2002).
16. Drummond, D., Hong, K. & Park, J. Liposome targeting to tumors using vitamin and growth factor receptors. *Vitam. Horm.* **60,** (2000).
17. Senter, P. D. & Springer, C. J. Selective activation of anticancer prodrugs by monoclonal antibody – enzyme conjugates. **53,** 247–264 (2001).

18. Allen, T. M. LIGAND-TARGETED THERAPEUTICS IN ANTICANCER THERAPY. *Nat. Rev. Cancer* **2,** (2002).
19. Scott, C. C., Vacca, F. & Gruenberg, J. Endosome maturation, transport and functions. *Semin. Cell Dev. Biol.* **31,** 2–10 (2014).
20. Enrich, C., Pol, a, Calvo, M., Pons, M. & Jackle, S. Dissection of the multifunctional 'Receptor-Recycling' endocytic compartment of hepatocytes. *Hepatology* **30,** 1115–1120 (1999).
21. Grant, B. D. & Donaldson, J. G. Pathways and mechanisms of endocytic recycling. *Nat. Rev. Mol. Cell Biol.* **10,** 597–608 (2009).
22. You, J., Zhang, G. & Li, C. Exceptionally High Payload of Doxorubicin in Hollow Gold Nanospheres for Near-Infrared Light-Triggered Drug Release. *ACS Nano* **4,** 1033–1041 (2010).
23. Ritchie, M., Tchistiakova, L. & Scott, N. Implications of receptor-mediated endocytosis and intracellular trafficking dynamics in the development of antibody drug conjugates. *MAbs* **5,** 13–21 (2014).
24. Paulos, C. M., Reddy, J. A., Leamon, C. P., Turk, M. J. & Low, P. S. Ligand binding and kinetics of folate receptor recycling in vivo: impact on receptor-mediated drug delivery. *Mol. Pharmacol.* **66,** 1406–14 (2004).
25. Bostwick, D. G., Pacelli, A., Blute, M., Roche, P. & Murphy, G. P. Prostate specific membrane antigen expression in prostatic intraepithelial neoplasia and adenocarcinoma. *Cancer* **82,** 2256–2261 (1998).
26. Liu, T. *et al.* Expression of prostate specific membrane antigen (PSMA) in prostatic adenocarcinoma and prostatic intraepithelial neoplasia. *Eur. J. Nucl. Med. Mol. Imaging* **40,** 1629–30 (2013).
27. Bostwick, D. G., Pacelli, A., Blute, M., Roche, P. & Murphy, G. P. Prostate specific membrane antigen expression in prostatic intraepithelial neoplasia and adenocarcinoma. *Cancer* **82,** 2256–2261 (1998).
28. Silver, a & Fair, R. Prostate-specific Membrane Antigen Expression in Normal and Malignant Human Tissues. *Clin. Cancer Res.* **3,** 81–85 (1997).
29. Trover, J. K., Beckett, M. Lou & Wright, G. L. Detection and characterization of the prostate-specific membrane antigen (PSMA) in tissue extracts and body fluids. *Int. J. Cancer* **62,** 552–558 (1995).
30. Ghosh, A. & Heston, W. D. W. Tumor target prostate specific membrane antigen (PSMA) and its regulation in prostate cancer. *J. Cell. Biochem.* **91,** 528–39 (2004).
31. Mlcochová, P., Barinka, C., Tykvart, J., Sácha, P. & Konvalinka, J. Prostate-specific membrane antigen and its truncated form PSM'. *Prostate* **69,** 471–9 (2009).
32. Sweat, S. D., Pacelli, A., Murphy, G. P. & Bostwick, D. G. Prostate-specific membrane antigen expression is greatest in prostate adenocarcinoma and lymph node metastases. *Urology* **52,** 637–640 (1998).
33. Chang, S., Reuter, V. & Heston, W. Five different anti-prostate-specific membrane antigen (PSMA) antibodies confirm PSMA expression in tumor-associated neovasculature. *Cancer Res.* 3192–3198 (1999). at <http://cancerres.aacrjournals.org/content/59/13/3192.short>
34. Jr, O. B. G. *et al.* Interaction of prostate specific membrane antigen with clathrin and the adaptor protein complex-2. 1199–1203 (2007).

35. Su, Y. *et al.* PSMA specific single chain antibody-mediated targeted knockdown of Notch1 inhibits human prostate cancer cell proliferation and tumor growth. *Cancer Lett.* **338,** 282–91 (2013).
36. Dassie, J. P. *et al.* Targeted Inhibition of Prostate Cancer Metastases with an RNA Aptamer to Prostate-specific Membrane Antigen. *Mol. Ther.* **22,** 1910–22 (2014).
37. Rege, K., Patel, S., Megeed, Z. & Yarmush, M. Amphipathic peptide-based fusion peptides and immunoconjugates for the targeted ablation of prostate cancer cells. *Cancer Res.* 6368–6376 (2007). doi:10.1158/0008-5472.CAN-06-3658
38. Akhtar, N. H., Pail, O., Saran, A., Tyrell, L. & Tagawa, S. T. Prostate-specific membrane antigen-based therapeutics. *Adv. Urol.* **2012,** 973820 (2012).
39. English, D. P., Roque, D. M. & Santin, A. D. HER2 Expression Beyond Breast Cancer: Therapeutic Implications for Gynecologic Malignancies. *Mol. Diagn. Ther.* **17,** 85–99 (2013).
40. Gutierrez, C. & Schiff, R. HER2: Biology, detection, and clinical implications. *Arch. Pathol. Lab. Med.* **135,** 55–62 (2011).
41. Iqbal, N. Human epidermal growth factor receptor 2 (HER2) in cancers: overexpression and therapeutic implications. *Mol. Biol. Int.* **2014,** Article ID 852748, 9 pages (2014).
42. English, D. P., Roque, D. M. & Santin, A. D. HER2 Expression Beyond Breast Cancer: Therapeutic Implications for Gynecologic Malignancies. *Mol. Diagn. Ther.* **17,** 85–99 (2013).
43. Garnock-Jones, K. P., Keating, G. M. & Scott, L. J. Trastuzumab: A review of its use as adjuvant treatment in human epidermal growth factor receptor 2 (HER2)-positive early breast cancer. *Drugs* **70,** 215–39 (2010).
44. Vu, T. & Claret, F. X. Trastuzumab: updated mechanisms of action and resistance in breast cancer. *Front. Oncol.* **2,** 62 (2012).
45. Ahmad, S., Gupta, S., Kumar, R., Varshney, G. C. & Raghava, G. P. S. Herceptin resistance database for understanding mechanism of resistance in breast cancer patients. *Sci. Rep.* **4,** 4483 (2014).
46. Thiel, K. W. *et al.* Delivery of chemo-sensitizing siRNAs to HER2+-breast cancer cells using RNA aptamers. *Nucleic Acids Res.* **40,** 6319–37 (2012).
47. Korkaya, H. & Wicha, M. S. HER2 and Breast Cancer Stem Cells: More than Meets the Eye. *Cancer Res.* **73,** 3489–3493 (2013).
48. Daniels, T. R., Delgado, T., Rodriguez, J. a, Helguera, G. & Penichet, M. L. The transferrin receptor part I: Biology and targeting with cytotoxic antibodies for the treatment of cancer. *Clin. Immunol.* **121,** 144–58 (2006).
49. Hsu, V. W., Bai, M. & Li, J. Getting active: protein sorting in endocytic recycling. *Nat. Rev. Mol. Cell Biol.* (2012). doi:10.1038/nrm3332
50. Tortorella, S. & Karagiannis, T. C. Transferrin Receptor-Mediated Endocytosis: A Useful Target for Cancer Therapy. *J. Membr. Biol.* **247,** 291–307 (2014).
51. Daniels, T. R., Delgado, T., Helguera, G. & Penichet, M. L. The transferrin receptor part II: targeted delivery of therapeutic agents into cancer cells. *Clin. Immunol.* **121,** 159–76 (2006).
52. Roberts, R. L., Fine, R. E. & Sandra, a. Receptor-mediated endocytosis of transferrin at the blood-brain barrier. *J. Cell Sci.* **104 (Pt 2,** 521–32 (1993).

53. Qian, Z., Li, H., Sun, H. & Ho, K. Targeted Drug Delivery via the Transferrin Receptor-mediated endocytosis pathway. *Pharmacol. Rev.* **54,** 561–587 (2002).
54. Leoh, L. S., Daniels-Wells, T. R., Martínez-Maza, O. & Penichet, M. L. Insights into the effector functions of human IgG3 in the context of an antibody targeting transferrin receptor 1. *Mol. Immunol.* 1–9 (2015). doi:10.1016/j.molimm.2015.07.001
55. Yhee, J. Y. *et al.* Tumor-targeting transferrin nanoparticles for systemic polymerized siRNA delivery in tumor-bearing mice. *Bioconjug. Chem.* **24,** 1850–60 (2013).
56. Watts, E. R. & Dennis, M. Boosting Brain Uptake of a Therapeutic Antibody by Reducing Its Affinity for a Transcytosis Target. *Sci. Transl. Med.* **44,** (2011).
57. Mcknight, G. S., Lee, D. C. & Palmiter, R. D. Transferrin Gene Expression. *Biol. Chem.* **255,** 148–153 (1979).
58. Widera, a, Norouziyan, F. & Shen, W.-C. Mechanisms of TfR-mediated transcytosis and sorting in epithelial cells and applications toward drug delivery. *Adv. Drug Deliv. Rev.* **55,** 1439–1466 (2003).
59. Burke, D. H. Cell-penetrating RNAs: new keys to the castle. *Mol. Ther.* **20,** 251–3 (2012).
60. Schrama, D., Reisfeld, R. a. & Becker, J. C. Antibody targeted drugs as cancer therapeutics. *Nat. Rev. Drug Discov.* **5,** 147–159 (2006).
61. Scott, A. M., Wolchok, J. D. & Old, L. J. Antibody therapy of cancer. *Nat. Rev. Cancer* **12,** 278–87 (2012).
62. Peer, D. *et al.* Nanocarriers as an emerging platform for cancer therapy. *Nat. Nanotechnol.* **2,** 751–60 (2007).
63. Ruigrok, V. J. B., Levisson, M., Eppink, M. H. M., Smidt, H. & van der Oost, J. Alternative affinity tools: more attractive than antibodies? *Biochem. J.* **436,** 1–13 (2011).
64. Hu, C., Yin, J., Chau, D., Cherwonogrodzky, J. & Hu, W.-G. Active Immunity Induced by Passive IgG Post-Exposure Protection against Ricin. *Toxins (Basel).* **6,** 380–393 (2014).
65. Weiner, L. M. & Carter, P. Tunable antibodies. *Nat. Biotechnol.* **23,** 556–557 (2005).
66. Tjandra, J. J., Ramadi, L. & McKenzie, I. F. Development of human anti-murine antibody (HAMA) response in patients. *Immunol. Cell Biol.* **68 (Pt 6),** 367–376 (1990).
67. Harding, F. a., Stickler, M. M., Razo, J. & DuBridge, R. B. The immunogenicity of humanized and fully human antibodies: Residual immunogenicity resides in the CDR regions. *MAbs* **2,** 256–265 (2010).
68. Seidel, U. J. E., Schlegel, P. & Lang, P. Natural Killer Cell Mediated Antibody-Dependent Cellular Cytotoxicity in Tumor Immunotherapy with Therapeutic Antibodies. *Front. Immunol.* **4,** 1–8 (2013).
69. Stewart, R., Hammond, S. a, Oberst, M. & Wilkinson, R. W. The role of Fc gamma receptors in the activity of immunomodulatory antibodies for cancer. *J. Immunother. Cancer* **2,** 29 (2014).
70. Weiner, G. J. Building better monoclonal antibody-based therapeutics. *Nat. Rev. Cancer* **15,** 361–370 (2015).
71. Lowe, D. *et al. Aggregation, stability, and formulation of human antibody therapeutics*. *Advances in Protein Chemistry and Structural Biology* **84,** (Elsevier Inc., 2011).
72. Keefe, A. D., Pai, S. & Ellington, A. Aptamers as therapeutics. *Nat. Rev. Drug Discov.* **9,** 537–50 (2010).

73. Wakankar, A. a. *et al.* Physicochemical stability of the antibody - Drug conjugate trastuzumab-DM1: Changes due to modification and conjugation processes. *Bioconjugate Chem.* **21,** 1588–1595 (2010).
74. White, R. R. *et al.* Inhibition of rat corneal angiogenesis by a nuclease-resistant RNA aptamer specific for angiopoietin-2. *Proc. Natl. Acad. Sci. U. S. A.* **100,** 5028–5033 (2003).
75. Lao, Y.-H., Phua, K. K. L. & Leong, K. W. Aptamer Nanomedicine for Cancer Therapeutics: Barriers and Potential for Translation. *ACS Nano* **9,** 2235–2254 (2015).
76. Wahid, F., Shehzad, A., Khan, T. & Kim, Y. Y. MicroRNAs: synthesis, mechanism, function, and recent clinical trials. *Biochim. Biophys. Acta* **1803,** 1231–43 (2010).
77. Biondi, E., Maxwell, A. W. R. & Burke, D. H. A small ribozyme with dual-site kinase activity. *Nucleic Acids Res.* **40,** 7528–40 (2012).
78. Vinkenborg, J. L., Karnowski, N. & Famulok, M. Aptamers for allosteric regulation. *Nat. Chem. Biol.* **7,** 519–27 (2011).
79. Ellington, A. D. & Szostak, J. W. In vitro selection of RNA molecules that bind specific ligands. *Nature* **346,** 818–22 (1990).
80. Tuerk, C. & Gold, L. Systematic evolution of ligands by exponential enrichment: RNA ligands to bacteriophage T4 DNA polymerase. *Science (80-.).* **249,** 505–510 (1990).
81. Huang, Y. Z. *et al.* RNA aptamer-based functional ligands of the neurotrophin receptor, TrkB. *Mol. Pharmacol.* **82,** 623–35 (2012).
82. Ng, E. W. M. *et al.* Pegaptanib, a targeted anti-VEGF aptamer for ocular vascular disease. *Nat. Rev. Drug Discov.* **5,** 123–132 (2006).
83. Javier, D. J., Nitin, N., Levy, M., Ellington, A. & Richards-Kortum, R. Aptamer-targeted gold nanoparticles as molecular-specific contrast agents for reflectance imaging. *Bioconjug. Chem.* **19,** 1309–12 (2008).
84. Pei, X., Zhang, J. & Liu, J. Clinical applications of nucleic acid aptamers in cancer (Review). *Mol. Clin. Oncol.* 341–348 (2014). doi:10.3892/mco.2014.255
85. Port, J. D. & Bristow, M. R. Aptamer Therapy for Heart Failure? *Circ. Res.* **109,** 982–983 (2011).
86. Vater, a. *et al.* A Mixed Mirror-image DNA/RNA Aptamer Inhibits Glucagon and Acutely Improves Glucose Tolerance in Models of Type 1 and Type 2 Diabetes. *J. Biol. Chem.* **288,** 21136–21147 (2013).
87. Vinores, S. a. Pegaptanib in the treatment of wet, age-related macular degeneration. *Int. J. Nanomedicine* **1,** 263–268 (2006).
88. Ferrara, N., Gerber, H.-P. & LeCouter, J. The biology of VEGF and its receptors. *Nat. Med.* **9,** 669–76 (2003).
89. Lauderdale, F., Vegas, L. & Sciences, V. Pegaptanib 1-Year Systemic Safety Results from a Safety–Pharmacokinetic Trial in Patients with Neovascular Age-Related Macular Degeneration. *Ophthalmology* **114,** 1702–1712.e2 (2007).
90. Haruna, I. & Spiegelman, S. Recognition of size and sequence by an RNA replicase. *Proc. Natl. Acad. Sci.* **54,** 1189–1193 (1965).
91. Mayer, G. The chemical biology of aptamers. *Angew. Chem. Int. Ed. Engl.* **48,** 2672–89 (2009).
92. Robertson, D. L. & Joyce, G. F. Selection in vitro of an RNA enzyme that specifically cleaves single-stranded DNA. *Nature* **344,** 467–468 (1990).

93. Colas, P. *et al.* Genetic selection of peptide aptamers that recognize and inhibit cyclin-dependent kinase 2. *Nature* **380,** 548–550 (1996).
94. Crawford, M., Woodman, R. & Ferrigno, P. K. Peptide aptamers: Tools for biology and drug discovery. *Briefings Funct. Genomics Proteomics* **2,** 72–79 (2003).
95. McKeague, M. & Derosa, M. C. Challenges and opportunities for small molecule aptamer development. *J. Nucleic Acids* **2012,** 748913 (2012).
96. Chiu, T.-C. & Huang, C.-C. *Aptamer-Functionalized Nano-Biosensors*. *Sensors* **9,** (2009).
97. Zimbres, F. M., Tárnok, A., Ulrich, H. & Wrenger, C. Aptamers: novel molecules as diagnostic markers in bacterial and viral infections? *Biomed Res. Int.* **2013,** 731516 (2013).
98. Darmostuk, M., Rimpelová, S., Gbelcová, H. & Ruml, T. Current approaches in SELEX: An update to aptamer selection technology. *Biotechnol. Adv.* (2015). doi:10.1016/j.biotechadv.2015.02.008
99. Radom, F., Jurek, P. M., Mazurek, M. P., Otlewski, J. & Jeleń, F. Aptamers: Molecules of great potential. *Biotechnol. Adv.* **31,** 1260–1274 (2013).
100. Cerchia, L. & de Franciscis, V. Targeting cancer cells with nucleic acid aptamers. *Trends Biotechnol.* **28,** 517–25 (2010).
101. Rusconi, C. P. *et al.* RNA aptamers as reversible antagonists of coagulation factor IXa. *Nature* **419,** 90–94 (2002).
102. Rusconi, C. P. *et al.* Antidote-mediated control of an anticoagulant aptamer in vivo. *Nat. Biotechnol.* **22,** 1423–8 (2004).
103. Chan, M. Y. *et al.* Phase 1b Randomized Study of Antidote-Controlled Modulation of Factor IXa Activity in Patients With Stable Coronary Artery Disease. *Circulation* **117,** 2865–2874 (2008).
104. Lee, J. F., Stovall, G. M. & Ellington, A. D. Aptamer therapeutics advance. *Curr. Opin. Chem. Biol.* **10,** 282–9 (2006).
105. Pieken, W., Olsen, D., Benseler, F., Aurup, H. & Eckstein, F. Kinetic characterization of ribonuclease-resistant 2'-modified hammerhead ribozymes. *Science (80-.).* **253,** 314–317 (1991).
106. Keefe, A. D. & Cload, S. T. SELEX with modified nucleotides. *Curr. Opin. Chem. Biol.* **12,** 448–56 (2008).
107. Dua, P., Kim, S. & Lee, D.-K. Nucleic acid aptamers targeting cell-surface proteins. *Methods* **54,** 215–25 (2011).
108. Wilson, C. in (ed. Stanley T. Crooke) 773–800 (CRC Press, 2007).
109. Padilla, R. & Sousa, R. A Y639F/H784A T7 RNA polymerase double mutant displays superior properties for synthesizing RNAs with non-canonical NTPs. *Nucleic Acids Res.* **30,** e138 (2002).
110. Chelliserrykattil, J. & Ellington, A. D. Evolution of a T7 RNA polymerase variant that transcribes 2′-O-methyl RNA. *Nat. Biotechnol.* **22,** 1155–1160 (2004).
111. Ozer, A., Pagano, J. M. & Lis, J. T. New Technologies Provide Quantum Changes in the Scale, Speed, and Success of SELEX Methods and Aptamer Characterization. *Mol. Ther. Nucleic Acids* **3,** e183 (2014).
112. Schmidt, K. S. *et al.* Application of locked nucleic acids to improve aptamer in vivo stability and targeting function. *Nucleic Acids Res.* **32,** 5757–65 (2004).

113. Nolte, A; Klußmann, S.; Bald, R; Erdmann, VA; Fürste, J. & Nolte, A; Klussmann, S; Bald, R; Erdmann, VA; Furste, J. Mirror-design of L-oligonucleotide ligands binding to L-arginine. *Nat. Biotechnol.* **14,** 1116 – 1119 (1996).
114. Klussmann, S., Nolte, a, Bald, R., Erdmann, V. a & Furste, J. P. Mirror-image RNA that binds D-adenosine. *Nat. Biotechnol.* **14,** 1112–1115 (1996).
115. Tolle, F., Brändle, G. M., Matzner, D. & Mayer, G. A Versatile Approach Towards Nucleobase-Modified Aptamers. *Angew. Chem. Int. Ed. Engl.* 1–5 (2015). doi:10.1002/anie.201503652
116. Rohloff, J. C. *et al.* Nucleic Acid Ligands With Protein-like Side Chains: Modified Aptamers and Their Use as Diagnostic and Therapeutic Agents. *Mol. Ther. Nucleic Acids* **3,** e201 (2014).
117. Burmeister, P. E. *et al.* Direct In Vitro Selection of a 2′-O-Methyl Aptamer to VEGF. *Chem. Biol.* **12,** 25–33 (2005).
118. Ahrens, K., Karlas, A. & Editor, S. RNA Interference from Biology to Therapeutics. 243–257 (2013). doi:10.1007/978-1-4614-4744-3
119. Peng, L. U., Stephens, B. J., Bonin, K., Cubicciotti, R. & Guthold, M. A Combined Atomic Force / Fluorescence Microscopy Technique to Select Aptamers in a Single Cycle From a Small Pool of Random Oligonucleotides. **381,** 372–381 (2007).
120. M Sassanfar; Szostak J. An RNA motif that binds ATP. *Nature* **364,** 550–553 (1993).
121. Alam, K. K., Chang, J. L. & Burke, D. H. FASTAptamer: A Bioinformatic Toolkit for High-throughput Sequence Analysis of Combinatorial Selections. *Mol. Ther. Acids* **4,** e230 (2015).
122. Mendonsa, S. D. & Bowser, M. T. In vitro evolution of functional DNA using capillary electrophoresis. *J. Am. Chem. Soc.* **126,** 20–21 (2004).
123. Ahmad, K. M. *et al.* Probing the Limits of Aptamer Affinity with a Microfluidic SELEX Platform. *PLoS One* **6,** e27051 (2011).
124. Tok, J. B.-H. & Fischer, N. O. Single microbead SELEX for efficient ssDNA aptamer generation against botulinum neurotoxin. *Chem. Commun.* 1883 (2008). doi:10.1039/b717936g
125. Mayer, G. *et al.* Fluorescence-activated cell sorting for aptamer SELEX with cell mixtures. *Nat. Protoc.* **5,** 1993–2004 (2010).
126. Yan, A. & Levy, M. in **1103,** 241–265 (2014).
127. Shangguan, D. *et al.* Aptamers evolved from live cells as effective molecular probes for cancer study. *Proc. Natl. Acad. Sci. U. S. A.* **103,** 11838–43 (2006).
128. Cheng, C., Chen, Y. H., Lennox, K. a, Behlke, M. a & Davidson, B. L. In vivo SELEX for Identification of Brain-penetrating Aptamers. *Mol. Ther. Nucleic Acids* **2,** e67 (2013).
129. Knight, R. Analyzing partially randomized nucleic acid pools: straight dope on doping. *Nucleic Acids Res.* **31,** 30e–30 (2003).
130. Kimoto, M., Yamashige, R., Matsunaga, K., Yokoyama, S. & Hirao, I. Generation of high-affinity DNA aptamers using an expanded genetic alphabet. *Nat. Biotechnol.* **31,** 453–7 (2013).
131. Zhou, J. & Rossi, J. Cell-specific aptamer-mediated targeted drug delivery. *Oligonucleotides* **21,** 1–10 (2011).

132. Liu, Y. *et al.* Aptamers selected against the unglycosylated EGFRvIII ectodomain and delivered intracellularly reduce membrane-bound EGFRvIII and induce apoptosis. *Biol. Chem.* **390,** 137–144 (2009).
133. Ye, M. *et al.* Generating Aptamers by Cell-SELEX for Applications in Molecular Medicine. *Int. J. Mol. Sci.* **13,** 3341–53 (2012).
134. Hicke, B. J. *et al.* Tenascin-C aptamers are generated using tumor cells and purified protein. *J. Biol. Chem.* **276,** 48644–54 (2001).
135. Hicke, B. J. *et al.* Tumor targeting by an aptamer. *J. Nucl. Med.* **47,** 668–78 (2006).
136. Hernandez, L. I. *et al.* Methods for Evaluating Cell-Specific, Cell-Internalizing RNA Aptamers. *Pharmaceuticals (Basel).* **6,** 295–319 (2013).
137. Wilner, S. E. *et al.* An RNA alternative to human transferrin: a new tool for targeting human cells. *Mol. Ther. Nucleic Acids* **1,** e21 (2012).
138. Zhu, J., Huang, H., Dong, S., Ge, L. & Zhang, Y. Progress in aptamer-mediated drug delivery vehicles for cancer targeting and its implications in addressing chemotherapeutic challenges. *Theranostics* **4,** 931–44 (2014).
139. Bagalkot, V., Farokhzad, O. C., Langer, R. & Jon, S. An aptamer-doxorubicin physical conjugate as a novel targeted drug-delivery platform. *Angew. Chem. Int. Ed. Engl.* **45,** 8149–52 (2006).
140. Zhu, G. *et al.* Self-assembled aptamer-based drug carriers for bispecific cytotoxicity to cancer cells. *Chem. Asian J.* **7,** 1630–6 (2012).
141. Zhu, G. *et al.* Self-assembled, aptamer-tethered DNA nanotrains for targeted transport of molecular drugs in cancer theranostics. *Proc. Natl. Acad. Sci. U. S. A.* **110,** 7998–8003 (2013).
142. Kruspe, S., Mittelberger, F., Szameit, K. & Hahn, U. Aptamers as drug delivery vehicles. *ChemMedChem* **9,** 1998–2011 (2014).
143. Huang, Y.-F. *et al.* Molecular assembly of an aptamer-drug conjugate for targeted drug delivery to tumor cells. *Chembiochem* **10,** 862–8 (2009).
144. Boyacioglu, O., Stuart, C. H., Kulik, G. & Gmeiner, W. H. Dimeric DNA Aptamer Complexes for High-capacity-targeted Drug Delivery Using pH-sensitive Covalent Linkages. *Mol. Ther. Nucleic Acids* **2,** e107 (2013).
145. Zeman, S. M., Phillips, D. R. & Crothers, D. M. Characterization of covalent adriamycin-DNA adducts. *Proc. Natl. Acad. Sci. U. S. A.* **95,** 11561–5 (1998).
146. Fire, A. *et al.* Potent and specific genetic interference by double-stranded RNA in Caenorhabditis elegans. *Nature* **391,** 806–811 (1998).
147. Dykxhoorn, D. M., Novina, C. D. & Sharp, P. a. Killing the messenger: short RNAs that silence gene expression. *Nat. Rev. Mol. Cell Biol.* **4,** 457–67 (2003).
148. Hannon, G. J. RNA interference. *Nature* **418,** 244–251 (2002).
149. Huang, C., Li, M., Chen, C. & Yao, Q. Small interfering RNA therapy in cancer: mechanism, potential targets, and clinical applications. *Expert Opin. Ther. Targets* **12,** 637–645 (2008).
150. McNamara, J. O. *et al.* Cell type-specific delivery of siRNAs with aptamer-siRNA chimeras. *Nat. Biotechnol.* **24,** 1005–15 (2006).
151. Zhou, J. & Rossi, J. J. Aptamer-targeted cell-specific RNA interference. *Silence* **1,** 4 (2010).

152. Dassie, J. P. *et al.* Systemic administration of optimized aptamer-siRNA chimeras promotes regression of PSMA-expressing tumors. *Nat. Biotechnol.* **27,** 839–49 (2009).
153. Chu, T. C., Twu, K. Y., Ellington, A. D. & Levy, M. Aptamer mediated siRNA delivery. *Nucleic Acids Res.* **34,** e73 (2006).
154. Zhou, J. *et al.* Selection, characterization and application of new RNA HIV gp 120 aptamers for facile delivery of Dicer substrate siRNAs into HIV infected cells. *Nucleic Acids Res.* **37,** 3094–109 (2009).
155. Yoo, H., Jung, H., Kim, S. A. & Mok, H. Multivalent comb-type aptamer-siRNA conjugates for efficient and selective intracellular delivery. *Chem. Commun. (Camb).* **50,** 6765–7 (2014).
156. Farokhzad, O. C. *et al.* Nanoparticle-aptamer bioconjugates: a new approach for targeting prostate cancer cells. *Cancer Res.* **64,** 7668–72 (2004).
157. Xing, H., Tang, L., Yang, X., Hwang, K. & Wang, W. Selective delivery of an anticancer drug with aptamer-functionalized liposomes to breast cancer cells in vitro and in vivo. *J. Mater. Chem. ...* 5288–5297 (2013). doi:10.1039/c3tb20412j
158. Kim, D., Jeong, Y. Y. & Jon, S. A drug-loaded aptamer-gold nanoparticle bioconjugate for combined CT imaging and therapy of prostate cancer. *ACS Nano* **4,** 3689–96 (2010).
159. Tong, G. J., Hsiao, S. C., Carrico, Z. M. & Francis, M. B. Viral capsid DNA aptamer conjugates as multivalent cell-targeting vehicles. *J. Am. Chem. Soc.* **131,** 11174–8 (2009).
160. Li, N., Larson, T., Nguyen, H. H., Sokolov, K. V & Ellington, A. D. Directed evolution of gold nanoparticle delivery to cells. *Chem. Commun. (Camb).* **46,** 392–4 (2010).
161. Zhao, N., You, J., Zeng, Z., Li, C. & Zu, Y. An ultra pH-sensitive and aptamer-equipped nanoscale drug-delivery system for selective killing of tumor cells. *Small* **9,** 3477–84 (2013).
162. Bruno, J. G. A review of therapeutic aptamer conjugates with emphasis on new approaches. *Pharmaceuticals (Basel).* **6,** 340–57 (2013).
163. Wang, A. Z. *et al.* Superparamagnetic iron oxide nanoparticle-aptamer bioconjugates for combined prostate cancer imaging and therapy. *ChemMedChem* **3,** 1311–5 (2008).
164. Farokhzad, O. C. *et al.* Targeted nanoparticle-aptamer bioconjugates for cancer chemotherapy in vivo. *Proc. Natl. Acad. Sci. U. S. A.* **103,** 6315–20 (2006).
165. Zhang, L. *et al.* Co-delivery of hydrophobic and hydrophilic drugs from nanoparticle-aptamer bioconjugates. *ChemMedChem* **2,** 1268–71 (2007).
166. Persidis, A. Cancer multidrug resistance. *Nat. Biotechnol.* **18,** 18–20 (1999).
167. Bonizzi, G. & Karin, M. The two NF-κB activation pathways and their role in innate and adaptive immunity. *Trends Immunol.* **25,** 280–288 (2004).
168. Nakanishi, C. & Toi, M. Nuclear factor-kappaB inhibitors as sensitizers to anticancer drugs. *Nat. Rev. Cancer* **5,** 297–309 (2005).
169. Sims, J. T. *et al.* Imatinib reverses doxorubicin resistance by affecting activation of STAT3-dependent NF-κB and HSP27/p38/AKT pathways and by inhibiting ABCB1. *PLoS One* **8,** e55509 (2013).
170. Zhao, N. *et al.* MicroRNA-26b suppresses the NF-κB signaling and enhances the chemosensitivity of hepatocellular carcinoma cells by targeting TAK1 and TAB3. *Mol. Cancer* **13,** 35 (2014).

171. Li, X., Zhao, Q. & Qiu, L. Smart ligand: aptamer-mediated targeted delivery of chemotherapeutic drugs and siRNA for cancer therapy. *J. Control. Release* **171,** 152–62 (2013).
172. Gao, Y. & Wang, A. H.-J. Crystal Structures of Four Morpholino-Doxorubicin Anticancer Drugs Complexed with d(CGTACG) and d(CGATCG): Implications in Drug-DNA Crosslink. *J. Biomol. Struct. Dyn.* **13,** 103–117 (1995).
173. Frederick, C. a *et al.* Structural comparison of anticancer drug-DNA complexes: adriamycin and daunomycin. *Biochemistry* **29,** 2538–2549 (1990).
174. Dans, P. D. *et al.* Unraveling the sequence-dependent polymorphic behavior of d(CpG) steps in B-DNA. *Nucleic Acids Res.* **42,** 11304–20 (2014).
175. Zadeh, J. & Steenberg, C. NUPACK: Analysis and Design of Nucleic Acid Systems. *J. Comput. Chem.* (2011). doi:10.1002/jcc
176. Shu, D., Shu, Y., Haque, F., Abdelmawla, S. & Guo, P. Thermodynamically stable RNA three-way junction for constructing multifunctional nanoparticles for delivery of therapeutics. *Nat. Nanotechnol.* **6,** 658–67 (2011).
177. Camp, E. R. *et al.* Transferrin receptor targeting nanomedicine delivering wild-type p53 gene sensitizes pancreatic cancer to gemcitabine therapy. *Cancer Gene Ther.* **20,** 222–228 (2013).
178. Bonmati-Carrion, M. A., Alvarez-Sánchez, N., Hardeland, R., Madrid, J. A. & Rol, M. A. A Comparison of B16 Melanoma Cells and 3T3 Fibroblasts Concerning Cell Viability and ROS Production in the Presence of Melatonin, Tested Over a Wide Range of Concentrations. *Int. J. Mol. Sci.* **14,** 3901–20 (2013).
179. Kratz, F. *et al.* Transferrin conjugates of doxorubicin: synthesis, characterization, cellular uptake, and in vitro efficacy. *J. Pharm. Sci.* **87,** 338–46 (1998).
180. Sorkin, A. & von Zastrow, M. Signal transduction and endocytosis: close encounters of many kinds. *Nat. Rev. Mol. Cell Biol.* **3,** 600–614 (2002).
181. Wu, C., Han, D., Chen, T. & Peng, L. Building a multifunctional aptamer-based DNA nanoassembly for targeted cancer therapy. *J. Am. Chem. Soc.* (2013). doi:10.1021/ja4094617
182. Pintogonzalezhowell, D. Deoxyribonuclease II is a lysosomal barrier to transfection. *Mol. Ther.* **8,** 957–963 (2003).
183. Inoue, S., Setoyama, Y. & Odaka, A. Doxorubicin treatment induces tumor cell death followed by immunomodulation in a murine neuroblastoma model. *Exp. Ther. Med.* **7,** 703–708 (2014).
184. Vermes, I. & Haanen, C. A novel assay for apoptosis flow cytometric detection of phosphatidylserine expression on early apoptotic cells using fluorescein labelled annexin V. *J. Immunol. Methods* **184,** 39–51 (1995).
185. Carlo Riccardi and Ildo Nicoletti. Analysis of apoptosis by propidium iodide staining and flow cytometry. *Nat. Protoc.* **1,** 1458 – 1461 (2006).
186. Zou, G.-M. Cancer initiating cells or cancer stem cells in the gastrointestinal tract and liver. *J. Cell. Physiol.* **217,** 598–604 (2008).
187. Ohkuma, M. *et al.* Absence of CD71 Transferrin Receptor Characterizes Human Gastric Adenosquamous Carcinoma Stem Cells. *Ann. Surg. Oncol.* **19,** 1357–1364 (2012).
188. Lin, H.-H. *et al.* Tracking and Finding Slow-Proliferating/Quiescent Cancer Stem Cells with Fluorescent Nanodiamonds. *Small* **11,** 4394–4402 (2015).

189. Bottero, V. *et al.* Activation of nuclear factor kappaB through the IKK complex by the topoisomerase poisons SN38 and doxorubicin: a brake to apoptosis in HeLa human carcinoma cells. *Cancer Res.* **61,** 7785–91 (2001).
190. Cao, L.-P., Song, J.-L., Yi, X.-P. & Li, Y.-X. Double inhibition of NF-κB and XIAP via RNAi enhances the sensitivity of pancreatic cancer cells to gemcitabine. *Oncol. Rep.* **29,** 1659–65 (2013).
191. Gilmore, T. D. & Herscovitch, M. Inhibitors of NF-kappaB signaling: 785 and counting. *Oncogene* **25,** 6887–99 (2006).
192. Cooper, J. a *et al.* Attenuation of interleukin-8 production by inhibiting nuclear factor-kappaB translocation using decoy oligonucleotides. *Biochem. Pharmacol.* **59,** 605–13 (2000).
193. Shimizu, H. *et al.* NF-κB decoy oligodeoxynucleotides ameliorates osteoporosis through inhibition of activation and differentiation of osteoclasts. *Gene Ther.* **13,** 933–41 (2006).
194. De Stefano, D. *et al.* Oligonucleotide decoy to NF-kappaB slowly released from PLGA microspheres reduces chronic inflammation in rat. *Pharmacol. Res.* **60,** 33–40 (2009).
195. Yang, J., Chen, H., Vlahov, I. R., Cheng, J.-X. & Low, P. S. Evaluation of disulfide reduction during receptor-mediated endocytosis by using FRET imaging. *Proc. Natl. Acad. Sci. U. S. A.* **103,** 13872–7 (2006).
196. Chen, Z. *et al.* Receptor-mediated delivery of engineered nucleases for genome modification. *Nucleic Acids Res.* **41,** e182 (2013).
197. Giannetti, A. *et al.* FRET-based protein–DNA binding assay for detection of active NF-κB. *Sensors Actuators B Chem.* **113,** 649–654 (2006).
198. Nakamura, H. *et al.* Prevention and regression of atopic dermatitis by ointment containing NF-kB decoy oligodeoxynucleotides in NC/Nga atopic mouse model. *Gene Ther.* **9,** 1221–9 (2002).
199. Tan, Y. Codelivery of NF-κB Decoy-Related Oligodeoxynucleotide Improves LPD-Mediated Systemic Gene Transfer. *Mol. Ther.* **6,** 804–812 (2002).
200. Kocisko, D. a. *et al.* Potent antiscrapie activities of degenerate phosphorothioate oligonucleotides. *Antimicrob. Agents Chemother.* **50,** 1034–1044 (2006).
201. Lorenz, P., Baker, B. F., Bennett, C. F. & Spector, D. L. Phosphorothioate antisense oligonucleotides induce the formation of nuclear bodies. *Mol. Biol. Cell* **9,** 1007–23 (1998).
202. Shibuya, T. *et al.* A double-strand decoy DNA oligomer for NF-kappaB inhibits TNFalpha-induced ICAM-1 expression in sinusoidal endothelial cells. *Biochem. Biophys. Res. Commun.* **298,** 10–16 (2002).
203. Esposito, C. L. *et al.* Multifunctional Aptamer-miRNA Conjugates for Targeted Cancer Therapy. *Mol. Ther.* **22,** 1151–63 (2014).
204. Zhou, J., Bobbin, M. L., Burnett, J. C. & Rossi, J. J. Current progress of RNA aptamer-based therapeutics. *Front. Genet.* **3,** 234 (2012).
205. Dias, N. & Stein, C. a. Antisense Oligonucleotides : Basic Concepts and Mechanisms Minireview Antisense Oligonucleotides : Basic Concepts and Mechanisms. *Cancer Res.* **1,** 347–355 (2002).
206. Boulares, A. H. *et al.* Role of Poly(ADP-ribose) Polymerase (PARP) Cleavage in Apoptosis. *J. Biol. Chem.* **274,** 22932–22940 (1999).

207. Dai, Y. *et al.* A Smac-mimetic sensitizes prostate cancer cells to TRAIL-induced apoptosis via modulating both IAPs and NF-kappaB. *BMC Cancer* **9,** 392 (2009).
208. Lopes, R. B., Gangeswaran, R., McNeish, I. a, Wang, Y. & Lemoine, N. R. Expression of the IAP protein family is dysregulated in pancreatic cancer cells and is important for resistance to chemotherapy. *Int. J. Cancer* **120,** 2344–52 (2007).
209. Bednarski, B. K., Baldwin, A. S. & Kim, H. J. Addressing reported pro-apoptotic functions of NF-kappaB: targeted inhibition of canonical NF-kappaB enhances the apoptotic effects of doxorubicin. *PLoS One* **4,** e6992 (2009).
210. Teicher, B. a. Tumor models for efficacy determination. *Mol. Cancer Ther.* **5,** 2435–2443 (2006).
211. Chen, C. B. *et al.* Aptamer-based endocytosis of a lysosomal enzyme. *Proc. Natl. Acad. Sci. U. S. A.* **105,** 15908–13 (2008).
212. Zuker, M. Mfold web server for nucleic acid folding and hybridization prediction. *Nucleic Acids Res.* **31,** 3406–3415 (2003).
213. Huang, Z. *et al.* One RNA aptamer sequence, two structures: a collaborating pair that inhibits AMPA receptors. *Nucleic Acids Res.* **37,** 4022–32 (2009).
214. You, M. & Jaffrey, S. R. Structure and Mechanism of RNA Mimics of Green Fluorescent Protein. *Annu. Rev. Biophys.* **44,** 187–206 (2015).
215. Weill, L. Selection and evolution of NTP-specific aptamers. *Nucleic Acids Res.* **32,** 5045–5058 (2004).
216. Easton, L. E., Shibata, Y. & Lukavsky, P. J. Rapid, nondenaturing RNA purification using weak anion-exchange fast performance liquid chromatography. *RNA* **16,** 647–653 (2010).
217. Column, A. *et al.* High-Resolution Separations of Oligonucleotides on a New Strong. **54,** 53–54 (2004).
218. Anderson, a C., Scaringe, S. a, Earp, B. E. & Frederick, C. a. HPLC purification of RNA for crystallography and NMR. *RNA* **2,** 110–7 (1996).
219. Romanucci, V. *et al.* Hairpin oligonucleotides forming G-quadruplexes: new aptamers with anti-HIV activity. *Eur. J. Med. Chem.* **89,** 51–8 (2015).
220. Thayer, J. R., Wu, Y., Hansen, E., Angelino, M. D. & Rao, S. Separation of oligonucleotide phosphorothioate diastereoisomers by pellicular anion-exchange chromatography. *J. Chromatogr. A* **1218,** 802–8 (2011).
221. Buncek, M. *et al.* Unusual chromatographic behavior of oligonucleotide sequence isomers on two different anion exchange HPLC columns. *Anal. Biochem.* **348,** 300–6 (2006).
222. Zhang, M.-Z., Yu, R.-N., Chen, J., Ma, Z.-Y. & Zhao, Y.-D. Targeted quantum dots fluorescence probes functionalized with aptamer and peptide for transferrin receptor on tumor cells. *Nanotechnology* **23,** 485104 (2012).
223. Potty, A. S. R., Kourentzi, K., Fang, H., Schuck, P. & Willson, R. C. Biophysical characterization of DNA and RNA aptamer interactions with hen egg lysozyme. *Int. J. Biol. Macromol.* **48,** 392–7 (2011).
224. Fang, X., Cao, Z., Beck, T. & Tan, W. Molecular aptamer for real-time oncoprotein platelet-derived growth factor monitoring by fluorescence anisotropy. *Anal. Chem.* **73,** 5752–7 (2001).
225. Green, L. S. *et al.* Inhibitory DNA ligands to platelet-derived growth factor B-chain. *Biochemistry* **35,** 14413–24 (1996).

226. Khalil, I. a, Kogure, K., Akita, H. & Harashima, H. Uptake pathways and subsequent intracellular trafficking in nonviral gene delivery. *Pharmacol. Rev.* **58,** 32–45 (2006).
227. Kusano, T ; Steinmetz, D ; Hendrickson, W. ; et al. Direct evidence for specific binding of the replicative origin of the Escherichia coli chromosome to the membrane. *J. Bacteriol.* **158,** 313–6. (1984).
228. Le, N. C. H., Gubala, V., Gandhiraman, R. P., Daniels, S. & Williams, D. E. Evaluation of different nonspecific binding blocking agents deposited inside poly(methyl methacrylate) microfluidic flow-cells. *Langmuir* **27,** 9043–51 (2011).
229. Ng, P. P. *et al.* An anti-transferrin receptor-avidin fusion protein exhibits both strong proapoptotic activity and the ability to deliver various molecules into cancer cells. *Proc. Natl. Acad. Sci. U. S. A.* **99,** 10706–11 (2002).
230. Schmid, S. L. & Carter, L. L. ATP is required for receptor-mediated endocytosis in intact cells. *J. Cell Biol.* **111,** 2307–18 (1990).
231. Iwasa, A. *et al.* Cellular uptake and subsequent intracellular trafficking of R8-liposomes introduced at low temperature. *Biochim. Biophys. Acta - Biomembr.* **1758,** 713–720 (2006).
232. Huotari, J. & Helenius, A. Endosome maturation. *EMBO J.* **30,** 3481–500 (2011).
233. Loke, S. L. *et al.* Characterization of oligonucleotide transport into living cells. *Proc. Natl. Acad. Sci. U. S. A.* **86,** 3474–8 (1989).
234. Juliano, R. L., Ming, X., Carver, K. & Laing, B. Cellular uptake and intracellular trafficking of oligonucleotides: implications for oligonucleotide pharmacology. *Nucleic Acid Ther.* **24,** 101–13 (2014).
235. Ming, X. Cellular delivery of siRNA and antisense oligonucleotides via receptor-mediated endocytosis. *Expert Opin. Drug Deliv.* **8,** 435–49 (2011).
236. Bien-Ly, N. *et al.* Transferrin receptor (TfR) trafficking determines brain uptake of TfR antibody affinity variants. *J. Exp. Med.* **211,** 233–44 (2014).
237. Joseph R. Lakowicz. in *Principles of Fluorescence Spectroscopy* (ed. Springer) 353–381 (2006).
238. Martinez, H. M., Maizel, J. V & Shapiro, B. a. RNA2D3D: a program for generating, viewing, and comparing 3-dimensional models of RNA. *J. Biomol. Struct. Dyn.* **25,** 669–83 (2008).
239. D.A. Case, T.A. Darden, T.E. Cheatham, III, C.L. Simmerling, J. Wang, R.E. Duke, R. Luo, R.C. Walker, W. Zhang, K.M. Merz, B. Roberts, S. Hayik, A. Roitberg, G. Seabra, J. Swails, A.W. Goetz, I. Kolossváry, K.F. Wong, F. Paesani, J. Vanicek, R.M. Wolf, J., and P. A. K. AMBER 12. (2012). at <http://ambermd.org/>
240. Rencher, A. C. *'Methods of Multivariate Analysis'. IIE Transactions* **37,** (2002).
241. Madura, J. D. *et al.* Electrostatics and diffusion of molecules in solution: simulations with the University of Houston Brownian Dynamics program. *Comput. Phys. Commun.* **91,** 57–95 (1995).
242. Paige, J. S., Wu, K. Y. & Jaffrey, S. R. RNA mimics of green fluorescent protein. *Science* **333,** 642–6 (2011).
243. Warner, K. D. *et al.* Structural basis for activity of highly efficient RNA mimics of green fluorescent protein. *Nat. Struct. Mol. Biol.* 1–8 (2014). doi:10.1038/nsmb.2865
244. Pothoulakis, G., Ceroni, F., Reeve, B. & Ellis, T. The Spinach RNA aptamer as a characterization tool for synthetic biology. *ACS Synth. Biol.* **3,** 182–187 (2013).

245. Mattick, J. S. & Clark, M. B. RNA lights up. *Nat. Biotechnol.* **29,** 883–4 (2011).
246. Strack, R. L., Disney, M. D. & Jaffrey, S. R. A superfolding Spinach2 reveals the dynamic nature of trinucleotide repeat-containing RNA. *Nat. Methods* **10,** 1219–24 (2013).
247. Song, W., Strack, R. L., Svensen, N. & Jaffrey, S. R. Plug-and-play fluorophores extend the spectral properties of Spinach. *J. Am. Chem. Soc.* **136,** 1198–201 (2014).
248. Filonov, G. S., Moon, J. D., Svensen, N. & Jaffrey, S. R. Broccoli: rapid selection of an RNA mimic of green fluorescent protein by fluorescence-based selection and directed evolution. *J. Am. Chem. Soc.* **136,** 16299–308 (2014).
249. Ponchon, L. & Dardel, F. Recombinant RNA technology: the tRNA scaffold. *Nat. Methods* **4,** 571–576 (2007).
250. Huang, H. *et al.* A G-quadruplex-containing RNA activates fluorescence in a GFP-like fluorophore. *Nat. Chem. Biol.* **10,** 686–91 (2014).
251. Signore, G., Nifosì, R., Albertazzi, L., Storti, B. & Bizzarri, R. Polarity-sensitive coumarins tailored to live cell imaging. *J. Am. Chem. Soc.* **132,** 1276–88 (2010).
252. Han, K. Y., Leslie, B. J., Fei, J., Zhang, J. & Ha, T. Understanding the Photophysics of the Spinach–DFHBI RNA Aptamer–Fluorogen Complex To Improve Live-Cell RNA Imaging. *J. Am. Chem. Soc.* **135,** 19033–19038 (2013).
253. Luchowski, R. *et al.* Single Molecule Studies of Multiple-Fluorophore Labeled Antibodies. Effect of Homo-FRET on the Number of Photons Available Before Photobleaching. *Curr. Pharm. Biotechnol.* **9,** 411–420 (2008).
254. Mörl, M. & Marchfelder, A. The final cut. *EMBO Rep.* **2,** 17–20 (2001).
255. Filonov, G. S., Kam, C. W., Song, W. & Jaffrey, S. R. In-Gel Imaging of RNA Processing Using Broccoli Reveals Optimal Aptamer Expression Strategies. *Chem. Biol.* **22,** 649–660 (2015).
256. Murphy, J. E., Padilla, B. E., Hasdemir, B., Cottrell, G. S. & Bunnett, N. W. Endosomes: a legitimate platform for the signaling train. *Proc. Natl. Acad. Sci. U. S. A.* **106,** 17615–22 (2009).
257. Engedal, N. & Mills, I. G. *Endosomal signaling and oncogenesis*. *Methods in Enzymology* **535,** (Elsevier Inc., 2014).